Design of Novel Garnet Persistent Phosphors Activated with Lanthanide and Chromium Ions with Tunable Long Persistent Luminescence from Visible to Near Infrared Region

Jian Xu

Contents

Chapter 1

General Introduction

1.1. Luminescence

The term “Luminescence” (“Lumineszenz” in German) was firstly proposed by a German physicist, Eilhard Wiedemann, for “all those phenomena of light which are not solely conditioned by the rise in temperature”. By the rise in temperature, he referred to the fact that all liquids and solids can emit more and more radiation with shorter and shorter wavelengths as their temperature is continuously raised above absolute zero (0 K), which is called black-body radiation.[1] Black-body radiation is a type of electromagnetic radiation within or surrounding a body in thermodynamic equilibrium with its environment, which has a specific spectrum and intensity that depends only on the temperature (shown in Fig. 1.1).[2]

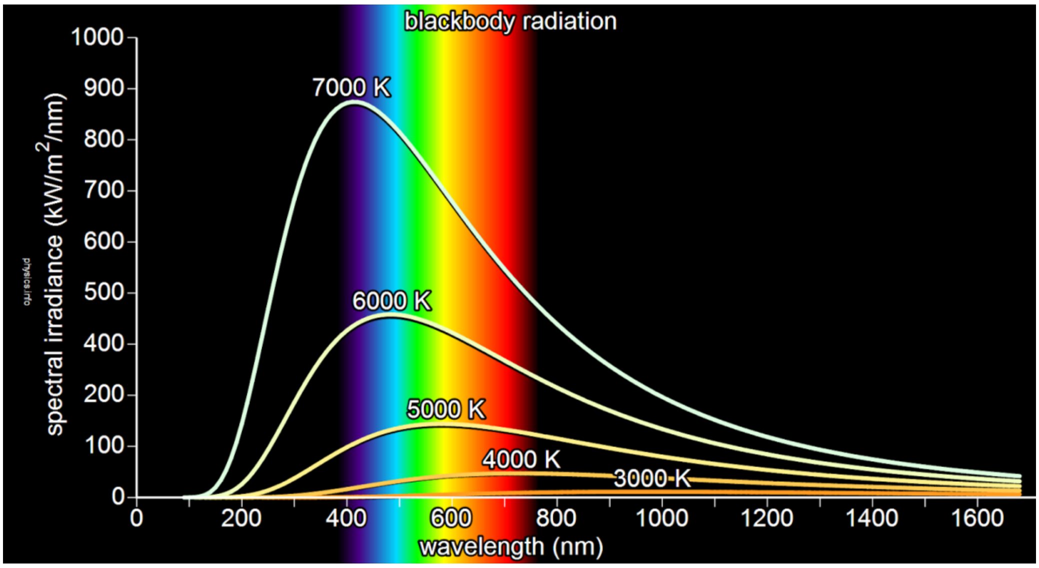

Figure 1.1. Spectral irradiance as a function of different wavelengths and temperatures[2]

In contrast to such kind of incandescence or “hot light”, luminescence is a kind of “cold light” or “cold-body radiation”, which is mainly caused by chemical reaction, mechanical action on a solid, absorption and emission of photons, bombardment by ionizing radiation, *etc* (shown in Table. 1.1). Note that in this dissertation, I only focus on two types of luminescence that are photoluminescence (PL) and thermoluminescence (TL).

PL is a kind of spontaneous electromagnetic radiation after the absorption of photons. The electron located at the ground state (equilibrium state with the lowest energy) can be excited to the excited state (disequilibrium state with higher energy) after absorbing certain photon energy, then the electronic transition of the electron from the excited state to the ground state gives a type of radiated photons, named as radiative transition. On the other hand, the electron located at the excited state also can relax to the ground state without radiation of photons but thermal energy or heat energy, which is named as non-radiative transition. Usually, the radiative transition is always accompanied by the non-radiative transition acting as a “contributor” to the luminescence. In my case, I wish to improve the possibility of the radiative transition against the non-radiative transition as possible as I can, so more absorbed photons can be transferred to be emitted photons not the thermal energy with high efficiency.

TL is another kind of luminescence that is performed by a phosphor material [the word “phosphor” derives from the Greek “φωσφοροζ”, combining “φωσ” (light) and “φερω” (to carry), and meaning light carrying],[3] when previously absorbed energy from electromagnetic radiation or other ionizing radiation is re-emitted as light upon heating. The excited electrons under pre-excitation (also named as “pre-charging”) can be trapped (electron trapping process), for extended periods of time by some localized defects (i.e. lattice defects or impurities) with certain energy levels. Quantum-mechanically, these energy levels are stationary states which possess no typical time dependence; however, they are not stable energetically. Heating the phosphor material enables the de-trapping process of the captured electrons in these localized defects inducing the luminescence at a given temperature. The typical characteristics of TL, especially the temperature dependence properties, make it crucial for the research of persistent luminescence as well as persistent phosphors. The mechanism of electron trapping and de-trapping processes will be discussed in detail in Section 2.3.

Table 1.1. Different types of luminescence phenomena and excitation sources

Luminescence	Excitation sources
Photoluminescence	**Photons**
Thermoluminescence	**Heat energy**
Mechanoluminescence	**Mechanical action**
Electroluminescence	**Electric current**
Cathodoluminescence	**Electrons**
Radioluminescence	**High energy particles**
Chemiluminescence	**Chemical reaction**

1.2. Persistent luminescence

Persistent luminescence (PersL), also known as ‘‘glow-in-the-dark’’, which is the main topic of this dissertation, is a specific type of luminescence that can last for seconds, minutes or even hours after ceasing excitation sources [ultraviolet (UV) light in most cases and visible light in rare cases]. Although, the term “persistent luminescence” is somewhat arbitrary, many different names are given to describe this special luminescence phenomenon such as “long-lasting”, “afterglow”, “phosphorescence”, “long-lasting phosphorescence (LLP)”, *etc.* After voting by the participants in the 1st International Workshop on Persistent Phosphors (Phosphors 2011) held in Ghent, Belgium, “persistent luminescence” was selected to be the most suitable and preferably unique name for this luminescence phenomenon. Therefore, the phosphors showing PersL are referred to be “persistent phosphors”.[4]

PersL was once considered as a mysterious phenomenon in the ancient time, and firstly described in a Chinese miscellaneous note called *“Xiang-shan Ye Lu”* written by Wen Ying, published in the Song dynasty (960-1279 A.D.) (see Fig. 1.2). A cow painting, by an artist named Zhi-e Xu, could be remained visible during the night and was considered to have inexplicable magic. The special ink composed of persistent phosphors used in these paintings were apparently obtained from Japan, where raw materials, such as calcium from seashells and sulfur from volcanic activities, used for the synthesis of sulfide persistent phosphors occur naturally.[3]

江南徐知諤爲潤州節度使温之少子也美姿度喜畜
奇玩蠻商得一鳳頭乃飛禽之枯骨也彩翠奪目朱
冠紺毛金嘴如生正類大雄雞廣五寸其腦平正可
爲枕諤償錢五十萬又得畫牛一軸晝則嚙草欄外
夜則歸臥欄中諤獻後主煜煜持貢闕下太宗張後
苑以示羣臣俱無知者惟僧錄贊寧曰南倭（烏和反）海
水或減則灘磧微露倭人拾方諸蚌胎中有餘淚數
滴者得之和色著物則晝隱而夜顯沃焦山時或風
欽定四庫全書　（湘山野錄　卷下）　十五
撓飄擊忽有石落海岸得之滴水磨色染物則晝顯
而夜晦諸學士皆以爲無稽寧曰見張騫海外異記
後杜鎬檢三館書目果見於六朝舊本書中載之
眞宗深念稼穡聞占城稻耐旱西天菉豆子多而粒大
各遣使以珍貨求其種占城得種二十石至今在處
播之西天中印土得菉豆種二石不知今之菉豆是
否始植於後苑秋成日宣近臣嘗之仍賜占稻及西
天菉豆御詩

Figure 1.2. Copy of the Chinese text describing the acquisition of a luminescent painting for a compilation of historical and folk tales[3]

In 1602, an Italian shoemaker, V. Casciarolo observed bright PersL from a mineral barite in darkness, later to be known as the famous Bologna stone. According to present knowledge, the material actually was not the mineral barite itself but rather the reduced product, barium sulfide (BaS) with Cu^+ impurity, and the luminescence mainly originates from the Cu^+: $3d^9 4s \rightarrow 3d^{10}$ transition.[5] At that time, during the decades following the discovery of the bright emission from the Bologna stone, this phenomenon did not cease to arouse the interest of both scientists and laymen, and even several books were written on this miraculous phenomenon (see Fig. 1.3).[6]

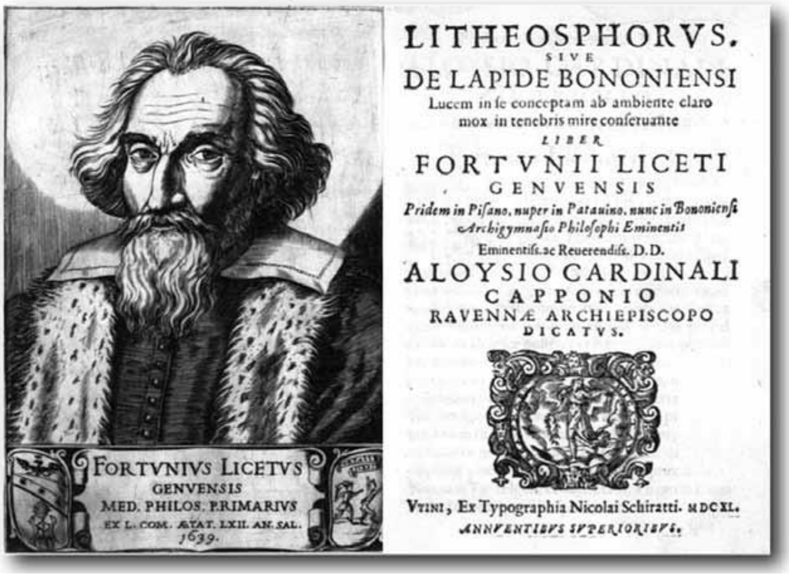

FORTVNIVS LICETVS
GENVENSIS
MED. PHILOS. PRIMARIVS
EX L. COM. ÆTAT. LXII. AN. SAL.
1639.

LITHEOSPHORVS.
SIVE
DE LAPIDE BONONIENSI
Lucem in ſe conceptam ab ambiente claro
mox in tenebris mire conſeruante
LIBER
FORTVNII LICETI
GENVENSIS
Pridem in Piſano, nuper in Patauino, nunc in Bononienſi
Archigymnaſio Philoſophi Eminentis
Eminentiſs. ac Reuerendiſs. D.D.
ALOYSIO CARDINALI
CAPPONIO
RAVENNÆ ARCHIEPISCOPO
DICATVS.

VTINI, Ex Typographia Nicolai Schiratti. MDCXL.
ANNVENTIBVS SVPERIORIBVS.

Figure 1.3. The book "*Litheosphorus Sive de Lapide Bononiensi*" written by Fortunius Licetus (Bologna, Italy, 1640) on the persistent luminescence of the Bologna stone[6]

Until the end of the 20th century, very little research was done on the development of persistent phosphors and the understanding of physical meaning behind. For many decades, zinc sulfide (ZnS) doped with copper (and later co-doped with cobalt) was the most famous and widely used persistent phosphor.[7] It was used in many commercial products including watch dials, luminous paints and glow-in-the-dark toys, *etc*. However, the brightness and duration that could be achieved with this material was rather weak and short for practical purposes. In order to solve this problem, traces of radioactive elements such as promethium, radium or tritium were often introduced in the phosphors as doping ions to stimulate and improve the brightness and duration of the light emission under the continuous irradiation of α- and/or β-rays produced by radioactive decay of these radioactive ions.[8] But still, the PersL performance of these materials is far behind the requirements of the real practical or industrial applications.

By the 1990s, there was increased public concern regarding the health problems and environmental pollution caused by radioactive elements. In addition, there was a decrease in the annual sales of watches with persistent phosphors based on radioactive elements, while the demand for clocks with the storage-type (chargeable by indoor illumination, fluorescent lamp in most cases) persistent phosphors increased despite their relatively weak persistent luminance.[8] Considering the potentially huge market behind of persistent phosphors, Nemoto & Co., Ltd.（根本特殊化学株式会社）in Japan, whose major business is the development, manufacture, and sales of persistent phosphors, decided to develop novel persistent phosphors with high brightness and long duration, especially without environment-unfriendly radioactive doping ions. Finally, on Mar. 12th, 1993. T. Matsuzawa’s R&D team successfully developed the well-known green persistent phosphor, $SrAl_2O_4$:Eu^{2+}-Dy^{3+} with ten-fold higher brightness and longer duration compared with that of the ZnS-based persistent phosphors (see Fig. 1.4).[8,9] In 1996, T. Matsuzawa and his co-workers published the milestone research article titled “A New Long Phosphorescent Phosphor with High Brightness, $SrAl_2O_4$:Eu^{2+}-Dy^{3+}” in the *Journal of the Electrochemistry Society*,[9] and sent a big shockwave to the relatively unpopular field of PersL and persistent phosphors at that time. Then, this phosphor rapidly replaced its predecessor, ZnS-based persistent phosphors in the business market which had been used for nearly one century. Although, even till now, the physical meaning and the PersL mechanism about this material is still an open question and under debate, this paper[9] marked the beginning of a renewed search for different and better persistent phosphors emitting in different wavelength regions, and has already been cited by 1095 times (Web of Science, on Jan. 18th, 2017) during the past 20 years.

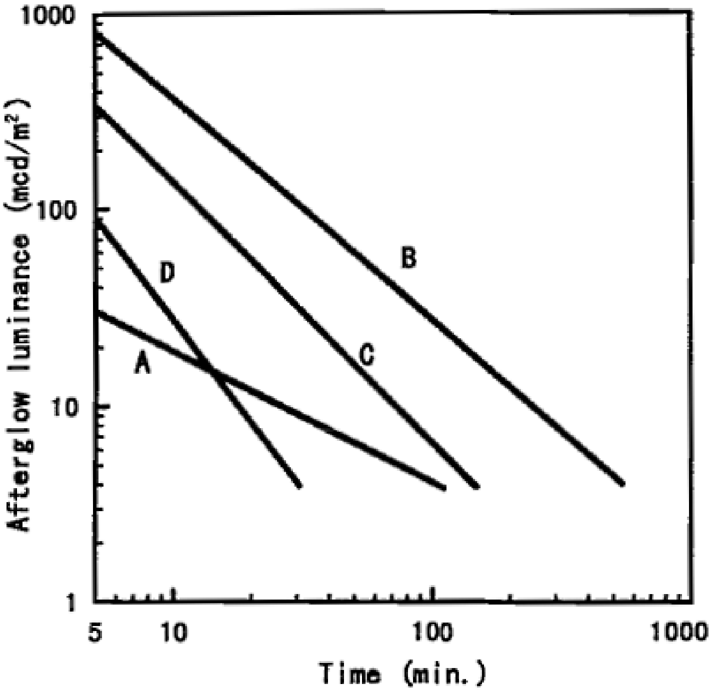

Figure 1.4. Phosphorescence characteristics measured at 22 ℃ after 10 min exposure to 200 lx of D_{65} light (the standard light with the color temperature of 6504 K). A: $SrAl_2O_4:Eu^{2+}$, B: $SrAl_2O_4:Eu^{2+}$, Dy^{3+}; C: $SrAl_2O_4:Eu^{2+}$, Nd^{3+}; D: commercially used ZnS:Cu, Co phosphors[9]

1.2.1. Application of persistent luminescence in the visible light region

The visible light is the portion of electromagnetic spectrum that is visible to human eyes, usually ranging from 380 to 750 nm (see Fig. 1.5). The spectrum does not, however, contains all the colors that human eyes can distinguish. For example, pink, magenta or purple are absent because they can be made only by a mixture of multiple wavelengths. Colors containing only one wavelength are also called pure colors or spectral colors, a typical example is the pure green color due to the Er^{3+}:$^4S_{3/2} \rightarrow {}^4I_{15/2}$ transition located at 555 nm observed in many different Er^{3+} doped phosphors.

It is worth noting that, although the visible light can be observed and distinguished by human eyes, the sensitivity or response of human eyes for different colors is quite different. Fig. 1.5 gives two visions of human eyes, one is the photopic vision and the other is the scotopic vision. Photopic vision is the vision of human eyes under well-lit conditions (luminance from 10 to 10^8 cd/m^2),[10] which allows color perception, mediated by cone cells, and a significantly high visual acuity and temporal resolution. On the other hand, scotopic vision is the vision of human eyes under relatively low light conditions (luminance from 10^{-3} to 10^{-6} cd/m^2).[10] Since cone cells in human eyes are nonfunctional under low light conditions, the scotopic vision is produced exclusively through rod cells which are most sensitive to wavelengths of light around 500 nm (green-blue) and insensitive to wavelengths longer than ~640 nm (red). The cover of sensitivity ranges from the scotopic vision to the photopic vision provides the vision throughout the whole visible light spectrum, and the maximum efficiency of the photopic vision is 683 lm/W at 555 nm (green).

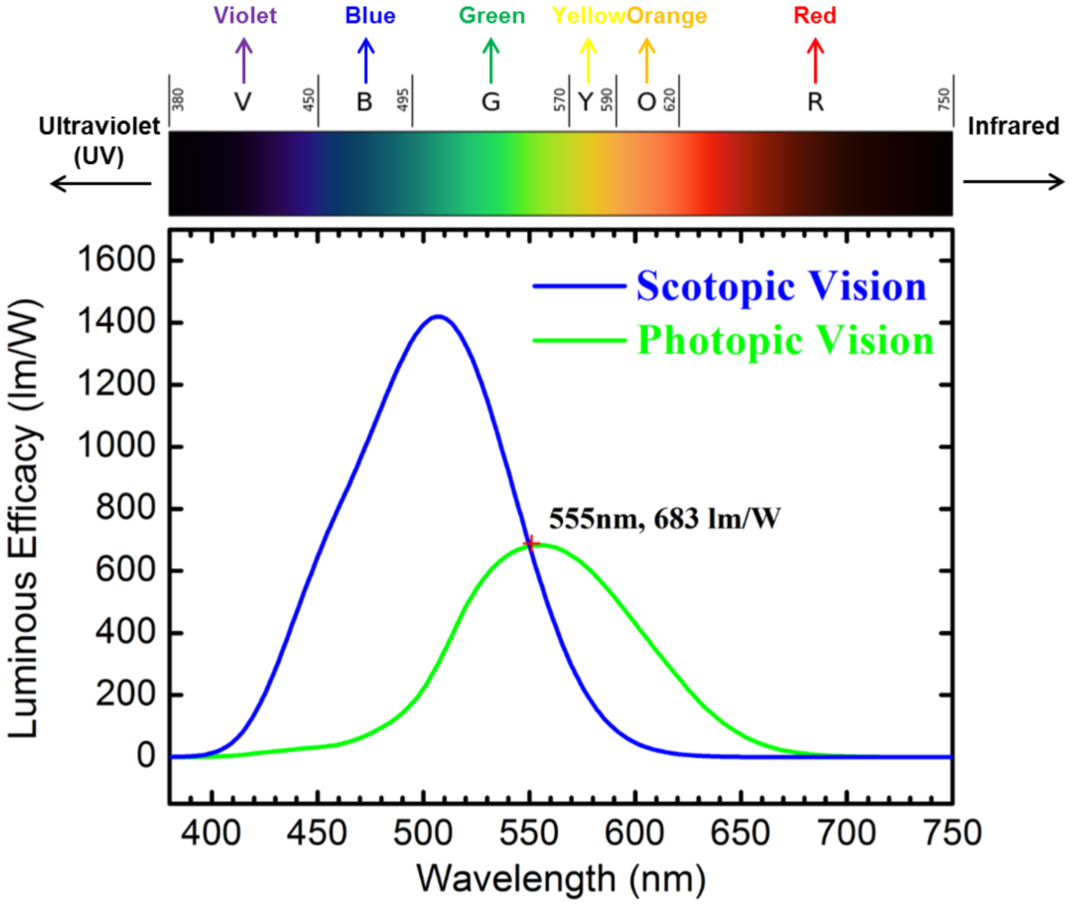

Figure 1.5. Visible light region *V.S.* scotopic and photopic visions of human eyes

As mentioned before, persistent phosphors emitting visible light have already been commercialized for watch dials, toys, and safety signage applications, such as emergency exit signs in buildings and guiding strips in the aisles of airplanes (see Fig. 1.6).[11] Since Red, Green, and Blue (RGB) are the three primary colors that can be added together in various ways to reproduce a broad array of colors. Developing persistent phosphors emitting RGB PersL with high brightness and long duration is particularly important for practical applications. Fig. 1.7 gives the photographs and corresponding PersL emission spectra of three representative persistent phosphors, $Y_2O_2S:Eu^{2+}$-Mg^{3+}-Ti^{4+} (red), $SrAl_2O_4:Eu^{2+}$-Dy^{3+} (green) and $Sr_2MgSi_2O_7:Eu^{2+}$-Dy^{3+} (blue) as an example.[6] Bright RGB PersL was clearly observed from these pellet samples after ceasing the UV excitation source.

It is also worth noting that, since the red color is much less sensitive to human eyes compared with blue and green colors, radiance (in unit of $mW/Sr/m^2$) is more accurate than luminance (in unit of mcd/m^2) to evaluate the "brightness" of different persistent phosphors, especially whose emitting wavelength is at the edge or out of the range of the visible light (i.e. UV or infrared).[12]

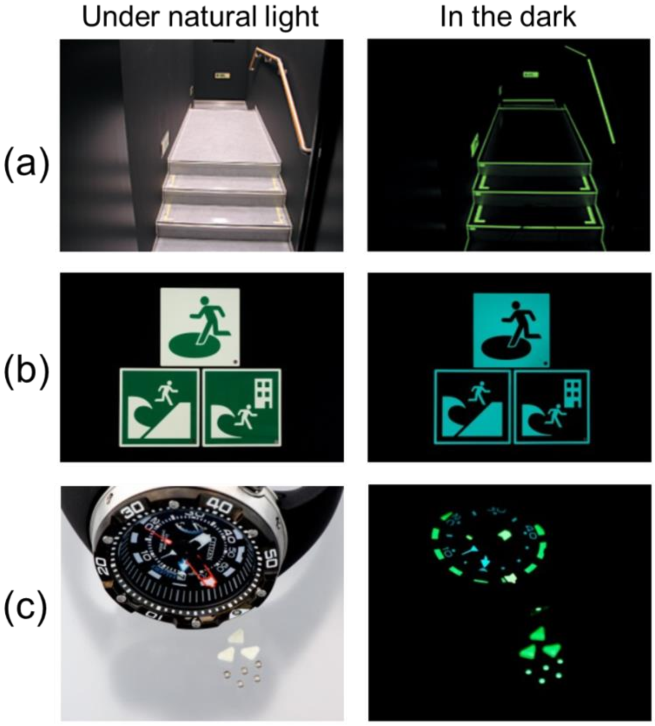

Figure 1.6. Application examples of persistent phosphors (Nemoto & Co., Ltd.): (a) night-vision signs (b) emergency exit signs (c) watch dials[11]

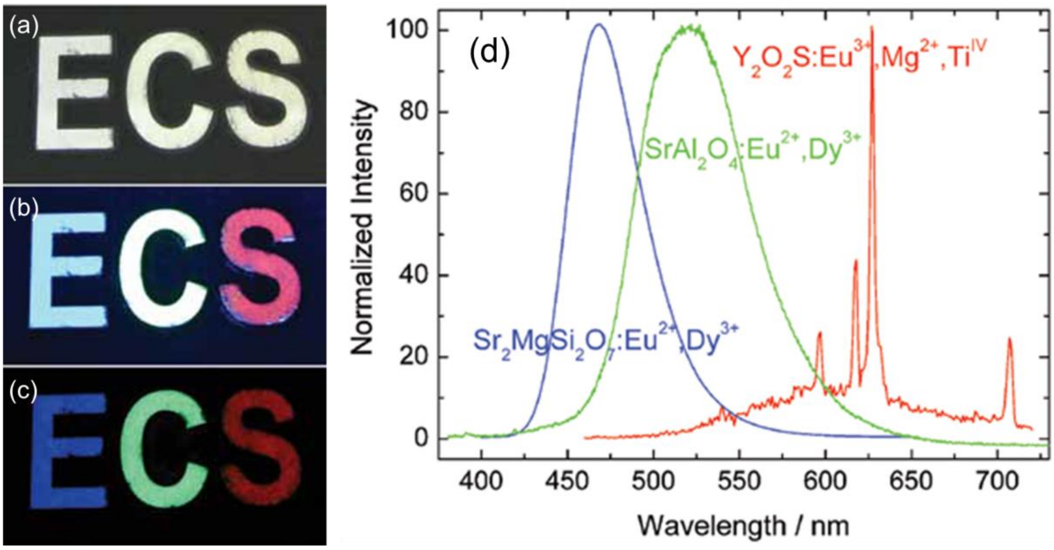

Figure 1.7. RGB persistent phosphors: Y_2O_2S:Eu^{2+}-Mg^{3+}-Ti^{4+} (red), $SrAl_2O_4$:Eu^{2+}-Dy^{3+} (green), $Sr_2MgSi_2O_7$:Eu^{2+}-Dy^{3+} (blue); (a) under day light (b) under UV excitation (c) in the dark (d) corresponding persistent luminescence spectra after ceasing the UV excitation[6]

1.2.2. Application of persistent luminescence in the near-infrared region

Near-infrared (NIR) is an invisible radiant energy, electromagnetic radiation with longer wavelengths than those of visible light, extending from the nominal red edge of the visible light spectrum at ~700 nm to ~2500 nm. Most of the thermal radiation emitted by objects around room temperature (*RT*) at ~300 K is infrared and invisible (see Fig. 1.1). Typical applications including optical imaging, physiological diagnostics, functional neuroimaging, and telecommunication, *etc* are working within this very important and popular wavelength region.

Optical imaging, also commonly referred as fluorescence imaging, is one of the most promising imaging techniques and is expected to be an alternative for other well established imaging techniques, such as magnetic resonance imaging (MRI), computed tomography (CT), electron tomography (ET), positron emission tomography (PET), and X-ray imaging, *etc*. The technique basically requires luminescent bio-markers/probes and advanced detection machines. Thus, the current interest in this research field is focused on the development of efficient optical detectors/sensors and the discovery of novel luminescent materials as fluorescent probes.

As typical fluorescent bio-markers/probes for bio-imaging, such as organic dyes, semiconductor quantum dots (QDs), fluorescent proteins, *etc* have already been widely used and studied for several decades. However, most of them suffer from a high photo-bleaching rate (photochemical destruction of a fluorophore under light exposure, especially UV light), poor signal-to-noise ratio (SNR) due to auto-fluorescence from living bodies (i.e. proteins are well known to give emission under UV light exposure), and poor bio-compatibility (organic dyes and most of the QDs are potentially toxic), which limits their practical applications in bio-fields.[13]

In principle, these bio-markers/probes give emission by the usual fluorescence process, in which a high energy excitation source (i.e. UV light) is used to excite a fluorophore, and the emission thereby is observed in the visible light region, which is used for the visualization of different bio-information. However, when it comes to the *in vivo* bio-imaging, the performance of these bio-markers/probes becomes rather bad since the penetration depth of UV and visible light for living bodies is very limited (mm scale) so that high SNR from a considerable deep depth (cm scale) of the living body is usually difficult to be obtained (see Fig. 1.8).[14] Therefore, NIR-to-NIR fluorescence bio-markers/probes (excitation and emission wavelengths are both in the NIR region) were recently proposed considering much deeper penetration depth for living bodies using NIR light than that of the UV or visible light.[15,16]

Persistent phosphors, as mentioned before, can exhibit “self-sustained” PersL for even several hours after ceasing excitation sources. Hence, persistent phosphors with NIR PersL charged by UV light before injection into living bodies can be used as long-lasting bio-markers/probes for the *in vivo* bio-imaging. The exclusion of real-time external illumination totally removes the auto-fluorescence as background noise, avoids the complicated background subtraction procedures and thus improves the SNR remarkably. In 2007, Q. le Masne de Chermont et al firstly reported and demonstrated the *in vivo* bio-imaging technique using NIR persistent phosphors ($Ca_{0.2}Zn_{0.9}Mg_{0.9}Si_2O_6$:$Eu^{2+}$, Dy^{3+}, Mn^{2+}) as shown in Fig. 1.9,[17] this new generation excitation-free bio-imaging technique totally avoids the auto-fluorescence effects from living bodies (mouse), and gives a high SNR for the mouse imaging.

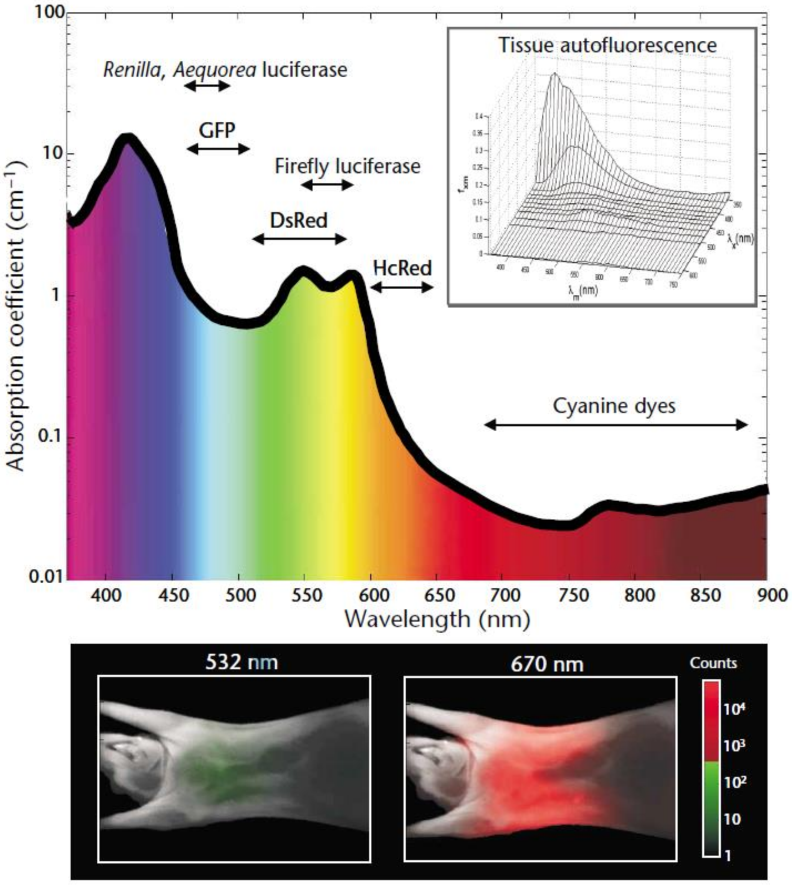

Figure 1.8. Interaction of light with tissue: the absorption coefficient of light in tissue is dependent on wavelength and results from absorbers such as hemoglobins, lipids and water. The insert shows auto-fluorescence spectra obtained *in vivo* at different excitation wavelengths. Note the much lower tissue auto-fluorescence at longer wavelengths. The mouse images at the bottom show experimentally measured photon counts through the body of a nude mouse at 532 nm (left) and 670 nm (right). Signal in the NIR range is ~4 orders of magnitude stronger compared with that in the green range under otherwise identical conditions, illustrating the advantages for imaging with NIR photons[14]

Seven years later, in 2014, the second generation NIR persistent phosphor ($ZnGa_2O_4$:Cr^{3+}) was successfully developed by T. Maldiney, B. Viana, A. Bessière and C. Richard et al,[18] and applied for *in vivo* bio-imaging (see Fig. 1.10). Compared with the previous $Ca_{0.2}Zn_{0.9}Mg_{0.9}Si_2O_6$:$Eu^{2+}$, Dy^{3+}, Mn^{2+} persistent phosphor, the novel $ZnGa_2O_4$:Cr^{3+} persistent phosphor emits much brighter NIR PersL due to the highly efficient Cr^{3+}: ^2E (^2G)→$^4A_2$ (^4F) transition (*R*-line) and the anti-site defect related N_2-line. The SNR was over 6 times in the liver zone of the mouse compared with that using a coventional QDs bio-probe because of the unique non-auto-fluorescence merit using persistent phosphors. This new bio-imaging technology has soon become quite attractive and motive the fast development of NIR persistent phosphors.[19-23]

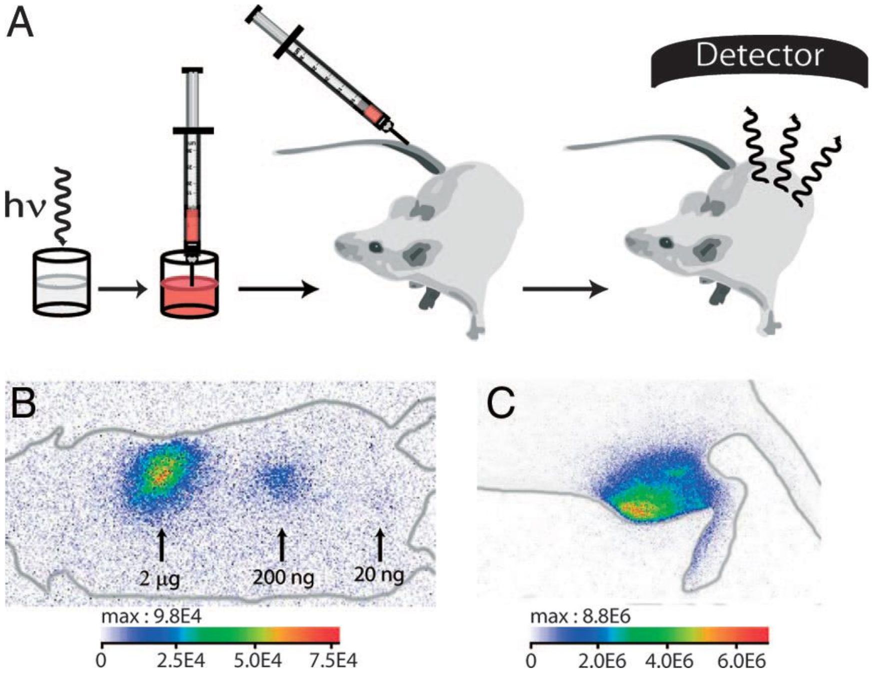

Figure 1.9. Principles of *in vivo* experiments and first in vivo images: (A) A suspension containing a proper amount of nano-particles (NPs) is excited with an UV lamp and is directly injected to an anesthetized mouse. The signal is then acquired with an intensified CCD camera. (B) Image of three injections of NPs. The different localizations are labeled with arrows, and the corresponding NP amounts are indicated. The acquisition was performed during the 2 min after injection. (C) Image of an intramuscular injection corresponding to a 90 s acquisition[17]

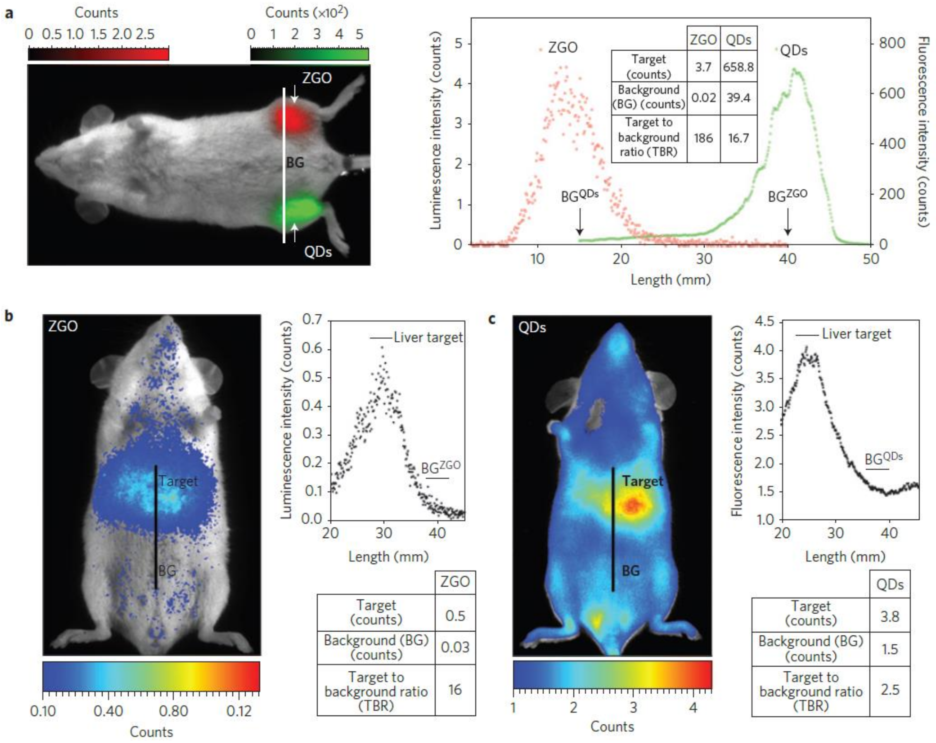

Figure 1.10. *In vivo* comparison of negatively charged QDs and persistent luminescent nano-particles (PLNPs): a–c, after intramuscular (a) and after intravenous (b,c) injection in healthy mice[18]

It is also worth noting that, although this new bio-imaging technology has soon become a hot research topic while the most reported emission region of NIR persistent phosphors are located in the first biological window (NIR-I, 650-950 nm), partially due to the easy availability of commercial Si-detectors that work well in this region.

Since the Rayleigh scattering (varies as λ^{-4}, here λ is the wavelength) decrease with increasing wavelength, two more biological windows called the second (NIR-II, 1000-1350 nm) and the third (NIR-III, approximately from 1500 nm to 1800 nm) ones are defined, which fall on either side of a strong water absorption band centered around 1450 nm (see Fig. 1.11). Compared with the NIR-I window, these two windows, give much lower scattering coefficient leading potentially to an improved resolution quality and deeper penetration depth.[24-27] Moreover, thanks to the recent development of affordable InGaAs detectors that possess adequate sensitivity and high quantum efficiency in the wavelength region above 1000 nm and up to 1650 nm, the shift of the luminescent wavelength of the bio-imaging probe from the NIR-I to the NIR-II/III window is definitely demanded. However, even for NIR-to-NIR fluorescence bio-probes using real-time excited PL for *in vivo* imaging, only a few candidates are available for such a long wavelength. Therefore, the development of nontoxic and bio-compatible persistent phosphors suitable for the NIR-II/III window, still remains a big challenge.[15,16]

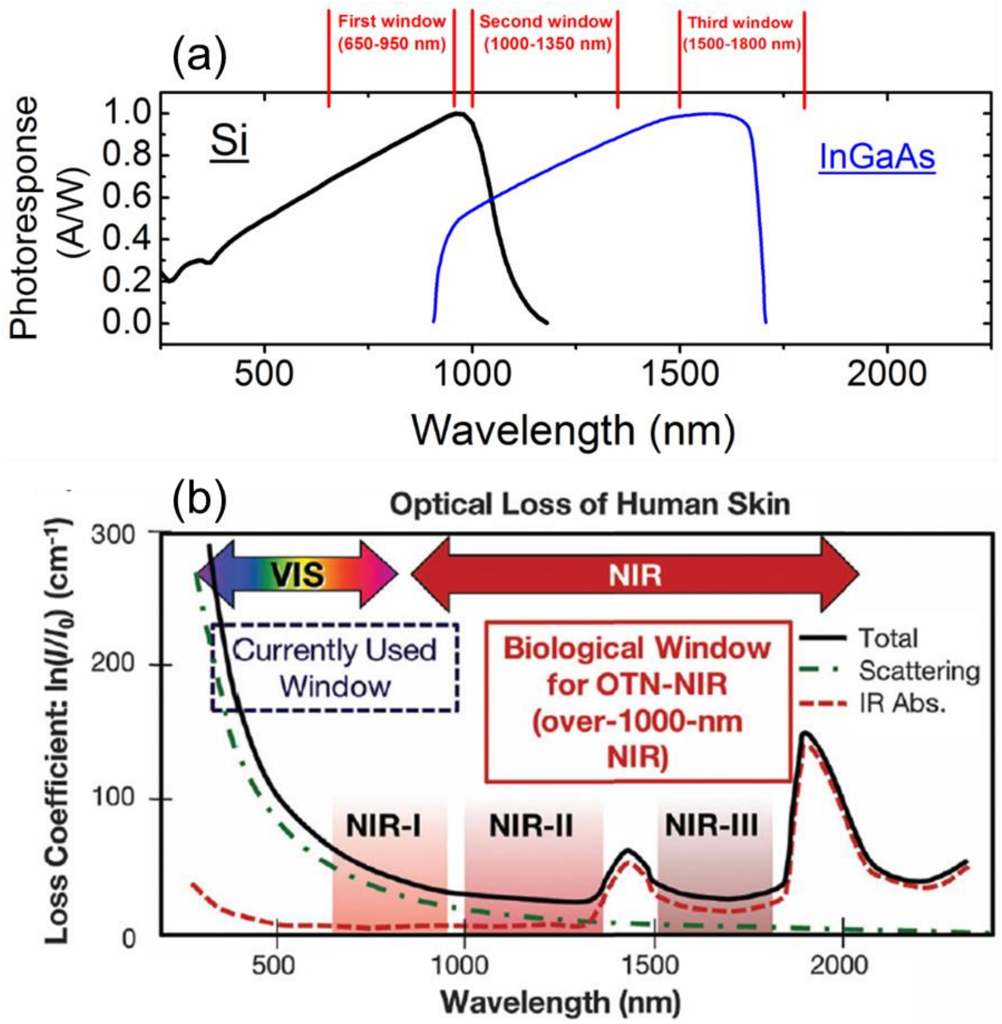

Figure 1.11. (a) Response curves of Si and InGaAs photo-diode detectors (b) the absorption spectrum of human skin showing the first (NIR-I), second (NIR-II) and third (NIR-III) biological windows[15]

1.3. Outline of this dissertation

In Chapter 1, we start from two applications of persistent phosphors (i) safety signage/night vision applications in the visible light region; (ii) *in vivo* bio-imaging applications in the NIR region. Brief histories, important progresses, some existing problems, and personal perspectives are introduced. As described in this part, although persistent luminescence was observed and firstly recorded in China nearly 1000 years ago, the progress on the understanding of this mysterious “self-sustained” luminescence phenomenon and the development of new persistent phosphors with high brightness and long duration is rather slow. Until 1993, T. Matsuzawa et al from Nemoto & Co., Ltd. (Japan) dropped a bomb to this “unpopular” research field because of the discovery of the super long green persistent phosphor, $SrAl_2O_4:Eu^{2+}$-Dy^{3+}. Since then, this “unpopular” research field becomes more and more “popular”, great efforts have been made on either understanding the mechanism of persistent luminescence or developing novel persistent phosphors with different emitting colors. As a result, numerous persistent phosphors emitting long persistent luminescence in the visible light region have been successfully developed, and some of them have been commercialized for watch dials, toys, and safety signage, *etc* that are now commonly used in our daily lives. On the other hand, in 2007, Q. le Masne de Chermont et al from France gave anthor shockwave to this research field since they demonstrated that NIR persistent phosphors can be used as a new generation bio-probes for *in vivo* bio-imaging with high signal-to-noise ratio. The merits of such kind of NIR perssistent luminescence nano-particles (PLNPs) like excitation-free, non-auto-fluorescence, long monitoring time, deep penetration for living bodies, *etc* describe a bright and pormising future for the *in vivo* bio-imaging, and thus motive the fast development of NIR persistent phosphors, especially in the recent 3-4 years

In Chapter 2, basic knowledge on luminescence is summarized. Starting from the *f-f* and *f-d* transitions from lanthanide ions, and *d-d* transitions from transition metal ions (emphasized on Cr^{3+}). The progress playing an important role in the dynamics of persistent luminescence, the electron trapping-detrapping process, is discussed. Finally, as the only disscussed crystal structure in this dissertation, garnet structure in the form of $A_3B_2C_3O_{12}$ is briefly introduced, its flexible structure for either doping with rare-earth ions in the *A* site or transition metal ions in the *B*, *C* sites acts as fundamentals in my research life.

In Chapter 3, blue-light-chargeable $Y_3Al_2Ga_3O_{12}$ (YAG*G*):Ce^{3+}-Cr^{3+} green transparent ceramic persistent phosphors with different thicknesses were fabricated by solid state reaction and vacuum sintering method. Compared with an opaque YAG*G*:Ce^{3+}-Cr^{3+} ceramic phosphor of the same composition, the corresponding transparent ceramic phosphors exhibited brighter persistent luminescence after ceasing blue light excitation (460 nm) due to a typical “volume effect” of transparent materials. The duration that the persistent luminescence intensity reaches 2 mcd/m^2 of the YAG*G*:Ce^{3+}-Cr^{3+} transparent ceramic (846 min) with 2.8 mm thickness was nearly twice of that of the compacted pellet made of the most widely used $SrAl_2O_4$:Eu^{2+}-Dy^{3+} commercial powder (433 min).

In Chapter 4, based on the vacuum referred binding energy (*VRBE*) diagram of the $Y_3Al_2Ga_3O_{12}$ (YAG*G*) host, Pr^{3+}, Nd^{3+}, Tb^{3+}, Dy^{3+} ions were selected and co-doped with Cr^{3+} ions to develop novel persistent phosphors. Since the energy gaps between the ground states of Pr^{3+}/Tb^{3+} and the top of valence band (*VB*) are large enough so that Pr^{3+}/Tb^{3+} ions can be stable hole traps, collaborating with Cr^{3+} electron traps to induce the long persistent luminescence. The persistent luminance duration upon 0.32 mcd/m^2 of the YAG*G*:Pr-Cr and YAG*G*:Tb-Cr samples due to Pr^{3+} (orange) and Tb^{3+} (light green) emission could reach about 8 h and 12 h, respectively. However, because of the small energy gaps between the ground states of Nd^{3+}/Dy^{3+} and the top of *VB*, Nd^{3+}/Dy^{3+} ions cannot act as stable hole traps. Therefore, the persistent luminescent intensities of YAG*G*:Nd-Cr and YAG*G*:Dy-Cr samples are quite weak and dominated mainly by the deep-red transition of Cr^{3+}.

In Chapter 5, a novel red ceramic phosphor: $Y_3Al_{5-x}Ga_xO_{12}$:Cr^{3+} (YAG*G*:Cr^{3+}, x from 0 to 5), showing bright persistent luminescence was developed by conventional solid-state reaction method. After ceasing UV illumination, the radiance of this material was nearly 5 times higher than that of the commonly used $ZnGa_2O_4$:Cr^{3+} red persistent phosphor. This behavior was mainly attributed to the efficient electron trapping and detrapping processes and one could adjust electron trap depth through different Ga^{3+} contents.

In Chapter 6, we developed bright deep-red persistent phosphors of Cr^{3+}-Eu^{3+} co-doped $Gd_3Al_{5-x}Ga_xO_{12}$ garnets (GAG*G*:Cr^{3+}-Eu^{3+}), in which only Cr^{3+} ion shows emission bands centered at 730 nm after ceasing UV illumination and Eu^{3+} ion acts as an excellent electron trap capturing one electron to be Eu^{2+} with tunable trap depth by varying conduction band with Ga^{3+} content, x. The persistent radiance of the GG*G*:Cr^{3+}-Eu^{3+} (x=5) sample at 1 h after ceasing UV light is approximately 25 times higher than that of the Cr^{3+} singly doped GG*G* sample, and is over 6 times higher than that of the widely used $ZnGa_2O_4$:Cr^{3+} red persistent phosphor.

In Chapter 7, we developed a persistent phosphor of $Y_3Al_2Ga_3O_{12}$ doped with Nd^{3+}, Ce^{3+}, Cr^{3+} ions (YAG*G*:Nd-Ce-Cr) exhibiting long (>10 h) persistent luminescence at multi-wavelengths of around 880, 1064, and 1335 nm due to *f*-*f* transitions of Nd^{3+} and at 505 nm due to the Ce^{3+}:$5d_1 \rightarrow 4f$ transition. The intense near-infrared (NIR) persistent luminescence bands from Nd^{3+} match well with the first (650~950 nm) and second (1000~1350 nm) bio-imaging windows. The NIR persistent radiance of the YAG*G*:Nd-Ce-Cr phosphor (0.33×10^{-1} mW/Sr/m^2) at 60 min after ceasing blue light illumination was over 2 times higher than that of the widely used $ZnGa_2O_4$:Cr^{3+} red persistent phosphor (0.15×10^{-1} mW/Sr/m^2).

In Chapter 8, by utilizing efficient persistent energy transfer from Ce^{3+} to Er^{3+}, we have successfully developed a novel garnet persistent phosphor of $Y_3Al_2Ga_3O_{12}$ doped with Er^{3+}, Ce^{3+}, Cr^{3+} ions (YAG*G*:Er-Ce-Cr) exhibiting long (>10 h) near-infrared (NIR) persistent luminescence (PersL) in the broad range from 1450 nm to 1670 nm due to the typical Er^{3+}:$^4I_{13/2} \rightarrow {}^4I_{15/2}$ transition in garnet. The NIR PersL bands of Er^{3+} match well with the third bio-imaging window (NIR-III, approximately from 1500 nm to 1800 nm) and the response curve of InGaAs detectors. The photon emission rate (8.33×10^{17} cps/Sr/m^2) of the YAG*G*:Er-Ce-Cr persistent phosphor at 10 min after ceasing blue light illumination was over two times higher than that of the widely used $ZnGa_2O_4$:Cr^{3+} deep-red persistent phosphor (3.30×10^{17} cps/Sr/m^2). We also show the first PersL imaging by a commercial InGaAs camera monitoring Er^{3+} emission indicating that this material can be a promising candidate for *in-vivo* bio-imaging in the NIR-III window.

In Chapter 9, we have successfully developed six different Cr^{3+} singly-doped garnets with cubic structure of $A_3B_2C_3O_{12}$: $Y_3Ga_{4.99}Cr_{0.01}O_{12}$ (YG*G*:Cr), $Gd_3Ga_{4.99}Cr_{0.01}O_{12}$ (GG*G*:Cr), $Lu_3Ga_{4.99}Cr_{0.01}O_{12}$ (LuG*G*:Cr), $Y_3Sc_{1.99}Cr_{0.01}Ga_3O_{12}$ (YSG*G*:Cr), $Gd_3Sc_{1.99}Cr_{0.01}Ga_3O_{12}$ (GSG*G*:Cr) and $Lu_3Sc_{1.99}Cr_{0.01}Ga_3O_{12}$ (LuSG*G*:Cr), which exhibit persistent luminescence due to Cr^{3+} emission matching well with both the response curve of the Si detector and the wavelength region of the first biological window (NIR-I). The main emission band of Cr^{3+} in garnet hosts can be easily tunable from the sharp *R*-line emission due to the $^2E\ (^2G) \rightarrow {}^4A_2\ (^4F)$

transition in the strong crystal field strength to the broad band emission due to the $^4T_2$ (^{4}F)→$^4A_2$ (^{4}F) transition in the weak one when Lu^{3+} in the *A* site and Ga^{3+} in the *B* site are respectively replaced by larger cations, Y^{3+}/Gd^{3+} and Sc^{3+}. Especially the GSG*G*:Cr sample, its *R*-line emission was totally disappeared while only the broad band emission peaked at around 770 nm was observed, and its persistent radiance (0.54×10^{-1} mW/Sr/m^2) at 60 min after ceasing the UV excitation was over three times higher than that of the widely used ZGO:Cr deep-red persistent phosphor (0.15×10^{-1} mW/Sr/m^2) at *RT*. Furthermore, based on the knowledge of 4*f* energy levels of lanthanide ions in the host referred binding energy (*HRBE*) diagram of GSG*G* host, four trivalent lanthanides (Sm^{3+}, Eu^{3+}, Tm^{3+}, Yb^{3+}) whose 2+ *GS* located below the bottom of *CB* were selected as potential candidates to be an electron trap in order to enhance the Cr^{3+} PersL. Among them, Yb^{3+} could introduce a new electron trap with a TL glow peak located around 330 K overlapped with the intrinsic defect (photochromic center)-related electron trap in garnet host, and the persistent radiance of the GSG*G*:Cr-Yb sample (1.56×10^{-1} mW/Sr/m^2) at 60 min after ceasing the UV excitation was enhanced to be nearly three times higher than that of the GSG*G*:Cr persistent phosphor (0.54×10^{-1} mW/Sr/m^2) at *RT*.

References

[1] E. N. Harvey, *A History of Luminescence: From the Earliest Times until 1900;* American Philosophical Society: Philadelphia, PA, 1957.

[2] https://260h.pbworks.com/w/page/69071363/Beginnings%20of%20Quantum%20Mechanics

[3] W. M. Yen and M. J. Weber, *Inorganic Phosphors: Compositions, Preparation and Optical Properties;* CRC Press, Boca Raton, FL, 2004, pp. 445-446.

[4] P. F. Smet, D. Poelman, and M. P. Hehlen, *Opt. Mater. Express.* 2012, 2(4), 452−454.

[5] Y. Lin, Z. Tang, Z. Zhang, X. Wang, J. Zhang, *J. Mat. Sci. Lett.* 2011, 2, 1505-1506.

[6] J. Hölsä, *Electrochem. Soc. Interface*. 2009, 18 (4), 42−45.

[7] K. van den Eeckhout, P. F. Smet and D. Poelman, *Materials*. 2010, 3, 2536.

[8] J. Ueda, *Towards Future Earth;* Kaisei Publishing Co., Ltd. Chiyoda-ku, Tokyo, Japan, 2016,

pp. 130.

[9] T. Matsuzawa, Y. Aoki, N. Takeuchi, Y. Murayama, *J. Electrochem. Soc.* 1996, 143, 2670-2673.

[10] J. Pokorny, V. C. Smith, G. Verriest, and A. J. L. G. Pinckers, *Congenital and Acquired Color Vision Defects,* Grune & Stratton, 1979

[11] https://www.nemoto.co.jp/

[12] Y. Zhuang, Y. Katayama, J. Ueda, and S. Tanabe, *Opt. Mater.* 2014, 36, 1907-1912.

[13] S. K. Singh, *RSC Adv.* 2014, 4, 58674-58698.

[14] R. Weissleder and V. Ntziachristos, *Nat. Med.* 2003, 9, 123-128

[15] E. Hemmer, N. Venkatachalam, H. Hyodo, A. Hattori, Y. Ebina, H. Kishimoto and K. Soga, *Nanoscale*. 2013, 5, 11339-11361.

[16] E. Hemmer, A. Benayas, F. Légaré and F. Vetrone, *Nanoscale Horiz.*, 2016, 1, 168-184.

[17] Q. le Masne de Chermont, C. Chanéac, J. Seguin, F. Pellé, S. Maîtrejean, J. P. Jolivet, D. Gourier, M. Bessodes and D. Scherman, *Proc. Natl. Acad. Sci. U.S.A*. 2007,104, 9266-9271.

[18] T. Maldiney, A. Bessière, J. Seguin, E. Teston, S. K. Sharma, B. Viana, A. J. J. Bos, P. Dorenbos, M. Bessodes, D. Gourier, D. Scherman and C. Richard, *Nat. Mater*., 2014, 13, 418-426.

[19] K. Van Den Eeckhout, D. Poelman and P. F. Smet, *Materials*. 2013, 6, 2789-2818.

[20] B. Viana, S. K. Sharma, D. Gourier, T. Maldiney, E. Teston, D. Scherman and C. Richard, *J. Lumin*., 2016, 170, 879-887.

[21] F. Liu, W. Yan, Y. J. Chuang, Z. Zhen, J. Xie and Z. Pan, *Sci. Rep*., 2013, 3, 1554-1562.

[22] Z. W. Pan, Y. Y. Lu and F. Liu, *Nat. Mater*., 2012, 11, 58-63.

[23] Y. Li, M. Gecevicius and J. Qiu, *Chem. Soc. Rev.* 2016, 45, 2090-2136.

[24] D. J. Naczynski, M. C. Tan, M. Zevon, B. Wall, J. Kohl, A. Kulesa, S. Chen, C. M. Roth, R. E. Riman and P. V. Moghe, *Nat. Commun*., 2013, 4, 2199 (10 pp).

[25] L. A. Sordillo, Y. Pu, S. Pratavieira, Y. Budansky and R. R. Alfano, *J. Biomed. Opt*., 2014, 19, 056004 (6 pp).

[26] L. A. Sordillo, S. Pratavieira, Y. Pu, K. S. Ramirez, L. Shi, L. Zhang, Y. Budansky and R. R. Alfano, *Proc. of SPIE*. 2014, 8940, 89400V (7 pp).

[27] A. M. Smith, M. Mancini, and S. Nie, *Nature. Nanotech.* 2009, 4, 710-711.

Chapter 2

Theoretical Background

2.1. Luminescence center of lanthanide ions

2.1.1. Rare earth elements

Rare earth elements are a group of 17 elements in the periodic table including 15 lanthanides (Ln) [from Lanthanum (La) to Lutetium (Lu)], as well as Scandium (Sc) and Yttrium (Y) (see Fig. 2.1).[1] Scandium and Yttrium are considered to be rare earth elements because they tend to occur in the same ore deposits as the lanthanides and exhibit similar chemical properties. Note that, despite their name, rare earth elements sometimes are not really rare or even relatively plentiful in the Earth's crust. A typical example is Cerium (Ce), which is the 25th most abundant element at 68 parts per million (ppm), as abundant as copper (Cu). On the other hand, rare earth elements tend to occur together in nature and are difficult to separate from one to another, and also the highly concentrated minerals with rare earth elements are not often found in economically exploitable ore deposits, which make them usually more expensive than most base metals such as iron (Fe), copper (Cu), aluminum (Al), or nickel (Ni), *etc*.

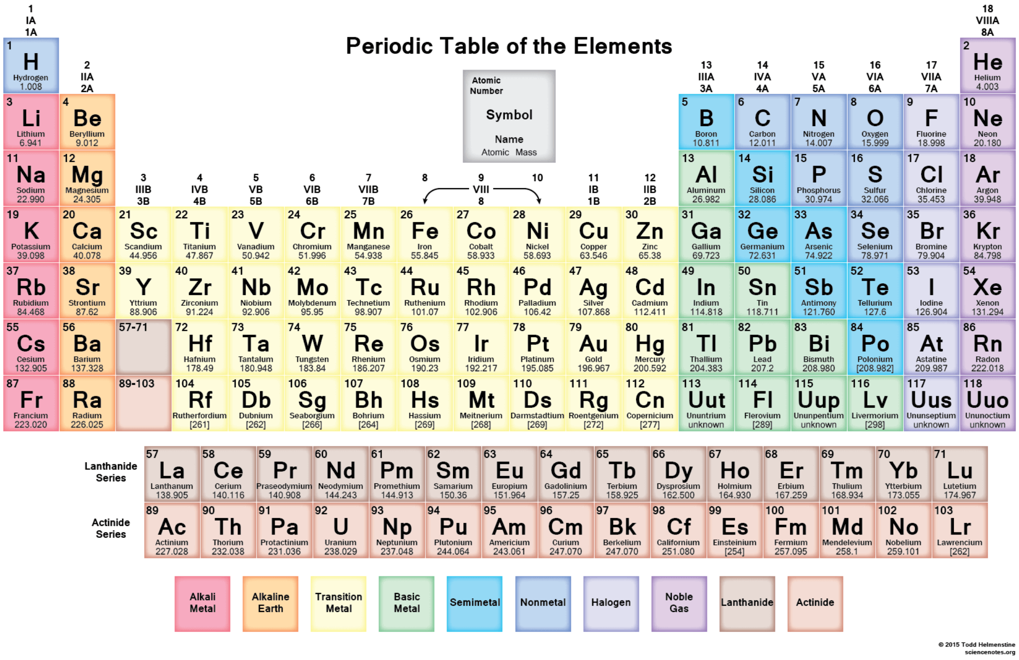

Figure 2.1. The periodic table of different elements[1]

2.1.2. Lanthanide ions

In presentations of the periodic table, the lanthanides are customarily shown as an additional row below the main body of the table. The electron configurations of the lanthanides and their tri-valent state ions are described below:

Ln (Z=57~71):$1s^2 2s^2 2p^6 3s^2 3p^6 3d^{10} 4s^2 4p^6 4d^{10} 4f^n 5s^2 5p^6 5d^1 6s^2$=[Xe]$(4f)^n 5d^1 6s^2$

Ln^{3+} (Z=57~71):$1s^2 2s^2 2p^6 3s^2 3p^6 3d^{10} 4s^2 4p^6 4d^{10} 4f^n 5s^2 5p^6$=[Xe]$(4f)^n$

In general, the lanthanides exhibit tri-valent states (Ln^{3+}) while some of them also show di-valent (i.e. Eu^{2+}, Yb^{2+}) and tetra-valent (i.e. Ce^{4+}, Pr^{4+} or Tb^{4+}) states according to different host materials or preparation conditions. All the Ln^{3+} ions have unfilled/filled electron shell structure $4f^n$ (n=1-14) (shown in Table 2.1), the partially/fully occupied $4f^n$ electrons of these Ln^{3+} ions are not in the outer shell and well shielded by the filled $5s^2$ and $5p^6$ orbitals (see Fig. 2.2), the ligand and/or crystal field environment thereby has only a very weak influence on the electronic cloud of Ln^{3+} ions even in solid crystal materials. Therefore, the energy levels of Ln^{3+} ions remain nearly unchanged in different material hosts, but exhibit only a minor deviation due to the nephelauxetic effect caused by the Ln-to-ligand bonding, which reduces the effective positive charge on nucleus compared with its free Ln^{3+} ion counterpart, and also makes effects on its energy levels by a few cm^{-1}. Therefore, such weak interaction is mainly responsible for the fine spectral structure of Ln^{3+} ions, and the well-resolved energy levels of Ln^{3+} ions lead to sharp absorption and emission transitions in spectral shapes.

Fig. 2.3 gives the typical 4*f* energy levels of different Ln^{3+} doping ions in a low-symmetry crystal, LaF_3.[2] This diagram gives a general idea of the 4*f* energy level locations of all Ln^{3+} ions and helps us for the analysis of unknown spectra in different material hosts, and also to determine or even predict the exact energy level positions of target Ln^{3+} ions.[3]

It is also worth noting that, when one electron transit between the 4*f* and 5*d* orbitals, the electronic transition is named as the $4f^n \leftrightarrow 4f^{n-1}5d$ (*f*-*d*) transition. The *f*-*d* transition is often observed in di-valent (i.e. Eu^{2+}, Yb^{2+}) and tri-valent (i.e. Ce^{3+}, Pr^{3+} or Tb^{3+}) lanthanide ions. Since the 5*d* orbital is in the outer shell and more dependent on the ligand and/or crystal field environment than the 4f^n orbital in different material hosts, the *f*-*d* transitions usually exhibit broad bands in spectra due to the Frank-Condon offset between the two parabolas of 4*f* and 5*d* orbitals in the configuration coordinate diagram.[5]

Table 2.1. Atomic numbers, names, electron configurations and radii of lanthanide atoms as well as the corresponding tri-valent ions[3]

Atomic No.	Lanthanide	Ln^{3+} (ground states)	Radii of Ln^{3+} (Å)
58	**Cerium (Ce)**	$4f^1 5s^2 5p^6$ ($^4F_{5/2}$)	1.034
59	**Praseodymium (Pr)**	$4f^2 5s^2 5p^6$ ($^3H_4$)	1.013
60	**Neodymium (Nd)**	$4f^3 5s^2 5p^6$ ($^4I_{9/2}$)	0.995
61	**Promethium (Pm)**	$4f^4 5s^2 5p^6$ ($^5I_4$)	0.980
62	**Samarium (Sm)**	$4f^5 5s^2 5p^6$ ($^6H_{5/2}$)	0.964
63	**Europium (Eu)**	$4f^6 5s^2 5p^6$ ($^7F_0$)	0.950
64	**Gadolinium (Gd)**	$4f^7 5s^2 5p^6$ ($^8S_{7/2}$)	0.938
65	**Terbium (Tb)**	$4f^8 5s^2 5p^6$ ($^7F_6$)	0.923
66	**Dysprosium (Dy)**	$4f^9 5s^2 5p^6$ ($^6H_{15/2}$)	0.908
67	**Holmium (Ho)**	$4f^{10} 5s^2 5p^6$ ($^5I_8$)	0.894
68	**Erbium (Er)**	$4f^{11} 5s^2 5p^6$ ($^4I_{15/2}$)	0.881
69	**Thulium (Tm)**	$4f^{12} 5s^2 5p^6$ ($^3H_6$)	0869
70	**Ytterbium (Yb)**	$4f^{13} 5s^2 5p^6$ ($^2F_{7/2}$)	0.858
71	**Lutetium (Lu)**	$4f^{14} 5s^2 5p^6$ ($^1S_0$)	0.848

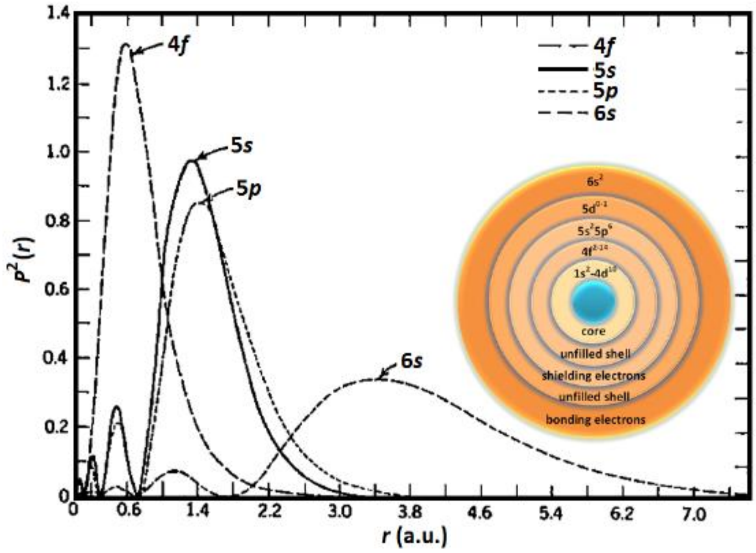

Figure 2.2. Shielding effect of 4*f* orbitals by 5*s* and 5*p* orbitals[4]

2.1.3. 4*f* energy levels of lanthanide ions

A major outcome from the electronic spectra of Ln^{3+} ions is the assignment of these numerous 4f^n energy levels, which is of particularly useful for their applications.

For multi-electron free (gaseous) Ln^{3+} ions, the energy levels of each electronic configuration will be split into a series of energy levels, owing to the interaction between the electron orbital magnetic moment and the spin magnetic moment. These states can be described under the Russell-Saunders scheme by the multiplet $^{2S+1}L_J$ composed of $(2S+1)(2L+1)$ states, where S and L denote the total electron spin and orbital angular momenta, respectively. The values of L=0, 1, 2, 3, 4, 5, 6, 7, 8 are used to be designated by the letters S, P, D, F, G, H, I, K, L in spectroscopy. Due to the coupling of the orbital angular momentum and the spin angular momentum in quantum mechanics, these multiplets ^{2S+1}L are usually composed of total 2J +1 possible microstates, where J is the total (i.e. vector sum of S and L) angular momenta.[5]

When it comes to the coupling scheme of the orbital angular momentum and the spin angular momentum, LS coupling (Russell-Saunders coupling) is the most commonly used coupling scheme for Ln^{3+} ions, in view of their much stronger electrostatic interaction between different 4f electrons relative to their spin-orbit interaction. In this model, the spin momenta s_i and orbital momenta l_i of all the electrons are first coupled by exchange interaction to form a total spin and orbital angular momenta S and L, respectively, and then the total spin angular momentum S couples with the total orbital angular momentum L into the total angular momentum J. According to this coupling scheme, the possible microstates can be descried by $^{2S+1}L_J$. For example, for $4f^1$ configuration of Ce^{3+}, there are two multiplets, that is, $^2F_{5/2}$ and $^2F_{7/2}$, where S=1/2, L=3, and J =5/2 or 7/2. For $4f^n$ configurations of other Ln^{3+} ions, the allowed spectroscopic multiplets or terms were summarized in Table 2.2.[3]

It is worth noting that some qualitative rules are very helpful to understand the energy levels of Ln^{3+} ions. One of the well-known qualitative rules is Hund's rule, which has the following guidelines: (1) the terms (or states) with the largest S values have the lowest energy values among all the terms of an electron configuration. Among these terms, those with the highest L values have the lowest energy values (2) for the terms in configuration with a number of electrons equal or exceeding that of the half-filled shell, the larger the J value, the lower the energy. On the other hand, if the number of electrons lower than that of half-filled shell, then the smaller the J value, the lower the energy.[5]

Table 2.2. Allowed spectroscopic multiplets or terms for $4f^{n}$ electrons of tri-valent lanthanide ions[3]

Ln^{3+} ions	Configurations	Spectroscopic multiplets or terms
Ce^{3+}, Yb^{3+}	f^{1}, f^{13}	$^{2}F^{1}$
Pr^{3+}, Tm^{3+}	f^{2}, f^{12}	$^{1}S^{1}$, $^{1}D^{1}$, $^{1}G^{1}$, $^{1}I^{1}$, $^{3}P^{1}$, $^{3}H^{1}$
Nd^{3+}, Er^{3+}	f^{3}, f^{11}	$^{2}P^{1}$, $^{2}D^{2}$, $^{2}F^{2}$, $^{2}G^{2}$, $^{2}H^{2}$, $^{2}I^{1}$, $^{2}K^{1}$, $^{2}L^{1}$, $^{4}S^{1}$, $^{4}D^{1}$, $^{4}F^{1}$, $^{4}G^{1}$, $^{4}I^{1}$
Pm^{3+}, Ho^{3+}	f^{4}, f^{10}	$^{1}S^{2}$, $^{1}D^{4}$, $^{1}F^{1}$, $^{1}G^{4}$, $^{1}H^{2}$, $^{1}I^{3}$, $^{1}K^{1}$, $^{1}L^{2}$, $^{1}N^{1}$, $^{3}P^{3}$, $^{3}D^{2}$, $^{3}F^{4}$, $^{3}G^{3}$, $^{3}H^{4}$, $^{3}I^{2}$, $^{3}K^{2}$, $^{3}L^{1}$, $^{3}M^{1}$, $^{5}S^{1}$, $^{5}D^{1}$, $^{5}F^{1}$, $^{5}G^{1}$, $^{5}I^{1}$
Sm^{3+}, Dy^{3+}	f^{5}, f^{9}	$^{2}P^{4}$, $^{2}D^{5}$, $^{2}F^{7}$, $^{2}G^{6}$, $^{2}H^{7}$, $^{2}I^{5}$, $^{2}K^{5}$, $^{2}L^{3}$, $^{2}M^{2}$, $^{2}N^{1}$, $^{2}O^{1}$, $^{4}S^{1}$, $^{4}P^{2}$, $^{4}D^{3}$, $^{4}F^{4}$, $^{4}G^{4}$, $^{4}H^{3}$, $^{4}I^{3}$, $^{4}K^{2}$, $^{4}L^{1}$, $^{4}M^{1}$, $^{6}P^{1}$, $^{6}F^{1}$, $^{6}H^{1}$
Eu^{3+}, Tb^{3+}	f^{6}, f^{8}	$^{1}S^{2}$, $^{1}P^{1}$, $^{1}D^{6}$, $^{1}F^{4}$, $^{1}G^{8}$, $^{1}H^{4}$, $^{1}I^{7}$, $^{1}K^{3}$, $^{1}L^{4}$, $^{1}M^{2}$, $^{1}N^{2}$, $^{1}Q^{1}$, $^{3}P^{6}$, $^{3}D^{5}$, $^{3}F^{9}$, $^{3}G^{7}$, $^{3}H^{9}$, $^{3}I^{6}$, $^{3}K^{6}$, $^{3}L^{3}$, $^{3}M^{3}$, $^{3}N^{1}$, $^{3}O^{1}$, $^{5}S^{1}$, $^{5}P^{1}$, $^{5}D^{3}$, $^{5}F^{2}$, $^{5}G^{3}$, $^{5}H^{2}$, $^{5}I^{2}$, $^{5}K^{1}$, $^{5}L^{1}$, $^{7}F^{1}$
Gd^{3+}	f^{7}	$^{2}S^{2}$, $^{2}P^{5}$, $^{2}D^{7}$, $^{2}F^{10}$, $^{2}G^{10}$, $^{2}H^{9}$, $^{2}I^{9}$, $^{2}K^{7}$, $^{2}L^{5}$, $^{2}M^{4}$, $^{2}N^{2}$, $^{2}O^{1}$, $^{2}Q^{1}$, $^{4}S^{2}$, $^{4}P^{2}$, $^{4}D^{6}$, $^{4}F^{5}$, $^{4}G^{7}$, $^{4}H^{5}$, $^{4}I^{5}$, $^{4}K^{3}$, $^{4}L^{3}$, $^{4}M^{1}$, $^{4}N^{1}$, $^{6}P^{1}$, $^{6}D^{1}$, $^{6}F^{1}$, $^{6}G^{1}$, $^{6}H^{1}$, $^{6}I^{1}$, $^{8}S^{1}$

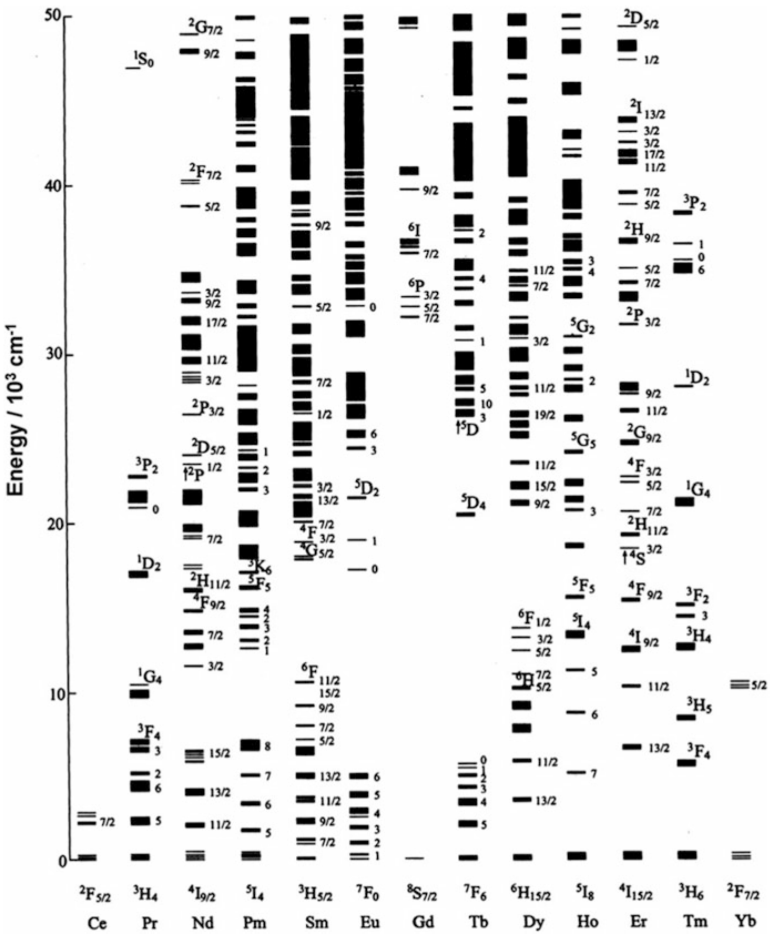

Figure 2.3. Energy level diagrams of tri-valent lanthanide ions doped in a low-symmetry crystal LaF_3[2]

2.2. Luminescence center of transition metal ions (Cr^{3+})

The wave-functions of five 3*d* electron orbitals are different as shown in Fig. 2.4(a). For a free ion, the energies of the five 3*d* orbitals are identical, and are determined by an electron kinetic energy and a central field potential caused by the inner electron field so that these orbitals are degenerate.

However, when the cation is incorporated into a crystal, the surroundings or environments of the cations are changed. For example, if the cation is surrounded by six anions (octahedral coordination), as the red dots shown in Fig. 2.4(b), the energies of x^2-y^2 and z^2 orbitals are increased, because of the electron repulsion from the surrounding anions located at the orientation of x^2-y^2 and z^2 orbitals. In order to keep energy reservation of the whole system, the energies of the other three orbitals are decreased. On the other hand, when the cation is incorporated into a tetrahedral crystal field with four anions as marked by blue dots [see Fig. 2.4(b) again], the energies of xy, yz, xz orbitals are higher than the other two orbitals, totally the opposite situation to that in the octahedral crystal field.[6]

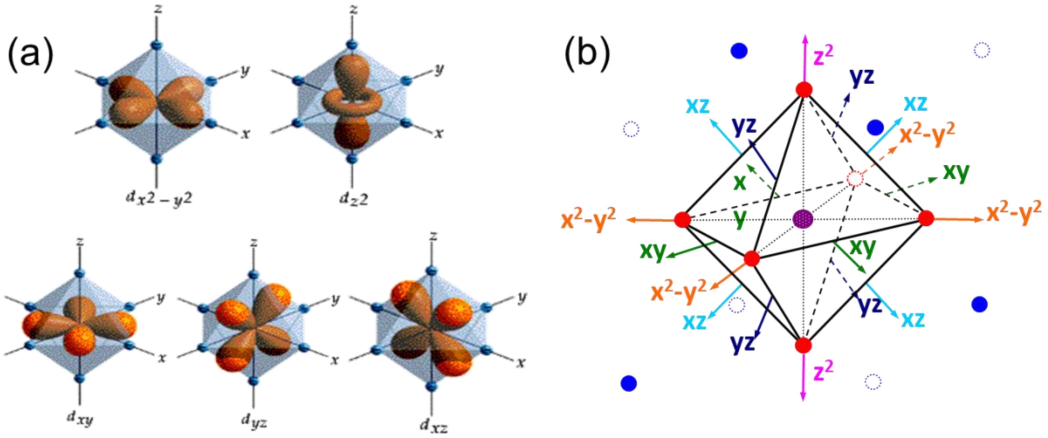

Figure 2.4. (a) Five sub-orbitals of the *d* orbital (b) interaction between the *d*-orbital-electrons of a central cation and surrounding anions with octahedral or tetrahedral coordination[6]

Here, I take Cr^{3+} as an example to introduce the typical *d*-*d* transition of transition metal ions, and also Cr^{3+} is the only transition metal ion I focused on in this dissertation.

The electronic configuration of Cr^{3+} is $3d^3$ in the outer *d* orbital. We notice that in a real crystal, the most common crystal field is either octahedral or tetrahedral fields.

As mentioned before, the lowest state (ground state) of a transition metal ion is triplet T_{2g} orbital (xy, yz, xz) in a regular octahedral field and doublet E orbital (x^2-y^2, z^2) in a regular tetrahedral field. Consider that when the Cr^{3+} ion with three *d* electrons incorporated into the octahedral field with a triplet ground state, each electron occupies one orbital with a parallel spin. If Cr^{3+} ions are forcibly incorporated into the tetrahedral field with double ground state, one electron shows different (anti-parallel) spin to the other two electrons. According to Pauling's rule, the energy of ground state will lower when the electrons show parallel spin also when the orbitals are half-occupied. Generally, Cr^{3+} ions are stable only in the octahedral field.

According to the Tanabe-Sugano diagram[7,8] of the $3d^3$ electronic configuration shown in Fig. 2.5, in which the energies (*E*) from the ground state level are plotted against the crystal field (*Dq*), both in the unit of *B* (Racah parameter). In the free ion, the ground state is the $^4A_2(^4F)$ state, and the energy location of each level depends on the crystal field strength, which is descripted by *Dq/B*. Generally, the luminescence of Cr^{3+} is attributed from the lowest excited state to the ground state. When Cr^{3+} is incorporated into a weak crystal field, the emission is mainly due to the $^4T_2\,(^4F)\rightarrow{}^4A_2\,(^4F)$ transition (spin allowed). On the other hand, when Cr^{3+} is incorporated into a strong crystal field, the emission is mainly due to $^2E\,(^2G)\rightarrow{}^4A_2\,(^4F)$ transition (spin forbidden), the so-called *R*-line (ruby-line). There is a cross-point region between the energy levels of $^4T_2\,(^4F)$ and $^2E\,(^2G)$ which represents the intermediate crystal field region between the weak and strong ones. Therefore, the emission band of Cr^{3+} is quite related to the crystal field strength of material hosts, and can be easily tunable from sharp line emission to broad band emission, which we call it "crystal field engineering" (see the detailed discussion in Chapter 9)

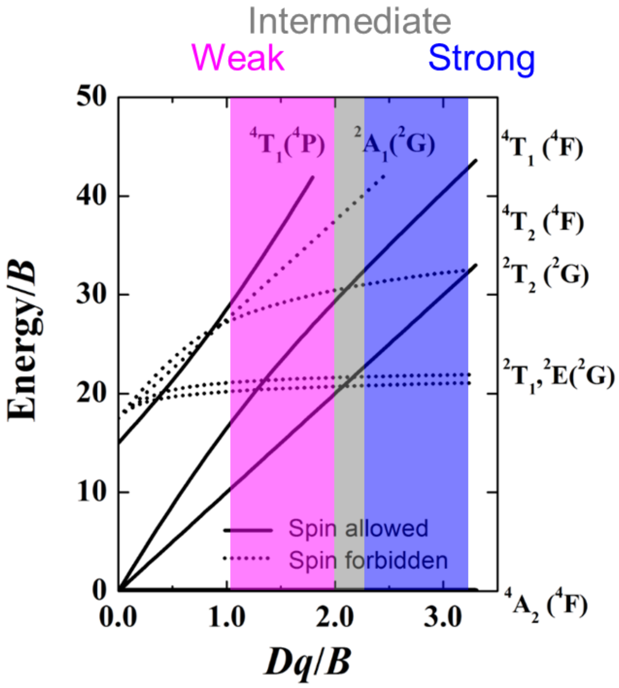

Figure 2.5. The Tanabe-Sugano (d^3) diagram

2.3. Electron trapping-detrapping processes

Till now, despite the fast development and considerable research on persistent phosphors, the detailed mechanism of persistent luminescence is still an open question. The most acceptable one can be qualitatively explained by an electron trapping-detrapping process[9]: when persistent phosphors are excited by ultraviolet (UV) light (visible light in rare cases), electron-hole (*e*-*h*) pairs are generated, if the excited state is close to the bottom of the conduction band (*CB*) with small energy gap, the excited electron can “jump” into the *CB* with thermal activation energy. Then, the excited electron through *CB* is captured by the electron trap, which is usually called trapping process [see Fig. 2.6(a)]. The electron trap is a quasi-stable state and energetically unstable. However, directly relaxation to ground states is strictly forbidden; an energy barrier makes the state stable if necessary energy is not offered to the system. The quasi-stable state is generally induced by lattice defects in the host material or impurity ions introduced on purpose. They are usually termed “electron traps” or “electron trapping centers” in the field of persistent phosphors.

The captured or stored electrons can be released by thermal stimulation to *CB* being re-combined with holes followed by persistent luminescence, or more precisely to say is a kind of thermoluminescence (TL), which is called the detrapping process [see Fig. 2.6(b)]. During a series of processes, “trap depth (ε_T)” which represents the energy gap between the bottom of *CB* and the electron trap is crucial since it determines the behavior of persistent luminescence such as initial emission intensity and luminescence duration.

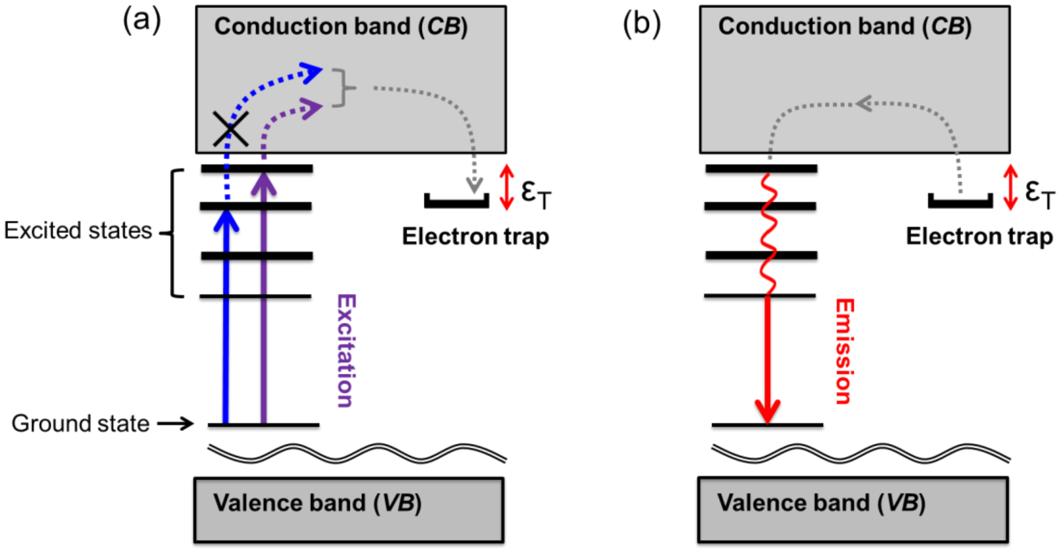

Figure 2.6. Electron trapping (a) and detrapping (b) processes in persistent phosphors

2.4. Garnet structure

The history of garnets dates back to the Bronze Age, and they have been used for thousands of years as abrasives, because of their hardness, and as gemstones, related to their high refractive index and beautiful coloring through incorporation of transition metal ions into the octahedral or tetrahedral sites. The English word “Garnet” originates from the Latin ‘‘Granatum’’, which means many grains and is related to the pomegranate fruit, having many red seeds that resemble some of the dark red garnet gemstones in structure and color.[10,11]

Garnet structure in the form of $A_3B_2C_3O_{12}$ is belonging to the cubic crystal system with space group of O_h^{10}-$Ia\bar{3}d$, in which three types of cation sites able to be occupied by different cation ions: (i) the *A* site, 24(c) dodecahedral site (D_2 point symmetry) with a coordination number eight (CN=8), (ii) the *B* site, 16(a) octahedral site (S_6

point symmetry) with a coordination number six (CN=6), and (iii) the C site, 24(d) tetrahedral site (S_4 point symmetry) with a coordination number four (CN=4). Therefore, the garnet structure can be regarded as an interconnected dodecahedra, octahedra and tetrahedra with shared oxygen atoms at the corners of the polyhedra with a 160 atom body-centered unit cell as shown in Fig 2.7.

Considering the high tolerability of these three cation sites (i.e. the larger dodecahedral sites are ideal for lanthanide ions while the smaller octahedral sites are of the appropriate size for Cr^{3+} ions), lanthanide ions and/or transition metal ions doped garnet materials have been widely used for many applications, such as Ce^{3+} doped garnets for *w*-LEDs and scintillators,[12,13] Nd^{3+}, $Cr^{3+/4+}$ doped garnets for the high power solid-state laser,[14,15] and Yb^{3+} doped garnets for the quantum cutting and down-conversion,[16] *etc*.

In this dissertation, I make full use of this flexible crystal structure, and successfully developed different garnet transparent ceramic persistent phosphors emitting "bright" persistent luminescence in the visible light region as well as in the near-infrared (NIR) region (see Fig 2.8.)

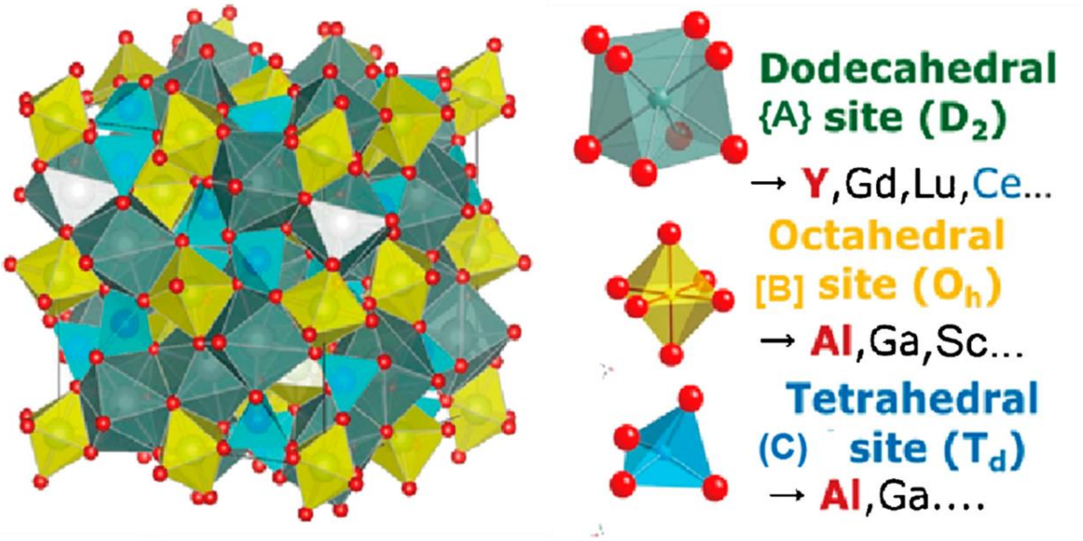

Figure 2.7. Schematic of the garnet crystal structure and the coordination atoms of polyhedrons for different sites[10]

Figure 2.8. Garnet transparent ceramic persistent phosphors prepared in Tanabe Lab (a) under fluorescent lamp (b) under UV (254 nm) lamp (c) in the dark; samples from left to right: $Y_3Al_2Ga_3O_{12}$(YAG*G*):Ce-Cr (chapter 3), $Y_3Al_2Ga_3O_{12}$(YAG*G*):Tb-Cr (chapter 4), $Gd_3Al_2Ga_3O_{12}$(GAG*G*):Ce-Cr, $Y_3Al_2Ga_3O_{12}$(YAG*G*):Pr-Cr (chapter 4), $Y_3Al_2Ga_3O_{12}$(YAG*G*):Cr (chapter 5), $Gd_3Ga_5O_{12}$(GG*G*):Cr-Eu (chapter 6)

References

[1] https://sciencenotes.org/periodic-table-wall-chart/

[2] W. T. Carnall, G. L. Goodman, K. Rajnak and R. S. Rana. *J. Chem. Phy.* 1989, 90, 3443-3457.

[3] X. Chen, Y. Liu and D. Tu, *Lanthanide-Doped Luminescent Nanomaterials-From Fundamentals to Bioapplications*; Springer-Verlag, Berlin Heidelberg, 2014

[4] V. A. G. Rivera, F. A. Ferri and E. Marega, *Localized Surface Plasmon Resonances: Noble Metal Nanoparticle Interaction with Rare-Earth Ions*, DOI: 10.5772/50753

[5] S. Shionoya and W. M. Yen, *Phosphor Handbook*, CRC Press, Boca Raton, 1999

[6] Y. Zhuang, Ph. D thesis: Red to near-infrared luminescent materials activated by transition metals for *in vivo* imaging and telecommunication application, Kyoto University, 2014.3

[7] Y. Tanabe and S. Sugano. *J. Phys. Soc. Jpn.* 1954, 9, 753-766.

[8] Y. Tanabe and S. Sugano. *J. Phys. Soc. Jpn.* 1954, 9, 766-779.

[9] P. Dorenbos, *J. Electrochem. Soc.*, 2005, 152, H107-H110.

[10] J. Ueda, *J. Ceram. Soc. Jpn*., 2015, 123, 1059-1064.

[11] Z. Xia, and A. Meijerink, *Chem. Soc. Rev.* 2017, DOI:10.1039/C6CS00551A

[12] G. Blasse and A. Bril. *Appl. Phys. Lett*. 1967, 11, 53-54.

[13] S. Nishiura, S. Tanabe, K. Fujioka, and Y. Fujimoto. *Opt. Mater.* 2011, 33, 688-691.

[14] A. A. Kaminskii, *Crystalline Lasers: Physical Processes and Operating Schemes*; CRC Press, New York, 1996.

[15] A. Ikesue and Y. L. Aung. *Nat. Photon.* 2008, 2, 721-727.

[16] J. Ueda and S. Tanabe. *J. Appl. Phys.* 2009, 106, 043101 (5 pp).

Chapter 3

Fabrication of Ce^{3+}-Cr^{3+} co-doped yttrium aluminium gallium garnet transparent ceramic phosphors with super long persistent luminescence

Abstract:

YAG*G*:Ce^{3+}-Cr^{3+} transparent ceramics (TCs) with different thicknesses were fabricated by solid state reaction and vacuum sintering. Compared with an opaque YAG*G*:Ce^{3+}-Cr^{3+} ceramic phosphor of the same composition, the corresponding TC phosphors exhibited brighter persistent luminescence after ceasing blue excitation (460 nm) due to a typical "volume effect" of transparent materials. The duration that the persistent luminescence intensity reaches 2 mcd/m^2 of the YAG*G*:Ce^{3+}-Cr^{3+} TC was nearly twice of that of the compacted pellet made of $SrAl_2O_4$:Eu^{2+}-Dy^{3+} commercial powder.

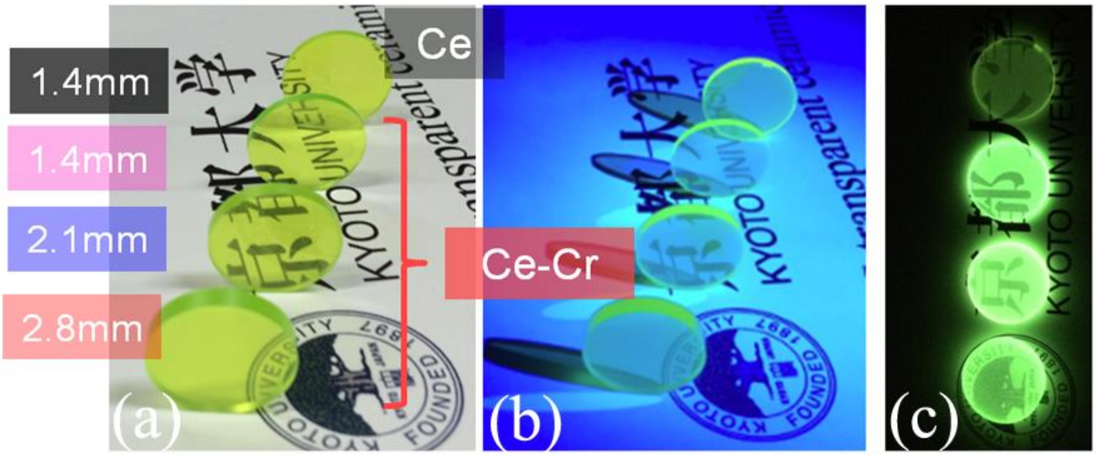

Photographs of YAG*G*:Ce^{3+} and YAG*G*:Ce^{3+}-Cr^{3+} transparent ceramics (a) under fluorescent lamp (b) under 460 nm illumination (c) at 300 s after ceasing 460 nm illumination

3.1. Introduction

Persistent luminescence represents the light emission lasting from several minutes to hours after ceasing excitation sources. Such kind of persistent phosphors have attracted a great attention in the last two decades after Matsuzawa et al. discovered the $SrAl_2O_4$:Eu^{2+}-Dy^{3+} phosphors with the brightest and longest persistent luminescence among all the persistent phosphors ever reported.[1] This phosphor emits green light at 520 nm attributed to Eu^{2+}:5*d*→4*f* transition and can efficiently be excited by UV light at 360 nm or fluorescent lamps containing violet light. Currently, white-light emitting diodes (w-LEDs), generally composed of blue LED chips and YA*G*:Ce^{3+} yellow phosphors, are replacing fluorescent lamps due to their high luminous efficiency, long lifetime, and low electric consumption as indoor illumination.[2] Considering the fact that $SrAl_2O_4$:Eu^{2+}-Dy^{3+} phosphors cannot efficiently be charged by visible light even by blue light,[3] blue-light-chargeable long persistent phosphors have been a focus of potential applications such as night-vision signs and safety way guidance systems.

Recently, we have reported a novel persistent ceramic phosphors with composition of $Y_3Al_{5-x}Ga_xO_{12}$ (YAG*G*):Ce^{3+}-Cr^{3+} (x=2.5, 3, 3.5) which can emit bright green emission due to Ce^{3+}:5d_1→4*f* transition lasting for several hours after ceasing the blue light excitation.[4] In this material, the threshold of photoionization between 5d_1 energy level of Ce^{3+} and the bottom of the conduction band (C.B) with photo-stimulation can be decreased by Ga^{3+} substitution in B, C sites of $\{A\}_3[B]_2(C)_3O_{12}$ garnet matrix, where {A}, [B], and (C) represent the cations at the dodecahedral, octahedral, and tetrahedral sites, respectively.[5] Cr^{3+} ions can work as electron traps with ideal trap depth for persistent luminescence working at room temperature (RT). Furthermore, the trap depth, which represents the energy gap between the bottom of CB and the electron trap, can also be optimized via modifying Ga^{3+} substitution contents.

In addition, Ga^{3+} substituted garnet belongs to the famous garnet family “yttrium aluminium garnet (YAG)” of cubic isotropic crystal for solid-state lasers,[6-7] scintillators[8-9] and w-LED[10-11] applications. Such garnet compositions can be realized to be transparent ceramics (TCs) once high density and satisfactory optical transparency are obtained by advanced ceramic processing techniques.[12] Recently, our group firstly fabricated $Gd_3Al_2Ga_3O_{12}$ (GAG*G*):Ce^{3+}-Cr^{3+} TCs with yellow persistent luminescence using a simple one-step solid-state reaction method (directly sintered from raw oxide powder to target ceramics).[13] Although, the thickness of the GAG*G*:Ce^{3+}-Cr^{3+} TC was only 0.542 mm, it still performed longer persistent luminescence than that of the corresponding opaque one because the excitation light can penetrate through the sample and induce the carrier formation inside the TC sample due to its lower optical scattering coefficient than pellet or powder.

In this paper, we obtained high optical quality YAG*G*:Ce^{3+} and YAG*G*:Ce^{3+}-Cr^{3+} TCs via one step solid-state reaction method using vacuum sintering process. Thickness effect of specimens was investigated for the new ceramic persistent phosphors and we found that the duration upon 2 mcd/m^2 after 460 nm blue excitation for the 2.8 mm thickness TC specimen reaches more than 14 hours, which to the best our knowledge, is the longest persistent duration ever reported.

3.2. Experimental procedures

YAG*G*:Ce^{3+} and YAG*G*:Ce^{3+}-Cr^{3+} TCs with composition of $(Y_{0.995}Ce_{0.005})_3Al_2Ga_3O_{12}$ and $(Y_{0.995}Ce_{0.005})_3Al_{1.999}Ga_3O_{12}:Cr_{0.001}$ were fabricated by solid-state reaction method. The chemicals of Y_2O_3, Al_2O_3, Ga_2O_3, CeO_2 (4N purity) and Cr_2O_3 (3N purity) were used as raw materials. The starting powder was mixed by ball milling method with ZrO_2 ceramic balls and anhydrous alcohol for several hours. 0.8-1.2 wt% tetraethyl orthosilicate (TEOS) and 0.8-1.5 wt% dispersant[10] were added as sintering aid and surfactant during ball milling process, respectively. The mixed powder was dried at 80 ℃ for 36 h and compacted to form a ceramic green body (ϕ20 mm × 3-6 mm thick) under uniaxial pressing of 50 MPa without further cold isostatic pressing (CIP), then pre-heated at 800 ℃ for 60 h in air to remove the organic substances, and finally sintered at 1600-1650 ℃ for 10-20 h under vacuum atmosphere. The as-sintered specimens were double-mirror polished using a copper plate and diamond slurry.

The in-line optical transmittance of TCs was measured by UV–VIS-NIR spectrometer (UV-3600, SHIMADZU, Japan). Microstructure observations including surface and fractured surface of the as-sintered YAG*G*:Ce^{3+} and YAG*G*:Ce^{3+}-Cr^{3+} TCs were examined by scanning electron microscopy (SEM, JSM-890, JEOL, Japan). Before surface SEM observations, the polished specimens were thermally etched in air at 1400 ℃ for 2 h. Photoluminescence (PL) and persistent luminescence (PersL) spectra were measured by a luminance-measurement setup composed of a CCD spectrometer (MCPD-BB, Otsuka Electronics, Japan), a fiber, and a collimator lens. A combination of a 300W Xe lamp (MAX-302, Asahi Spectra, Japan) and a band-pass filter (460 nm) was used as the excitation source. A 470 nm shot-cut filter was set in front of the CCD spectrometer to cut off excitation signals. Thermoluminescence (TL) glow curves monitoring the Ce^{3+} luminescence were measured using a combination of the Xe lamp with a 460 nm band-pass filter and a photomultiplier tube (R3896, Hamamatsu Photonics, Japan), which was combined with a 475 nm short-cut filter and a 600 nm long-cut filter to filter out all the light except the Ce^{3+} luminescence. The specimens were set in a cryostat (Helitran LT3, Advanced Research Systems, USA) to control temperatures. The ceramic specimen was firstly excited by UV light (250-400 nm) at 130 K for 10 min, after waiting for 10 min, then finally heated at 10 K/min to 600 K. Persistent luminescent decay curves were obtained at 25 ℃ using the same photomultiplier tube and filters as the TL measurement. Then, the decay curves were calibrated to the absolute luminance (in unit of mcd/m^2) by using a radiance meter (Glacier X, B&W Tek Inc, Japan).

3.3. Results and discussion

Fig. 3.1(a) shows the photograph of the YAG*G*:Ce^{3+} and YAG*G*:Ce^{3+}-Cr^{3+} TCs (both are 1.4 mm thickness) with yellow-green appearance, through which we can clearly recognize the words below by naked eye owing to their high optical transparency. The in-line optical transmittance of the YAG*G*:Ce^{3+} and

YAG*G*:Ce^{3+}-Cr^{3+} TCs at 1200 nm reach to 76.6% and 75.4%, respectively. Two broad absorption bands are observed at about 450 and 340 nm due to the transitions from the 4*f* level to the lowest $5d_1$ and the second lowest $5d_2$ levels of Ce^{3+} ions, respectively. Besides, an additional broad band at about 620 nm appears in the Cr^{3+} co-doped specimen ascribed to the transition from $^4A_2$ to $^4T_2$ of Cr^{3+}. SEM microstructures of surface and fractured surface of the two specimens are shown in Fig. 3.1(b)-(e). Micro-pores randomly exist on the surface of the Cr^{3+} co-doped specimen (see Fig. 3.1c), which may act as scattering centers (see Fig. 3.1b). The average gain size $\overline{D}$ can be determined by linear intercept method[14] as the structure consists of equiaxed grains of regular polyhedral shape with particular size distribution and only continuous grain growth occurs. Lines of equal length are ruled randomly in SEM photographs, the number of grains along those lines is counted and then average grain size $\overline{D}$ can be estimated according to Eq. (1) where $\overline{L}$ is the average intercept length over the number of grains counted along the lines.

$$\overline{D} = 1.56\overline{L} \tag{1}$$

The uniform grain sizes of the YAG*G*:Ce^{3+} and YAG*G*:Ce^{3+}-Cr^{3+} TCs are calculated to be 8 and 6 μm, respectively. The fracture mode of the two specimens is mainly intercrystalline type. (see Fig. 3.1d and e).

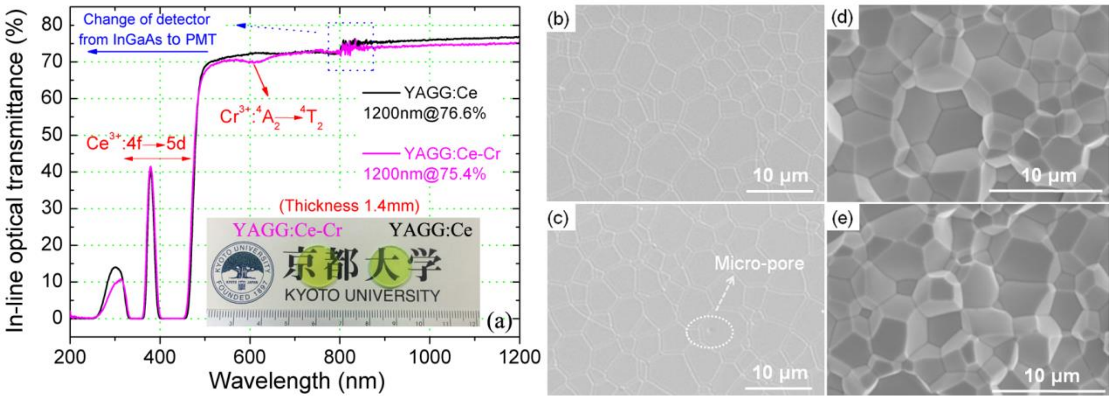

Figure 3.1. (a) Photograph and in-line optical transmittance of YAG*G*:Ce^{3+} and YAG*G*:Ce^{3+}-Cr^{3+} transparent ceramics as well as scanning electron microscope (SEM) photographs of the double polished surfaces of (b) YAG*G*:Ce^{3+} (c) YAG*G*:Ce^{3+}-Cr^{3+} and fracture surfaces of (d) YAG*G*:Ce^{3+} (e) YAG*G*:Ce^{3+}-Cr^{3+} transparent ceramics

PL and PersL spectra of the YAG*G*:Ce^{3+}-Cr^{3+} specimen under and after 460 nm blue excitation are shown in Fig. 3.2. PersL spectra were recorded at various times after stopping blue irradiation for 5 min. The spectral shapes of PL and PersL are similar in showing two broad bands from about 470 to 700 nm. The main broad band centered at 515 nm is due to the $5d_1 \rightarrow 4f$ electronic transition of Ce^{3+} while a small broad band centered at around 700 nm is due to the $^2E \rightarrow ^4A_2$ transition of Cr^{3+}. The persistent behavior of the YAG*G*:Ce^{3+}-Cr^{3+} specimen can also be intuitively recognized by the inserted photographs at different irradiation conditions.

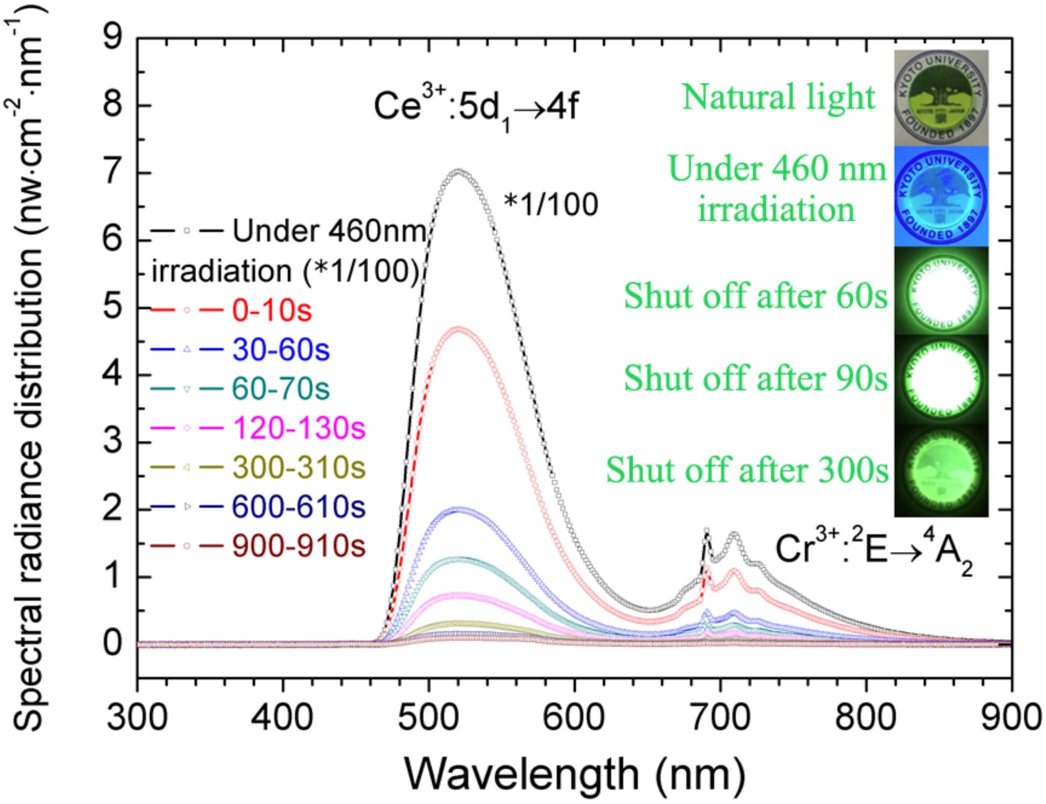

Figure 3.2. Photoluminescence (PL) and persistent luminescence (PersL) of the YAG*G*:Ce^{3+}-Cr^{3+} transparent ceramic under and after 460 nm irradiation for 5 min

Fig. 3.3 gives the photographs and persistent luminescent decay curves after 460 nm blue irradiation for 5 min of YAG*G*:Ce^{3+} and YAG*G*:Ce^{3+}-Cr^{3+} TCs with different thicknesses (1.4 mm, 2.1 mm, 2.8 mm) compared with the opaque YAG*G*:Ce^{3+}-Cr^{3+} ceramic pellet phosphor (Ga=3) and compacted ceramic pellet made of the $SrAl_2O_4$:Eu^{2+}-Dy^{3+} commercial powder (LumiNova GLL300FFS, Nemoto & Co. Ltd., Japan).[4] The luminance after 5 min, 20 min, 60 min and duration upon 2 mcd/m^2 of those specimens are presented in Table. 3.1. It is indicated that the Cr^{3+} co-doped specimens exhibit brighter persistent luminescence than the Ce^{3+} single doped one. The duration upon 2 mcd/m^2 of YAG*G*:Ce^{3+}-Cr^{3+} specimen (480 min) is over 26 times longer than that of the YAG*G*:Ce^{3+} specimen (18 min) with the same thickness (1.4 mm). It is worth noting that 2 mcd/m^2 is the minimum value used for emergency guidance signs set by Japan Industry Standard (JIS). When the thickness of the YAG*G*:Ce^{3+}-Cr^{3+} TC is further increased from 1.4 mm to 2.8 mm, the persistent behavior increases notably as well, especially for the 2.8 mm thickness specimen, its luminance can reach to 88 mcd/m^2 after ceasing excitation source for 60 min, and the duration is nearly 846 min which is about three times longer than that of the YAG*G*:Ce^{3+}-Cr^{3+} (Ga=3) pellet phosphor with the same chemical composition and even twice of that of the most famous and widely used green persistent phosphors: $SrAl_2O_4$:Eu^{2+}-Dy^{3+}.

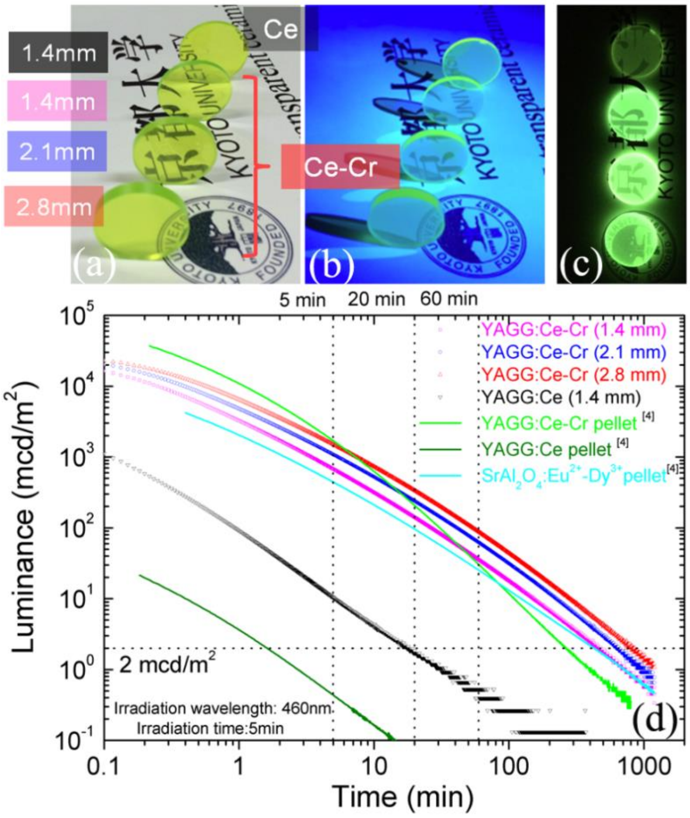

Figure 3.3. Photographs of YAG*G*:Ce^{3+} and YAG*G*:Ce^{3+}-Cr^{3+} transparent ceramics (a) under fluorescent lamp (b) under 460 nm irradiation (c) 300 s after 460 nm irradiation and (d) corresponding persistent decay curves after 460 nm irradiation for 5 min (YAG*G*:Ce^{3+}, YAG*G*:Ce^{3+}-Cr^{3+} and $SrAl_2O_4$:Eu^{2+}-Dy^{3+} ceramic pellets as references)

Table 3.1. Luminance and duration of YAG*G*:Ce^{3+} and YAG*G*:Ce^{3+}-Cr^{3+} transparent ceramics with different thicknesses after 460 nm irradiation for 5 min compared with YAG*G*:Ce^{3+}, YAG*G*:Ce^{3+}-Cr^{3+} and $SrAl_2O_4$:Eu^{2+}-Dy^{3+} ceramic pellets

	5 min (mcd/m^2)	20 min (mcd/m^2)	60 min (mcd/m^2)	Duration upon 2 mcd/m^2 (min)
YAG*G*:Ce^{3+} (1.4mm)	**10.4**	**1.7**	**0.5**	**18**
YAG*G*:Ce^{3+}-Cr^{3+} (1.4mm)	**676**	**141**	**35**	**480**
YAG*G*:Ce^{3+}-Cr^{3+} (2.1mm)	**1085**	**240**	**62**	**649**
YAG*G*:Ce^{3+}-Cr^{3+} (2.8mm)	**1507**	**339**	**88**	**846**
YAG*G*:Ce^{3+} [4]	**0.43**	**0.06**	**-**	**1.6**
YAG*G*:Ce^{3+}-Cr^{3+} [4]	**1695**	**208**	**30**	**265**
$SrAl_2O_4$:Eu^{2+}-Dy^{3+} [4]	**443**	**96**	**25**	**433**

Compared with former results of YAG*G*:Ce^{3+}-Cr^{3+} persistent phosphors,[4] the corresponding TC of such material seems to show brighter persistent luminescence than other phosphors of powder or pellet. This behavior is quite in accordance with the result of the GAG*G*:Ce^{3+}-Cr^{3+} TC made by our group.[13] In the TC phosphors, not only the surface but also the interior of the TC specimen can be excited under irradiation owing to their lower optical scattering coefficient than that of powder or conventional opaque pellet. In powder and opaque specimens, only the surface part can efficiently be excited due to the strong scattering of the excitation light. For a TC persistent phosphor, the persistent luminance can be increased with increasing sample thickness, which is regarded as “volume effect”.

On the other hand, we found that the Ce^{3+} single doped TC specimen also performed much higher persistent luminescence than the result reported before (see Table. 3.1).[4] Such difference was mainly attributed to the preparation condition difference between air sintering and vacuum sintering for the two specimens since in the reductive atmosphere during vacuum sintering, oxygen vacancies ($V_O^{\cdot\cdot}$) are usually formed and act as additional electron traps to capture the excited electrons through the CB and release them with thermal stimulation. In YSG*G*:Ce^{3+} persistent phosphors,[15] such kind of electron traps play an important role in the final persistent luminescence behavior.

In order to clarify the trapping and detrapping mechanism of YAG*G*:Ce^{3+} and YAG*G*:Ce^{3+}-Cr^{3+} TCs, thermoluminescence (TL) measurement were carried out as shown in Fig. 3.4. Glow peaks of the TL glow curves monitoring Ce^{3+} luminescence of the YAG*G*:Ce^{3+} and YAG*G*:Ce^{3+}-Cr^{3+} specimens are very close to RT while for the Cr^{3+} co-doping specimen, the intensity increases about 36 times higher compared with the Ce^{3+} single doped one. The trap depth between the bottom of C.B and the electron trap can be roughly estimated from the peak temperature of glow curves using the following equation:[16]

$$E_T = T_m/500 \qquad (2)$$

where E_T is the trap depth and T_m is the peak temperature of the TL glow curve. The trap depth of YAG*G*:Ce^{3+} and YAG*G*:Ce^{3+}-Cr^{3+} TCs is approximately 0.60 eV, which is suitable for trapping and re-combination process of excited electrons working at RT.

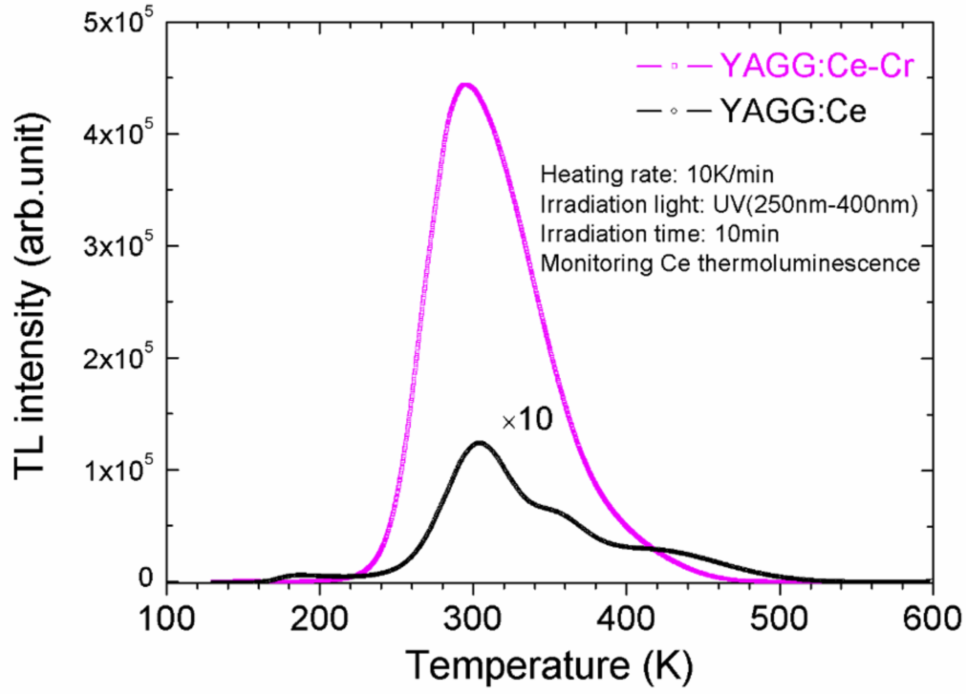

Figure 3.4. Thermoluminescence (TL) glow curves of the YAG*G*:Ce^{3+} and YAG*G*:Ce^{3+}-Cr^{3+} transparent ceramics after UV (250-400 nm) irradiation for 10 min

3.4. Conclusion

In summary, green persistent phosphor of YAG*G*:Ce^{3+}-Cr^{3+} transparent ceramic (TC) was successfully fabricated by simple one-step solid state reaction method. The duration upon 2 mcd/m^2 of the YAG*G*:Ce^{3+}-Cr^{3+} TC (846 min) was nearly twice of that of the compacted pellet made of the $SrAl_2O_4$:Eu^{2+}-Dy^{3+} commercial powder (433 min). Such novel TC phosphors showing both high transparency and persistent luminescence possess great potentials for the future persistent illumination applications under w-LED irradiation containing blue light source.

Acknowledgement

I would like to acknowledge fruitful discussions on persistent phosphors with Prof. Bruno Viana from Chimie Paris-tech. This work was supported by JSPS KAKENHI Grant Numbers 25810136, 23350099.

References

[1] T. Matsuzawa, Y. Aoki, N. Takeuchi, Y. Murayama, J. Electrochem. Soc. 143 (1996) 2670-2673.

[2] S. Nakamura, G. Fasol, The Blue Laser Diode: GaN Based Light Emitters and Lasers, Springer, Berlin, 1997, pp. 216–221.

[3] H. Takasaki, S. Tanabe, T. Hanada, J. Ceram. Soc. Jpn. 104 (1996) 322-326.

[4] J. Ueda, K. Kuroishi, S. Tanabe, Appl. Phys. Lett. 104 (2014) 101904.

[5] J. Ueda, S. Tanabe, T. Nakanishi, J. Appl. Phys. 110 (2011) 053102.

[6] A. Ikesue, I. Furusato, K. Kamata, J. Am. Ceram. Soc. 78 (1995) 225–228.

[7] A. Ikesue, T. Kinoshita, K. Kamata, K. Yoshida, J. Am. Ceram. Soc. 78 (1995) 1033–1040.

[8] T. Yanagida, H. Takahashi, T. Ito, D. Kasama, M. Kokubun, K. Makishima, T. Yanagitani, IEEE Trans. Nucl. Sci. 52 (2005) 1836–1841.

[9] T. Yanagida, T. Itoh, H. Takahashi, M. Sato, T. Enoto, M. Kokubun, K. Makishima, T. Yanagitani, H. Yagi, T. Shigeta, T. Ito, Nucl. Instrum. Methods A. 579 (2007) 23-26.

[10] S. Nishiura, S. Tanabe, K. Fujioka, Y. Fujimoto, Opt. Mater. 33 (2011) 688-691.

[11] S. Nishiura, S. Tanabe, K. Fujioka, Y. Fujimoto, IOP Conf. Ser.: Mater. Sci. Eng. 18 (2011) 102005-102008.

[12] A. Ikesue, Y. Aung, Nat. Photonics. 2 (2008) 721–727.

[13] J. Ueda, K. Kuroishi, S. Tanabe, Appl. Phys. Express. 7 (2014) 062201.

[14] M.I. Mendelson, J. Am. Ceram. Soc. 52 (1969) 443-446.

[15] J. Ueda, K. Aishima, S. Nishiura, S. Tanabe, Appl. Phys. Express. 4 (2011) 042602.

[16] K. Van Den Eeckhout, P.F. Smet, D. Poelman, Materials. 3 (2010) 2536-2566.

Chapter 4

Novel persistent phosphors of lanthanide-chromium co-doped yttrium aluminum gallium garnet: design concept with vacuum referred binding energy diagram

Abstract:

We developed Pr^{3+}-Cr^{3+} and Tb^{3+}-Cr^{3+} co-doped $Y_3Al_2Ga_3O_{12}$ (YAG*G*) persistent phosphors with orange (Pr^{3+}) and light green (Tb^{3+}) persistent luminescence. Their persistent luminance duration upon 0.32 mcd/m^2 could reach about 8 h and 12 h, respectively. On the other hand, the persistent luminescence intensities of Nd^{3+}-Cr^{3+} and Dy^{3+}-Cr^{3+} co-doped YAG*G* samples are much weaker than those of the Pr^{3+}-Cr^{3+} and Tb^{3+}-Cr^{3+} co-doped ones, and the dominant persistent luminescence is mainly due to the deep-red transition of Cr^{3+}. The mechanism of different persistent luminescence behaviors of these four samples can well be explained by the vacuum referred binding energy (*VRBE*) diagram of lanthanide ions in the YAG*G* host. The stability of hole traps at the ground states of Pr^{3+}, Nd^{3+}, Tb^{3+} and Dy^{3+} ions and the possibility to collaborate with Cr^{3+} electron traps inducing long persistent luminescence are discussed in detail.

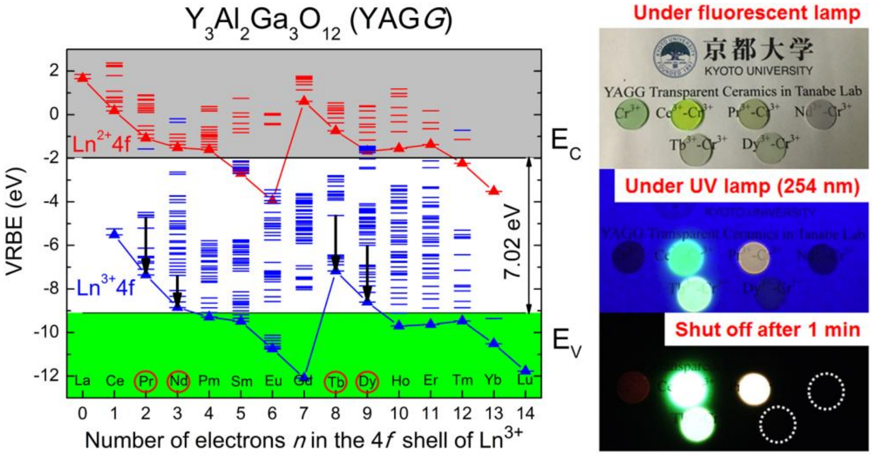

Use of the VRBE diagram to select stable hole traps inducing persistent luminescence

4.1. Introduction

Persistent luminescence (PersL), also denoted as "glow-in-the-dark" is a specific type of luminescence that can last for seconds, minutes to even hours, usually at room temperature (*RT*), after ceasing excitation sources.[1-3] It has passed over 20 years since the new generation green persistent phosphor, $SrAl_2O_4$:Eu^{2+}-Dy^{3+} (SAO:Eu-Dy) was reported and successfully commercialized for safety signage applications such as emergency exit signs in buildings and guiding strips in the aisle of airplanes.[4-10] Till now, despite the fast development and considerable research on persistent phosphors after this significant discovery, the detailed mechanism of PersL is still an open question. The most acceptable one can be qualitatively explained by an electron trapping-detrapping process: when persistent phosphors are excited by ultraviolet (UV) light (visible light in rare cases), electron-hole (*e*-*h*) pairs are generated and the excited electrons through conduction band (*CB*) are captured by electron traps. This process is usually called trapping process. Then the stored electrons can be released by thermal stimulation to *CB* (detrapping process) being re-combined with holes followed by PersL. During a series of processes, "trap depth" which represents the energy gap between the bottom of *CB* and the electron trap is crucial since it determines the behavior of PersL such as initial emission intensity and luminescence duration. Therefore, the nature of electron traps such as type, distribution, and energy level location has been extremely studied. However, few reports are concerning about the role of the other re-combination part, hole.[11-14] Similar to electron traps whose energy levels are located below the bottom of *CB*, the energy levels of hole traps also should be located above the top of valence band (*VB*). So the determination or even prediction of energy levels of doping ions in a host whether they can be selected as electron traps and/or hole traps is definitely important to design novel persistent phosphors.

Recently, we have reported garnet persistent phosphors with composition of Ce^{3+}, Cr^{3+} co-doped $Y_3Al_{5-x}Ga_xO_{12}$ (YAG*G*:Ce-Cr), in which Cr^{3+} acts as an efficient electron trap with ideal trap depth at x=3 for Ce^{3+} PersL working at *RT*.[15-17] The enhanced persistent luminance of the YAG*G*:Ce-Cr (x=3) transparent ceramic persistent phosphor at 60 min after ceasing blue excitation could reach 88 mcd/m^2, which is over three times higher than that of the compacted pellet made of commercial SAO:Eu-Dy powder (25 mcd/m^2).[18] On the other hand, we also developed Cr^{3+} singly-doped YAG*G* (YAG*G*:Cr) persistent phosphors with similar garnet matrix showing deep-red PersL (~690 nm), in which Cr^{3+} ions act both as emitting centers and trap centers.[19-20] The persistent radiance (in unit of mW/Sr/m^2) of the optimized composition (x=3) was even higher than that of the $ZnGa_2O_4:Cr^{3+}$ persistent phosphor, which is widely used for *in vivo* bio-imaging applications.[3,21-25]

4.2. Choice of lanthanide candidates in the YAG*G* host

The successful discovery of these Cr^{3+} singly- and co-doped YAG*G* persistent phosphors[15,19] motivates us to design improved ones with help of theoretical predictions, especially energy level locations of lanthanide ions in a specific host due to their wide adoption as emission centers and/or trap centers for PersL. Vacuum referred binding energy (*VRBE*) diagram of 15 lanthanides, proposed by Dorenbos,[26-32] provides a strong predicting power since the characteristic variation in electron and hole trapping depths of lanthanide ions is given by the shape of the two zigzag curves representing the ground states of divalent and trivalent lanthanide ions. Because the zigzag shape of two curves remain almost unchanged in different hosts due to the shielding effect of 5s^2 and 5p^6 orbitals on 4*f* orbitals, once the binding energy of the ground state for one lanthanide ion relative to the *CB* or *VB* is determined, those of 4*f* levels of all other lanthanides can be estimated fairly well by constructing this diagram.

According to the *VRBE* diagram of the YAG*G* host[16] shown in Fig. 4.1, besides Ce^{3+}, there are other four trivalent lanthanides (Pr^{3+}, Nd^{3+}, Tb^{3+}, Dy^{3+}) whose ground states are located above the top of *VB* indicating that they can be selected as potential candidates to be a hole trap. Therefore, in this work, Pr^{3+}-Cr^{3+}, Nd^{3+}-Cr^{3+}, Tb^{3+}-Cr^{3+}, Dy^{3+}-Cr^{3+} co-doped YAG*G* phosphors were prepared and their feasibility for PersL are discussed based on this diagram.

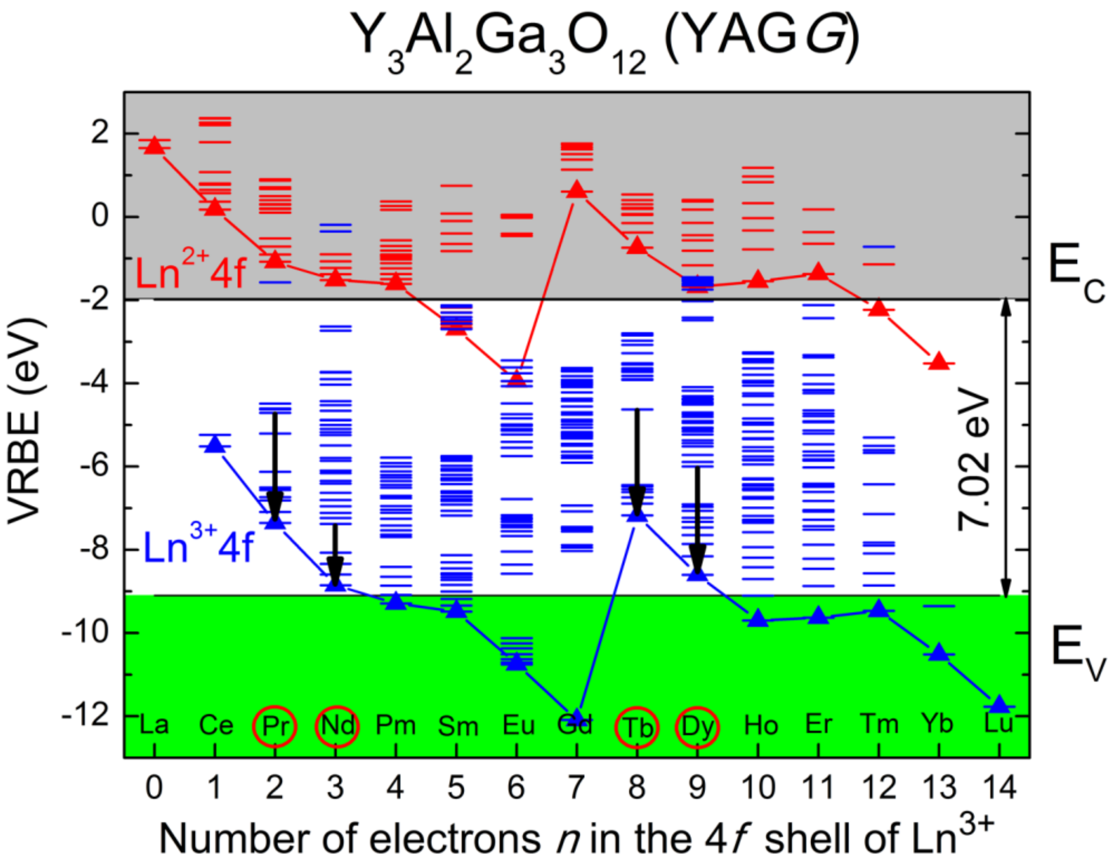

Figure 4.1. The *VRBE* diagram of divalent and trivalent lanthanide ions in YAG*G* (Ga=3) host

4.3. Experimental section

Transparent ceramics of $Y_{2.985}Pr_{0.015}Al_{1.999}Cr_{0.001}Ga_3O_{12}$ (YAG*G*:Pr-Cr), $Y_{2.97}Nd_{0.03}Al_{1.999}Cr_{0.001}Ga_3O_{12}$ (YAG*G*:Nd-Cr), $Y_{2.97}Tb_{0.03}Al_{1.999}Cr_{0.001}Ga_3O_{12}$ (YAG*G*:Tb-Cr), and $Y_{2.985}Dy_{0.015}Al_{1.999}Cr_{0.001}Ga_3O_{12}$ (YAG*G*:Dy-Cr) were fabricated by solid-state reaction method and vacuum sintering. The chemicals of Y_2O_3, Al_2O_3, Ga_2O_3 Pr_6O_{11}, Nd_2O_3, Tb_4O_7 and Dy_2O_3 with 4N purity and Cr_2O_3 with 3N purity were used as raw materials. The starting powder was mixed by ball milling method with anhydrous alcohol for several hours. The mixture powder was dried at 80 ℃ for 36 h and compacted to form a ceramic green body [ϕ20 mm×(2-3) mm] under uniaxial pressing of 50 MPa, and finally sintered at 1600-1650 ℃ for 10-20 h in vacuum atmosphere. The as-sintered samples were double-mirror polished to be thickness of 1.5±0.1 mm using a copper plate and diamond slurry. The transparent ceramics of $Y_{2.985}Ce_{0.015}Al_{1.999}Cr_{0.001}Ga_3O_{12}$ (YAG*G*:Ce-Cr)[18] and $Y_3Al_{1.99}Cr_{0.01}Ga_3O_{12}$ (YAG*G*:Cr)[19] prepared by the same method were used as reference samples. All the as-prepared samples were confirmed to be single phase (ICPDS: No. 089-6660) by XRD measurement (see Fig. 4.2).

Photoluminescence (PL) and PersL spectra of the YAG*G* samples were measured at 25 ℃ by a Si CCD spectrometer (QE65-Pro, Ocean Optics) and calibrated by a standard halogen lamp (SCL-600, Labsphere). A 300 W Xe-lamp (MAX-302, Asahi Spectra) with a UV mirror module (250-400 nm) was used as the excitation source for thermoluminescence (TL) two-dimensional (2D) plot measurements (see the schematic illustration of measurement setup in Fig. 4.3). The ceramic sample was set in a cryostat (Helitran LT3, Advanced Research Systems) to control temperatures and firstly illuminated by UV light at 150 K for 10 min, then heated up to 550 K at a rate of 10 K/min at 10 min after ceasing the illumination, and the TL signals were recorded by a PMT detector (R11041, Hamamatsu Photonics & Co. Ltd.,) covered with 350 nm short-cut and 750 nm long-cut filters. The same CCD spectrometer was operated simultaneously with the TL measurement to always monitor the emission spectra at different temperatures. All persistent luminescent decay curves of the samples after being excited for 5 min by the Xe-lamp with the UV module were measured at 25 ℃ using the same PMT detector. Then the decay curves were calibrated to the absolute intensity (luminance, in unit of mcd/m^2) using a radiance meter (Glacier X, B&W Tek Inc). Photographs of the samples were taken by a digital camera (EOS kiss X5, Canon) under the same setting conditions: exposure time - 0.1 s, ISO value - 1600, aperture value (*F* value) - 5.0.

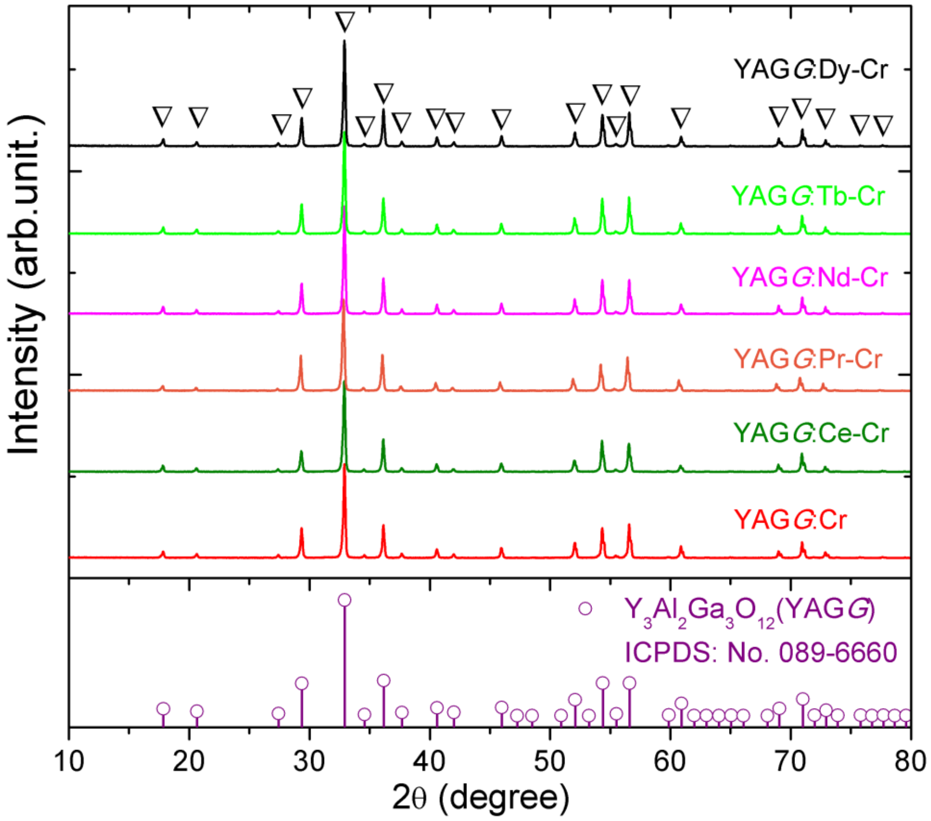

Figure 4.2. X-ray diffraction (XRD) patterns of the YAG*G*:Cr and YAG*G*:*Ln*-Cr (*Ln*=Ce, Pr, Nd, Tb, Dy) persistent phosphors

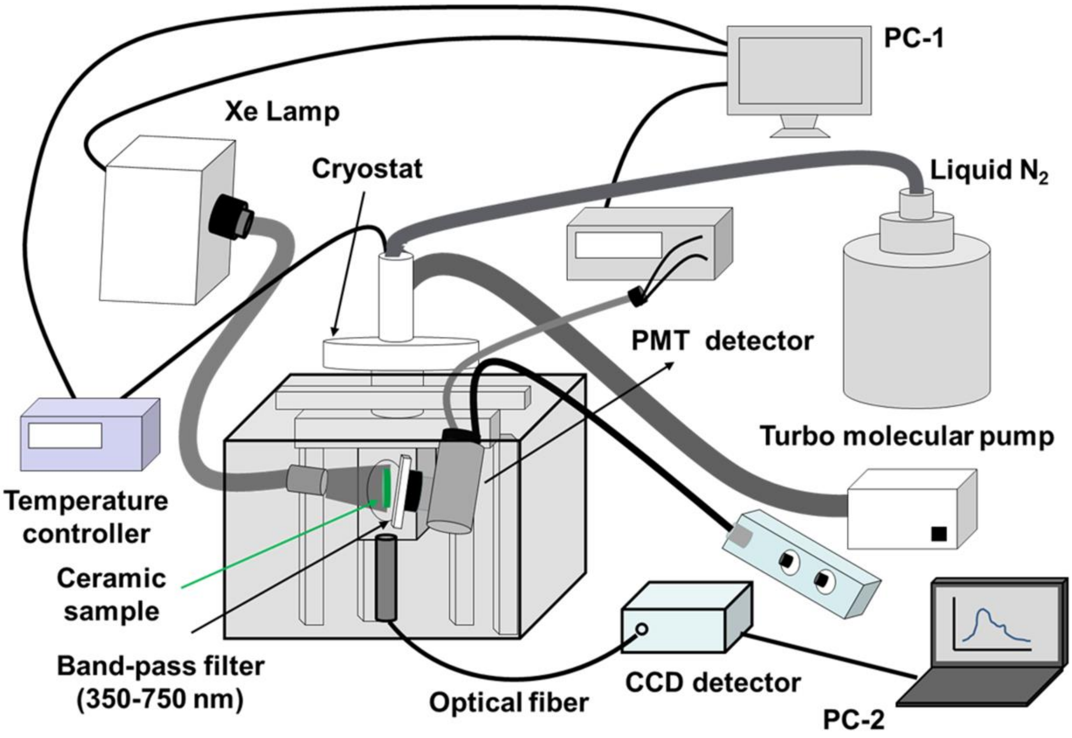

Figure 4.3. The measurement setup of thermoluminescence (TL) two-dimensional (2D) plot measurements

4.4. Results

4.4.1. PL and PersL spectra

Fig. 4.4 (a1)-(d1) show the PL spectra of the YAG*G*:*Ln*-Cr (*Ln*=Pr, Tb, Nd, Dy) phosphors excited by respective excitation wavelengths. The typical *f*-*f* transitions due to Pr^{3+}: $^3P_J \rightarrow ^3H_{4,5}$, $^1D_2 \rightarrow ^3H_4$, Tb^{3+}: $^5D_3$, $^5D_4 \rightarrow ^7F_J$, Nd^{3+}: $^4F_{3/2} \rightarrow ^4I_{9/2}$ and Dy^{3+}: $^4F_{9/2} \rightarrow ^6H_{15/2}$, $^6H_{13/2}$, $^6H_{11/2}$, $^6H_{9/2}$ are observed in YAG*G*:Pr-Cr, YAG*G*:Tb-Cr, YAG*G*:Nd-Cr and YAG*G*:Dy-Cr samples, respectively. Besides, Cr^{3+} luminescence bands are also observed in the YAG*G*:Pr-Cr and YAG*G*:Tb-Cr samples since the excitation wavelengths for Pr^{3+} (244 nm) and Tb^{3+} (235 nm) match well with the excitation band of Cr^{3+}: $^4A_2$ (^4F)$\rightarrow$$^4T_1$ (^4P). However, the excitation wavelengths for Nd^{3+} (354 nm) and Dy^{3+} (353 nm) mismatch the excitation bands of Cr^{3+}.[19,20] Therefore, the typical Cr^{3+} bands including "*R*-line": ^2E (^2G)$\rightarrow$$^4A_2$ (^4F) and its phonon sidebands (PSBs) were not observed in the YAG*G*:Nd-Cr sample while still exist in the YAG*G*:Dy-Cr sample. This is mainly attributed to the energy transfer from Dy^{3+}: $^4F_{9/2}$ to Cr^{3+}: $^4T_2$ (^4F) followed by *R*-line luminescence of Cr^{3+}.

After ceasing the UV (250-400 nm) excitation, the corresponding PersL spectra of the four YAG*G* persistent phosphors were recorded at different times, which are shown in Fig. 4.4 (a2)-(d2). The shapes of the PL and PersL spectra are nearly identical in the YAG*G*:Pr-Cr and YAG*G*:Tb-Cr samples, suggesting that the emission centers due to Pr^{3+} and Tb^{3+} are the same under and after excitation. However, the PersL spectra of the YAG*G*:Nd-Cr and YAG*G*:Dy-Cr samples are quite different from their PL spectra, in which PersL from Cr^{3+} is mainly dominant, and their PersL intensities are much weaker than those of the YAG*G*:Pr-Cr and YAG*G*:Tb-Cr samples.

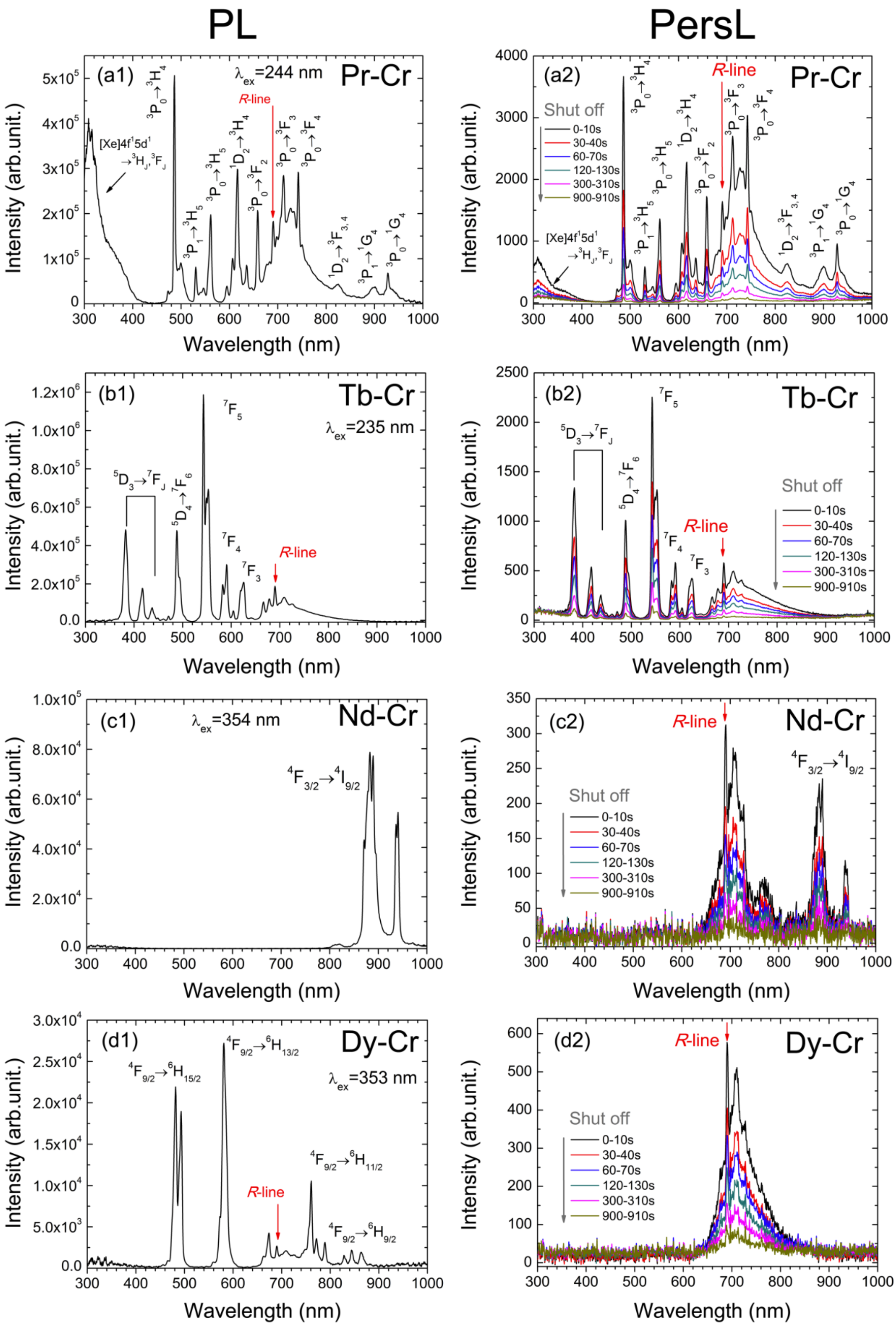

Figure 4.4. PL spectra of YAGG persistent phosphors co-doped with (a1) Pr-Cr (λ_{ex}=244 nm), (b1) Tb-Cr (λ_{ex}=235 nm), (c1) Nd-Cr (λ_{ex}=354 nm), (d1) Dy-Cr (λ_{ex}=353 nm) and corresponding PersL spectra (integrating time: 10 s) of (a2) Pr-Cr, (b2) Tb-Cr, (c2) Nd-Cr, (d2) Dy-Cr after ceasing UV (250-400 nm) illumination for 5 min

4.4.2. Persistent luminescent decay curves

Fig. 4.5(a)-(c) give the photographs of YAG*G*:*Ln*-Cr (*Ln*=Ce, Pr, Nd, Tb, Dy) transparent ceramic persistent phosphors together with one reference sample, YAG*G*:Cr, under and after UV (254 nm) excitation. All the samples show optical transparency, through which the letters below can be clearly recognized by naked eye. After ceasing the excitation, Ce-Cr, Pr-Cr, and Tb-Cr co-doped samples exhibit bright PersL due to Ce^{3+} (green), Pr^{3+} (orange) and Tb^{3+} (light green), respectively. The color coordinates of PersL in the CIE 1931 chromaticity diagram are (0.295, 0.553) for YAG*G*:Ce-Cr, (0.439, 0.367) for YAG*G*:Pr-Cr, and (0.313, 0.454) for YAG*G*:Tb-Cr samples (see Fig. 4.6). On the other hand, the Nd-Cr, Dy-Cr co-doped samples [white circles in Fig. 4.5(c)] showed very weak deep-red PersL (too weak to be recorded by the camera) due to Cr^{3+}, which was also observed in the YAG*G*:Cr reference sample.

The persistent luminescent decay curves in luminance unit of the YAG*G*:Pr-Cr and YAG*G*:Tb-Cr samples after ceasing UV (250-400 nm) illumination for 5 min are shown in Fig. 4.5(d), in which the decay profiles of the YAG*G*:Ce-Cr phosphor[18] and the compacted pellet made of the SAO:Eu-Dy commercial phosphor (LumiNova-GLL300FFS, Nemoto & Co. Ltd.,)[15] are also plotted as references. The luminance values at 60 min after ceasing the excitation were 35 mcd/m^2 for YAG*G*:Ce-Cr, 3.7 mcd/m^2 for YAG*G*:Pr-Cr, 6.1 mcd/m^2 for YAG*G*:Tb-Cr and 25 mcd/m^2 for SAO:Eu-Dy samples. Persistent luminance durations to reach a value of 0.32 mcd/m^2 were around 1469 min for YAG*G*:Ce-Cr, 499 min for YAG*G*:Pr-Cr, and 729 min for YAG*G*:Tb-Cr samples. Note that the luminance of 0.32 mcd/m^2 is the minimum value commonly used by the safety signage industry (about 100 times the sensitivity of the dark-adapted eye).[2]

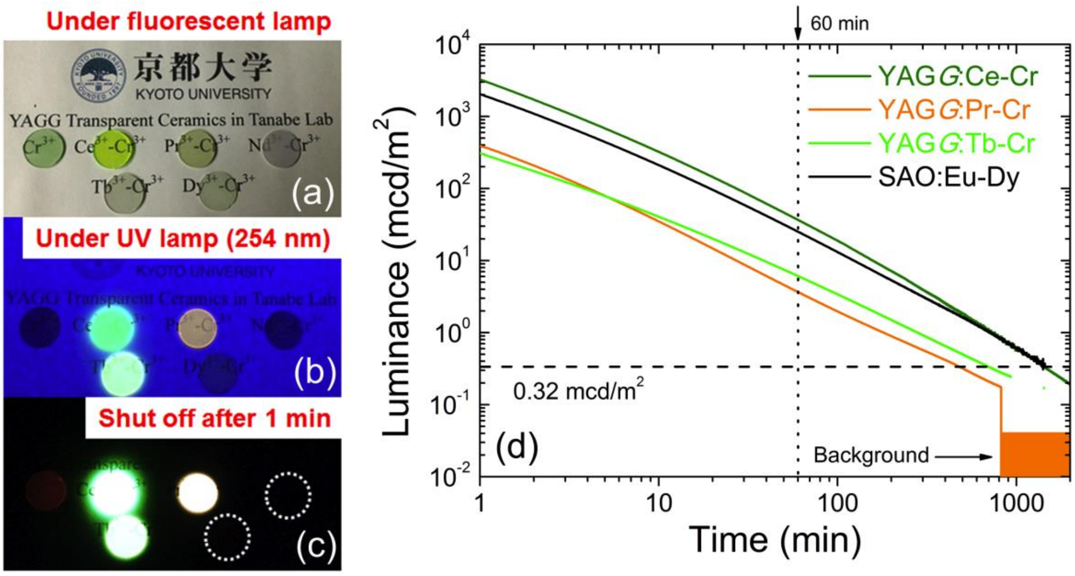

Figure 4.5. Photographs of Cr singly-, Ce-Cr, Pr-Cr, Nd-Cr, Tb-Cr, Dy-Cr co-doped YAG*G* transparent ceramic persistent phosphors (a) under fluorescent lamp (b) under UV (254 nm) lamp (c) at 1 min after shutting off the light (d) persistent luminance of Ce-Cr, Pr-Cr, Tb-Cr co-doped YAG*G* transparent ceramics compared with that of the commercial $SrAl_2O_4$:Eu-Dy persistent phosphor after ceasing excitation

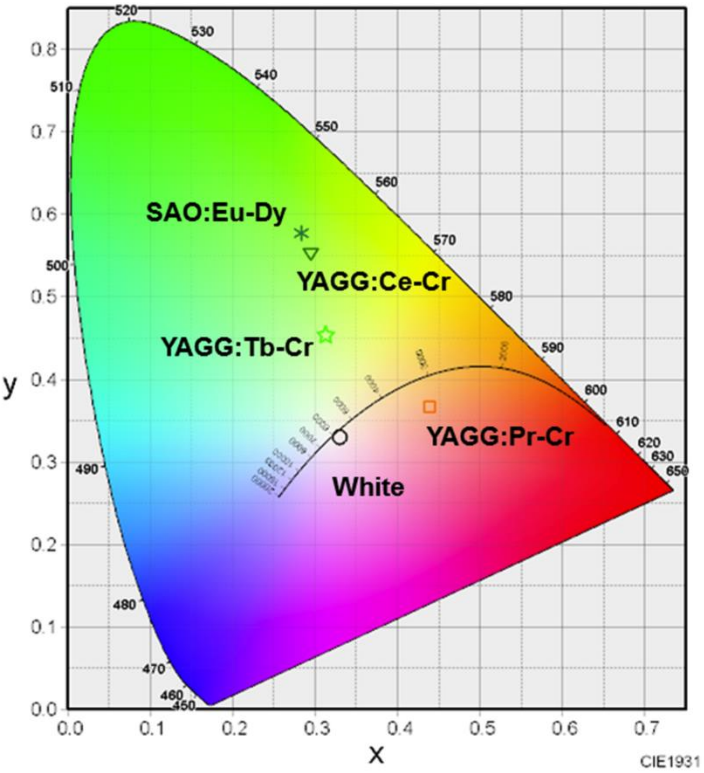

Figure 4.6. Persistent luminescent color coordinates of YAG*G*:Ce-Cr, YAG*G*:Pr-Cr and YAG*G*:Tb-Cr transparent ceramic persistent phosphors in CIE 1931 chromaticity diagram compared with that of the commercial $SrAl_2O_4:Eu^{2+}-Dy^{3+}$ green persistent phosphor

4.4.3. TL glow curves

Fig. 4.7 shows the contour plots (2D mapping) of TL glow curves of the YAG*G*:*Ln*-Cr (*Ln*=Pr, Tb, Nd, Dy) samples in order to see what kind of emission contributes to the TL glow peak at different temperatures. From the plots of the YAG*G*:Pr-Cr and YAG*G*:Tb-Cr samples in (a) and (b), it can be seen that at increased temperatures, the TL spectra are simply composed of two luminescence centers from Pr^{3+}/Tb^{3+} and Cr^{3+}, which agree well with their PersL spectra in Fig. 4.4(a2) and (b2). The intense TL glow peaks of the two samples are located at around *RT* so that they can show intense PersL at *RT*. However, in the Nd-Cr and Dy-Cr co-doped samples given in (c) and (d), the PersL intensities are much weaker than those of the Pr-Cr and Tb-Cr co-doped ones, in which the TL spectra are mainly composed of the broad band luminescence from Cr^{3+} (origin of PersL from Nd^{3+} will be discussed later in the next section). Especially for the YAG*G*:Dy-Cr sample, no sharp *f-f* transitions of Dy^{3+} are observed at any temperatures, which indicates that Dy^{3+} ions do not contribute to the PersL.

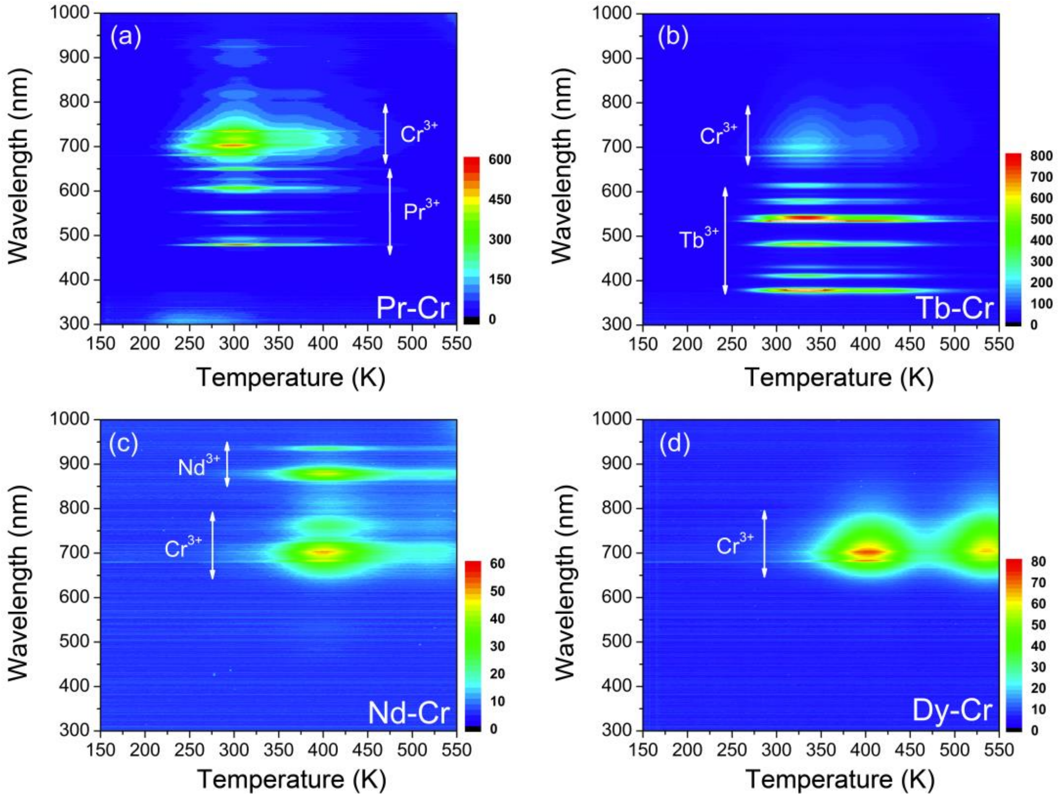

Figure 4.7. Wavelength-temperature (λ-T) contour plots of the (a) YAG*G*:Pr-Cr (b) YAG*G*:Tb-Cr (c) YAG*G*:Nd-Cr (d) YAG*G*:Dy-Cr transparent ceramic persistent phosphors

4.5. Discussion

According to the obtained results of the four YAG*G*:*Ln*-Cr (*Ln*=Pr, Nd, Tb, Dy) phosphors, they can be approximately divided into three groups: (i) Pr-Cr and Tb-Cr co-doped samples showing bright PersL mainly from Pr^{3+} and Tb^{3+} (ii) Dy-Cr co-doped one showing weak PersL only from Cr^{3+}. (iii) Nd-Cr co-doped one showing weak PersL both from Cr^{3+} and Nd^{3+}.

It is worth noting that human eyes are most sensitive to green and yellow emission; less sensitive to violet, blue, and red emission; UV and near-infrared (NIR) emission is totally invisible.[33] The photopic vision which is mediated by cone cells in human eyes allows color perception and shows a broad band sensitivity curve (from 380 to 780 nm) peaked at 555 nm with 683 lm/W luminous efficacy. The line emission due to Pr^{3+}:$^{3}P_{J\ (J=0,\,1,\,2)}\rightarrow{}^{3}H_{4,5}$, $^{1}D_{2}\rightarrow{}^{3}H_{4}$, and Tb^{3+}:$^{5}D_{4}\rightarrow{}^{7}F_{J\ (J=6,\,5,\,4,\,3)}$ in YAG*G*:Pr-Cr and YAG*G*:Tb-Cr samples matches well with the sensitivity curve of photopic vision (see Fig. 4.8). However, the luminous efficacy is almost zero in the deep-red to NIR region so that PersL from Cr^{3+} is difficult to be captured by human eyes.

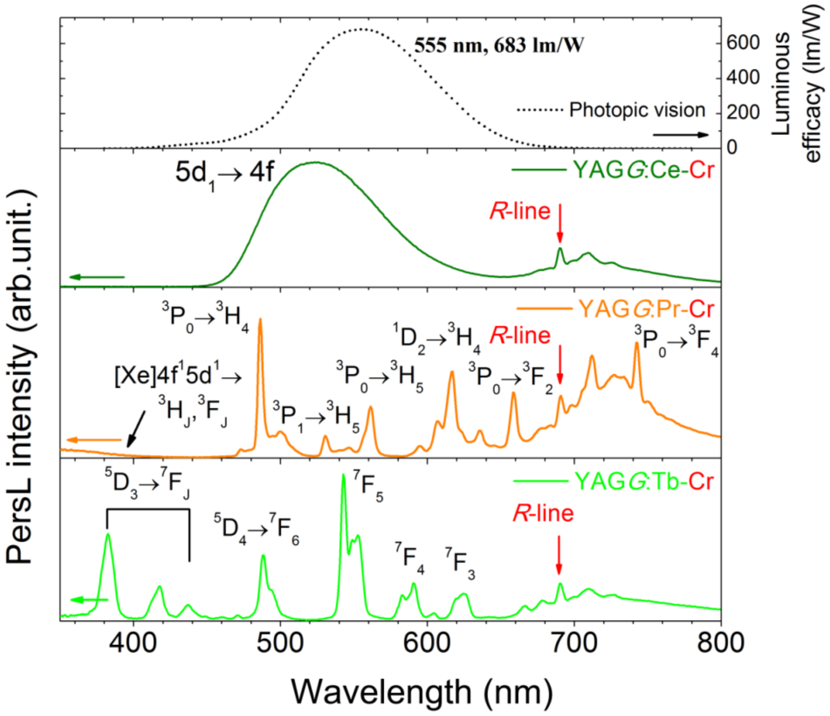

Figure 4.8. (a) Luminous efficacy of human eyes in photopic vision and persistent luminescent spectra of (b) YAG*G*:Ce-Cr (c) YAG*G*:Pr-Cr (d) YAG*G*:Tb-Cr persistent phosphors at 5 min after ceasing UV (250-400 nm) illumination

In Ln^{3+}-Cr^{3+} co-doped garnets, the PersL process usually occurs in four steps according to the electron trapping-detrapping model (the charging energy is assumed to be high enough to excite the electron into *CB*):

(1) $(e\text{-}h) \overset{h\nu}{\rightarrow} e^{-} + h^{+}$ [electron-hole generation]

(2) $Ln^{3+} + h^{+} \rightarrow Ln^{4+}$ or $(Ln^{3+} + h^{+})$ [hole trapping]

$\mathrm{Cr}^{3+} + e^{-} \rightarrow \mathrm{Cr}^{2+}$ or $(\mathrm{Cr}^{3+} + e^{-})$ [electron trapping]

(3) Ln^{4+} or $(Ln^{3+} + h^{+}) + e^{-} \rightarrow (Ln^{3+})^{*}$ [electron de-trapping from Cr^{2+} or $(\mathrm{Cr}^{3+}+e^{-})$ leading to Ln^{3+} in an excited state]

(4) $(Ln^{3+})^{*} \rightarrow Ln^{3+} + h\nu$ [radiative transition]

When e^{-} and h^{+} are generated under excitation (step 1), the Cr^{3+} ion acts as an efficient electron trap capturing one electron to be Cr^{2+} or $(\mathrm{Cr}^{3+}+e^{-})$,[16,19] and Ln^{3+} ion acts as a hole trap to be Ln^{4+} or $(Ln^{3+}+h^{+})$ (step 2). The Ln^{4+} $(Ln^{3+}+h^{+})$ ion is a re-combination center for the electron that is released from existing electron trap center Cr^{2+} $(\mathrm{Cr}^{3+}+e^{-})$ on heating, predominating the origin of the respective TL glow peak. During the thermal release of the electron from the Cr^{2+} $(\mathrm{Cr}^{3+}+e^{-})$ trap center with the following trapping on the Ln^{4+} $(Ln^{3+}+h^{+})$ center, the excited state of $(Ln^{3+})^{*}$ ion appears in the process of re-combination (step 3). The radiative transition from $(Ln^{3+})^{*}$ gives typical PersL of Ln^{3+} (step 4).

This mechanism can well explain the PersL behaviors of YAG*G*:Pr-Cr and YAG*G*:Tb-Cr samples since according to the *VRBE* diagram of the YAG*G* host (see Fig. 4.1), similar to Ce^{3+},[15,16] the ground states of Pr^{3+} ($^{3}\mathrm{H}_{4}$) and Tb^{3+} ($^{7}\mathrm{F}_{6}$) are located above the top of *VB* with large energy gap (1.78 eV for Pr^{3+}; 1.96 eV for Tb^{3+}). Therefore, the hole created at $\mathrm{Pr}^{3+}/\mathrm{Tb}^{3+}$ is difficult to move to *VB* when compared with moving a photo-induced electron into *CB* at *RT*. So $\mathrm{Pr}^{3+}/\mathrm{Tb}^{3+}$ ions can be a stable hole trap ($\mathrm{Pr}^{4+}/\mathrm{Tb}^{4+}$ or $\mathrm{Pr}^{3+}/\mathrm{Tb}^{3+}+h^{+}$), collaborating with the Cr^{3+} electron trap to induce the long PersL. Furthermore, similar to YAG*G*:Ce-Cr persistent phosphors,[15,16] the PersL behaviors such as initial emission intensity, luminescence duration and adapting temperature of the YAG*G*:Pr-Cr and YAG*G*:Tb-Cr persistent phosphors also can be tunable by changing Ga^{3+} substitution content in tetrahedral and/or octahedral sites of the YAG*G* host (taking YAG*G*:Pr-Cr orange persistent phosphors as an example, see Fig. 4.9 and Table 4.1).

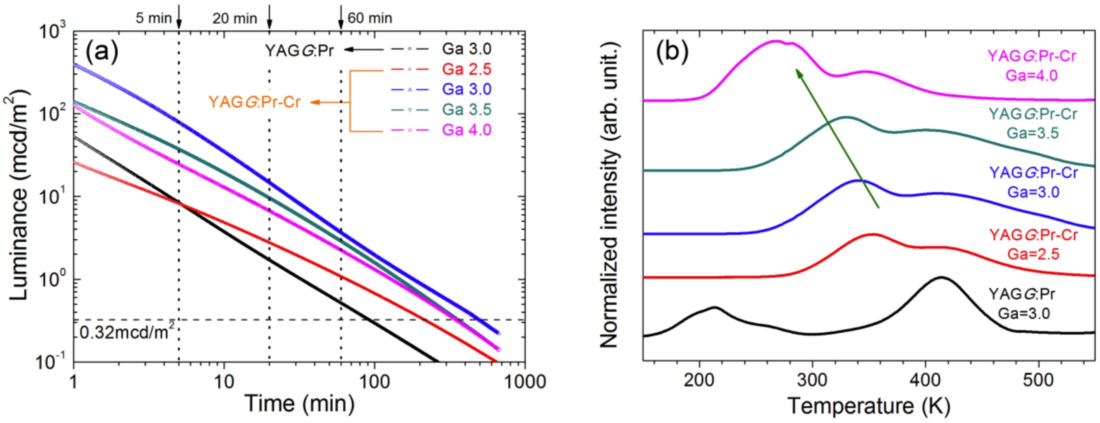

Figure 4.9. (a) Persistent luminescent decay curves recorded at 25 ℃ after ceasing UV (250-400 nm) illumination for 5 min of YAG*G*:Pr (Ga=3.0) and YAG*G*:Pr-Cr (Ga=2.5, 3.0, 3.5, 4.0) transparent ceramic persistent phosphors (b) normalized thermoluminescence (TL) glow curves of crresponding samples

Table 4.1. Luminance and duration of YAG*G*:Pr (Ga=3.0) and YAG*G*:Pr-Cr (Ga=2.5, 3.0, 3.5, 4.0) transparent ceramic persistent phosphors after ceasing UV (250-400 nm) illumination for 5 min

Sample composition	5 min (mcd/m^2)	20 min (mcd/m^2)	60 min (mcd/m^2)	Duration upon 0.32 mcd/m^2 (min)
YAG*G*:Pr^{3+} (Ga=3.0)	**8.4**	**1.7**	**0.51**	**93 ±1**
YAG*G*:Pr^{3+}-Cr^{3+} (Ga=2.5)	**8.2**	**2.8**	**1.07**	**216 ±1**
YAG*G*:Pr^{3+}-Cr^{3+} (Ga=3.0)	**79.1**	**14.8**	**3.66**	**499 ±1**
YAG*G*:Pr^{3+}-Cr^{3+} (Ga=3.5)	**37.4**	**9.6**	**2.87**	**359 ±1**
YAG*G*:Pr^{3+}-Cr^{3+} (Ga=4.0)	**24.6**	**6.7**	**2.24**	**349 ±1**

However, energy gap between the ground state of Dy^{3+} ($^6H_{15/2}$) and the top of *VB* is too small (0.54 eV) as described in this diagram, once a photo-induced hole is captured by Dy^{3+}, it will immediately escape into the *VB* so that it is quite difficult to form a stable hole trap at Dy^{3+} to be Dy^{4+} or ($Dy^{3+}+h^+$) at *RT*. As a consequence, the re-combination of *e-h* pairs may occur via a non-radiative approach so that PersL from the (Dy^{3+})* state is totally quenched (see Fig. 4.4(d2) and Fig. 4.7d). In this special case, Cr^{3+} ions take part in the PersL process since under UV illumination, Cr^{3+} itself can act both as a hole trap center to be Cr^{4+} ($Cr^{3+}+h^+$) and an electron trap center to be Cr^{2+} ($Cr^{3+}+e^-$).[19] The Cr^{4+} ($Cr^{3+}+h^+$) ion acts as a re-combination center for the electron that is released from the Cr^{2+} (Cr^{3+}+e^-) trap center followed by PersL due to Cr^{3+}. Considering the small amount of doping concentration of Cr^{3+} in this work (0.05 mol%, ten times lower than our previous report[19]), the observed weak PersL from Cr^{3+} in the YAG*G*:Dy-Cr sample is quite reasonable.

The PersL mechanism of the YAG*G*:Nd-Cr sample is more complicated than other samples. The ground state of Nd^{3+} ($^4I_{9/2}$) is quite close to the top of *VB* (energy gap: 0.29 eV, even smaller than that of Dy^{3+}) in the *VRBE* diagram. This indicates that Nd^{3+} cannot work as a stable hole trap to be Nd^{4+} or (Nd^{3+}+h^+) at *RT*. However, PersL from Nd^{3+} is still observed (see Fig. 4.4(c2) and Fig. 4.7c). This is mainly attributed to the persistent energy transfer from Cr^{3+} to Nd^{3+}, which is similar to the same process as that in the YAG*G* host where it occurs from Ce^{3+} to Nd^{3+}.[34] Since the emission band of donor (Cr^{3+}) matches well with the absorption band of acceptor (Nd^{3+}), the resonant energy transfer takes place from Cr^{3+} to Nd^{3+} as that in $Y_3Al_5O_{12}$ (YAG)[35,36] (see Fig. 4.10). Therefore, the persistent energy transfer also occurs mainly from Cr^{3+}: ^2E (^2G) to Nd^{3+}: $^4F_{7/2}$, which is followed by rapid multi-phonon relaxation down to the $^4F_{3/2}$ excited level, and finally induces the sharp PersL bands of Nd^{3+}: $^4F_{3/2} \rightarrow {}^4I_J$ located at around 880 nm and longer wavelengths.

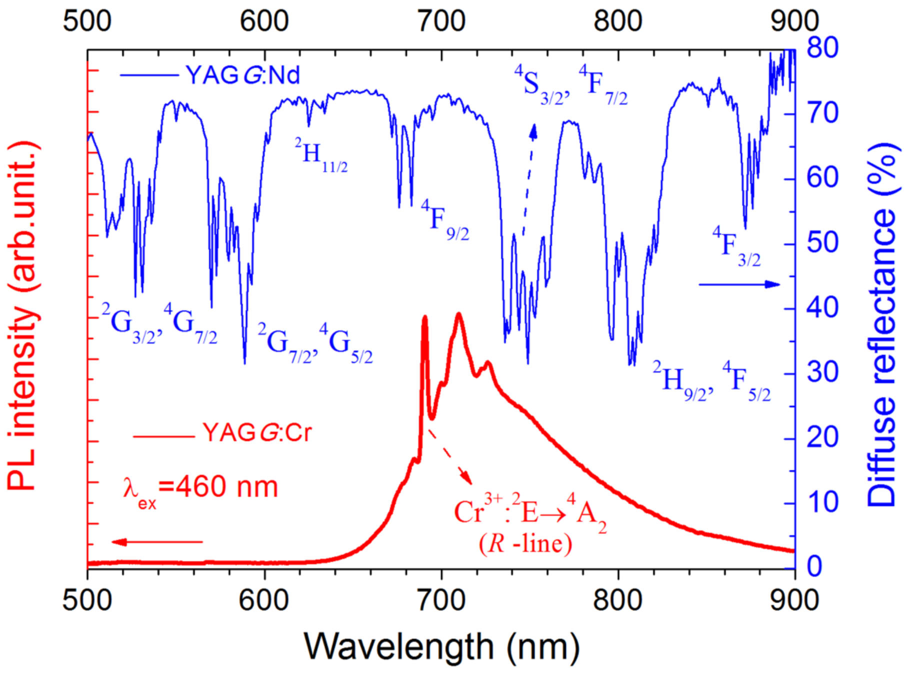

Figure 4.10. Photoluminescence (PL) spectrum (λex=460 nm) of the YAG*G*:Cr and diffuse reflectance of the YAG*G*:Nd ceramic samples

4.6. Conclusion

In summary, based on the *VRBE* diagram of the YAG*G* host, Pr^{3+}, Nd^{3+}, Tb^{3+}, Dy^{3+} ions were selected and co-doped with Cr^{3+} ions to develop novel persistent phosphors. Since the energy gaps between the ground states of Pr^{3+}/Tb^{3+} and the top of *VB* are large enough so that Pr^{3+}/Tb^{3+} ions can be stable hole traps, collaborating with Cr^{3+} electron traps to induce the long PersL. The persistent luminance duration upon 0.32 mcd/m^2 of the YAG*G*:Pr-Cr and YAG*G*:Tb-Cr samples due to Pr^{3+} (orange) and Tb^{3+} (light green) could reach about 8 h and 12 h, respectively. However, because of the small energy gaps between the ground states of Nd^{3+}/Dy^{3+} and the top of *VB*, Nd^{3+}/Dy^{3+} ions cannot act as stable hole traps. Therefore, the persistent luminescent intensities of YAG*G*:Nd-Cr and YAG*G*:Dy-Cr samples are quite weak and dominated mainly by the deep-red transition of Cr^{3+}.

With this paper, we introduced a way to design novel garnet persistent phosphors from the knowledge of energy levels of lanthanide dopants. Since lanthanide ions are widely used as emission centers and/or trap centers for PersL, this theoretical prediction diagram can be a useful guidance for choosing proper lanthanide ions, in a more general and convenient manner to design new storage phosphors in different matrices.

Acknowledgement

I would like to acknowledge Prof. Pieter Dorenbos from Delft University of Technology, Prof. Bruno. Viana from Chimie-Paris Tech and Prof. Peter A. Tanner from the Hong Kong Institute of Education, who stayed at Kyoto University as visiting professors, for fruitful discussions on persistent phosphors and luminescence mechanisms.

References

[1] K. van den Eeckhout, P. F. Smet and D. Poelman, *Materials*., 2010, **3**, 2536.

[2] K. van den Eeckhout, D. Poelman and P. F. Smet, *Materials*., 2013, **6**, 2789.

[3] B. Viana, S. K. Sharma, D. Gourier, T. Maldiney, E. Teston, D. Scherman and C. Richard, *J. Lumin*., 2016, **170**, 879.

[4] Y. Murayama, N. Takeuchi, Y. Aoki and T. Matsuzawa, US Patent, 5.242.006, 1995.

[5] H. Takasaki, S. Tanabe and T. Hanada, *J. Ceram. Soc. Jpn*., 1996, **104**, 322.

[6] S. Tanabe and T. Hanada, *New Ceramics*., 1996, **9(10)**, 27. (in Japanese)

[7] T. Matsuzawa, Y. Aoki, N. Takeuchi and Y. Murayama, *J. Electrochem. Soc*., 1996, **143**, 2670.

[8] Y. Aoki, Y. Hirata, H. Sasai, T. Ohishi and N. Takeuchi, Japanese Patent, 208948, 1997.

[9] F. Clabau, X. Rocquefelte, S. Jobic, P. Deniard, M. H. Whangbo, A. Garcia and T. Le Mercier, *Chem. Mater*., 2005, **17**, 3904.

[10] J. Botterman and P. F. Smet, *Opt. Express*., 2015, **23**, A868.

[11] K. Chakrabarti, V. K. Mathur, J. F. Rhodes and R. J. Abbundi, *J. Appl. Phys*., 1988, **64**, 1363.

[12] A. Lecointre, A. Bessière, A. J. J. Bos, P. Dorenbos, B. Viana and S. Jacquart, *J. Phys. Chem. C*., 2011, **115**, 4217.

[13] H. Luo, A J J. Bos, and P. Dorenbos, *J. Phys. Chem. C*., 2016, **120**, 5916.

[14] B. Qu, B. Zhang, L. Wang, R. Zhou, X-C. Zeng and L. Li, *ACS Appl. Mater. Interfaces*., 2016, **8**, 5439.

[15] J. Ueda, K. Kuroishi and S. Tanabe, *Appl. Phys. Lett*., 2014, **104**, 101904.

[16] J. Ueda, P. Dorenbos, A J J. Bos, K. Kuroishi and S. Tanabe, *J. Mater. Chem. C*., 2015, **3**, 5642.

[17] J. Ueda, *J. Ceram. Soc. Jpn*., 2015, **123**, 1059.

[18] J. Xu, J. Ueda, K. Kuroishi and S. Tanabe, *Scr. Mater*., 2015, **102**, 47.

[19] J. Xu, J. Ueda, Y. Zhuang, B. Viana and S. Tanabe, *Appl. Phys. Express*., 2015, **8**, 042602.

[20] Y. Katayama, B. Viana, D. Gourier, J. Xu and S. Tanabe, *Opt. Mater. Express*., 2016, **6**,1405.

[21] A. Bessière, S. Jacquart, K. Priolkar, A. Lecointre, B. Viana and D. Gourier, *Opt. Express*., 2011, **19**(11), 10131.

[22] T. Maldiney, A. Bessière, J. Seguin, E. Teston, S. K. Sharma, B. Viana, A. J. J. Bos, P. Dorenbos, M. Bessodes, D. Gourier, D. Scherman and C. Richard, *Nat. Mater*., 2014, **13**, 418.

[23] T. Maldiney, B. Ballet, M. Bessodes, D. Scherman and C. Richard, *Nanoscale*., 2014, **6**, 13970.

[24] A. Bessière, S. K. Sharma, N. Basavaraju, K. R. Priolkar, L. Binet, B. Viana, A. J. J. Bos, T. Maldiney, C. Richard, D. Scherman and D. Gourier, *Chem. Mater*., 2014, **26**, 1365.

[25] D. Gourier, A. Bessière, S. K. Sharma, L. Binet, B. Viana, N. Basavaraju and K. R. Priolkar, *J.*

Phys Chem. Solids., 2014, **75**, 826.

[26] P. Dorenbos, *J. Phys.: Condens. Matter*., 2003, **15**, 8417.

[27] P. Dorenbos, *J. Lumin*., 2005, **111**, 89.

[28] P. Dorenbos, *J. Electrochem. Soc*., 2005, **152**, H107.

[29] P. Dorenbos, *J. Mater. Chem*., 2012, **22**, 22344.

[30] P. Dorenbos, *J. Lumin*., 2013, **134**, 310.

[31] F. T. You, A. J. J. Bos, Q. F. Shi, S. H. Huang and P. Dorenbos, *Phys. Rev. B*., 2012, **85**, 115101.

[32] A. J. J. Bos, P. Dorenbos, A. Bessière and B. Viana, *Radiat. Meas*., 2008, **43**, 222.

[33] Y. Zhuang, Y. Katayama, J. Ueda and S. Tanabe, *Opt. Mater*., 2014, **36**, 1907.

[34] J. Xu, S. Tanabe, A. D. Sontakke and J. Ueda, *Appl. Phys. Lett*., 2015, **107**, 081903.

[35] A. Ikesue, K. Kamata, and K. Yoshida, *J. Am. Ceram. Soc*., 1995, **78**, 2545.

[36] P. Samuel, G. A. Kumar, T. Yanagitani, H. Yagi, K-I Ueda and S. M. Babu, *Opt. Mater*., 2011, **34**, 303.

Chapter 5

$Y_3Al_{5-x}Ga_xO_{12}$:Cr^{3+}: a novel red persistent phosphor with high brightness

Abstract:

We report red persistent phosphors of $Y_3Al_{5-x}Ga_xO_{12}$:Cr^{3+} garnet (YAG*G*:Cr^{3+}, x from 0 to 5). In this material, Cr ions act both as emission centers and electron traps. The trap depth, which is regarded as the energy gap between the bottom of the conduction band and the electron trap, can be optimized via modifying Ga^{3+} substitution contents, x. After ceasing UV irradiation, the persistent luminescence of the YAG*G*:Cr^{3+} (x=3) phosphor was nearly 5 times higher than that of the widely used $ZnGa_2O_4$:Cr^{3+} red persistent phosphor. Such novel red persistent phosphors possess a great potential for an improved *in vivo* bio-imaging application.

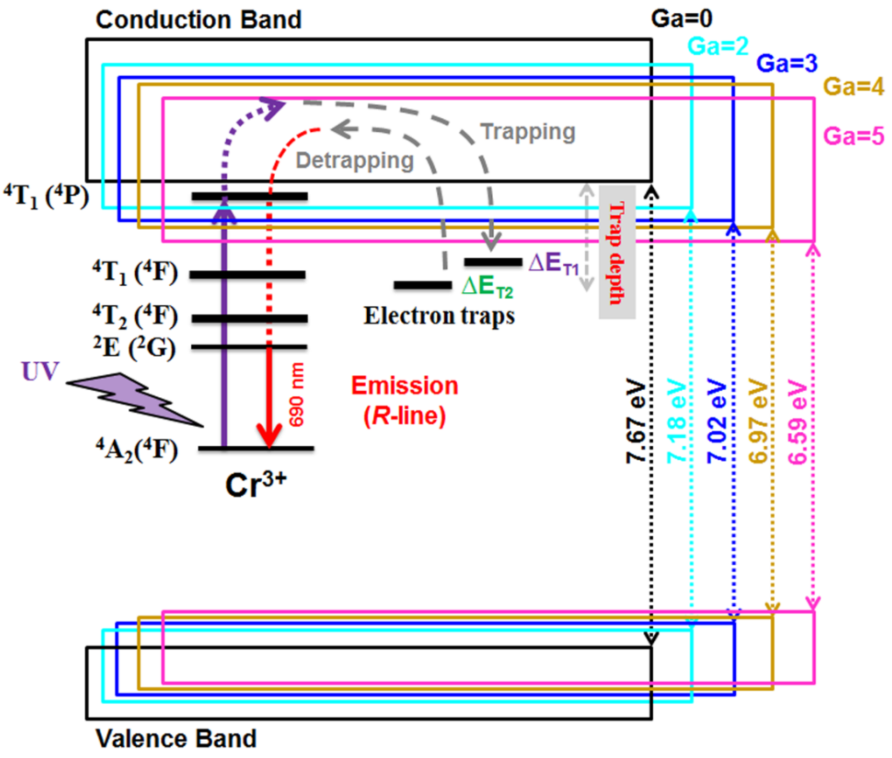

Band-gap engineering of the YA*G*-YAG*G* solid solutions with different Ga^{3+} contents

5.1. Introduction

Recently, the potential applications of red or near-infrared (NIR) persistent phosphors have expanded from night-vision security signs to *in vivo* bio-imaging systems.[1-4] Nano-particles with red/NIR persistent luminescence charged by ultraviolet (UV) light irradiation before injection into biological tissues can be used as long-lasting optical probes for the *in vivo* bio-imaging.[5-10] The exclusion of external irradiation can remove the possibility of auto-fluorescence/background noise and thus improves the signal-to-noise ratio greatly. This new application attracts much attention to the development of red/NIR persistent phosphors with brighter luminescence and longer afterglow. Till now, various red/NIR persistent phosphors have been studied for this purpose,[11,12,13] among them, Cr^{3+} doped phosphors are considered to be highly desirable candidates since Cr^{3+} ion with $3d^3$ electronic configuration allows a narrow-band emission close to 700 nm due to the highly efficient $^2E \rightarrow {}^4A_2$ transition (*R*-line).[14-17] Furthermore, this emission range matches well with the optical window (from 650 to 1300 nm) where deeper penetration distance through biological tissues can be detected by optical signals.[18]

However, only a few Cr^{3+} doped red/NIR long persistent phosphors have been reported so far,[11,12,13] which are mainly gallate or aluminate based materials such as $Zn_3Ga_2Ge_2O_{10}:Cr^{3+}$,[19] $LiGa_5O_8:Cr^{3+}$,[20] $LaAlO_3:Cr^{3+}$,[21] and spinel materials like $ZnGa_2O_4:Cr^{3+}$ [3,4,6-10,22-25] and $MgGa_2O_4:Cr^{3+}$ [26,27] because of the strong substitutability of Cr^{3+} for Ga^{3+} in distorted octahedral coordination owing to their similar ionic radius. In garnet structure, Cr^{3+} doping ions are also commonly used for tunable laser and solar concentrators[28,29] since they can stably substitute in B site of the $\{A\}_3[B]_2(C)_3O_{12}$ garnet matrix where {A}, [B], and (C) represent the cations at the dodecahedral, octahedral, and tetrahedral sites, respectively. We have already reported a novel persistent ceramic phosphor with composition of $Y_3Al_{5-x}Ga_xO_{12}$ (YAG*G*):Ce^{3+}-Cr^{3+} (x=2.5, 3, 3.5) which can emit bright green luminescence (Ce^{3+}:$5d \rightarrow 4f$) lasting for several hours after ceasing the blue light excitation.[30] In this material, Cr^{3+} ions act as electron trapping centers and create an ideal trap depth for persistent luminescence working at room temperature (*RT*). Furthermore, by optimizing the trap depth via modifying Ga^{3+} substitution contents, the persistent luminance of the YAG*G*:Ce^{3+}-Cr^{3+} phosphor is even higher than that of a compact made of the commercial $SrAl_2O_4:Eu^{2+}$-Dy^{3+} powder phosphors pumped at the same wavelength.[30]

Although persistent phosphors with garnet structure exhibit a great potential for long persistent illumination applications, to the best of our knowledge, there are few reports concerning red persistent luminescence in garnet structure which can last only for less than several seconds.[31,32] Here, we report a series of novel red persistent phosphors $Y_3Al_{5-x}Ga_xO_{12}:Cr^{3+}$ (YAG*G*:Cr^{3+}) with bright persistent luminescence after ceasing UV irradiation for even more than 1 h, the corresponding radiance (in unit of $mW/Sr/m^2$) was nearly 5 times higher than that of the standard red persistent phosphor ($ZnGa_2O_4:Cr^{3+}$) widely used in the *in vivo* bio-imaging.[4]

5.2. Experimental procedures

YAG*G*:Cr^{3+} ceramic phosphors with composition of $Y_3Al_{4.99-x}Ga_xO_{12}:Cr_{0.01}$ (x=0, 2, 3, 4, 5) were fabricated by a solid-state reaction method. The chemicals of Y_2O_3 (99.99%), Al_2O_3 (99.99%), Ga_2O_3 (99.99%), and Cr_2O_3 (99.9%) were used as raw materials. The starting powder was mixed by ball milling method with ZrO_2 ceramic balls and anhydrous alcohol for several hours. The mixed powder was dried at 80 ℃ for 36 h, compacted to form a ceramic green body (ϕ20 mm × 3-4 mm) under uniaxial pressing of 50 MPa and finally sintered at 1600 ℃ for 10 h in air.

Photoluminescence excitation (PLE) spectrum was recorded using a fluorescence spectrophotometer (RF-5300PC, Shimadzu). Photoluminescence (PL) and persistent luminescence (PersL) spectra were measured by a CCD spectrometer (QE65-Pro, Ocean Optics) connected with an optical fiber. A combination of a 300W Xe lamp (MAX-302, Asahi Spectra) and an UV mirror module (250-380 nm) was used as the excitation source. Thermoluminescence (TL) glow curves monitoring the Cr^{3+} emission were measured by a combination of the Xe lamp and a silicon photodiode

(S-025-H, Electro-Optical Systems) which was shielded with a band-pass filter (350-750 nm) and a long-pass filter (>580 nm) to cut off the noise other than the TL signal. The pellet sample was set in a cryostat (Helitran LT3, Advanced Research Systems) to control temperatures and firstly excited by UV light (250-380 nm) at 130 K for 10 min, after waiting for 10 min, then finally heated up to 600 K at a rate of 10 K/min. Persistent luminescent decay curves were measured at 25 ℃ using the same photodiode as the TL measurement. Then, the decay curves were calibrated to the absolute radiance (in unit of $mW/Sr/m^2$) using a radiance meter (Glacier X, B&W Tek Inc).

5.3. Results and discussion

Fig. 5.1 illustrates the PLE spectrum monitoring 690 nm, PL and PersL spectra of the YAG*G*:Cr^{3+} (x=3) ceramic phosphor under and after UV (250-380 nm) excitation. In the PLE spectrum, the excitation bands centered at 283, 460, and 638 nm are ascribed to intra-3*d* transitions of Cr^{3+}: $^4A_2$ (^4F)→$^4T_1$ (^4P), $^4A_2$ (^4F)→$^4T_1$ (^4F), and $^4A_2$ (^4F)→$^4T_2$ (^4F), respectively. The PL and PersL spectral structure of the *R*-line at 690 nm and some phonon sidebands (PSB) due to thermal vibration of Cr^{3+} ions are consistent with those in the literature.[33-34] It is worth noting that the spectral shapes of PL and PersL are almost identical in the YAG*G*:Cr^{3+} phosphor which is quite different from the situation in $ZnGa_2O_4$:Cr^{3+}, where anti-site defects $Ga_{Zn}^{\bullet}$ of the $ZnGa_2O_4$ spinel structure are involved in the carrier trapping and recombination processes responsible for long persistent luminescence.[4,6,22-25] Although such anti-site defects have already been demonstrated and correspond to a possible existence of $Y_B^{\times}$, $Al_Y^{\times}$ or $Ga_Y^{\times}$ in garnet (B is the octahedral site occupied with Al and/or Ga ions),[35-41] it is not clear that they play an important role for persistent luminescence. Hence, we assume that the delayed charge recombination in PersL by trapping and detrapping processes occur through the same kind of Cr^{3+} centers as that in PL.

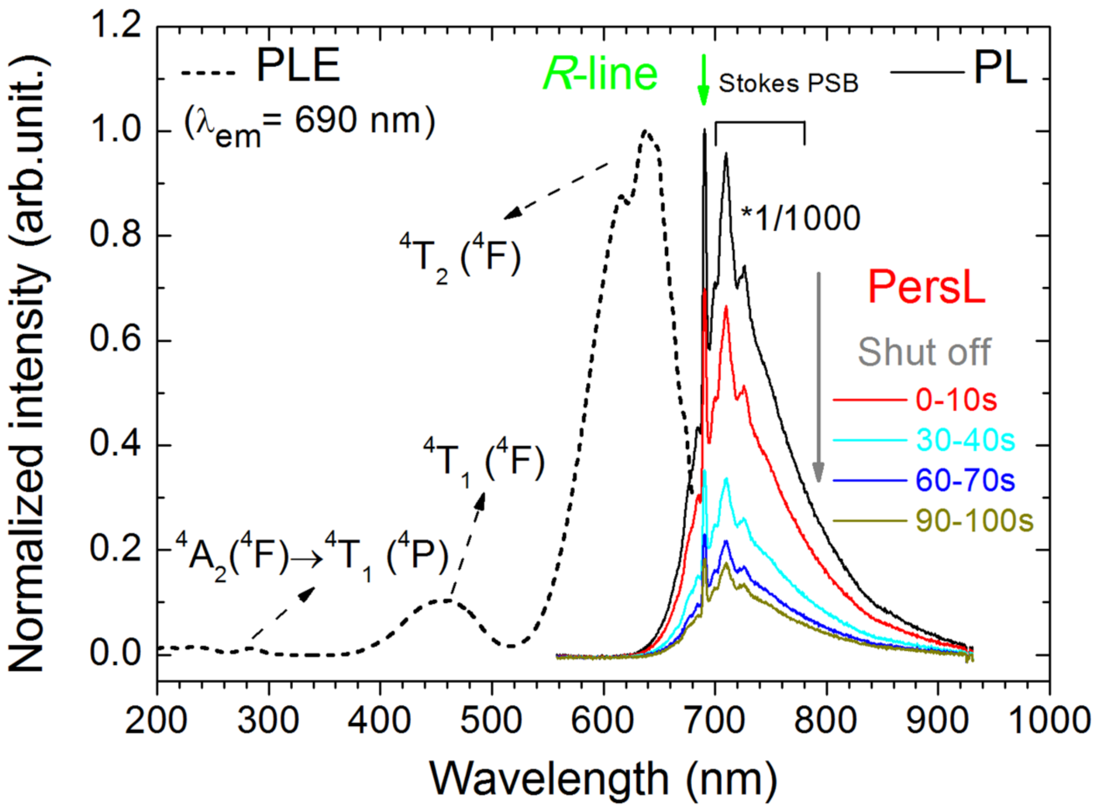

Figure 5.1. Photoluminescence excitation (PLE) spectrum monitoring 690 nm, photoluminescence (PL) and persistent luminescence (PersL) spectra (integral time 10 s) under and after UV (250-380 nm) excitation of the YAG*G*:Cr^{3+} (x=3) ceramic phosphor, respectively.

Fig. 5.2(a)-(c) gives the photographs of the YAG*G*:Cr^{3+} ceramic phosphors with different Ga^{3+} contents (Ga=0, 2, 3, 4, 5) before and after ceasing UV (254 nm) irradiation. All of the ceramic phosphors exhibit green appearance under fluorescent lamp and red persistent luminescence after ceasing the excitation source. Persistent luminescent decay curves after 5 min irradiation by xenon lamp connected with a UV module (250-380 nm) of the YAG*G*:Cr^{3+} ceramic phosphors are shown in Fig. 5.2(d). The persistent decay curve of the standard $ZnGa_2O_4$:Cr^{3+} ceramic phosphor previously reported by our group with the same experimental condition is also plotted as a reference.[23] It is worth noting that, for most persistent phosphors emitting visible lights, luminance (in units of cd/m^2 or mcd/m^2) is generally adopted to quantify the brightness of persistent phosphors in industrial patents or international standards.[42,43] For example the persistent decay duration should be the time between the end of the excitation and the moment when the decay intensity drops below 0.32 mcd/m^2, a value commonly used by the safety signage industry (about 100 times the sensitivity of the dark adapted eye)[13] However, deep-red to NIR persistent luminescence is less efficiently sensed by human eyes. Especially, the luminous efficacy in the scotopic vision is almost zero in the wavelength region longer than 650 nm. In this case, the radiance (in unit of $mW/Sr/m^2$) is more appropriate than luminance for the evaluation of red to NIR persistent luminescence.[12] Hence, we summarized the radiance after 5 min, 30 min and 60 min of those YAG*G*:Cr^{3+} ceramic samples in Table. 5.1, which suggests that the persistent decay behavior of the samples changes with varying Ga^{3+} substitution content. Furthermore, after ceasing the excitation source for 60 min, the radiance of the Ga=3 sample reaches 0.67×10^{-1} $mW/Sr/m^2$, nearly 5 times higher than that of the $ZnGa_2O_4$:Cr^{3+} phosphor (0.15×10^{-1} $mW/Sr/m^2$).

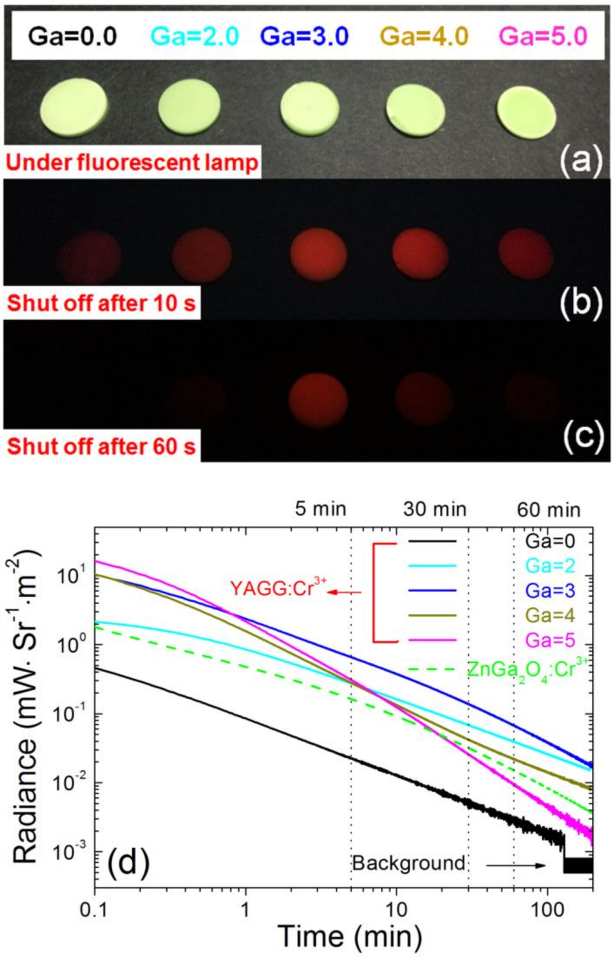

Figure 5.2. Photographs of the YAG*G*:Cr^{3+} ceramic phosphors with different Ga^{3+} contents (Ga=0, 2, 3, 4, 5) (a) under fluorescent lamp and ceasing UV (254 nm) irradiation (b) after 10 s and (c) 60 s, respectively (d) corresponding persistent decay curves compared with the $ZnGa_2O_4$:Cr^{3+} ceramic pellet. All of the samples were excited by UV light (250 to 380 nm) from a 300W xenon lamp for 5 min.

Table. 5.1. Radiance of YAG*G*:Cr^{3+} ceramic phosphors with different Ga^{3+} contents compared with the $ZnGa_2O_4$:Cr^{3+} ceramic pellet.[23]

	5 min	30 min	60 min
	(mW•Sr^{-1}•m^{-2})	(mW•Sr^{-1}•m^{-2})	(mW•Sr^{-1}•m^{-2})
YAG*G*:Cr^{3+} (Ga=0)	**0.22×10^{-1}**	**0.05×10^{-1}**	**0.03×10^{-1}**
YAG*G*:Cr^{3+} (Ga=2)	**2.75×10^{-1}**	**0.68×10^{-1}**	**0.39×10^{-1}**
YAG*G*:Cr^{3+} (Ga=3)	**6.59×10^{-1}**	**1.37×10^{-1}**	**0.67×10^{-1}**
YAG*G*:Cr^{3+} (Ga=4)	**2.79×10^{-1}**	**0.42×10^{-1}**	**0.22×10^{-1}**
YAG*G*:Cr^{3+} (Ga=5)	**3.09×10^{-1}**	**0.26×10^{-1}**	**0.10×10^{-1}**
$ZnGa_2O_4$:Cr^{3+} [23]	**1.63×10^{-1}**	**0.32×10^{-1}**	**0.15×10^{-1}**

In order to clarify the trapping and detrapping mechanism of YAG*G*:Cr^{3+} phosphors with different Ga^{3+} contents, TL measurements monitoring the Cr^{3+} luminescence are carried out as shown in Fig. 5.3(a). All of the samples exhibit two glow peaks (T_1, T_2 represent the lower and higher temperature, respectively) and both of them shift monotonously from high temperature to low temperature with increasing Ga^{3+} content [see Fig. 5.3(b)]. According to our former research results in Ce^{3+}-Cr^{3+} co-doped YAG*G* persistent phosphors,[30] co-doping with Cr^{3+} ions forms additional electron traps efficiently capturing excited electrons (Cr^{2+} or Cr^{3+}-e^-) and release them slowly with thermal stimulation. Here, for the Cr^{3+} single doped YAG*G* phosphors, the short-wavelength UV irradiation can lead to a decrease of Cr^{3+} ions concentration as a result of change of their valence state to Cr^{2+} and Cr^{4+}.[32,44] Thus, Cr^{3+} ions under irradiation can act both as deep acceptor centers, forming Cr^{4+} and as electronic trap centers Cr^{2+} (Cr^{3+}-e^-). The Cr^{4+} ions are recombination centers for electrons that are released from existing electronic trap centers Cr^{2+} (Cr^{3+}-e^-) on heating, predominating the origin of the respective TL glow peaks. During the thermal release of electrons from the Cr^{2+} (Cr^{3+}-e^-) trap centers with their next trapping on the Cr^{4+} levels, the excited state of ion $(Cr^{3+})^*$ appears in the process of recombination. Its radiative relaxation gives typical luminescence of Cr^{3+} ions as follows:

$$\mathrm{Cr_B^\times} + \overbrace{\mathrm{Cr_B^\times} \xrightarrow{h\nu\,(\mathrm{UV})} [\mathrm{Cr_B^\times} + e^-] + \mathrm{Cr_B^\bullet} \xrightarrow{kT} [\mathrm{Cr_B^\times}]^*}^{h\nu\,(\mathrm{Red})} + \mathrm{Cr_B^\times} \qquad (1)$$

where B represents the trivalent ions like Al^{3+} and/or Ga^{3+} occupying the B site (octahedral site) of the $\{A\}_3[B]_2(C)_3O_{12}$ garnet matrix, *k* is Boltzmann constant, T is absolute temperature.

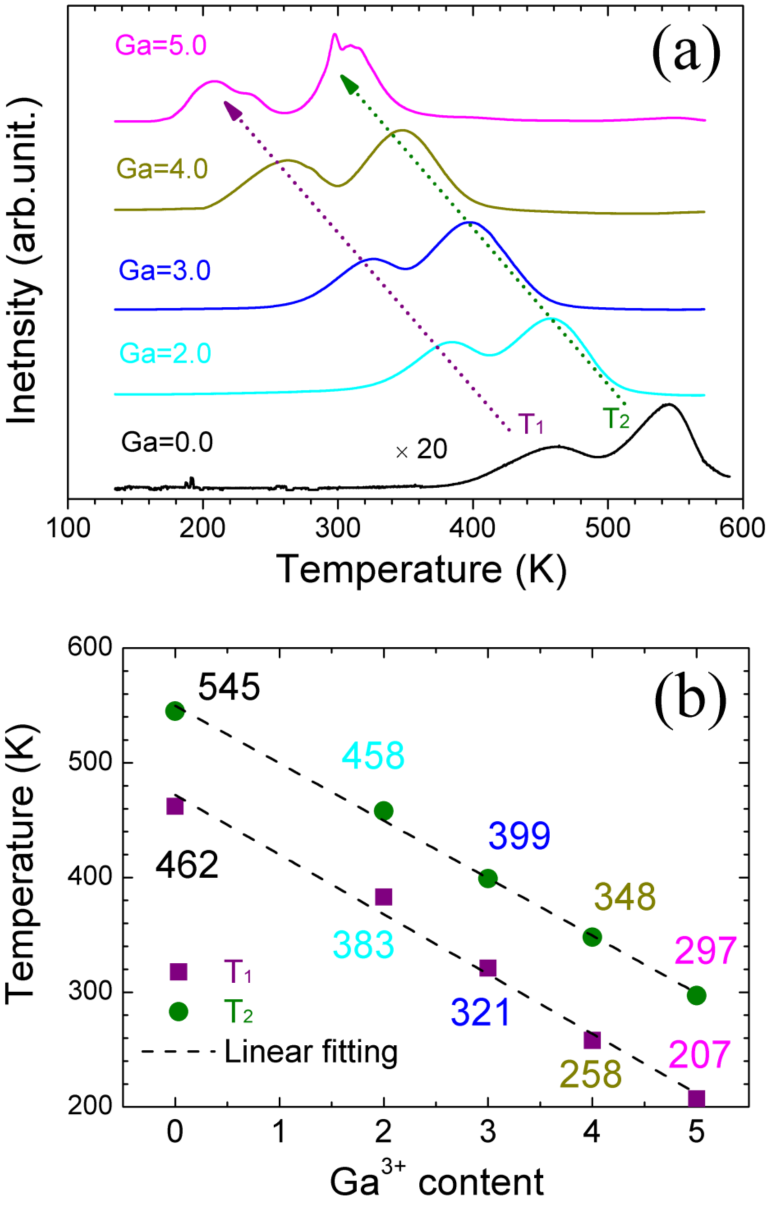

Figure 5.3. (a) Thermoluminescence (TL) glow curves monitoring the Cr^{3+} luminescence of the YAG*G*:Cr^{3+} ceramic phosphors with different Ga^{3+} contents (b) peak temperatures obtained by Gaussian fitting results of corresponding TL glow curves. All of the samples were excited by UV light (250 to 380 nm) from a 300W xenon lamp for 10 min.

The schematic illustration of the trapping and detrapping processes of the YAG*G*:Cr^{3+} ceramic phosphors is also given in Fig. 5.4 with the help of the band-gap energy data of YA*G*-YG*G* solid solution which is estimated by Dorenbos using exciton creation energy.[45] Furthermore, the peak temperature of the TL glow curve is related to the energy gap between the bottom of conduction band (*C.B*) and the electron trap.[46] Considering the two temperature peaks in TL glow curves of all the YAG*G*:Cr^{3+} samples, it indicates that there may be a trap distribution and/or quantum tunneling processes in such kind of materials.[47,48] The peak shift of these samples suggests that the trap depth can be modified by changing the Ga^{3+} content so that it is possible to control the persistent luminescent properties such as the initial persistent luminescence intensity and the duration time. For example, according to the decay curves shown in Fig. 5.2(d), the YAG*G*: Cr^{3+} sample (Ga=3) emits the highest persistent luminescence intensity at RT 1 h after ceasing the 5 min UV irradiation than that of other samples, while considering the working temperature in bio-imaging for human bodies or small animals (usually around 36 ℃), persistent behavior of YAG*G*: Cr^{3+} phosphors can also be easily tunable by changing Ga^{3+} contents to meet well with different practical requirements.

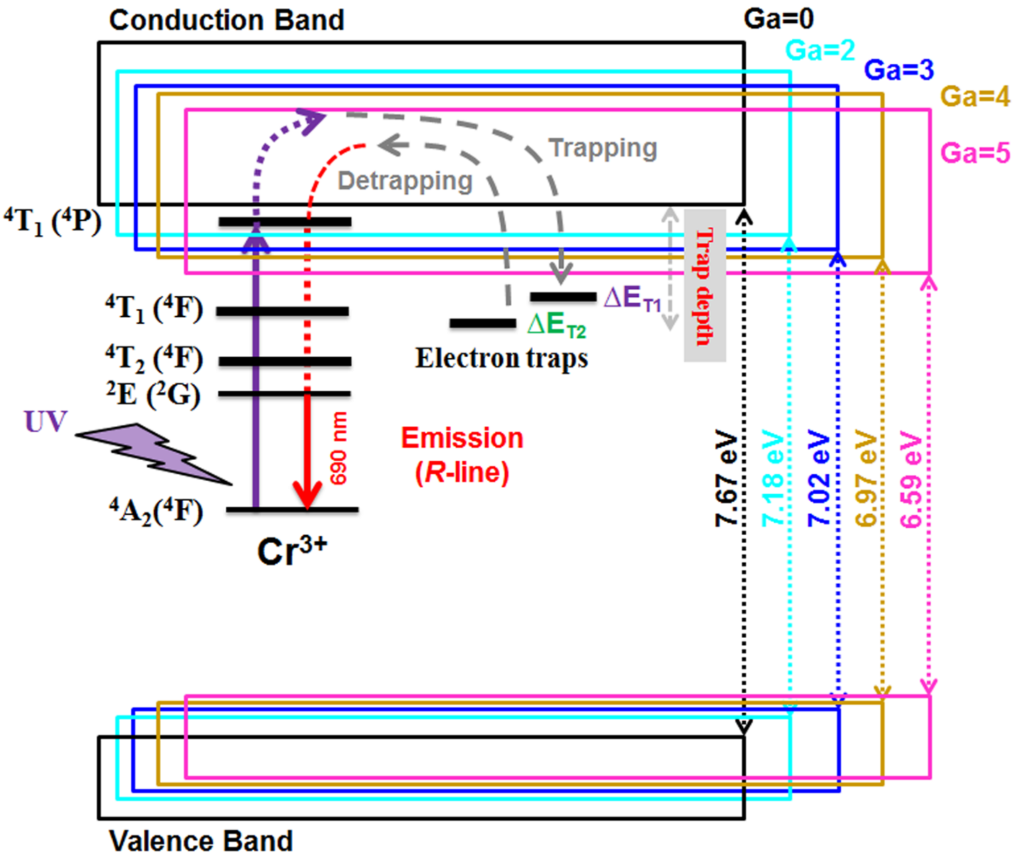

Figure 5.4. Schematic illustration of the trapping and detrapping processes of the YAG*G*:Cr^{3+} ceramic phosphors (band-gap energy of different YAG-YAG*G* solid solutions are referred by Ref. 45)

5.4. Conclusion

In summary, a novel red ceramic phosphor: YAG*G*:Cr^{3+}, showing bright persistent luminescence was developed. After ceasing UV irradiation, the radiance of this material was nearly 5 times higher than that of the commonly used $ZnGa_2O_4:Cr^{3+}$ red persistent phosphor. This behavior was mainly attributed to the efficient electron trapping and detrapping processes and one could adjust electron trap depth through different Ga^{3+} contents. Since garnet materials have been widely used for various applications, such novel red persistent phosphors are considered to possess a great potential for an improved *in vivo* bio-imaging application. Practical applications with better signal-to-noise ratio in the *in vivo* bio-imaging field can be expected in the near future by using YAG*G*:Cr^{3+} garnet nano-particles with bright red persistent luminescence.

Acknowledgement

This work was supported by JSPS KAKENHI Grant Number 25620184.

References

[1] Q. le Masne de Chermont, C. Chanéac, J. Seguin, F. Pellé, S. Maîtrejean, J.-P. Jolivet, D. Gourier, M. Bessodes, and D. Scherman, Proc. Natl. Acad. Sci. U.S.A. **104**, 9266 (2007).

[2] T. Maldiney, A. Lecointre, B. Viana, A. Bessière, M. Bessodes, D. Gourier, C. Richard, and D. Scherman, J. Am. Chem. Soc. **133**, 11810 (2011).

[3] T. Maldiney, G. Sraiki, B. Viana, D. Gourier, C. Richard, D. Scherman, M. Bessodes, K. Van den Eeckhout, D. Poelman, and P. F. Smet, Opt. Mater. Express. **2**, 261 (2012).

[4] T. Maldiney, A. Bessière, J. Seguin, E. Teston, S. K. Sharma, B. Viana, A. J. J. Bos, P. Dorenbos, M. Bessodes, D. Gourier, D. Scherman, and C. Richard, Nat. Mater. **13**, 418 (2014).

[5] T. Maldiney, C. Richard, J. Seguin, N. Wattier, M. Bessodes, and D. Scherman, ACS Nano. **5**, 854 (2011).

[6] A. Bessière, S. K. Sharma, N. Basavaraju, K. R. Priolkar, L. Binet, B. Viana, A. J. J. Bos, T. Maldiney, C. Richard, D. Scherman, and D. Gourier, Chem. Mater. **26**, 1365 (2014).

[7] S. K. Sharma, A. Bessière, N. Basavaraju, K. R. Priolkar, L. Binet, B. Viana, and D. Gourier, J. Lumin. **155**, 251 (2014).

[8] D. Gourier, A. Bessière, S. K. Sharma, L. Binet, B. Viana, N. Basavaraju, and K. R. Priolkar, J. Phys Chem. Solids. **75**, 826 (2014).

[9] T. Maldiney, B. Ballet, M. Bessodes, D. Scherman, and C. Richard, Nanoscale. **6**, 13970 (2014).

[10] N. Basavaraju, K. R. Priolkar, D. Gourier, S. K. Sharma, A. Bessière, and B. Viana, Phys. Chem. Chem. Phys. **17**, 1790 (2015).

[11] S. K. Singh, RSC Adv. **4**, 58674 (2014).

[12] Y. Zhuang, Y. Katayama, J. Ueda, and S. Tanabe, Opt. Mater. **36**, 1907 (2014).

[13] K. Van Den Eeckhout, D. Poelman, and P. F. Smet, Materials. **6**, 2789 (2013).

[14] T. H. Maiman, Nature. **187**, 493 (1960).

[15] F. Durville, B. Champagnon, E. Duval, and G. Boulon, J. Phys. Chem. Solids. **46**, 701 (1985).

[16] J. Ueda and S. Tanabe, J. Am. Ceram. Soc. **93**, 3084 (2010).

[17] D. Chen, J. Eur. Ceram. Soc. **34**, 4069 (2014).

[18] R. Weissleder, Nat. Biotechnol. **19**, 316 (2001).

[19] Z. Pan, Y.-Y. Lu, and F. Liu, Nat. Mater. **11**, 58 (2012).

[20] F. Liu, W. Yan, Y.-J. Chuang, Z. Zhen, J. Xie, and Z. Pan, Sci. Rep. **3**, 1554 (2013).

[21] Y. Katayama, H. Kobayashi, and S. Tanabe, Appl. Phys. Express. **8**, 012102 (2015).

[22] A. Bessière, S. Jacquart, K. Priolkar, A. Lecointre, B. Viana, and D. Gourier, Opt. Express. **19**, 10131 (2011).

[23] Y. Zhuang, J. Ueda, and S. Tanabe, Appl. Phys. Express. **6**, 052602 (2013).

[24] Y. Zhuang, J. Ueda, and S. Tanabe, J. Mater. Chem. C. **1**, 7849 (2013).

[25] Y. Zhuang, J. Ueda, S. Tanabe, and P. Dorenbos, J. Mater. Chem. C. **2**, 5502 (2014).

[26] N. Basavaraju, S. Sharma, A. Bessière, B. Viana, D. Gourier, and K. Priolkar, J. Phys. D: Appl. Phys. **46**, 375401 (2013).

[27] W. Zhang, Y. Wang, H. Li, X. Wang, and H. Zhao, Spectrosc. Spectr. Anal. **33**, 31 (2013).

[28] M. Yamaga, B. Henderson, and K. P. O. Donnell, J. Phys.: Condens. Matter. **1**, 9175 (1989).

[29] G. Boulon, Mater. Chem. Phys. **16**, 301 (1987).

[30] J. Ueda, K. Kuroishi, and S. Tanabe, Appl. Phys. Lett. **104**, 101904 (2014).

[31] G. Blasse, B. C. Grabmaier, and M. Ostertag, J. Alloys Compd. **200**, 17 (1993).

[32] L. Kostyk, A. Luchechko, Ya. Zakharko, O. Tsvetkova, and B. Kuklinski, J. Lumin. **129**, 312 (2009).

[33] P. R. Wamsley, and K. L. Bray, J. Lumin. **59**, 11 (1994).

[34] M. D. Seltzer, J. Chem. Educ. 72, 886 (1995).

[35] T. Kanai, M. Satoh, and I. Miura, J. Am. Ceram. Soc. **91**, 456 (2008).

[36] Y.-N. Xu and W. Y. Ching, Phys. Rev. B. **61**, 1817 (2000).

[37] M. Nikl, A. Vedda, M. Fasoli, I. Fontana, V. V. Laguta, E. Mihokova, J. Pejchal, J. Rosa, and K. Nejezchleb, Phys. Rev. B. **76**, 195121 (2007).

[38] M. Fasoli, A. Vedda, M. Nikl, C. Jiang, B. P. Uberuaga, D. A. Andersson, K. J. McClellan, and C. R. Stanek, Phys. Rev. B. **84**, 081102 (2011).

[39] K. Kamada, T. Endo, K. Tsutumi, T. Yanagida, Y. Fujimoto, A. Fukabori, A. Yoshikawa, J. Pejchal, and M. Nikl, Cryst. Growth. Des. **11**, 4484 (2011).

[40] C. R. Stanek, C. Jiang, S. K. Yadav, K. J. McClellan, B. P. Uberuaga, D. A. Andersson, and M. Nikl, Phys. Stat. Sol. (b). **250**, 244 (2013).

[41] C. R. Stanek, K. J. McClellan, M. R. Levy, and R. W. Grimes, Phys. Stat. Sol. RRL. **243**, 75 (2006).

[42] T. Matsuzawa, Y. Aoki, N. Takeuchi, and Y. Murayama, J. Electrochem. Soc. **143**, 2670 (1996).

[43] H. Takasaki, S. Tanabe, and T. Hanada, J. Ceram. Soc. Jpn. **104**, 322 (1996).

[44] A. Ikesue, K. Yoshida, and K. Kamata, J. Am. Ceram. Soc. **79**, 507 (1996).

[45] P. Dorenbos, J. Lumin. **134**, 310 (2013).

[46] K. Van Den Eeckhout, P. F. Smet and D. Poelman, Materials. **3**, 2536 (2010).

[47] A. Vedda, M. Nikl, M. Fasoli, E. Mihokova, J. Pejchal, M. Dusek, G. Ren, C. R. Stanek, K. J. McClellan, and D. D. Byler, Phys. Rev. B. **78**, 195123 (2008).

[48] K. Van Den Eeckhout, A. J. J. Bos, D. Poelman, and P. F. Smet, Phys. Rev. B. **87**, 045126 (2013).

Chapter 6

Design of deep-red persistent phosphors of $Gd_3Al_{5-x}Ga_xO_{12}$:Cr^{3+} transparent ceramics sensitized by Eu^{3+} as an electron trap using conduction band engineering

Abstract:

We developed bright deep-red persistent phosphors of Cr^{3+}-Eu^{3+} co-doped $Gd_3Al_{5-x}Ga_xO_{12}$ garnet (GAG*G*:Cr^{3+}-Eu^{3+}), in which only Cr^{3+} ion shows emission bands centered at 730 nm after ceasing UV illumination and Eu^{3+} ion acts as an excellent electron trap capturing one electron to be Eu^{2+} with tunable trap depth by varying conduction band with Ga^{3+} content, x. The persistent radiance of the GG*G*:Cr^{3+}-Eu^{3+} (x=5) sample at 1 h after ceasing UV light is approximately 25 times higher than that of the Cr^{3+} singly doped GG*G* sample, and is over 6 times higher than that of the widely used $ZnGa_2O_4$:Cr^{3+} red persistent phosphor.

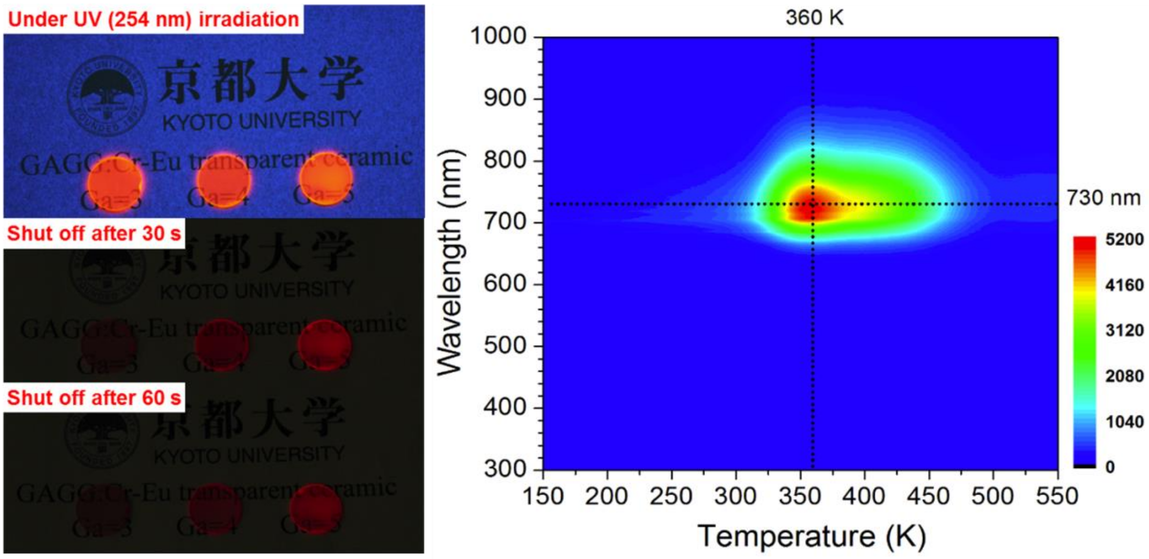

Eu^{3+} can act as efficient electron traps by tunning conduction band edge in the GAG*G* host

6.1. Introduction

Long persistent luminescence is a luminescent phenomenon that can last for minutes to hours, usually at room temperature (RT), after ceasing excitation sources. This process can be qualitatively explained by an electron transfer assumption[1,2]: when persistent phosphors are excited by ultraviolet (UV) light (visible light in some cases), electron-hole (*e*-*h*) pairs are generated and the excited electrons from the conduction band (CB) are captured by electron traps. This process is usually called trapping process. Then the stored electrons can be liberated by thermal stimulations to CB (detrapping process) being recaptured by a luminescent center, resulting in a kind of thermoluminescence (TL). Thus, the key point to design persistent phosphors with long duration is the possibility of tuning the "trap depth" between the bottom of CB and the electron trap to form a proper energy gap favorable for the detrapping process.[1-4] If the binding energy of an electron trap is predicted, this strategy to control the trap depth by changing the CB energy level is regarded as "CB engineering".

Recently, the CB engineering has been applied and proved to be a highly desirable strategy to develop new persistent phosphors in some aluminate/gallate based garnets (i.e. Ce^{3+}-doped YSG*G* (green),[5] YAG*G* (green)[6] and GAG*G* (yellow)[7] phosphors), in which the possibility of photoionization from the excited $5d_1$ energy level of Ce^{3+} to the bottom of CB with blue illumination can be increased by increasing Ga^{3+} substitution content, x for Al^{3+}.[8,9] We have also developed red persistent phosphor (~690 nm), Cr^{3+} doped YAG*G* with similar garnet matrix, where Cr^{3+} ions act both as emission centers and trap centers.[10] The persistent behavior of this material can systematically be tuned by changing Ga^{3+} content. The persistent radiance (in unit of $mW/Sr/m^2$) of the optimized composition was even higher than that of the $ZnGa_2O_4$:Cr^{3+} phosphor, which is used most widely for *in vivo* bio-imaging applications[11-14] since it was firstly reported by a French group.[15] Hence, the successes of CB engineering by Ga^{3+} substitution in garnets encourage us to design improved red persistent phosphors with brighter luminescence and longer afterglow.

The design concept in this paper is based on a theoretical assumption according to the Dorenbos theory[16,17] for garnet compounds.[18] This diagram proposed by Dorenbos provides strong predicting power since the characteristic variation in electron and hole trapping depths of lanthanide ions is given by the shape of the two zigzag curves representing the ground state (GS) of divalent and trivalent lanthanide ions, both of which show a minimum bottom at $4f^7$ configuration (Eu^{2+} and Gd^{3+}).[16] Because the zigzag shape of two curves remain nearly unchanged in different matrices, once the binding energy of the GS for one lanthanide ion relative to the host CB or valence band (VB) is determined, those of 4*f* (sometimes 5*d*) levels of all other 13 lanthanides can be estimated fairly well by the Dorenbos diagram. The suitability of Dy^{3+} and Nd^{3+} ions as excellent electron traps in Eu^{2+}-doped $SrAl_2O_4$ and $CaAl_2O_4$ persistent phosphors, respectively, was also explained well,[17] and the optimal trap depth for the longest persistent phosphors, $SrAl_2O_4:Eu^{2+}$-Dy^{3+} working at RT was proved to be ~0.65 eV.[19] Among all the trivalent lanthanide ions, Eu^{3+} ion would become the deepest electron trap to be Eu^{2+} ($4f^7$) and thus is considered to hardly act as a good sensitizer in most persistent phosphors working at RT. According to former results reported by Dorenbos's group, the energy level of Eu^{2+} GS is about 1.62 eV below CB in $Y_3Al_5O_{12}$ (YA*G*).[20] Since the band-gap energy of YA*G* is 7.67 eV and $Gd_3Al_{5-x}Ga_xO_{12}$ is 6.80 eV (x=3), 6.53 eV (x=4) and 6.48 eV (x=5), respectively,[18] considering the appropriate energy difference between YA*G* and $Gd_3Al_{5-x}Ga_xO_{12}$, we assume that the energy level of Eu^{2+} in GAG*G* and/or GG*G* may be suitable for persistent luminescence.

Based on these ideas, we choose Eu^{3+} as a potential sensitizer in the Cr^{3+}-doped $Gd_3Al_{5-x}Ga_xO_{12}$ (GAG*G*, x=3~5) composition[21] to design novel deep-red persistent phosphors with longer wavelength due to its weak crystal field. We found that the highest Ga^{3+} substitution (x=5) gave the best persistent luminescent properties among GAG*G*:Cr^{3+}-Eu^{3+} phosphors.

6.2. Experimental section

Transparent ceramics (TCs) of GAG*G*:Cr^{3+}-Eu^{3+} and GG*G*:Cr^{3+} with composition of $(Eu_{0.007}Gd_{0.993})_3Al_{5-x}Ga_xO_{12}$ (x=3, 4, 5) and $Gd_3Ga_5O_{12}$ doped with 0.05 mol% Cr^{3+} were fabricated by one step solid-state reaction method using vacuum sintering. The detailed information of preparation procedures is similar to our previous reports.[7,22]

The in-line optical transmittance of GAG*G*:Cr^{3+}-Eu^{3+} TCs was measured by UV-VIS-NIR spectrometer (Shimadzu, UV-3600). Microstructure observations including surface and fractured surface were examined by SEM (JEOL, JSM-890). Photoluminescence (PL) and persistent luminescence (PersL) spectra of the ceramic sample were measured by a CCD spectrometer (Ocean Optics, QE65-Pro) connected with an optical fiber. A combination of a 300 W Xe lamp (Asahi Spectra, MAX-302) with a UV mirror module (250-380 nm) was used as the excitation source for TL measurements. The ceramic sample was set in a cryostat (Advanced Research Systems, Helitran LT3) to control temperatures and firstly excited by UV light at 130 K for 10 min, then heated up to 600 K at a rate of 10 K/min after ceasing illumination for 10 min. The same CCD spectrometer was operated simultaneously with the TL measurement to always monitor TL spectra of the sample at different temperatures. Persistent luminescent decay curves were measured at 25 ℃ using the same photodiode as the TL measurement (Electro-Optical Systems, S-025-H). Then, the decay curves were calibrated to the absolute radiance (in unit of $mW/Sr/m^2$) using a radiance meter (B&W Tek Inc, Glacier X). Photographs of the TCs were taken by a digital camera (EOS kiss X5, Canon).

6.3. Results and discussion

Fig. 6.1(a) shows the PL spectrum of the GAG*G*:Cr^{3+}-Eu^{3+} (x=3) sample under UV (254 nm) excitation. The sample shows sharp luminescence bands owing to the 4f-4f transitions of Eu^{3+}: $^5D_0 \rightarrow {}^7F_J$ (J=0, 1, 2, 3, 4, 5, 6). The intense bands observed are due to $^5D_0 \rightarrow {}^7F_4$ at 708 nm and $^5D_0 \rightarrow {}^7F_1$ (magnetic dipole, MD) transition at 590 nm. Generally, the probability of $^5D_0 \rightarrow {}^7F_2$ electric dipole (ED) transition at 608~618 nm is very sensitive to the asymmetry of Eu^{3+} site,[23] while that of MD transition is independent of it. The ratio of the integrated intensity of the $^5D_0 \rightarrow {}^7F_2$ to $^5D_0 \rightarrow {}^7F_1$ transitions is much smaller compared with Y_2O_3 [24] and Y_2O_2S,[25] where Eu^{3+} ions take the Y-site with very low symmetry, resulting in strong luminescence at 610~620 nm with better color coordinates as a red phosphor. This small ratio indicates that Eu^{3+} ions substitute Gd^{3+} ions at dodecahedral sites in garnet, which is coordinated by eight O^{2-} ions in D_2 point symmetry.

After ceasing the UV excitation, the typical Eu^{3+} sharp emissions totally disappeared, instead, intra-3*d* transitions of Cr^{3+} composed of sharp *R*-line: $^2E \rightarrow {}^4A_2$ peaked at 695 nm and a broad emission band due to $^4T_2 \rightarrow {}^4A_2$ peaked at 713 nm become dominant as shown in Fig. 6.1(b). The complete difference between PL and PersL spectra of the GAG*G*:Cr^{3+}-Eu^{3+} phosphor shows that the emission centers change from Eu^{3+} to Cr^{3+} ions after stopping the UV illumination. Since the *10Dq* value of Cr^{3+} ion in GAG*G* with larger x (Ga content) is expected to be lower than that in YA*G* or GAG*G* with smaller x, the broad $^4T_2$ band at longer wavelength becomes more dominant than the *R*-line from ^2E level, which is dominant in a host with a large *10Dq* such as ruby.[26] This situation makes the mean wavelength of PersL in GAG*G* longer than those in Cr^{3+} singly-doped YAG*G* with the same or smaller x.[10]

Fig. 6.2(a) shows the photograph of the GAG*G*:Cr^{3+}-Eu^{3+} TCs (x=3, 4, 5, thickness of 1 mm), through which we can clearly recognize the words below by naked eye owing to their high optical transparency. Two broad absorption bands are observed centered at about 620 and 450 nm due to transitions of Cr^{3+}: $^4A_2(^4F) \rightarrow {}^4T_2(^4F)$ and $^4A_2(^4F) \rightarrow {}^4T_1(^4F)$, respectively. The weakness of the two bands is mainly due to the low doping concentration of Cr^{3+} (0.05 mol%). Besides, three sharp absorptions centered at 395, 312, 275 nm are ascribed to typical f-f transitions of Eu^{3+}: $^7F_0 \rightarrow {}^5L_6$, $^7F_0 \rightarrow {}^5H_3$, $^7F_0 \rightarrow {}^5F_2$, respectively and one intense absorption below 250 nm is attributed to the charge transfer band (CTB) of Eu^{3+}-O^{2-}. Fig. 6.2(b)-(c) give the SEM observations of the polished surface and fractured surface of the GAG*G*:Cr^{3+}-Eu^{3+} (x=3) ceramic sample. Almost no micro-pores or secondary phases are observed either on the surface, inside of grains or at grain boundaries leading to its high optical transparency.

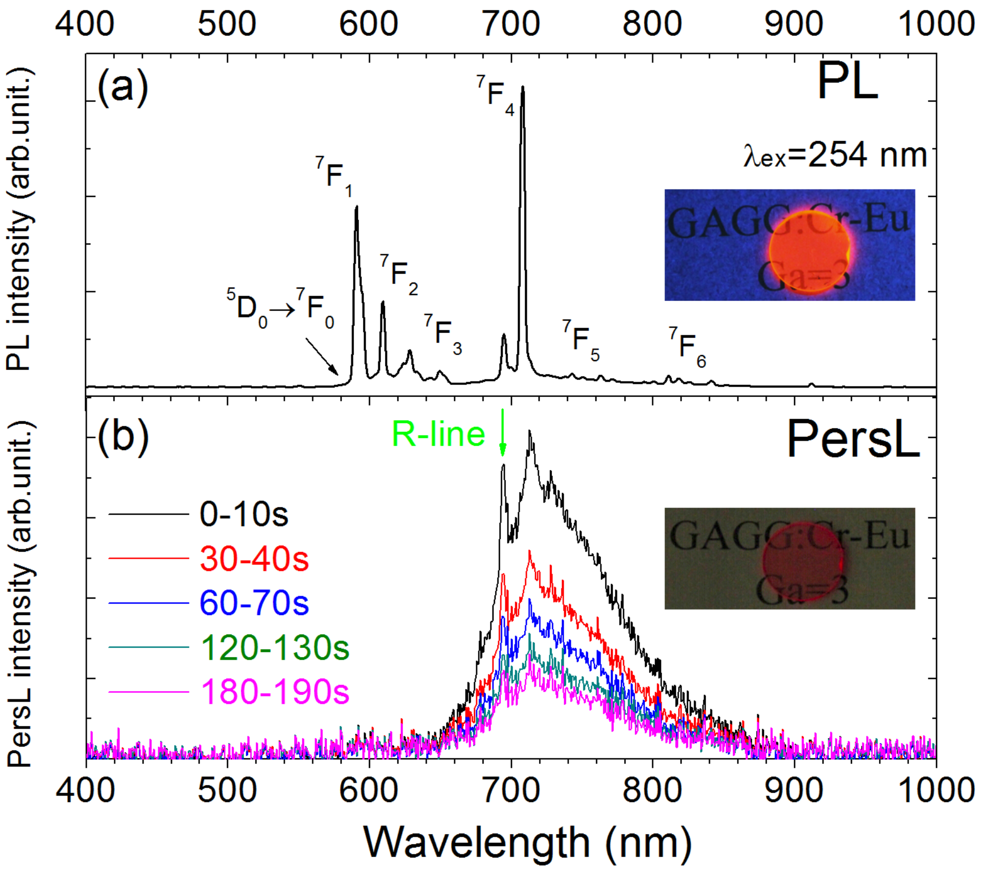

Figure 6.1. (a) PL and (b) PersL spectra of the GAGG:Cr^{3+}-Eu^{3} transparent ceramic (x=3).

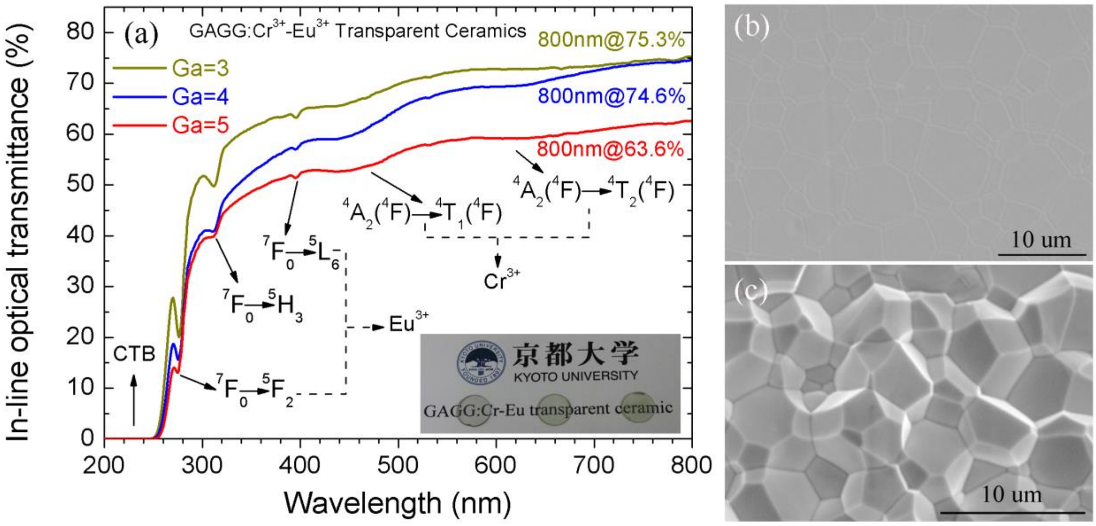

Figure 6.2. (a) In-line optical transmittance and photograph of GAGG:Cr^{3+}-Eu^{3+} transparent ceramics (thickness of 1 mm) with different Ga^{3+} contents as well as SEM observations of the (b) polished surface (c) fractured surface of the GAGG:Cr^{3+}-Eu^{3+} (x=3) transparent ceramic.

Fig. 6.3(a)-(c) show the photographs of the three bulk samples under and after UV (254 nm) illumination. Under UV excitation, all of the TCs look orange mainly due to the 590 nm PL band since the photopic sensitivity of human eyes becomes steeply higher in the wavelength region less than 620 nm,[4] while they look deep-red after ceasing the excitation. These color observations accord with the spectra shown in Fig. 6.1(a) and (b).

Persistent luminescent decay curves of the GAG*G*:Cr^{3+}-Eu^{3+} ceramic phosphors (x=3, 4, 5) after ceasing 5 min UV illumination are shown in Fig. 6.3(d). The persistent decay curves of the standard $ZnGa_2O_4$:Cr^{3+} ceramic phosphor under the same experimental condition previously reported by our group[27] and a Cr^{3+} singly doped GG*G* ceramic phosphor (x=5) are also plotted as references. The radiance values at 5 min, 30 min and 60 min after ceasing the excitation of the samples are summarized in Table. 6.1. The persistent radiance of GAG*G*:Cr^{3+}-Eu^{3+} phosphors increases monotonously with the increase of Ga^{3+} content, x. Furthermore, the persistent radiance at 1 h of the GG*G*:Cr^{3+}-Eu^{3+} (x=5) sample (0.97×10^{-1} mW/Sr/m^2) is approximately 25 times higher than that of the Cr^{3+} singly doped GG*G* sample (0.04×10^{-1} mW/Sr/m^2), and is over 6 times higher than that of the widely used $ZnGa_2O_4$:Cr^{3+} red persistent phosphor (0.15×10^{-1} mW/Sr/m^2).[27]

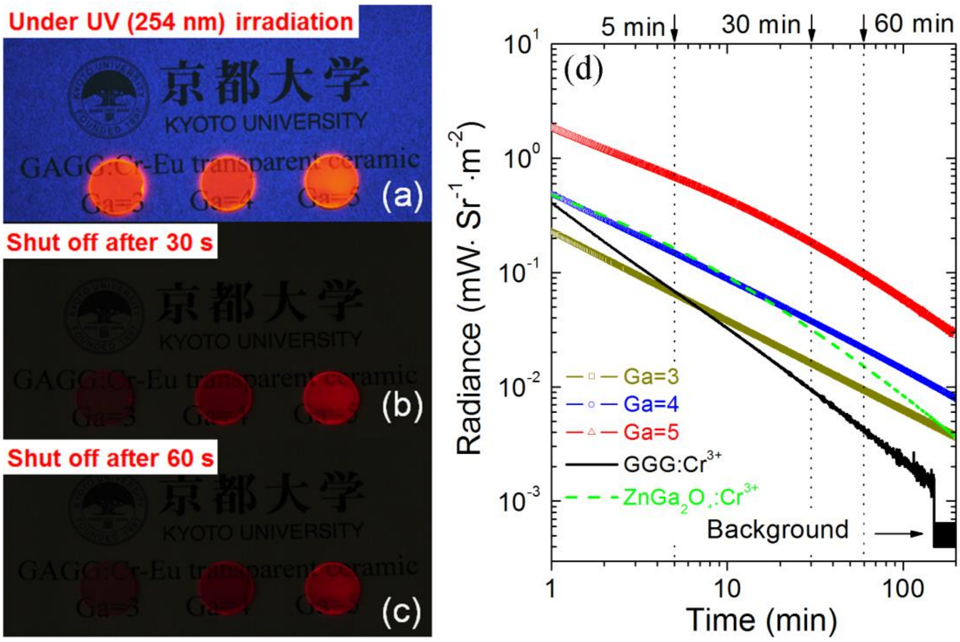

Figure 6.3. Photographs of the GAG*G*:Cr^{3+}-Eu^{3+} transparent ceramics (thickness of 1 mm) with

different Ga^{3+} contents (x=3, 4, 5) (a) under UV (254 nm) lamp (exposure of camera: 0.05 s) and (b) 30 s (c) 60 s after ceasing UV illumination (exposure of camera: 10 s), respectively. (d) persistent decay curves of the GAG*G*:Cr^{3+}-Eu^{3+} transparent ceramic phosphors with different Ga^{3+} contents

Table. 6.1. Radiance of GAG*G*:Cr^{3+}-Eu^{3+} transparent ceramic phosphors with different Ga^{3+} contents compared with GG*G*:Cr^{3+} and $ZnGa_2O_4$:Cr^{3+} ceramic phosphors[27].

	5 min (mW/Sr/m^2)	30 min (mW/Sr/m^2)	60 min (mW/Sr/m^2)
GAG*G*:Cr^{3+}-Eu^{3+} (x=3)	**0.65×10^{-1}**	**0.16×10^{-1}**	**0.09×10^{-1}**
GAG*G*:Cr^{3+}-Eu^{3+} (x=4)	**1.48×10^{-1}**	**0.38×10^{-1}**	**0.22×10^{-1}**
GAG*G*:Cr^{3+}-Eu^{3+} (x=5)	**6.84×10^{-1}**	**1.83×10^{-1}**	**0.97×10^{-1}**
GG*G*:Cr^{3+}	**0.69×10^{-1}**	**0.09×10^{-1}**	**0.04×10^{-1}**
$ZnGa_2O_4$:Cr^{3+}[27]	**1.63×10^{-1}**	**0.32×10^{-1}**	**0.15×10^{-1}**

TL glow curves of the GAG*G*:Cr^{3+}-Eu^{3+} samples (x=3~5) are shown in Fig. 6.4(a). The TL glow peak shifts monotonously from higher to lower temperature with increasing Ga^{3+} content (498 K, 408 K and 355 K for x=3, x=4, x=5, respectively). Since the TL peak temperature is correlated to the trap depth,[1] the downshift of the glow peak indicates that the trap depth becomes shallower. In Fig. 6.4(b), two-dimensional (2D) mapping of TL intensity was plotted in order to clarify what kind of emission contributes to the TL glow peak at different temperatures in the GG*G*:Cr^{3+}-Eu^{3+} phosphor (x=5, showing highest persistent brightness). From the contour mapping, it can be seen that at increased temperatures, the TL glow peak is simply composed of broad emission bands due to Cr^{3+} centered at about 730 nm. No sharp *f-f* transitions of Eu^{3+} are observed at any temperatures. Therefore, we conclude that the Eu^{3+} acts as an electron trapping center and changes into Eu^{2+} (Eu^{3+}-e^-) being located below CB. A schematic model is described by the inserted schematic illustration in Fig. 6.4(a). The detrapping rate, which is dominated by the trap depth (as well as temperature and frequency factor),[1] becomes faster with increasing Ga^{3+} content due to the downshift of CB level. Generally, not only in conventional phosphors for illumination applications, europium is also widely used as emission centers in persistent phosphors like well-known $SrAl_2O_4$:Eu^{2+}-Dy^{3+} (green),[19] $CaAl_2O_4$:Eu^{2+}-Nd^{3+} (blue)[28] and Y_2O_2S:Eu^{3+}-Ti^{4+}-Mg^{2+} (red)[29] phosphors. In this study, we lowered the CB level to decrease the trap depth from Eu^{2+} GS as possible as we can by full Ga^{3+} substitution for Al^{3+} in GAG*G* to finally be GG*G*, and have successfully developed a novel bright deep-red Cr^{3+} doped persistent phosphor in which Eu^{3+} ions act as an electron trap. A phosphor with such an unusual combination of emission and trap centers has never been reported before and we thus state as a new discovery.

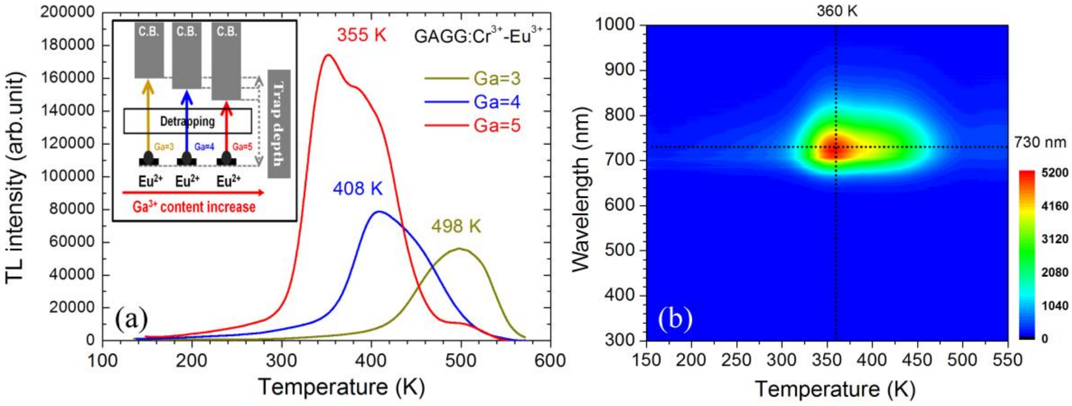

Figure 6.4. (a) Thermoluminescence (TL) glow curves of the GAG*G*:Cr^{3+}-Eu^{3+} transparent ceramic phosphors with different Ga^{3+} contents, schematic illustration inserted (b) wavelength-temperature (λ-T) contour plot of the GG*G*:Cr^{3+}-Eu^{3+} (x=5) transparent ceramic.

6.4. Conclusion

In summary, we successfully developed a series of transparent ceramic phosphors: GAG*G*:Cr^{3+}-Eu^{3+} with deep-red persistent luminescence and long duration time, in which Eu^{3+} ions act as an electron trap. The persistent radiance of the GG*G*:Cr^{3+}-Eu^{3+} (x=5) sample is over 6 times higher than that of the widely used $ZnGa_2O_4$:Cr^{3+} red persistent phosphor and its broad band persistent emission centered at 730 nm possesses deeper penetration capability through biological tissues. Practical applications in the *in vivo* bio-imaging field can be expected in the near future by using GG*G*:Cr^{3+}-Eu^{3+} nano-particles as optical probes.

Acknowledgement

I would like to acknowledge Prof. Bruno Viana from Chimie Paris-tech and Dr. Yixi Zhuang from Xiamen University for fruitful discussions on persistent phosphors. This work was supported by JSPS KAKENHI Grant Number 25620184.

References

[1] K. Van den Eeckhout, P. F. Smet, and D. Poelman, “Persistent luminescence in Eu^{2+}-doped compounds: a review,” Materials. **3**(4), 2536–2566 (2010).

[2] K. Van Den Eeckhout, D. Poelman, and P. F. Smet, “Persistent luminescence in non-Eu^{2+}-doped compounds: a review,” Materials. **6**(7), 2789–2818 (2013).

[3] S. K. Singh, “Red and near infrared persistent luminescence nano-probes for bioimaging and targeting applications,” RSC Adv. **4**(102), 58674–58698 (2014).

[4] Y. Zhuang, Y. Katayama, J. Ueda, and S. Tanabe, “A brief review on red to near-infrared persistent luminescence in transition-metal-activated phosphors,” Opt. Mater. **36**(11), 1907– 1912 (2014).

[5] J. Ueda, K. Aishima, S. Nishiura, and S. Tanabe, “Afterglow luminescence in Ce^{3+}-doped $Y_3Sc_2Ga_3O_{12}$ ceramics,” Appl. Phys. Express. **4**(4), 042602–042604 (2011).

[6] J. Ueda, K. Kuroishi, and S. Tanabe, “Bright persistent ceramic phosphors of Ce^{3+}-Cr^{3+}-codoped garnet able to store by blue light,” Appl. Phys. Lett. **104**(10), 101904–101907 (2014).

[7] J. Ueda, K. Kuroishi, and S. Tanabe, “Yellow persistent luminescence in Ce^{3+}-Cr^{3+}-codoped gadolinium aluminum gallium garnet transparent ceramics after blue-light excitation,” Appl. Phys. Express. **7**(6), 062201–062203 (2014).

[8] J. Ueda, S. Tanabe, and T. Nakanishi, “Analysis of Ce^{3+} luminescence quenching in solid solutions between $Y_3Ga_5O_{12}$ and $Y_3Al_5O_{12}$ by temperature dependence of photoconductivity measurement,” J. Appl. Phys. **110**(5)**,** 053102–053107 (2011).

[9] J. Ueda, K. Aishima, and S. Tanabe, “Temperature and compositional dependence of optical and optoelectronic properties in Ce^{3+}-doped $Y_3Sc_2Al_{3-x}Ga_xO_{12}$ (x = 0, 1, 2, 3),” Opt. Mater. **35**(11), 1952–1957 (2013).

[10] J. Xu, J. Ueda, Y. Zhuang, B. Viana, and S. Tanabe, “$Y_3Al_{5-x}Ga_xO_{12}$:Cr^{3+}: a novel red persistent phosphor with high brightness,” Appl. Phys. Express. **8**(4), 042602–042605 (2015).

[11] Y. Zhuang, J. Ueda, and S. Tanabe, “Tunable trap depth in $Zn(Ga_{1-x}Al_x)_2O_4$:Cr,Bi red persistent phosphors: considerations of high-temperature persistent luminescence and photostimulated persistent luminescence,” J. Mater. Chem. C. **1**(47), 7849–7855 (2013).

[12] Y. Zhuang, J. Ueda, S. Tanabe, and P. Dorenbos, “Band-gap variation and a self-redox effect

induced by compositional deviation in $Zn_xGa_2O_{3+x}$:Cr^{3+} persistent phosphors," J. Mater. Chem.C. **2**(28), 5502–5509 (2014).

[13] T. Maldiney, A. Bessière, J. Seguin, E. Teston, S. K. Sharma, B. Viana, A. J. J. Bos, P. Dorenbos, M. Bessodes, D. Gourier, D. Scherman, and C. Richard, "The in vivo activation of persistent nanophosphors for optical imaging of vascularization, tumours and grafted cells," Nat. Mater. **13**(4), 418–426 (2014).

[14] Z. Pan, Y.-Y. Lu, and F. Liu, "Sunlight-activated long-persistent luminescence in the near-infrared from Cr^{3+}-doped zinc gallogermanates," Nat. Mater. **11**(1), 58–63 (2011).

[15] A. Bessière, S. Jacquart, K. Priolkar, A. Lecointre, B. Viana, and D. Gourier, "$ZnGa_2O_4$:Cr^{3+}: a new red longlasting phosphor with high brightness," Opt. Express. **19**(11), 10131–10137 (2011).

[16] P. Dorenbos, "Systematic behaviour in trivalent lanthanide charge transfer energies," J. Phys.: Condens. Matter. **15**(49), 8417–8434 (2003).

[17] P. Dorenbos, "Mechanism of persistent luminescence in Eu^{2+} and Dy^{3+} codoped aluminate and silicate compounds," J. Electrochem. Soc. **152**(7), H107–H110 (2005).

[18] P. Dorenbos, "Electronic structure and optical properties of the lanthanide activated $RE_3(Al_{1-x}Ga_x)_5O_{12}$ (RE=Gd, Y, Lu) garnet compounds," J. Lumin. **134**, 310–318 (2013).

[19] T. Matsuzawa, Y. Aoki, N. Takeuchi, and Y. Murayama, "A new long phosphorescent phosphor with high brightness, $SrAl_2O_4$:Eu^{2+}, Dy^{3+}," J. Electrochem. Soc. **143**(8), 2670–2673 (1996).

[20] F. T. You, A. J. J. Bos, Q. F. Shi, S. H. Huang, and P. Dorenbos, "Thermoluminescence investigation of donor (Ce^{3+}, Pr^{3+}, Tb^{3+}) acceptor (Eu^{3+}, Yb^{3+}) pairs in $Y_3Al_5O_{12}$," Phys. Rev. B. **85**(11), 115101–115107 (2012).

[21] G. Blasse, B. C. Grabmaier, and M. Ostertag, "The afterglow mechanism of chromium-doped gadolinium gallium garnet," J. Alloy. Compd. **200**(1-2), 17–18 (1993).

[22] J. Xu, J. Ueda, K. Kuroishi, and S. Tanabe, "Fabrication of Ce^{3+}-Cr^{3+} co-doped yttrium aluminium gallium garnet transparent ceramic phosphors with super long persistent luminescence," Scr. Mater. (to be published).

[23] G. Blasse and A. Bril, "Structure and Eu^{3+}-fluorescence of lithium and sodium lanthanide silicates and germinates," J. Inorg. Nucl. Chem. **29**(9), 2231–2241 (1967).

[24] H. Forest and G. Ban, "Evidence for 2 symmetry sites in Y_2O_3-Eu^{+3}," J. Electrochem. Soc. **115**(3), C64 (1968).

[25] W. H. Fonger and C. W. Struck, “Eu^{+3} 5D resonance quenching to charge-transfer states in Y_2O_2S, La_2O_2S and LaOCl,” J. Chem. Phys. **52**(12), 6364 (1970).

[26] J. Ueda and S. Tanabe, “Preparation and optical property of glass ceramics containing ruby crystals,” J. Am. Ceram. Soc. **93**(10), 3084–3087 (2010).

[27] Y. Zhuang, J. Ueda, and S. Tanabe, “Enhancement of red persistent luminescence in Cr^{3+}-doped $ZnGa_2O_4$ phosphors by Bi_2O_3 codoping,” Appl. Phys. Express. **6**(5), 052602–052606 (2013).

[28] H. Yamamoto and T. Matsuzawa, “Mechanism of long phosphorescence of $SrAl_2O_4$:Eu^{2+}, Dy^{3+} and $CaAl_2O_4$:Eu^{2+}, Nd^{3+},” J. Lumin. **72-74**, 287–289 (1997).

[29] X. Wang, Z. Zhang, Z. Tang and Y. Lin, “Characterization and properties of a red and orange Y_2O_2S-based long afterglow phosphor,” Mater. Chem. Phys. **80**(1), 1–5 (2003).

Chapter 7

Near-infrared multi-wavelengths long persistent luminescence of Nd^{3+} ion through persistent energy transfer in Ce^{3+}, Cr^{3+} co-doped $Y_3Al_2Ga_3O_{12}$ for the first and second bio-imaging windows

Abstract:

We developed a persistent phosphor of $Y_3Al_2Ga_3O_{12}$ doped with Nd^{3+}, Ce^{3+}, Cr^{3+} ions (YAG*G*:Nd-Ce-Cr) exhibiting long (>10 h) persistent luminescence at multi-wavelengths of around 880, 1064, and 1335 nm due to *f-f* transitions of Nd^{3+} and at 505 nm due to Ce^{3+}:$5d_1 \rightarrow 4f$ transition. The intense near-infrared (NIR) persistent luminescence bands from Nd^{3+} match well with the first (650~950 nm) and second (1000~1400 nm) bio-imaging windows. The NIR persistent radiance of the YAG*G*:Nd-Ce-Cr phosphor (0.33×10^{-1} mW/Sr/m^2) at 60 min after ceasing blue light illumination was over 2 times higher than that of the widely used $ZnGa_2O_4$:Cr^{3+} red persistent phosphor (0.15×10^{-1} mW/Sr/m^2).

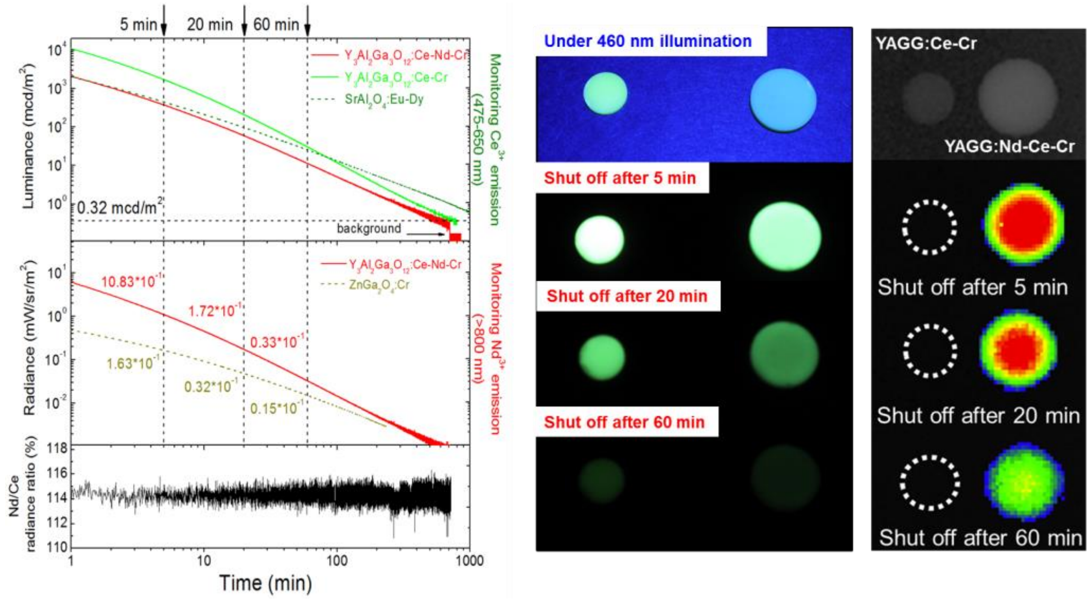

Realization of "bright" Nd^{3+} persistent luminescence by efficient energy transfer from Ce^{3+} to Nd^{3+}

7.1. Introduction

Recently, persistent phosphors (sometimes named as long-lasting phosphors) have attracted much attention for *in vivo* bio-imaging applications since these nano-particle phosphors charged by ultraviolet (UV) light (visible light in rare cases) before injection into biological tissues can emit red and/or near-infrared (NIR) persistent luminescence lasting for minutes to even several hours without further real-time illumination.[1-4] The exclusion of external illumination removes the possibility of autofluorescence as background noise and thus improves the signal-to-noise ratio remarkably. This application motivates the considerable development of red/NIR persistent phosphors with bright radiance and long afterglow.[5-8] However, only a few red/NIR long persistent phosphors have been reported so far, most of which are Cr^{3+} doped gallate- or aluminate-based materials,[9-14] and their emission regions are mostly located in the first bio-imaging window (NIR-I window, 650~950 nm).

Combined with fast development and availability of InGaAs detectors, the second bio-imaging window (NIR-II window, 1000~1400 nm) has promising advantages owing to its lower autofluorescence, deeper tissue penetration, and thus potentially higher spatial and temporal resolution than the NIR-I window.[15] Till now, although several types of optical probes for NIR-II window have been developed such as single-walled carbon nanotubes (SWNTs)[16] and semiconductor quantum dots (QDs) composed of highly toxic heavy metals,[17] the development of nontoxic and biocompatible luminescent materials emitting in the NIR region, especially in the NIR-II window, still remains a challenge. Although persistent phosphors can be promising candidates for bio-imaging, only few of them are suitable for the NIR-II window and their persistent durations are quite short (only up to few minutes),[18-20] which limits their practical applications.

Recently, a garnet persistent phosphor of Ce^{3+}, Cr^{3+} co-doped $Y_3Al_{5-x}Ga_xO_{12}$ (YAG*G*:Ce-Cr) has been developed by our group.[21-24] In this material, Cr^{3+} acts as an electron trap with ideal trap depth at x=3 for persistent luminescence of Ce^{3+} working at room temperature (RT). Based on our previous work, we developed a persistent phosphor of $Y_3Al_2Ga_3O_{12}$:Nd^{3+}, Ce^{3+}, Cr^{3+} (YAG*G*:Nd-Ce-Cr). This material can be excited by blue light (460 nm) and emit green persistent luminescence due to Ce^{3+}: $5d_1 \rightarrow 4f$ for over 10 h. Furthermore, thanks to the highly efficient energy transfer (ET) from Ce^{3+} to Nd^{3+} in garnet hosts,[25-27] it can also show NIR persistent luminescence for almost the same duration due to Nd^{3+}: $^4F_{3/2} \rightarrow {}^4I_{9/2}$, $^4I_{11/2}$, $^4I_{13/2}$ transitions, matching well with the NIR-I and NIR-II windows. A persistent phosphor with such a wide emission range (green to NIR) and long (>10 h) persistent duration has never been reported before and we thus state as a discovery.

7.2. Experimental section

YAG*G*:Nd-Ce-Cr and YAG*G*:Nd ceramic phosphors with the composition of $Y_{2.955}Ce_{0.015}Nd_{0.03}Al_{1.999}Cr_{0.001}Ga_3O_{12}$ and $Y_{2.97}Nd_{0.03}Al_2Ga_3O_{12}$, respectively were fabricated by a solid-state reaction method. Y_2O_3 (99.99%), Al_2O_3 (99.99%), Ga_2O_3 (99.99%), CeO_2 (99.99%), Nd_2O_3 (99.99%) and Cr_2O_3 (99.9%) were used as raw materials. The starting powder was mixed by ball milling method with anhydrous alcohol for several hours. The mixed powder was dried at 80 ℃ for 36 h, compacted to form a ceramic green body (ϕ20 mm, 2 mm thickness) under uniaxial pressing of 50 MPa, and finally sintered at 1600 ℃ for 24 h in air. The YAG*G*:Ce-Cr ($Y_{2.985}Ce_{0.015}Al_{1.999}Cr_{0.001}Ga_3O_{12}$) ceramic phosphor prepared by the same experimental procedure was used as a reference sample.[22]

The diffuse reflectance spectra of the ceramic samples were measured by a spectrophotometer (UV3600, Shimadzu) equipped with an integrating sphere. Photoluminescence (PL) spectra of the YAG*G*:Ce-Cr and YAG*G*:Nd-Ce-Cr samples were recorded in the range of 400-1600 nm by pumping with a 442 nm laser diode (LD) (NDHB510APA-E, Nichia Co. Ltd.,) excitation. The PL spectra were measured by a monochromator (G250, Nikon), a Si photodiode (PD) detector (S-025-H, Electro-Optical System Inc.,) from 400 to 800 nm and an InGaAs PD detector (IGA-030-H, Electro-Optical System Inc.,) from 800 to 1600 nm. All the PL spectra were calibrated by using a standard halogen lamp (SCL-600, Labsphere). Persistent luminescence (PersL) spectra of the two samples were measured by a Si CCD spectrometer (QE65-Pro, Ocean Optics) from 400 to 1000 nm and an InGaAs CCD spectrometer (NIR 512, Ocean Optics) from 1000 to 1600 nm connected with an optical fiber. All the PersL spectra were calibrated using the same halogen lamp. A 300 W Xe lamp (MAX-302, Asahi Spectra) with UV mirror module (250-400 nm) was used as the excitation source for thermoluminescence (TL) measurements. The ceramic sample was set in a cryostat (Helitran LT3, Advanced Research Systems) to control temperatures and firstly illuminated by UV light at 150 K for 10 min, then heated up to 550 K at a rate of 10 K/min at 10 min after ceasing the illumination, and the TL signals were recorded by the Si PD (spectral sensitivity covers from 300 to 1200 nm). The Si CCD spectrometer was operated simultaneously with the TL measurement to always monitor the TL spectra at different temperatures. All persistent luminescent decay curves of the samples after being excited for 5 min by the Xe lamp with a 460 nm band-pass filter were measured at 25 ℃ using the Si PD. In order to monitor the Ce^{3+} emission, the Si PD was covered with a short-cut filter (<475 nm) and a long-cut filter (>650 nm) to filter out all but the Ce^{3+} luminescence. Then the decay curves were calibrated to the absolute luminance (in unit of mcd/m^2) using a radiance meter (Glacier X, B&W Tek Inc). In order to monitor the Nd^{3+} luminescence, the Si PD was covered with an 800 nm short-cut filter to filter out all but the Nd^{3+} luminescence. Then the decay curves were calibrated to the absolute radiance (in unit of $mW/Sr/m^2$) using the same radiance meter. Photographs of the samples were taken by a digital camera (EOS kiss X5, Canon), and the settings remained constant: exposure time - 5 s, ISO value - 1600, aperture value (F value) - 5.0.

7.3. Results and discussion

Fig. 7.1(a) shows the PL spectra of the YAG*G*:Ce-Cr and YAG*G*:Nd-Ce-Cr samples under blue laser (442 nm) excitation. The YAG*G*:Ce-Cr sample exhibits an intense emission band centered at 505 nm, corresponding to the *f*-*d* transition from the lowest 5*d* energy level ($5d_1$) to the 4f ground state of Ce^{3+}. Besides, a weak emission band at around 690 nm is ascribed to the $^2E \rightarrow {}^4A_2$ transition (*R*-line) of Cr^{3+}. Comparing the PL spectrum of the YAG*G*:Ce-Cr sample with the diffuse reflectance of the Nd^{3+} singly doped YAG*G* sample (YAG*G*:Nd), the absorption bands ($^4I_{9/2} \rightarrow {}^2G_{3/2}$, $^4G_{7/2}$, $^2G_{7/2}$, $^4G_{5/2}$) of Nd^{3+} are overlapped with the emission range of Ce^{3+} indicating that the ET process from Ce^{3+} to Nd^{3+} can efficiently occur. This is confirmed by the decrease of Ce^{3+} emission intensity in the visible range and the presence of several sharp emission bands at around 880 nm, 1064 nm and 1335 nm owing to the *f*-*f* transitions of Nd^{3+}: $^4F_{3/2} \rightarrow {}^4I_{9/2}$, $^4I_{11/2}$, and $^4I_{13/2}$, respectively in the YAG*G*:Nd-Ce-Cr sample.

The PersL spectra of the YAG*G*:Nd-Ce-Cr sample recorded at different times after ceasing blue illumination are shown in Fig. 7.1(b). The persistent emission bands not only exhibit a broad band located at around 500 nm due to Ce^{3+}: $5d_1 \rightarrow 4f$ transition but also intense sharp bands located at NIR region (around 880 nm, 1064 nm and 1335 nm) due to *f*-*f* transitions of Nd^{3+}, which match well with the NIR-I and NIR-II windows. The identical shape of its PL and PersL spectra suggests that the emission centers are the same under and after excitation. Since the ET process from Ce^{3+} to Nd^{3+} occurs in PL, we assume that the similar energy transfer process called persistent energy transfer (persistent ET) also occurs in the YAG*G*:Nd-Ce-Cr phosphor after ceasing the excitation source. The phenomenon of the persistent ET has been confirmed previously in $CaAl_2O_4$:Tb^{3+}, Ce^{3+} [28,29] and $Sr_4Al_{14}O_{25}$:Cr^{3+}, Eu^{2+}, Dy^{3+} [30] persistent phosphors.

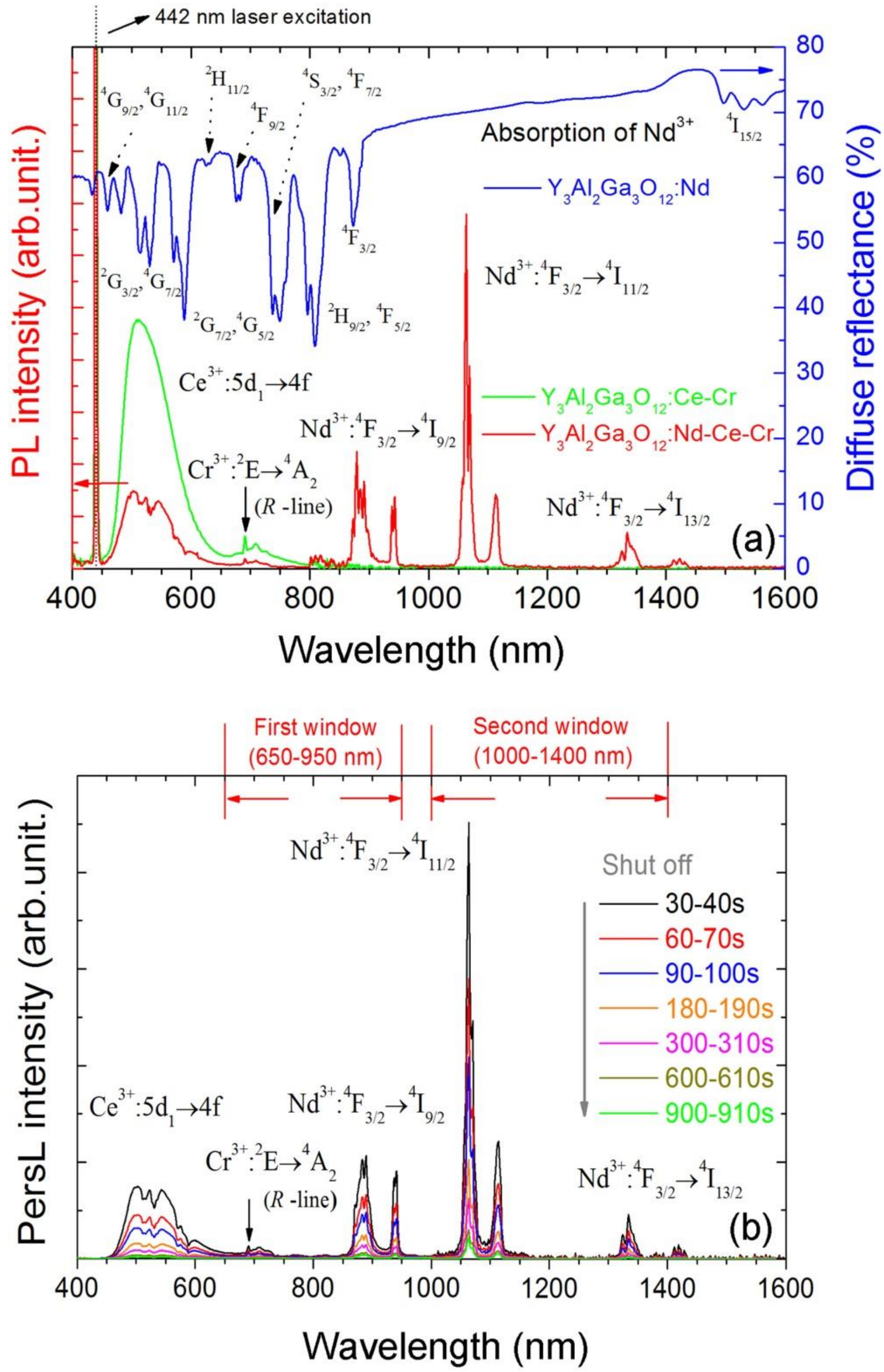

Figure 7.1. (a) PL spectra of the YAG*G*:Ce-Cr and YAG*G*:Nd-Ce-Cr ceramics as well as the diffuse reflectance of the YAG*G*:Nd ceramic (b) PersL spectra of the YAG*G*:Nd-Ce-Cr ceramic (integrating time: 10 s)

The persistent luminescent decay curve monitoring Ce^{3+} emission (475-650 nm) of the YAG*G*:Nd-Ce-Cr sample after ceasing blue light illumination is shown in Fig. 7.2(a), in which the decay curves of the standard YAG*G*:Ce-Cr ceramic phosphor and a compacted ceramic pellet made of the well-known $SrAl_2O_4$:Eu^{2+}-Dy^{3+} (SAO:Eu-Dy) commercial phosphor (LumiNova- GLL300FFS, Nemoto & Co. Ltd.,) under the same experimental condition are also plotted as references.[22] The luminance values at 60 min after ceasing the excitation are 11 mcd/m^2 for YAG*G*:Nd-Ce-Cr, 30 mcd/m^2 for YAG*G*:Ce-Cr, and 25 mcd/m^2 for SAO:Eu-Dy, respectively (see the photographs of the two ceramics under and after blue LED illumination in Fig. 7.2(d)). Persistent luminescence durations to reach a luminance of 0.32 mcd/m^2 in the YAG*G*:Nd-Ce-Cr ceramic is around 688 min, which is comparable with but slightly shorter than that of the YAG*G*:Ce-Cr (about 808 min) ceramic, due to quenching of visible Ce^{3+} emission by the ET to Nd^{3+}.[25] Note that the luminance value 0.32 mcd/m^2 is the minimum value commonly used by the safety signage industry (about 100 times the sensitivity of the dark-adapted eye).[2] Because of this long green persistent luminescence at wavelengths very sensitive to the human's photopic vision, the YAG*G*:Nd-Ce-Cr nano-sized phosphor synthesized by nano-technical methods can act as a fluorescence marker convenient for surgeons to roughly confirm or even trace the marked tissues directly by human eyes without any electronic detectors in the difficult conditions typical of surgery dissection.

The persistent luminescent decay curve monitoring Nd^{3+} emission (>800 nm) of the YAG*G*:Nd-Ce-Cr sample after ceasing the same illumination is shown in Fig. 7.2(b), in which the decay curve of the standard $ZnGa_2O_4$:Cr^{3+} (ZGO:Cr) ceramic under the same experimental condition is also plotted as a reference.[10] The NIR radiance value of the tri-doped sample at 60 min after ceasing the blue excitation (0.33×10^{-1} mW/Sr/m^2) is over 2 times higher than that of the widely used red persistent phosphor, ZGO:Cr (0.15×10^{-1} mW/Sr/m^2), indicating that this phosphor exhibits superior persistent luminescence both in the visible (Ce^{3+} emission) and NIR (Nd^{3+} emission) ranges.

The decay profiles of the Ce^{3+} and Nd^{3+} are quite similar in Fig. 7.2(a) and (b). The persistent radiance ratio (Nd^{3+}/Ce^{3+}) is plotted against the monitoring time of the whole decay curve as shown in Fig. 7.2(c). The result clearly suggests that the ratio remains almost constant (around 112-114%) with time, which supports that the persistent luminescence from both ions originates from common electron trapping and de-trapping processes, where the NIR persistent luminescence of Nd^{3+} is due to the persistent ET process from Ce^{3+} to Nd^{3+} in the garnet host.[25]

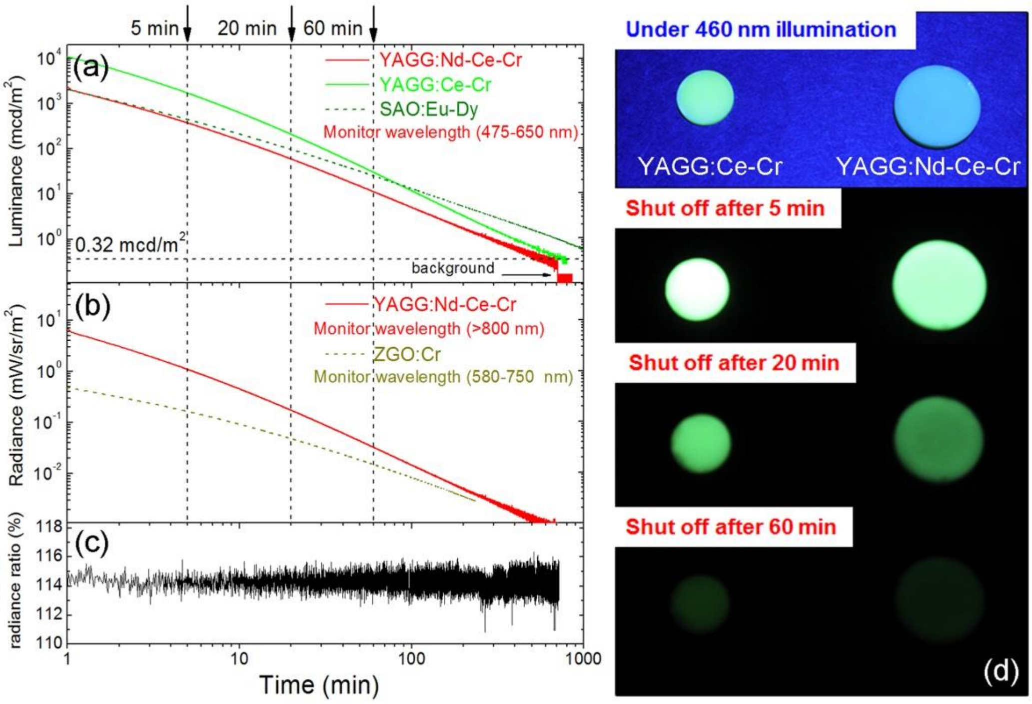

Figure 7.2. Persistent decay curves of the YAG*G*:Nd-Ce-Cr ceramic (a) luminance monitoring Ce^{3+} (YAG*G*:Ce-Cr and $SrAl_2O_4$:Eu^{2+}-Dy^{3+} ceramics as references) (b) radiance monitoring Nd^{3+} ($ZnGa_2O_4$:Cr^{3+} ceramic as a reference) (c) Nd^{3+}/Ce^{3+} radiance ratio (%) against the monitoring time of the decay curve (d) photographs of the YAG*G*:Ce-Cr and YAG*G*:Nd-Ce-Cr ceramics under and after blue LED lamp (460 nm, 3 W output) illumination

Fig. 7.3 shows the two-dimensional (2D) mappings of TL glow curves of the YAG*G*:Ce-Cr and YAG*G*:Nd-Ce-Cr samples in order to see what kind of emission contributes to the TL glow peak at different temperatures. From the contour plot of the YAG*G*:Ce-Cr sample in Fig. 7.3(a), it can be seen that at increased temperatures, the TL spectrum is simply composed of two emission bands from Ce^{3+} and Cr^{3+}. While in the YAG*G*:Nd-Ce-Cr sample (see Fig. 7.3(b)), the NIR emission of Nd^{3+} appears at the same time due to the persistent ET process, which agrees well with its PersL spectrum in Fig. 7.1(b). The intense TL glow peaks of both YAG*G*:Ce-Cr and YAG*G*:Nd-Ce-Cr samples lie in almost the same temperature range (around 295 K), close to RT and body temperature of Mammalia (around 36 ℃). Since the TL peak temperature is correlated to the energy gap between the bottom of conduction band (CB) and the electron trap,[31] the identical glow temperature of the two samples indicates the same trapping and de-trapping processes in both,[22] where Cr^{3+} works as an efficient electron trap with ideal trap depth for long persistent luminescence in the host composition of $Y_3Al_2Ga_3O_{12}$.

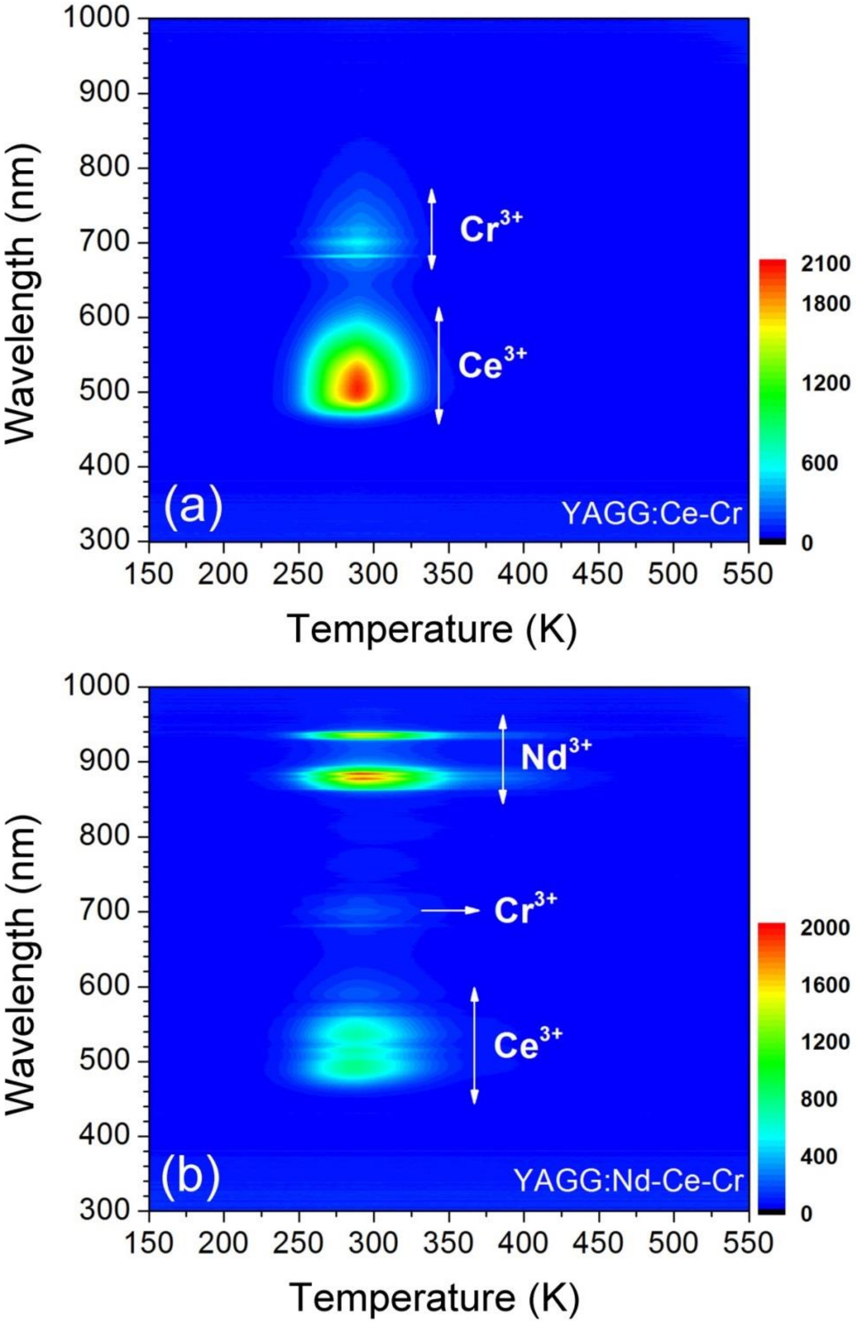

Figure 7.3. Wavelength-temperature (λ-T) contour plots of the (a) YAG*G*:Ce-Cr and (b) YAG*G*:Nd-Ce-Cr ceramics

The persistent luminescence mechanism of the YAG*G*:Nd-Ce-Cr phosphor is briefly explained by constructing the vacuum referred binding energy (VRBE) diagram[23, 32, 33] composed of Ce^{3+}, Nd^{3+}, Cr^{2+}, CB, and valence band (VB) energy levels in the $Y_3Al_2Ga_3O_{12}$ host (see Fig. 7.4). When the YAG*G*:Nd-Ce-Cr sample is charged by blue light, Ce^{3+} is promoted from the ground state ($^2F_{5/2}$) to the excited state of the lowest 5*d* energy level (5d_1), and the excited electron can "jump" into CB with thermal activation and then be trapped by the electron trapping center (Cr^{3+}).[22, 23] At that time, Ce^{3+} is photo-oxidized into Ce^{4+} or (Ce^{3+} + h^+) and Cr^{3+} is formed to be Cr^{2+} or (Cr^{3+} + e^-) after capturing an electron (process ①).

Then the de-trapping process takes place with thermal release of the captured electron from the Cr^{2+} (Cr^{3+} + e^-) trap, and finally the excited state of the Ce ion, $(Ce^{3+})^*$ appears after capturing the released electron in the recombination process (process ②). The radiative relaxation gives a broad band emission of Ce^{3+}: $5d_1 \rightarrow {}^2F_{5/2}$, $^2F_{7/2}$, and the resonant ET occurs at the same time to Nd^{3+} ion (process ③), which is followed by rapid multi-phonon relaxation down to the $^4F_{3/2}$ excited level, and then finally induces the sharp luminescence bands of Nd^{3+}: $^4F_{3/2} \rightarrow {}^4I_{9/2}$, $^4I_{11/2}$, and $^4I_{13/2}$.

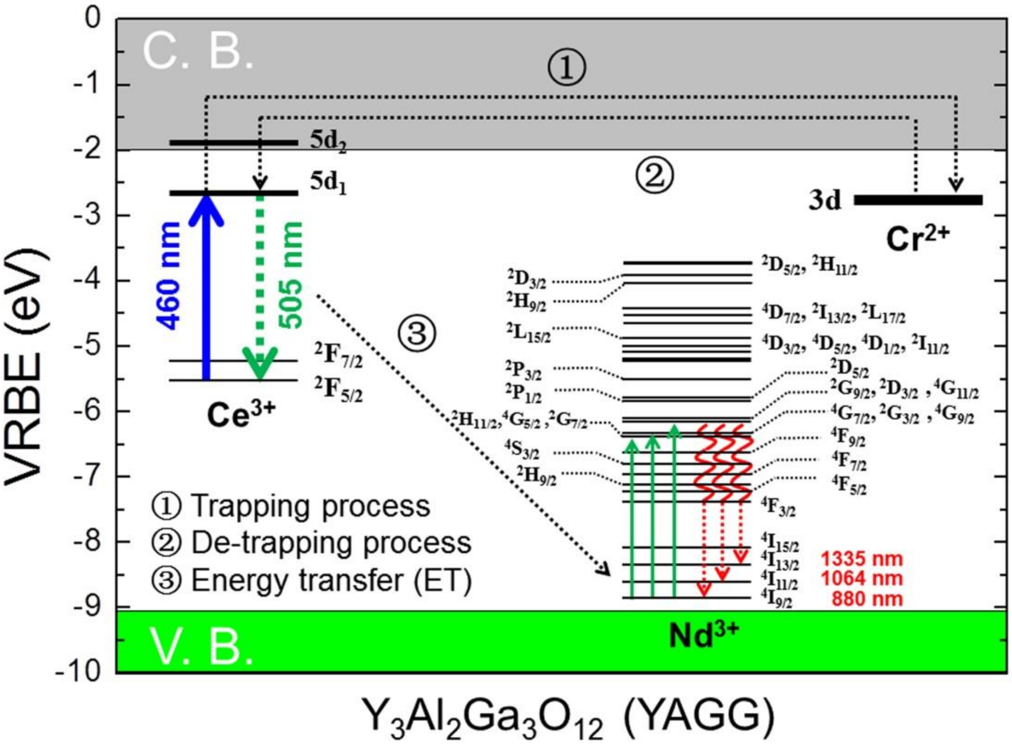

Figure 7.4. The VRBE diagram for Ce^{3+}, Nd^{3+} and Cr^{2+} energy levels in $Y_3Al_2Ga_3O_{12}$ (YAG*G*) host

7.4. Conclusion

In summary, we developed a persistent phosphor ($Y_3Al_2Ga_3O_{12}$:Nd^{3+}, Ce^{3+}, Cr^{3+}) with multi-wavelengths (green light to NIR) and long (>10 h) persistent luminescence, which can be effectively excited by blue light illumination. The persistent radiance of the YAG*G*:Nd-Ce-Cr phosphor is over 2 times higher in the NIR region than that of the widely used $ZnGa_2O_4$:Cr^{3+} red persistent phosphor at 60 min after ceasing the excitation due to an efficient persistent energy transfer from Ce^{3+} to Nd^{3+}. Since its NIR persistent luminescence bands match well with the NIR-I and NIR-II bio-imaging windows, multi-functional applications not only in the *in vivo* bio-imaging but also in the drug delivery and cancerous chemotherapy can be expected in the near future by using this material as a nano-sized bio-probe with surface modification connected with functional organic radical groups.

Acknowledgement

I would like to acknowledge Prof. Bruno. Viana who stayed at Kyoto University as a visiting professor for fruitful discussion on persistent phosphors and bio-imaging.

References

[1] S. K. Singh, RSC Adv. **4**, 58674 (2014).

[2] K. Van Den Eeckhout, D. Poelman, and P. F. Smet, Materials. **6**, 2789 (2013).

[3] Q. le Masne de Chermont, C. Chanéac, J. Seguin, F. Pellé, S. Maîrejean, J.-P. Jolivet, D. Gourier, M. Bessodes, and D. Scherman, Proc. Natl. Acad. Sci. U.S.A. **104**, 9266 (2007).

[4] T. Maldiney, A. Bessière, J. Seguin, E. Teston, S. K. Sharma, B. Viana, A. J. J. Bos, P. Dorenbos, M. Bessodes, D. Gourier, D. Scherman, and C. Richard, Nat. Mater. **13**, 418 (2014).

[5] Z. Pan, Y.-Y. Lu, and F. Liu, Nat. Mater. **11**, 58 (2012).

[6] T. Maldiney, C. Richard, J. Seguin, N. Wattier, M. Bessodes, and D. Scherman, ACS Nano. **5**, 854 (2011).

[7] T. Maldiney, A. Lecointre, B. Viana, A. Bessière, M. Bessodes, D. Gourier, C. Richard, and D. Scherman, J. Am. Chem. Soc. **133**, 11810 (2011).

[8] F. Liu, W. Yan, Y.-J. Chuang, Z. Zhen, J. Xie, and Z. Pan, Sci. Rep. **3**, 1554 (2013).

[9] A. Bessière, S. Jacquart, K. Priolkar, A. Lecointre, B. Viana, and D. Gourier, Opt. Express. **19**, 10131 (2011).

[10] Y. Zhuang, J. Ueda, and S. Tanabe, Appl. Phys. Express. **6**, 052602 (2013).

[11] Y. Zhuang, J. Ueda, and S. Tanabe, J. Mater. Chem. C. **1**, 7849 (2013).

[12] Y. Zhuang, J. Ueda, S. Tanabe, and P. Dorenbos, J. Mater. Chem. C. **2**, 5502 (2014).

[13] J. Xu, J. Ueda, and S. Tanabe, Opt. Mater. Express. **5**, 963 (2015).

[14] J. Xu, J. Ueda, Y. Zhuang, B. Viana, and S. Tanabe, Appl. Phys. Express. **8**, 042602 (2015).

[15] A. M. Smith, M. Mancini, and S. Nie, Nature. Nanotech. **4**, 710 (2009).

[16] X. Peng, N. Komatsu, S. Bhattacharya, T. Shimawaki, S. Aonuma, T. Kimura, and A. Osuka, Nature. Nanotech. **2**, 361 (2007).

[17] M. Bruchez, M. Moronne, P. Gin, S. Weiss, and A. P. Alivisatos, Science. **281**, 2013 (1998).

[18] J. Ueda, T. Shinoda, and S. Tanabe, Opt. Mater. Express. **3**, 787 (2013).

[19] N. Yu, F. Liu, X. Li, and Z. Pan, Appl. Phys. Lett. **95**, 231110 (2009).

[20] Y. Teng, J. Zhou, Z. Ma, M. M. Smedskjaer, and J. Qiu, J. Electrochem. Soc. **158**, K17 (2011).

[21] J. Ueda, S. Tanabe, and T. Nakanishi, J. Appl. Phys. **110,** 053102 (2011).

[22] J. Ueda, K. Kuroishi, and S. Tanabe, Appl. Phys. Lett. **104**, 101904 (2014).

[23] J. Ueda, P. Dorenbos, A. J. J. Bos, K. Kuroishi, and S. Tanabe, J. Mater. Chem. C. **3**, 5642 (2015).

[24] J. Xu, J. Ueda, K. Kuroishi, and S. Tanabe, Scripta. Mater. **102**, 47 (2015).

[25] S. Möller, A. Hoffmann, D. Knaut, J. Flottmann, and T. Jüstel, J. Lumin. **158**, 365 (2015).

[26] M. Yamaga, Y. Oda, H. Uno, K. Hasegawa, H. Ito, and S. Mizuno, J. Appl. Phys. **112**, 063508 (2012).

[27] J. X. Meng, J. Q. Li, Z. P. Shi, and K. W. Cheah, Appl. Phys. Lett. **93**, 221908 (2008).

[28] D. Jia, R. S. Meltzer, W. M. Yen, W. Jia, and X. J. Wang, Appl. Phys. Lett. **80**, 1535 (2002).

[29] D. Jia, X. J. Wang, W. Jia, and W. M. Yen, J. Appl. Phys. **93**, 148 (2003).

[30] R. Zhong, J. Zhang, X. Zhang, S. Lu, and X. J. Wang, Appl. Phys. Lett. **88**, 201916 (2006).

[31] K. Van den Eeckhout, P. F. Smet, and D. Poelman, Materials. **3**, 2536 (2010).

[32] P. Dorenbos, J. Electrochem. Soc. **152,** 107 (2005).

[33] P. Dorenbos, J. Lumin. **134**, 310 (2013).

Chapter 8

Near-infrared long persistent luminescence of Er^{3+} in garnet for the third bio-imaging window

Abstract:

By utilizing efficient persistent energy transfer from Ce^{3+} to Er^{3+}, we have successfully developed a novel garnet persistent phosphor of $Y_3Al_2Ga_3O_{12}$ doped with Er^{3+}, Ce^{3+}, Cr^{3+} ions (YAG*G*:Er-Ce-Cr) exhibiting long (>10 h) near-infrared (NIR) persistent luminescence (PersL) in the broad range from 1450 nm to 1670 nm due to the typical Er^{3+}:$^4I_{13/2}\rightarrow{}^4I_{15/2}$ transition in garnet. The NIR PersL bands of Er^{3+} match well with the third bio-imaging window (NIR-III, approximately from 1500 nm to 1800 nm) and the response curve of InGaAs detectors. The photon emission rate (8.33×10^{17} cps/Sr/m^2) of the YAG*G*:Er-Ce-Cr persistent phosphor at 10 min after ceasing blue light illumination was over two times higher than that of the widely used $ZnGa_2O_4$:Cr^{3+} deep-red persistent phosphor (3.30×10^{17} cps/Sr/m^2). We also show the first PersL imaging by a commercial InGaAs camera monitoring Er^{3+} emission indicating that this material can be a promising candidate for *in-vivo* bio-imaging in the NIR-III window.

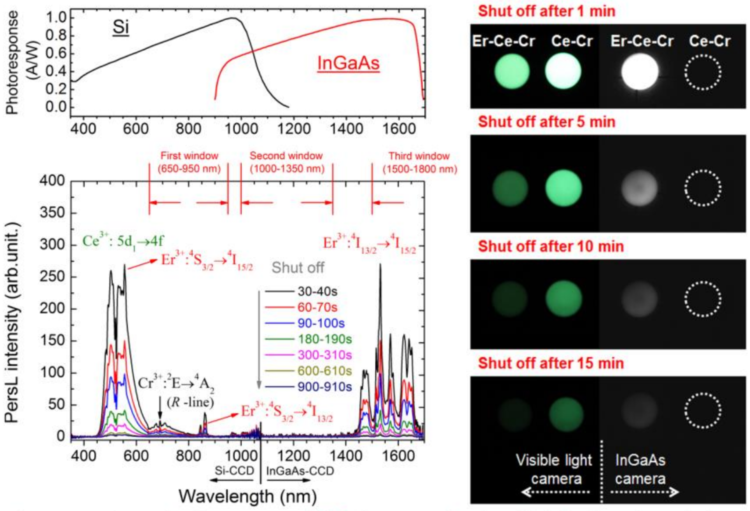

Long persistent luminescence of Er^{3+} in garnet for the third bio-imaging window

8.1. Introduction

Over 20 years has passed, since the new generation green persistent phosphor, $SrAl_2O_4$:Eu^{2+}-Dy^{3+} (SAO:Eu-Dy) was developed and successfully commercialized for watch dials, luminous paints, and safety guidance signs, *etc*.[1] Recently, the luminescent wavelength of persistent phosphors has extended from visible light to near-infrared (NIR),[2-6] which is suitable for *in vivo* bio-imaging due to the reduced scattering and minimal absorption coefficient when compared with visible light, allowing imaging of deep tissues. Furthermore, persistent phosphors in the form of nano-particles charged by ultraviolet (UV) light (visible light in rare cases) before injecting into small animals can emit NIR persistent luminescence (PersL) for minutes to even hours without further *in-situ* excitation. The exclusion of external illumination totally removes the autofluorescence as background noise, avoids the complicated background subtraction procedures and thus improves the signal-to-noise ratio (SNR) remarkably.[7-9] This new bio-imaging technology has soon become quite attractive while the most reported emission region of NIR persistent phosphors are located in the first biological window (NIR-I, 650-950 nm),[4-13] partially due to the easy availability of Si-detectors that work well in this region.

Since the Rayleigh scattering (varies as λ^{-4}, here λ is the wavelength) decrease with increasing wavelength, two more biological windows called the second (NIR-II, 1000-1350 nm)[14] and the third (NIR-III, approximately from 1500 nm to 1800 nm)[15-17] ones are defined, which fall on either side of a strong water absorption band centered around 1450 nm. Compared with the NIR-I window, these two windows, especially the NIR-III window gives much lower scattering coefficient leading potentially to an improved resolution quality and deeper penetration depth.[18-20] Moreover, thanks to the recent development of affordable InGaAs detectors that possess adequate sensitivity and high quantum efficiency in the wavelength region above 1000 nm and up to 1650 nm, the shift of the luminescent wavelength of the bio-imaging probe from the NIR-I to the NIR-III window is definitely demanded. However, even for NIR-to-NIR fluorescence bio-probes using real-time excited photoluminescence (PL) for *in vivo* imaging, only a few candidates are available for the NIR-III window including the single-walled carbon nanotubes (SWNTs)[16,21] and heavy metal based semiconductor quantum dots (QDs),[16,22] both of which suffer from their potential cytotoxicity for living bodies.[15-17] Therefore, the development of nontoxic and biocompatible luminescent materials emitting in the NIR-III window, still remains a big challenge.

Due to the typical $^4I_{13/2}\rightarrow^4I_{15/2}$ transition at around 1.55 μm and several important transitions such as the $^4S_{3/2}\rightarrow^4I_{15/2}$ one in green,[23] Er^{3+} ion has already played a key role in applications of eye-safe laser,[24] optical amplifiers in fiber telecommunication[25,26] and upconversion fluorescence[27,28] for long years. On the other hand, Er^{3+} is also considered as the most promising lanthanide ion whose emitting wavelength matches well with both the NIR-III window and the response curve of InGaAs detectors.[15-17] Pan *et al*[29] firstly observed the PersL from Er^{3+} through the so-called persistent energy transfer (ET) from Eu^{2+} in the well-known SAO:Eu-Dy persistent phosphor. However, compared with super long PersL (>10 h) from Eu^{2+} in green region, the PersL intensity and duration of Er^{3+} emission peaked at 1530 nm was much weaker and shorter (less than 10 min) after ceasing UV excitation. On the other hand, based on our previous work, in which a novel garnet persistent phosphor of Ce^{3+}, Cr^{3+} co-doped $Y_3Al_{5-x}Ga_xO_{12}$ (YAG*G*:Ce-Cr) was developed and Cr^{3+} acts as an efficient electron trap with ideal trap depth at x=3 for PersL of Ce^{3+} working at room temperature (*RT*),[30-33] we successfully developed a persistent phosphor of $Y_3Al_2Ga_3O_{12}$:Nd^{3+}, Ce^{3+}, Cr^{3+} (YAG*G*:Nd-Ce-Cr) emitting long PersL (>10 h) at 880 nm, 1064 nm, and 1335 nm due to *f-f* transitions of Nd^{3+} through efficient persistent ET from Ce^{3+}.[34] It is also worth noting that, as well as the Er^{3+} emission mainly composed of the C-band (1530-1565 nm) and the L-band (1565-1625 nm) usually observed in many hosts,[35-40] it exhibits an extended U-band (1625-1675 nm) in garnet hosts owing to the large Stark splitting of the terminal $^4I_{15/2}$ level.[41,42] In this paper, we give an example that how to realize Er^{3+} long PersL through efficient persistent ET process from Ce^{3+} in a garnet host and show the first PersL imaging for the NIR-III window by an InGaAs camera.

8.2. Experimental section

YAG*G*:Er-Ce-Cr, YAG*G*:Ce-Er and YAG*G*:Er ceramic phosphors with the compositions of $Y_{2.925}Ce_{0.015}Er_{0.06}Al_{1.999}Cr_{0.001}Ga_3O_{12}$, $Y_{2.925}Ce_{0.015}Er_{0.06}Al_2Ga_3O_{12}$ and $Y_{2.94}Er_{0.06}Al_2Ga_3O_{12}$, respectively were fabricated by a conventional solid-state reaction method. Y_2O_3 (99.99%), Al_2O_3 (99.99%), Ga_2O_3 (99.99%), CeO_2 (99.99%), Er_2O_3 (99.99%) and Cr_2O_3 (99.9%) were used as raw materials. The starting powder was mixed by a ball milling method (Premium Line P-7, Fritsch Co. Ltd.,) with anhydrous alcohol for several hours. The mixed powder was dried at 80 ℃ for 36 h, compacted to form a ceramic green body (ϕ20 mm, 2 mm thickness) under uniaxial pressing of 50 MPa, and finally sintered at 1600 ℃ for 10 h in air. The YAG*G*:Ce-Cr ($Y_{2.985}Ce_{0.015}Al_{1.999}Cr_{0.001}Ga_3O_{12}$) and YAG*G*:Ce ($Y_{2.985}Ce_{0.015}Al_2Ga_3O_{12}$) ceramic phosphors prepared by the same experimental procedure were used as reference samples. All the as-prepared samples were confirmed to be single phase (ICPDS: No. 089-6660) by XRD measurement (see Fig. 8.1).

The diffuse reflectance spectrum of the YAG*G*:Er ceramic sample was measured by a spectrophotometer (UV3600, Shimadzu) equipped with an integrating sphere. The lifetime measurement of the YAG*G*:Ce and YAG*G*:Ce-Er samples were recorded with a compact fluorescence lifetime spectrometer (Quantaurus-Tau-C11367, Hamamatsu Photonics & Co. Ltd.,) using a 405 nm picosecond pulsed LED as an excitation source. Photoluminescence (PL) spectra of the YAG*G*:Ce, YAG*G*:Er and YAG*G*:Ce-Er ceramic samples by pumping with a 405 nm laser diode (LD) (SDL-405-LM-100T, Shanghai Dream Lasers Technology Co. Ltd.,) and the YAG*G*:Ce-Cr and YAG*G*:Er-Ce-Cr samples by pumping with a 442 nm LD (NDHB510APA-E, Nichia Co. Ltd.,) were recorded in the range of 350-1670 nm. The PL spectra were measured by a monochromator (G250, Nikon) equipped with a Si photodiode (PD) detector (S-025-H, Electro-Optical System Inc.,) from 350 to 1100 nm and an InGaAs PD detector (IGA-030-H, Electro-Optical System Inc.,) from 1100 to 1670 nm (see the schematic illustration of measurement setup in Fig. 8.2). All the PL spectra were calibrated by using a standard halogen lamp (SCL-600, Labsphere).

Persistent luminescence (PersL) spectrum of the YAG*G*:Er-Ce-Cr sample was measured by a Si CCD spectrometer (QE65-Pro, Ocean Optics) from 350 to 1075 nm and an InGaAs CCD spectrometer (NIR-Quest512, Ocean Optics) from 1075 to 1700 nm connected with an optical fiber. All the PersL spectra were calibrated using the same halogen lamp. A 300 W Xe lamp (MAX-302, Asahi Spectra) with an UV mirror module (250-400 nm) was used as the excitation source for thermoluminescence (TL) two-dimensional (2D) plot measurements. The ceramic sample was set in a cryostat (Helitran LT3, Advanced Research Systems) to control temperatures and firstly illuminated by UV light at 100 K for 10 min, then heated up to 600 K at a rate of 10 K/min at 10 min after ceasing the illumination, and the TL signals were recorded by a PMT detector (R11041, Hamamatsu Photonics & Co. Ltd.,) covered with 475nm short-cut and 650 nm long-cut filters to monitor Ce^{3+} emission and the same InGaAs PD detector covered with a 1000 nm short-cut filter to monitor NIR emission of Er^{3+}. The same Si CCD and InGaAs CCD spectrometers were operated simultaneously with the TL measurement to monitor the emission spectra at different temperatures. All persistent luminescent decay curves of the YAG*G*:Er-Ce-Cr sample after being excited for 5 min by the Xe lamp with a 460 nm band-pass filter were measured at 25 ℃ using the same PMT or InGaAs PD detectors (see the schematic illustration of measurement setup in Fig. 8.3). In order to monitor the Ce^{3+} emission, the PMT detector was covered with 475 nm short-cut and 650 nm long-cut filters to filter out all but the Ce^{3+} luminescence. Then the decay curves were calibrated to the absolute luminance (in unit of mcd/m^2) using a radiance meter (Glacier X, B&W Tek Inc). In order to monitor the Er^{3+} luminescence, the InGaAs PD was covered with a 1000 nm short-cut filter to filter out all but the Er^{3+} luminescence. Then the decay curves were calibrated to the photon emission rate (in unit of cps/Sr/m^2) using the same radiance meter calculated by the absolute radiance (in unit of mW/Sr/m^2) divided by photon energy (photon energy: $E=hc/\lambda$, where h is the Planck constant, c is the speed of light in vacuum and λ is the wavelength). The Photographs of the YAG*G*:Ce-Cr and YAG*G*:Er-Ce-Cr samples after charging by a 455 nm LED lamp (M445L3, THORLABS, Inc.,) for 5 min were taken by a digital camera (EOS kiss X5, Canon) for the visible light region, and the settings remained constant: exposure time - 1 s, ISO value - 1600, aperture value (*F* value) - 5.0. The photographs for the short-wave infrared (SWIR) region (~900-1700 nm) were taken by a bio-imaging machine (NIS-OPT, Shimadzu) equipped with an InGaAs camera (Xeva-1.7-320, TE3 cooling system down to 223 K) after charging by the same 455 nm LED for 5 min, and the integrating time was set to be 0.04 s.

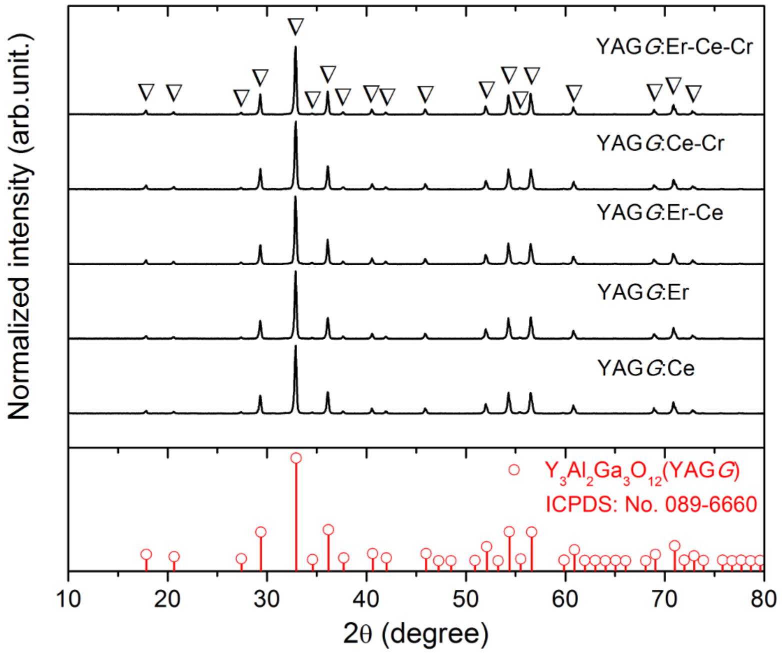

Figure 8.1. X-ray diffraction (XRD) patterns of the YAG*G*:Ce, YAG*G*:Er, YAG*G*:Er-Ce, YAG*G*:Ce-Cr and YAG*G*:Er-Ce-Cr ceramic samples

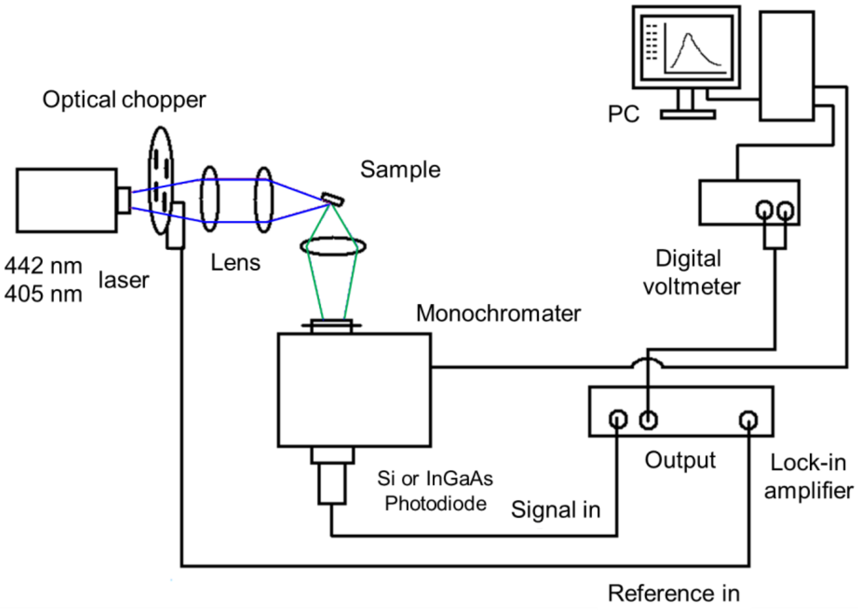

Figure 8.2. The measurement setup of photoluminescence (PL)

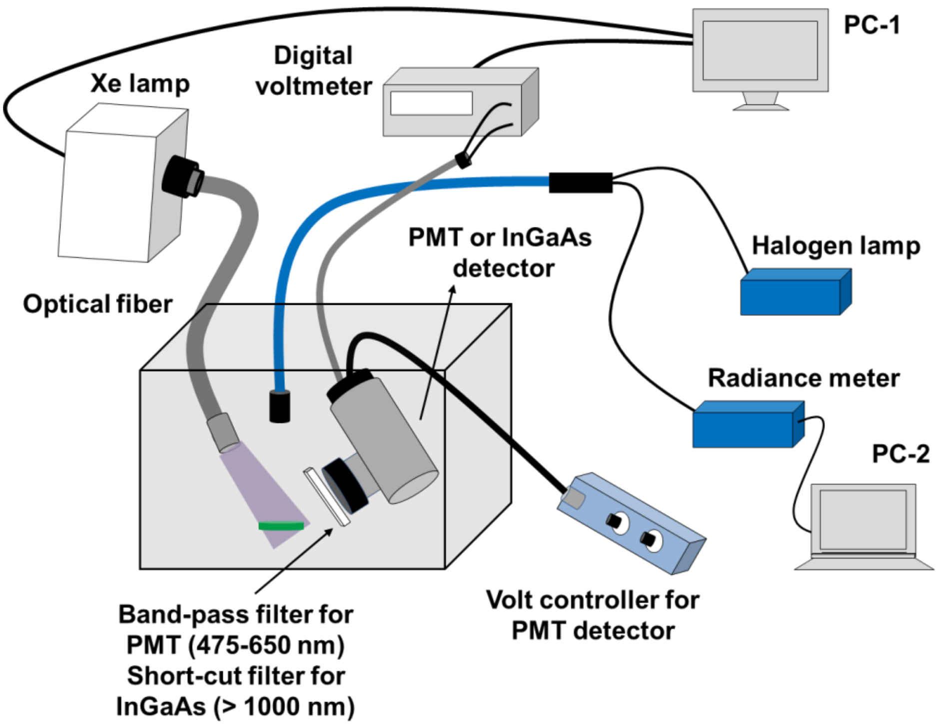

Figure 8.3. The measurement setup of persistent luminescent decay curves

8.3. Results and discussion

8.3.1. Efficient energy transfer from Ce^{3+} to Er^{3+} in YAG*G* host

Fig. 8.4(a)-(c) show the PL spectra of the YAG*G*:Ce, YAG*G*:Er and YAG*G*:Ce-Er samples under 405 nm laser excitation. Both the broad band emission from Ce^{3+}:$5d_1 \rightarrow 4f$ peaked at 500 nm and sharp-line emission bands from Er^{3+}:${}^4S_{3/2} \rightarrow {}^4I_{15/2}$ peaked at 555 nm, the ${}^4S_{3/2} \rightarrow {}^4I_{13/2}$ band peaked at 862 nm, and the ${}^4I_{13/2} \rightarrow {}^4I_{15/2}$ band peaked at 1532 nm in the YAG*G*:Ce-Er sample are clearly observed. Especially for the ${}^4I_{13/2} \rightarrow {}^4I_{15/2}$ transition, similar to that in the $Y_3Al_5O_{12}$ (YA*G*) host[40-44], broadly splitted bands ranging from 1450 to 1670 nm in the YAG*G* host are also observed. On the other hand, the emission bands due to the Er^{3+}:${}^4I_{11/2} \rightarrow {}^4I_{15/2}$ transition peaked at 966 nm and 1013 nm are almost quenched in the YAG*G*:Ce-Er sample compared with that in the YAG*G*:Er sample, which can be attributed to the ET from Er^{3+}:${}^4I_{11/2} \rightarrow {}^4I_{13/2}$ to Ce^{3+}:${}^2F_{7/2} \leftarrow {}^2F_{5/2}$, the famous "cross-relaxation process" in the Ce^{3+}-Er^{3+} pair[45] as shown in Fig. 8.4(d). This process can efficiently facilitate the population of the $^4I_{13/2}$ level and simultaneously improves the emission intensity of the Er^{3+}:$^4I_{13/2}\rightarrow{}^4I_{15/2}$ transition dramatically.[45]

Fig. 8.4(e) shows that the lifetime of the Ce^{3+}:5d_1 level declines from 34.1 ns to 12.2 ns after Er^{3+} co-doping, indicating extra decay pathways due to the non-radiative ET from Ce^{3+} to Er^{3+} in the YAG*G*:Ce-Er sample. The total decay rate (W_{tot}) of the 5d_1 level in the YAG*G*:Ce sample is given by

$$W_{\mathrm{tot}} = A + W_{\mathrm{MP}} = \tau_{Ce}^{-1} \tag{1}$$

where A is the radiative rate, W_{MP} is the multi-phonon relaxation rate, and τ_{Ce} is the lifetime of the 5d_1 level in the YAG*G*:Ce sample. In the YAG*G*:Ce-Er sample, the extra decay pathways mainly from the 5d_1 level of Ce^{3+} to the $^4F_{7/2}$ and $^2H_{11/2}$ levels of Er^{3+} are generated as shown in Fig. 8.4(d). The total decay rate in the co-doped sample is given by

$$W_{\mathrm{tot}} = A + W_{\mathrm{MP}} + W_{\mathrm{ET}} = \tau_{Ce,Er}^{-1} \tag{2}$$

where W_{ET} is the ET rate and $\tau_{\mathrm{Ce,Er}}$ is the lifetime of the 5d_1 level of Ce^{3+} in the YAG*G*:Ce-Er sample. So the ET efficiency (η_{ET}) is given by

$$\eta_{\mathrm{ET}} = \frac{W_{\mathrm{ET}}}{A+W_{\mathrm{MP}}+W_{\mathrm{ET}}} = 1 - \frac{\tau_{Ce,Er}}{\tau_{Ce}} \tag{3}$$

Thus, the efficiency can be estimated to be ~64% indicating that not only in YA*G*,[43,44] but also in YAG*G* host, efficient ET can occur from Ce^{3+} to Er^{3+} (although energy transfer between Cr^{3+} and Er^{3+} also occurs, to simplify the mechanism in this paper, Cr^{3+} is assumed to act only as an electron trap due to its very low doping concentration).

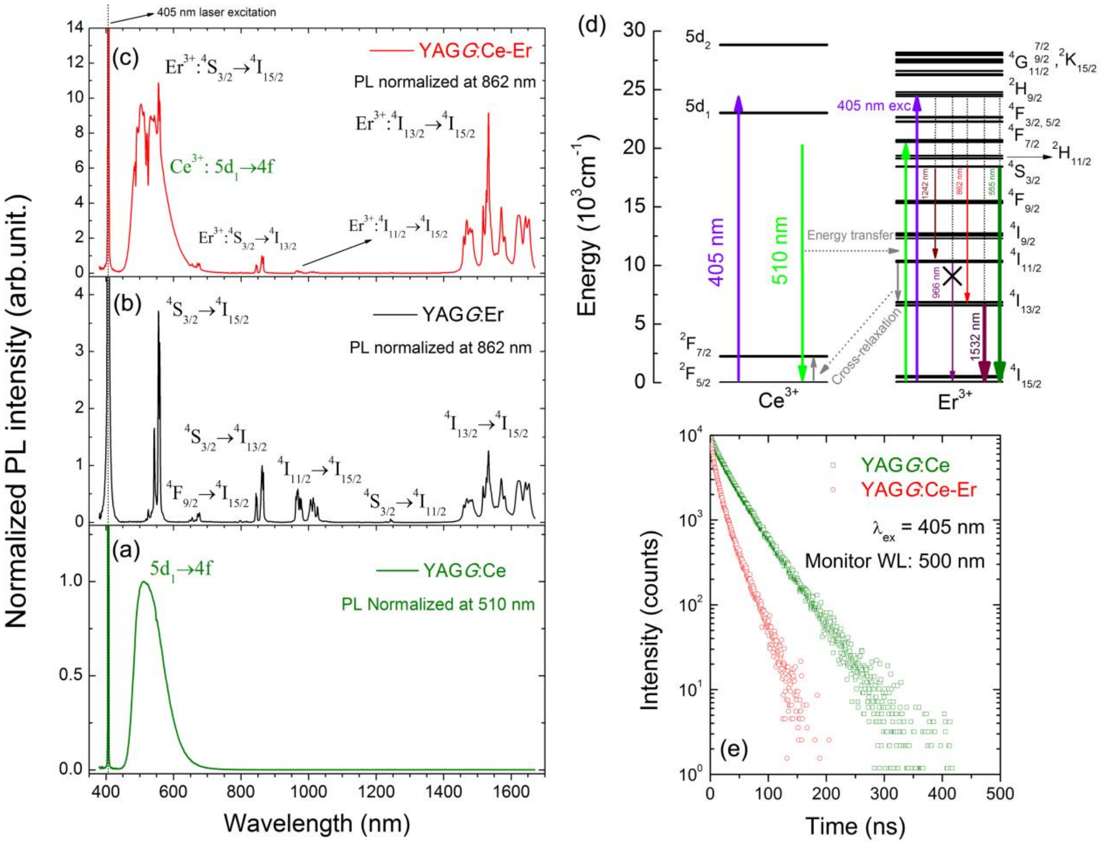

Figure 8.4. PL spectra of the (a) YAG*G*:Ce (b) YAG*G*:Er and (c) YAG*G*:Ce-Er ceramic samples under 405 nm laser excitation (d) energy level diagrams of Ce^{3+} and Er^{3+} (e) fluorescence decay curves of the YAG*G*:Ce and YAG*G*:Ce-Er ceramic samples (λ_{ex}=405 nm and λ_{em}=500 nm)

8.3.2. PL and PersL spectra

Fig. 8.5(a) shows the PL spectra of the YAG*G*:Ce-Cr and YAG*G*:Er-Ce-Cr samples under blue laser (442 nm) excitation. The YAG*G*:Ce-Cr sample exhibits an intense emission band peaked at 505 nm due to the parity allowed $5d_1\rightarrow4f$ transition of Ce^{3+}.[46-48] Besides, a weak emission band peaked at around 690 nm is attributed to the Cr^{3+}:$^2E(^2G)\rightarrow{}^4A_2(^4F)$ transition (the so-called *R*-line). Comparing the PL spectrum of the YAG*G*:Ce-Cr sample with the diffuse reflectance of the Er^{3+} singly doped YAG*G* sample (YAG*G*:Er), the absorption bands ($^4I_{15/2}\rightarrow{}^4F_{3/2,\,5/2,\,7/2}$, $^2H_{11/2}$, $^4S_{3/2}$) of Er^{3+} are largely overlapped with the emission band of Ce^{3+} indicating that the ET process from Ce^{3+} to Er^{3+} can efficiently occur. This is confirmed by the decrease of Ce^{3+} emission intensity in the visible range and the presence of several sharp emission bands at around 555 nm, 862 nm and 1532 nm owing to the *f*-*f* transitions of

Er^{3+}:$^4S_{3/2}\rightarrow{}^4I_{15/2}$, $^4I_{13/2}$, and $^4I_{13/2}\rightarrow{}^4I_{15/2}$, respectively in the YAG*G*:Er-Ce-Cr sample. The quenching of the Er^{3+}:$^4I_{11/2}\rightarrow{}^4I_{15/2}$ bands peaked at 966 nm and 1013 nm is also observed as that in the YAG*G*:Ce-Er sample due to the cross-relaxation process mentioned in the section 8.3.1.

The PersL spectra of the YAG*G*:Er-Ce-Cr sample recorded at different times after ceasing blue light illumination are shown in Fig. 8.5(b). The persistent emission bands not only exhibit a broad band peaked at around 500 nm due to Ce^{3+}:$5d_1\rightarrow 4f$ transition but also intense sharp bands located at NIR region (around 862 nm and 1532 nm) due to the *f*-*f* transitions of Er^{3+}. Especially the PersL bands in the range of 1450-1670 nm match well with the NIR-III window. The identical shape of PL and PersL spectra of the YAG*G*:Er-Ce-Cr sample suggests that the emission centers are the same under and after excitation. Since the efficient ET process from Ce^{3+} to Er^{3+} was confirmed in the YAG*G*:Ce-Er sample shown in Fig. 8.4(e), we assume that the efficient persistent ET also occurs in the YAG*G*:Er-Ce-Cr phosphor after ceasing the blue light illumination.

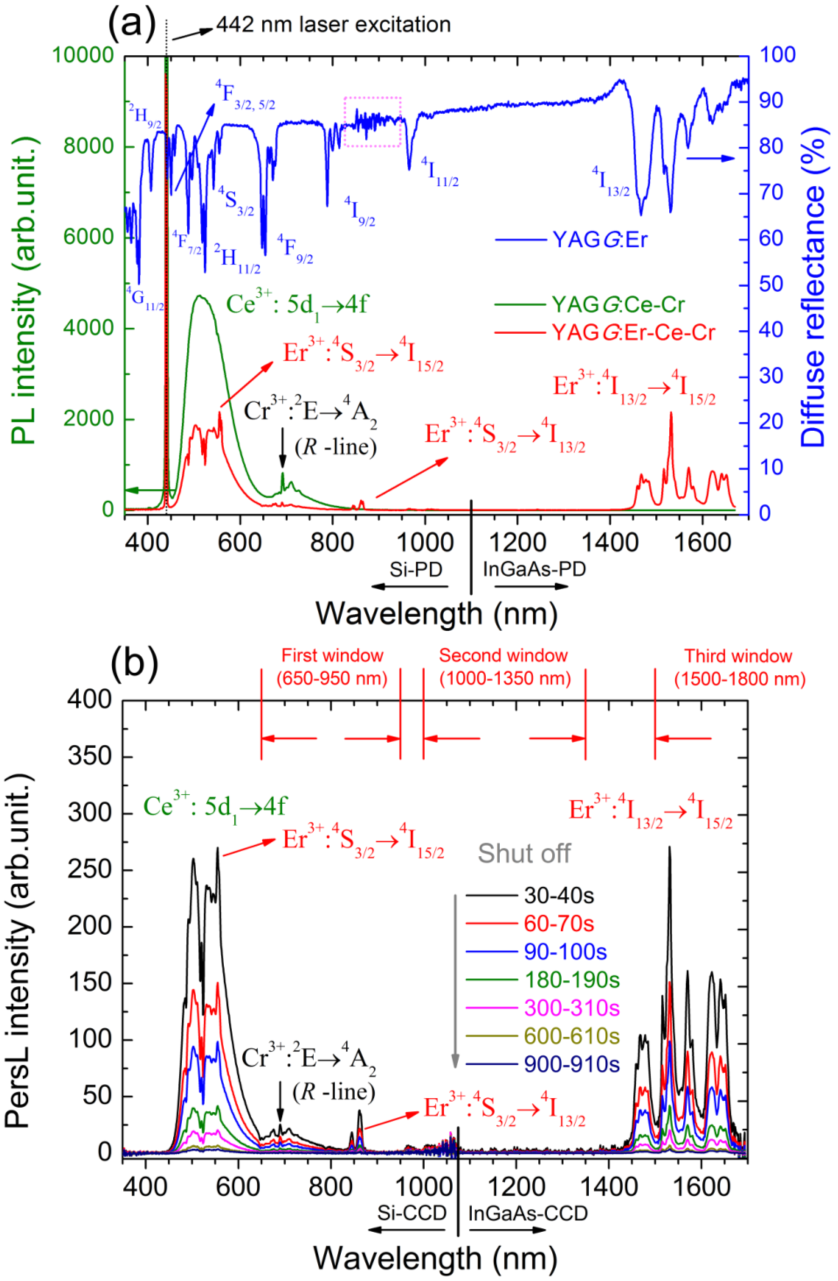

Figure 8.5. (a) PL spectra of the YAG*G*:Ce-Cr and YAG*G*:Er-Ce-Cr ceramic samples (λ_{ex}=442 nm) as well as the diffuse reflectance of the YAG*G*:Er ceramic sample (pink-dotted-line area is the detector change region from PMT to PbS) (b) PersL spectra of the YAG*G*:Er-Ce-Cr ceramic sample (integrating time: 10 s) after ceasing the blue light illumination

8.3.3. Persistent luminescent decay curves

The persistent luminescent decay curve monitoring the Ce^{3+} emission (475-650 nm) of the YAG*G*:Er-Ce-Cr sample after ceasing the blue light illumination is shown in Fig. 8.6(a), in which the decay curves of the standard YAG*G*:Ce-Cr ceramic phosphor and a compacted ceramic pellet made of the commercial SAO:Eu-Dy phosphor (LumiNova- GLL300FFS, Nemoto & Co. Ltd.,) under the same experimental condition are also plotted as references.[30] The luminance values at 10 min after ceasing the excitation are 58 mcd/m^2 for YAG*G*:Er-Ce-Cr, 627 mcd/m^2 for YAG*G*:Ce-Cr, and 211 mcd/m^2 for SAO:Eu-Dy. [(see the photographs of the two samples after ceasing blue LED illumination in Fig. 8.6(c)]. Persistent luminescent duration to reach a luminance value of 0.32 mcd/m^2 in the YAG*G*:Er-Ce-Cr sample is around 213 min, which is much shorter than that of the YAG*G*:Ce-Cr sample (about 808 min), due to quenching effect of the green Ce^{3+} emission by the non-radiative persistent ET to Er^{3+} (note that the luminance value 0.32 mcd/m^2 is the minimum value commonly used by the safety signage industry, about 100 times the sensitivity of the dark-adapted eye).[49]

The persistent luminescent decay curve monitoring Er^{3+} NIR emission (>1000 nm) of the YAG*G*:Er-Ce-Cr sample after ceasing the same blue light illumination is shown in Fig. 8.6(b), in which the decay curve of the standard $ZnGa_2O_4$:Cr^{3+} (ZGO:Cr, emitting wavelength peaked at 695 nm) sample under the same experimental condition is also plotted as a reference.[50] The NIR photon emission rate of the YAG*G*:Er-Ce-Cr sample for the NIR-III window at 10 min after ceasing the blue light excitation (8.33×10^{17} cps/Sr/m^2) is over two times higher than that of the widely used deep-red persistent phosphor, ZGO:Cr (3.30×10^{17} cps/Sr/m^2) for the NIR-I window (summarized in Table 8.1), which indicates that this persistent phosphor exhibits excellent PersL in NIR region by Er^{3+} as well as visible light region by Ce^{3+}. In Fig. 8.6(d), we exhibit the first PersL imaging by a commercial InGaAs camera[51] for the two garnet ceramic phosphors. Although the YAG*G*:Ce-Cr sample shows bright green PersL by a digital camera in the visible light region [see Fig. 8.6 (c)], no signal can be captured by the InGaAs camera due to its lack of PersL in the short-wave infrared (SWIR, ~900-1700 nm) region. Since the InGaAs camera is only sensitive to the luminescence located in the SWIR region, the PersL imaging from Er^{3+} in the YAG*G*:Er-Ce-Cr sample was nicely recorded even using a very short integrating time (0.04 s, the maximum value to avoid the saturation of Er^{3+} PersL intensity at 1 min after ceasing the blue light excitation). This result clearly proves that Er^{3+} PersL is intense and long enough to be recorded by an InGaAs camera.

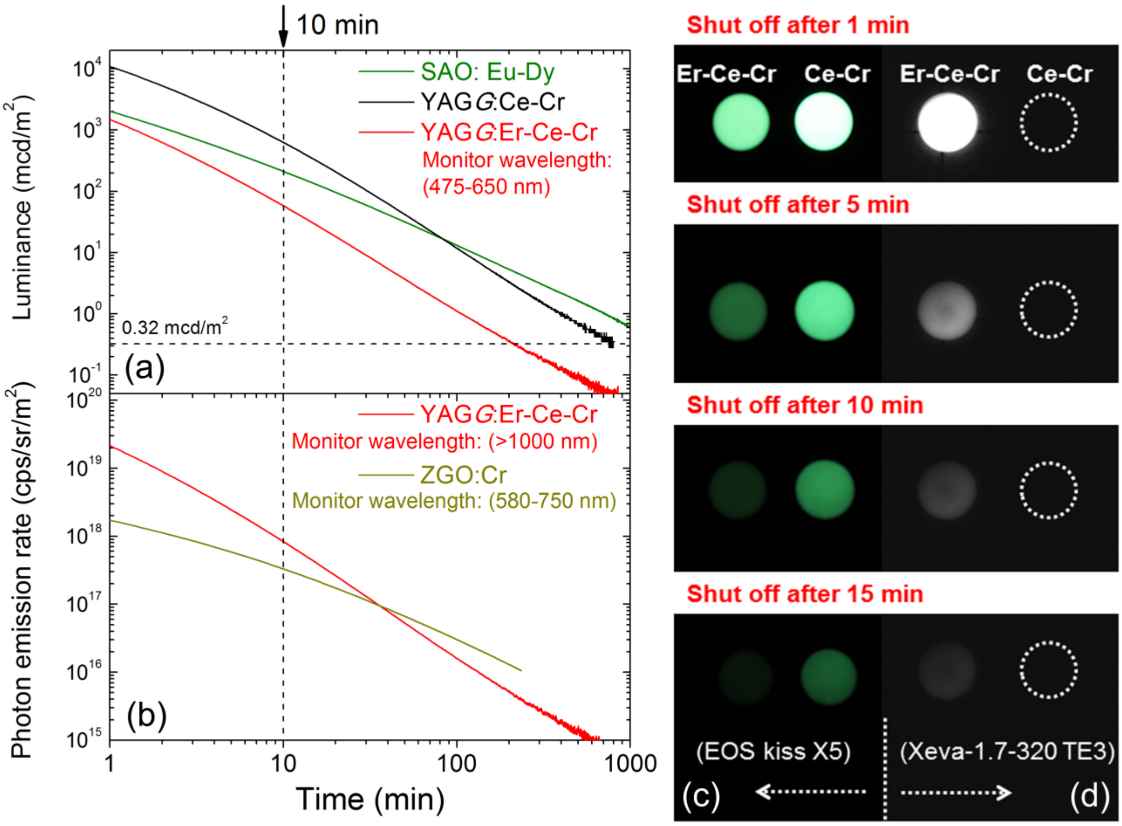

Figure 8.6. Persistent luminescent decay curves of the YAG*G*:Er-Ce-Cr ceramic sample (a) luminance monitoring Ce^{3+} emission (YAG*G*:Ce-Cr and SAO:Eu-Dy ceramic samples as references) (b) photon emission rate monitoring Er^{3+} emission (ZGO:Cr ceramic sample as a reference) and photo images of the YAG*G*:Ce-Cr and YAG*G*:Er-Ce-Cr ceramic samples after blue LED (455 nm, 1 W output) illumination for 5 min (c) taken by a digital camera (EOX kiss X5) with exposure time: 1 s, ISO value: 1600, aperture value (*F* value): 5.0 (d) taken by a SWIR camera (Xeva-1.7-320 TE3) with integrating time: 0.04 s

Table. 8.1. Luminance (mcd/m^2), radiance (mW/Sr/m^2) and photon emission rate (cps/Sr/m^2) of the YAG*G*:Er-Ce-Cr sample after ceasing 460 nm excitation for 5 min compared with that of the YAG*G*:Ce-Cr, $SrAl_2O_4$:Eu-Dy and $ZnGa_2O_4$:Cr reference samples

Composition	10 min (mcd/m^2)	10 min (mW/Sr/m^2)	10 min (cps/Sr/m^2)
YAG*G*:Er-Ce-Cr	**58**	**1.08×10^{-1}**	**8.33×10^{17}**
YAG*G*: Ce-Cr [30]	**627**	**-**	**-**
$SrAl_2O_4$:Eu-Dy [30]	**211**	**-**	**-**
$ZnGa_2O_4$:Cr [50]	**-**	**0.92×10^{-1}**	**3.30×10^{17}**

8.3.4. Thermoluminescence (TL) glow curves and 2D contour plots

Fig. 8.7(a) and (c) show the TL glow curves of the YAG*G*:Ce-Cr and YAG*G*:Er-Ce-Cr samples monitoring only Ce^{3+} emission, respectively. Although the intensity of the Ce^{3+} emission in the YAG*G*:Er-Ce-Cr sample is much weaker than that in the YAG*G*:Ce-Cr sample due to the persistent ET from Ce^{3+} to Er^{3+}, both of the glow peaks are located at around 300 K. This suggests that PersL from Ce^{3+} is originated from the same electron trap, Cr^{3+}, in both samples with the same trap depth or more precisely with the same trap distribution.[31,34] Therefore, the thermal activation energy which is required to clean up the electrons captured by the traps is the same.[31]

For TL measurements monitoring the visible light region, the black-body radiation has nearly no effects on the TL read-out when the heating temperature is lower than 600 K. On the other hand, when monitoring NIR emission, the excessive effect of black-body radiation on the TL read-out must be taken into account.[52,53] Fig. 8.7(b) and (d) show the TL glow curves of the YAG*G*:Ce-Cr and YAG*G*:Er-Ce-Cr samples monitoring only NIR emission (>1000 nm), respectively. Since there is no contributed PersL from the YAG*G*:Ce-Cr sample at the wavelength region over 1000 nm, only intense black-body radiation from the sample and partially from the measurement setup is observed. However, for the YAG*G*:Er-Ce-Cr sample, the additional TL glow curve centered at around 300 K is also observed after subtracting the intense black-body radiation signal (blue-line by subtracting the black-dotted-curve from the red-dotted-line), which is ascribed to the PersL from Er^{3+} in the NIR region.

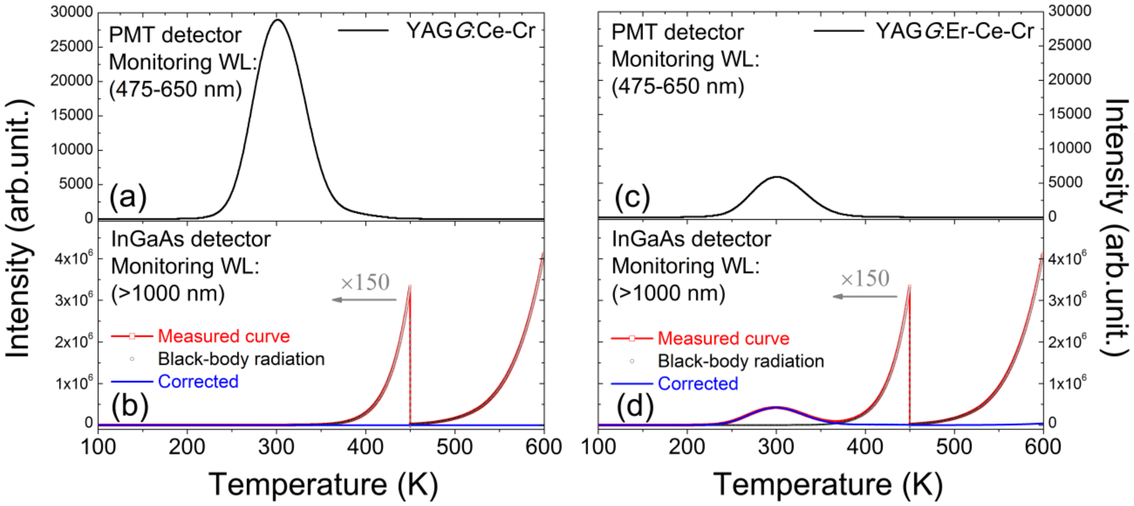

Figure 8.7. TL glow curves of the YAG*G*:Ce-Cr ceramic sample monitored by the (a) PMT detector in the range of 475-650 nm, (b) InGaAs detector in the range of over 1000 nm and the YAG*G*:Er-Ce-Cr ceramic sample monitored by the (c) PMT detector in the range of 475-650 nm, and (d) InGaAs detector in the range of over 1000 nm

Fig. 8.8 shows the TL two-dimensional (2D) contour plots of the YAG*G*:Ce-Cr and YAG*G*:Er-Ce-Cr samples in order to see what kind of emission bands contributes to the TL glow peak at different temperatures. From the contour plots of the YAG*G*:Ce-Cr sample in Fig. 8.8 (a) and (b), it can be seen that at increased temperatures, the TL spectrum is simply composed of two emission bands from Ce^{3+} and Cr^{3+}, and no contributed emission except strong black-body radiation in the NIR region (1300-1700 nm, above ~500 K) is observed. On the other hand, in the YAG*G*:Er-Ce-Cr sample as shown in Fig. 8.8(c) and (d), besides the emission bands from Ce^{3+} and Cr^{3+}, the NIR emission band of Er^{3+} appears at the same temperature range, which agrees well with its PersL spectrum in Fig. 8.5(b). The intense TL glow peaks of both YAG*G*:Ce-Cr and YAG*G*:Er-Ce-Cr samples lie in almost the same temperature range (around 300 K), close to *RT* and body temperature of Mammalia (around 310 K). Since the TL peak temperature is correlated to the energy gap between the bottom of conduction band and the electron trap,[49] the identical glow temperature of the two samples indicates the same electron trapping and de-trapping process[54] in both, where Cr^{3+} works as an efficient electron trap with ideal trap depth for long PersL in the host of $Y_3Al_2Ga_3O_{12}$.[30-33]

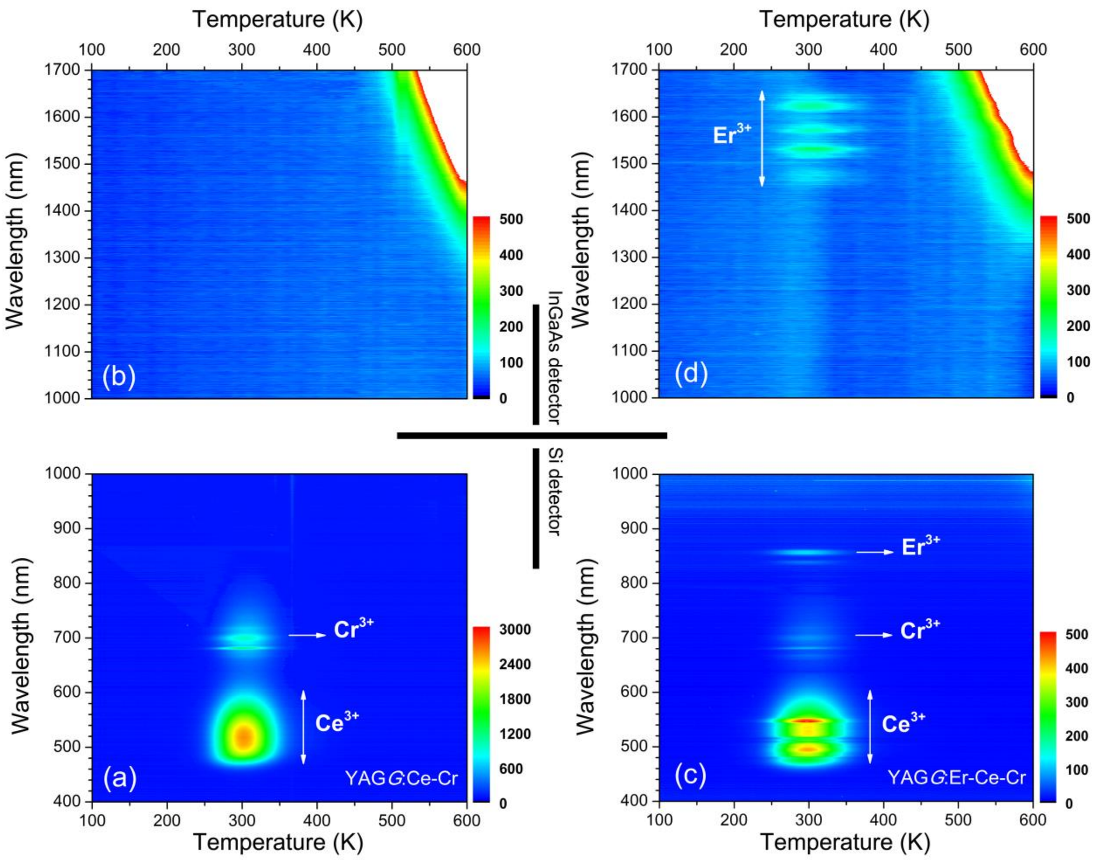

Figure 8.8. Wavelength-temperature (λ-T) contour plots of the (a), (b) YAG*G*:Ce-Cr and (c), (d) YAG*G*:Er-Ce-Cr ceramic samples

8.3.5. Persistent luminescence mechanism

The persistent luminescence mechanism of the YAG*G*:Er-Ce-Cr persistent phosphor is briefly explained by constructing the vacuum referred binding energy (*VRBE*) diagram[31,55,56] composed of Ce^{3+}, Er^{3+}, Cr^{2+}, conduction band (*C.B*), and valence band (*V.B*) energy levels in the $Y_3Al_2Ga_3O_{12}$ host (see Fig. 8.9). When the YAG*G*:Er-Ce-Cr sample is charged by blue light, the electron located at the ground state ($^2F_{5/2}$) of Ce^{3+} is promoted to the excited state of the lowest 5*d* energy level ($5d_1$). Since the energy gap between the bottom of *C.B* and the $5d_1$ level is small, the excited electron can "jump" into *C.B* with thermal assisted activation energy at *RT* and then be trapped by the electron trapping center (Cr^{3+}).[30,31] At that time, Ce^{3+} is photo-oxidized into Ce^{4+} or (Ce^{3+} + h^+) and Cr^{3+} changes into Cr^{2+} or (Cr^{3+} + e^-) after capturing one electron (process ①).[31,56]

Then the de-trapping process occurs with thermal release of the captured electron from the Cr^{2+} (Cr^{3+} + e^-) trap, and finally the excited state of the Ce ion, $(Ce^{3+})^*$ appears after capturing the released electron in the re-combination process (process ②). The radiative relaxation gives a broad band emission of Ce^{3+}:$5d_1 \rightarrow {}^2F_{5/2}$, ${}^2F_{7/2}$, and the resonant ET process takes place nearly at the same time to Er^{3+} ion (process ③), which is followed by rapid multi-phonon relaxation down to the ${}^4S_{3/2}$ and ${}^4I_{13/2}$ excited levels leading to the sharp luminescence bands of Er^{3+}: ${}^4S_{3/2} \rightarrow {}^4I_{15/2}$ in green and ${}^4I_{13/2} \rightarrow {}^4I_{15/2}$ in the NIR region.

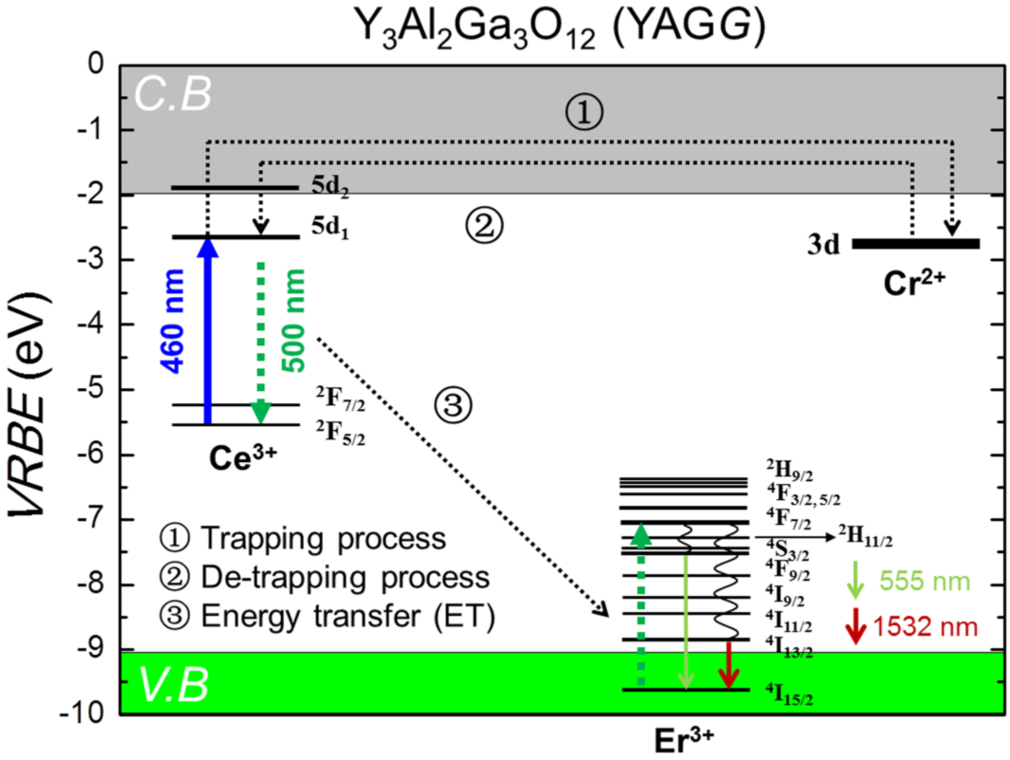

Figure 8.9. The *VRBE* diagram including selected energy levels of Ce^{3+}, Er^{3+}, and Cr^{2+} in the $Y_3Al_2Ga_3O_{12}$ (YAG*G*) host

8.4. Conclusion

In summary, we have successfully developed a blue-light-chargeable NIR persistent phosphor ($Y_3Al_2Ga_3O_{12}$:Er^{3+}, Ce^{3+}, Cr^{3+}) with long (>10 h) persistent luminescence due to the typical Er^{3+}:${}^4I_{13/2} \rightarrow {}^4I_{15/2}$ transition ranging from 1450 nm to 1670 nm in garnet. The NIR PersL bands from Er^{3+} through efficient persistent energy transfer from Ce^{3+} match well with the NIR-III window, and its photon emission rate

(8.33×10^{17} cps/Sr/m^2) at 10 min after ceasing blue light (460 nm) illumination was over two times higher than that of the widely used $ZnGa_2O_4$:Cr^{3+} deep-red persistent phosphor (3.30×10^{17} cps/Sr/m^2). We also showed the first persistent luminescence imaging with high intensity and long duration by a commercial InGaAs camera. *In vivo* bio-imaging in the NIR-III window with improved optical resolution quality and deep tissue penetration depth can be expected in the near future by using this material (in the form of nano-particles) as a functionalized bio-probe.

Acknowledgement

I would like to acknowledge Dr. Morgane Pellerin from Chimie-Paris Tech, Dr. Laura Wortmann and Prof. Kohei Soga from Tokyo University of Science for supporting persistent luminescence imaging by the Xeva-1.7-320 TE3 InGaAs camera.

This work was financially supported by a Grant-in-Aid for JSPS Fellows (No. 16J09849).

References

[1] T. Matsuzawa, Y. Aoki, N. Takeuchi and Y. Murayama, *J. Electrochem. Soc.*, 1996, **143**, 2670-2673.

[2] K. Van Den Eeckhout, D. Poelman and P. F. Smet, *Materials*. 2013, **6**, 2789-2818.

[3] D. Dutczak, T. Jüstel, C. Ronda and A. Meijerink, *Phys. Chem. Chem. Phys.*, 2015, **17**, 15236-15249.

[4] S. K. Singh, *RSC Adv.*, 2014, **4**, 58674-58698.

[5] Y. Zhuang, Y. Katayama, J. Ueda and S. Tanabe, *Opt. Mater.*, 2014, **36**, 1907-1912.

[6] B. Viana, S. K. Sharma, D. Gourier, T. Maldiney, E. Teston, D. Scherman and C. Richard, *J. Lumin.*, 2016, **170**, 879-887.

[7] Q. le Masne de Chermont, C. Chanéac, J. Seguin, F. Pellé, S. Maîtrejean, J. P. Jolivet, D. Gourier, M. Bessodes and D. Scherman, *Proc. Natl. Acad. Sci. U.S.A.* 2007,**104**, 9266-9271.

[8] F. Liu, W. Yan, Y. J. Chuang, Z. Zhen, J. Xie and Z. Pan, *Sci. Rep.*, 2013, **3**, 1554-1562.

[9] T. Maldiney, A. Bessière, J. Seguin, E. Teston, S. K. Sharma, B. Viana, A. J. J. Bos, P. Dorenbos, M. Bessodes, D. Gourier, D. Scherman and C. Richard, *Nat. Mater*., 2014, **13**, 418-426.

[10] A. Bessière, S. Jacquart, K. Priolkar, A. Lecointre, B. Viana and D. Gourier, *Opt. Express*. 2011, **19**, 10131-10137.

[11] Z. W. Pan, Y. Y. Lu and F. Liu, *Nat. Mater*., 2012, **11**, 58-63.

[12] Y. Katayama, J. Ueda and S. Tanabe, *Opt. Mater. Express*. 2014, **4**, 613-623.

[13] J. Xu, J. Ueda, Y. Zhuang, B. Viana and S. Tanabe, *Appl. Phys. Express*. 2015, **8**, 042602 (4 pp).

[14] A. M. Smith, M. Mancini and S. Nie, *Nature. Nanotech*., 2009, **4**, 710-711.

[15] E. Hemmer, N. Venkatachalam, H. Hyodo, A. Hattori, Y. Ebina, H. Kishimoto and K. Soga, *Nanoscale*. 2013, **5**, 11339-11361.

[16] E. Hemmer, A. Benayas, F. Légaré and F. Vetrone, *Nanoscale Horiz*., 2016, **1**, 168-184.

[17] J-C. G. Bünzli, *J. Lumin*., 2016, **170**, 866-878.

[18] D. J. Naczynski, M. C. Tan, M. Zevon, B. Wall, J. Kohl, A. Kulesa, S. Chen, C. M. Roth, R. E. Riman and P. V. Moghe, *Nat. Commun*., 2013, **4**, 2199 (10 pp).

[19] L. A. Sordillo, Y. Pu, S. Pratavieira, Y. Budansky and R. R. Alfano, *J. Biomed. Opt*., 2014, **19**, 056004 (6 pp).

[20] L. A. Sordillo, S. Pratavieira, Y. Pu, K. S. Ramirez, L. Shi, L. Zhang, Y. Budansky and R. R. Alfano, *Proc. of SPIE*. 2014, **8940**, 89400V (7 pp).

[21] K. Welsher, Z. Liu, D. Daranciang and H. Dai, *Nano Lett*., 2008, **8**, 586-590.

[22] W. Y. Liu, A. Y. Chang, R. D. Schaller and D. V. Talapin, *J. Am. Chem. Soc*., 2012, **134**, 20258-20261.

[23] S. Tanabe, *Int. J. Appl. Glass Sci*., 2015, **6**, 305-328.

[24] E. Snitzer and R. Woodcock, *Appl. Phys. Lett.*, 1965, **6**, 45-46.

[25] M. Nakazawa, M. Tokuda, K. Washio and Y. Asahara, *Opt. Lett*., 1984, **9**, 312-314.

[26] E. Desurvire, J. Simpson and P. C. Becker, *Opt. Lett.*, 1987, **12**, 888-890.

[27] F. Auzel, *C. R. Acad. Sci. (Paris)*. 1966, **262**, 1016-1019.

[28] F. Auzel, *C.R. Acad. Sci. (Paris)*. 1966, **263**, 819-821.

[29] N. Yu, F. Liu, X. Li and Z. W. Pan, *Appl. Phys. Lett*., 2009, **95**, 231110 (3 pp).

[30] J. Ueda, K. Kuroishi and S. Tanabe, *Appl. Phys. Lett*., 2014, **104**, 101904 (4 pp).

[31] J. Ueda, P. Dorenbos, A. J. J. Bos, K. Kuroishi and S. Tanabe, *J. Mater. Chem. C*. 2015, **3**, 5642-5651.

[32] J. Ueda, *J. Ceram. Soc. Jpn*., 2015, **123**, 1059-1064.

[33] J. Xu, J. Ueda, K. Kuroishi and S. Tanabe, *Scr. Mater*., 2015, **102**, 47-50.

[34] J. Xu, S. Tanabe, A. D. Sontakke and J. Ueda, *Appl. Phys. Lett*., 2015, **107**, 081903 (4 pp).

[35] A. A. Kaminskii, *Crystalline Lasers: Physical Processes and Operating Schemes*, CRC Press, New York, 1996, pp. 187-188.

[36] S. Tanabe and T. Hanada, *J. Non-Cyst. Solids.* 1996, **196**, 101-105.

[37] S. Tanabe, N. Sugimoto, S. Ito and T. Hanada, *J. Lumin.*, 2000, **87**, 670-672.

[38] M. Nishi, S. Tanabe, K. Fujita, K. Hirao and G. Pezzotti, *Solid State Commun*., 2004, **132**, 19-23.

[39] S. Ono and S. Tanabe, *IEEE J. Quantum Electron.* 2004, **40**, 1704-1708.

[40] M. Nishi, S. Tanabe, M. Inoue, M. Takahashi, K. Fujita and K. Hirao, *Opt. Mater.*, 2005, **27**, 655-662.

[41] Y. Shiota, S. Tanabe, T. Hanada and Y. Maeda, *J. Ceram. Soc. Jpn*., 1999, **107**, 1201-1205.

[42] M. Nishi, S. Tanabe, K. Fujita and K. Hirao, *J. Alloy Compd*., 2006, **408-412**, 788-790.

[43] J. Zhou, Y. Teng, X. Liu, S. Ye, Z. Ma and J. Qiu, *Phys. Chem. Chem. Phys.*, 2010, **12**, 13759-13762.

[44] Q. Wang, L. Su, H. Li, L. Zheng, X. Xu, H. Tang, X. Guo, D. Jiang and J. Xu, *Phys. Status Solidi A*. 2011, **208**, 2839-2842.

[45] Z. Meng, T. Yoshimura, K. Fukue, M. Higashihata, Y. Nakata and T. Okada, *J. Appl. Phys.*, 2000, **88**, 2187-2190.

[46] Y. Luo and Z. Xia, *J. Phys. Chem. C*. 2014, **118**, 23297-23305.

[47] J. Ueda, P. Dorenbos, A. J. J. Bos, A. Meijerink and S. Tanabe, *J. Phys. Chem. C*. 2015, **119**, 25003-25008.

[48] V. Khanin, I. Venevtsev, P. Rodnyi and C. Ronda, *Radiat. Meas.*, 2016, **90**, 104-108.

[49] K. Van den Eeckhout, P. F. Smet and D. Poelman, *Materials*. 2010, **3**, 2536-2566.

[50] Y. Zhuang, J. Ueda and S. Tanabe, *Appl. Phys. Express*. 2013, **6**, 052602 (4 pp).

[51] http://www.xenics.com/sites/default/files/leaflets/xb-081_01_xeva-1.7-320_te3_lowres.pdf

[52] E. P. Manche, *Rev. Sci. Instrum.*, 1978, **49**, 715-717.

[53] F. Liu, Y. Liang, Y. Chen and Z. W. Pan, *Adv. Optical. Mater.*, 2016, **4**, 562-566.

[54] P. Dorenbos, *J. Electrochem. Soc.*, 2005, **152**, H107-H110.

[55] P. Dorenbos, *J. Lumin.*, 2013, **134**, 310-318.

[56] J. Xu, J. Ueda and S. Tanabe, *J. Mater. Chem. C*. 2016, **4**, 4380-4386.

Chapter 9

Tailoring deep-red persistent luminescence of Cr^{3+} by crystal field engineering and selecting proper lanthanide sensitizers as additional electron traps based on the host referred binding energy *(HRBE)* diagram in garnet hosts

Abstract:

Garnet structure ($A_3B_2C_3O_{12}$) with three cation sites is a flexible host material widely used for *w*-LEDs, solid-state laser, scintillators and so on. In this work, we have successfully developed six different Cr^{3+} doped garnets: $Y_3Ga_{4.99}Cr_{0.01}O_{12}$ (YG*G*:Cr), $Gd_3Ga_{4.99}Cr_{0.01}O_{12}$ (GG*G*:Cr), $Lu_3Ga_{4.99}Cr_{0.01}O_{12}$ (LuG*G*:Cr), $Y_3Sc_{1.99}Cr_{0.01}Ga_3O_{12}$ (YSG*G*:Cr), $Gd_3Sc_{1.99}Cr_{0.01}Ga_3O_{12}$ (GSG*G*:Cr) and $Lu_3Sc_{1.99}Cr_{0.01}Ga_3O_{12}$ (LuSG*G*:Cr), which exhibit persistent luminescence (PersL) due to Cr^{3+} emission matching well with both the response curve of the crystalline silicon (c-Si) detector and the wavelength region of the first biological (NIR-I) window. The main emission band of Cr^{3+} in garnet hosts can be easily tunable from the sharp *R*-line emission due to the ^2E (^2G)→$^4A_2$ (^4F) transition in the strong crystal field strength to the broad band emission due to the $^4T_2$ (^4F)→$^4A_2$ (^4F) transition in the weak one when Lu^{3+} in the *A* site and Ga^{3+} in the *B* site are respectively replaced by larger cations, Y^{3+}/Gd^{3+} and Sc^{3+}. Especially the GSG*G*:Cr sample, its *R*-line emission was totally disappeared while only the broad band emission peaked at around 770 nm was observed, and its persistent radiance (0.54×10^{-1} mW/Sr/m^2) at 60 min after ceasing the ultraviolet (UV) excitation was over three times higher than that of the widely used $ZnGa_2O_4:Cr^{3+}$ deep-red persistent phosphor (0.15×10^{-1} mW/Sr/m^2) at room temperature (*RT*). Furthermore, based on the knowledge of 4*f* energy levels of

lanthanide ions in the host referred binding energy (*HRBE*) diagram of GSG*G* host, four trivalent lanthanides (Sm^{3+}, Eu^{3+}, Tm^{3+}, Yb^{3+}) whose 2+ ground states located below the bottom of the conduction band (*CB*) were selected as potential candidates to be an electron trap in order to enhance the Cr^{3+} PersL. Among them, Yb^{3+} could introduce a new electron trap with a thermoluminescence (TL) glow peak located around 330 K overlapped with the intrinsic defect (photochromic center)-related electron trap in garnet host, and the persistent radiance of the GSG*G*:Cr-Yb sample (1.56×10^{-1} mW/Sr/m^2) at 60 min after ceasing the UV excitation was enhanced to be nearly three times higher than that of the GSG*G*:Cr persistent phosphor (0.54×10^{-1} mW/Sr/m^2) at *RT*.

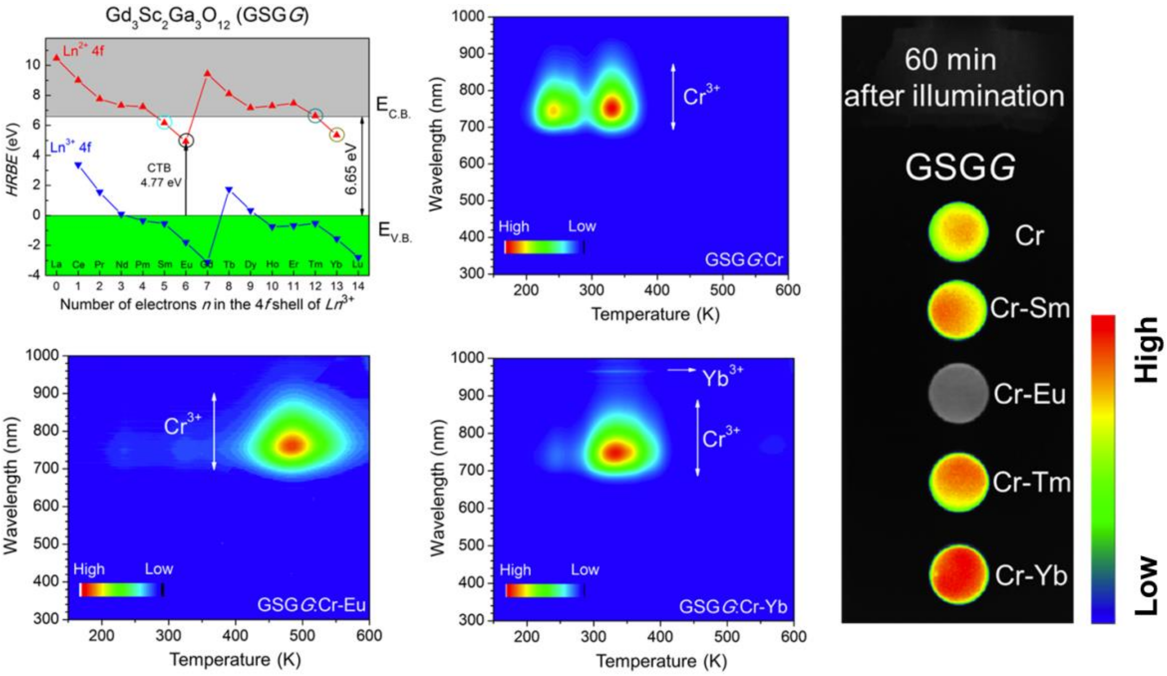

Design of Cr^{3+}-Ln^{3+} co-doped deep-red garnet persistent phosphors using *HRBE* diagram

9.1. Introduction

Persistent luminescence (PersL), also known as ‘‘glow-in-the-dark’’, is a specific type of luminescence that can last for seconds, minutes or even hours after ceasing excitation sources. It was once considered as a mysterious phenomenon in the ancient time, and firstly described in a Chinese miscellaneous note called *“Xiang-shan Ye Lu”* published in the Song dynasty (960-1279 A.D.). A cow painting using a special ink mixed by sulfide persistent phosphors from Japan (composed of calcium from seashells and sulfur from volcanic activities) glows in the dark to have inexplicable magic.[1] In 1602, an Italian shoemaker, V. Casciarolo observed bright PersL from a mineral barite [more precisely, the reduction product of the mineral barite, barium sulfide (BaS) with the mono-valent copper (Cu^+) impurity] in darkness, later to be known as the famous Bologna stone.[2] Since then, numerous persistent phosphors have been reported, while it was only in 1996 that this research field began to attract much wider interest due to the discovery of the new generation green persistent phosphor, $SrAl_2O_4$:Eu^{2+}, Dy^{3+} (SAO:Eu-Dy).[3]

Till now, persistent phosphors emitting visible lights (mainly from blue to green) represented by SAO:Eu-Dy have been successfully commercialized for watch dials, luminous paints, out-door illumination and safety signage, *etc*.[4-6] On the other hand, much more attention has been paid to red or even near-infrared (NIR) persistent phosphors since their emitting wavelength is suitable for *in vivo* bio-imaging due to the reduced scattering and minimal absorption coefficient when compared with ultraviolet (UV) and visible light, allowing imaging of deep biological tissues.[7-11] Furthermore, red/NIR persistent phosphors in the form of nano-particles charged by UV light (visible light in rare cases) before injecting into small animals can emit long PersL without real-time *in-situ* excitation. The exclusion of external illumination totally removes the autofluorescence as background noise, avoids complicated background subtraction procedures and thus improves the signal-to-noise ratio (SNR) remarkably.[7,12-14] This new bio-imaging technology has soon become a hot research topic[15] and motivated the fast development of different red/NIR persistent phosphors with bright radiance and long duration. Among them, Cr^{3+} doped ones are considered to be promising candidates since Cr^{3+} ion with the $3d^3$ electronic configuration allows highly efficient *d*-*d* transitions located at around 700 nm, which matches well with the first biological window (NIR-I, 650 to 950 nm) as well as the response curve of commercial Si-detectors.[16] However, only a few Cr^{3+} doped red/NIR long persistent phosphors have been reported so far, which are mainly gallate based ones such as $Zn_3Ga_2Ge_2O_{10}$:Cr^{3+},[17,18] $ZnGa_2O_4$:Cr^{3+},[19,20] $LiGa_5O_8$:Cr^{3+},[13] and $MgGa_2O_4$:Cr^{3+},[21] *etc.*, because of the strong substitutability of Cr^{3+} for Ga^{3+} in the distorted octahedral coordination owing to their similar ionic radius.

Garnet structure in the form of $A_3B_2C_3O_{12}$ is belonging to the cubic crystal system with space group of O_h^{10}-$Ia\bar{3}d$,[22] in which three types of cation sites able to be occupied by different cation ions: (i) the *A* site, 24(c) dodecahedral site (D_2 point symmetry) with a coordination number eight (CN=8), (ii) the *B* site, 16(a) octahedral site (S_6 point symmetry) with a coordination number six (CN=6), and (iii) the C site, 24(d) tetrahedral site (S_4 point symmetry) with a coordination number four (CN=4). Therefore, the garnet structure can be regarded as an interconnected dodecahedra, octahedra and tetrahedra with shared oxygen atoms at the corners of the polyhedra as shown in Figure 9.1. Considering the high tolerability of these three cation sites (i.e. the larger dodecahedral sites are ideal for lanthanide ions while the smaller octahedral sites are of the appropriate size for Cr^{3+} ions), versatile doping strategies can be utilized to obtain different garnet matrices with different crystal fields.[23,24] Considering the emission band of Cr^{3+} is quite related to the crystal field strength of hosts and can be easily tunable from the sharp *R*-line emission due to the ^2E (^2G)$\rightarrow$$^4A_2$ (^4F) transition in the strong crystal field strength to the broad band emission due to the $^4T_2$ (^4F)$\rightarrow$$^4A_2$ (^4F) transition in the weak one because of different electron-phonon couplings,[24,25] the dominant emission band of Cr^{3+} in garnet is expected to be quite controllable by tailoring the local crystal fields of different hosts, which is called “crystal field engineering”.

On the other hand, in contrast to the characteristics of transition metal ions like Cr^{3+} that the electron in the outermost *d* orbital strongly interacts with the arrangement of surrounding ligands, the 4*f* orbitals of lanthanide ions are well shielded from the bonding forces of ligands by $5s^2$ and $5p^6$ orbitals. Therefore, once the binding energy of the 4*f* ground state (*GS*) for one lanthanide ion relative to the conduction band *(CB)* or the valence band *(VB)* is determined, those of 4*f* levels of all other lanthanides in a certain material host can be estimated fairly well by constructing either host referred binding energy *(HRBE)* or vacuum referred binding energy *(VRBE)* diagrams.[26-30] Since lanthanide ions are widely adopted as electron trap centers (hole trap centers in rare cases[31,32]) for developing novel persistent phosphors or enhancing PersL intensities in present phosphors, these theoretical prediction diagrams can be a very useful guide to choose proper lanthanide ions as efficient electron traps inducing desirably long PersL.[28,31,33,34] Fortunately, as mentioned before, the *A* site in garnet structure is extremely suitable for doping lanthanide ions as activators, which has already achieved a huge success in various applications such as Ce^{3+} doped garnets for *w*-LEDs and scintillators,[35,36] Nd^{3+} doped garnets for the high power solid-state laser,[37,38] and Yb^{3+} doped garnets for the quantum cutting and down-conversion.[39]

Recently, we have developed Cr^{3+} singly-doped $Y_3Al_{5-x}Ga_xO_{12}$ (YAG*G*:Cr) garnet persistent phosphors showing deep-red PersL peaked at 690 nm, in which Cr^{3+} ions act both as emitting centers and trap centers. The persistent radiance (in unit of $mW/Sr/m^2$) of the optimized composition (x=3) after ceasing UV illumination at room temperature (*RT*) was nearly 5 times higher than that of the widely used $ZnGa_2O_4$:Cr^{3+} (ZGO:Cr) deep-red persistent phosphor.[40] On the other hand, we lowered the *CB* level by full Ga^{3+} substitution for Al^{3+} in the Cr^{3+} singly-doped $Gd_3Al_{5-x}Ga_xO_{12}$ (GAG*G*:Cr) garnet to be $Gd_3Ga_5O_{12}$ (GG*G*:Cr) in order to decrease the electron trap depth (representing the energy gap between the bottom of *CB* and the electron trap) from the *GS* of Eu^{2+} as possible as we can, and firstly developed a bright deep-red persistent phosphor (GG*G*:Cr-Eu) in which Eu^{3+} ions can act as additional electron traps to greatly enhance the PersL intensity of the GG*G*:Cr phosphor over 20 times at *RT*.[41]

The successful discovery of these Cr^{3+} singly- and Cr^{3+}-Ln^{3+} co-doped garnet persistent phosphors motivates us to make full use of the flexible garnet structure and systematically design novel red/NIR persistent phosphors for the NIR-I window. In this work, photoluminescence (PL) and PersL properties of six different garnets are investigated in detail and we introduce a facile way to develop Cr^{3+} doped garnet persistent phosphors using both the crystal field engineering to tune the emission band of Cr^{3+} and the *HRBE* diagram to select suitable lanthanide ions as efficient electron traps to further enhance the Cr^{3+} PersL intensity.

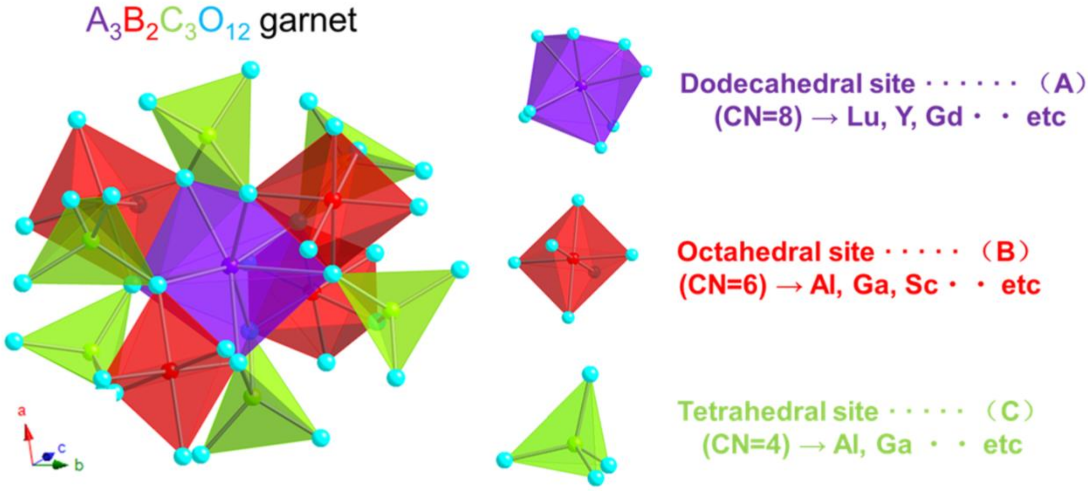

Figure 9.1. Garnet structure ($A_3B_2C_3O_{12}$) with three different cation sites

9.2. Experimental section

9.2.1. Sample preparation

Six Cr^{3+} singly-doped garnet ceramic samples with the compositions of $Y_3Ga_{4.99}Cr_{0.01}O_{12}$ (YG*G*:Cr), $Gd_3Ga_{4.99}Cr_{0.01}O_{12}$ (GG*G*:Cr), $Lu_3Ga_{4.99}Cr_{0.01}O_{12}$ (LuG*G*:Cr), $Y_3Sc_{1.99}Cr_{0.01}Ga_3O_{12}$ (YSG*G*:Cr), $Gd_3Sc_{1.99}Cr_{0.01}Ga_3O_{12}$ (GSG*G*:Cr), $Lu_3Sc_{1.99}Cr_{0.01}Ga_3O_{12}$ (LuSG*G*:Cr) and four Cr^{3+}-Ln^{3+} co-doped garnet ceramic samples with the compositions of $Gd_{2.997}Sm_{0.003}Sc_{1.99}Cr_{0.01}Ga_3O_{12}$ (GSG*G*:Cr-Sm), $Gd_{2.997}Eu_{0.003}Sc_{1.99}Cr_{0.01}Ga_3O_{12}$ (GSG*G*:Cr-Eu), $Gd_{2.997}Tm_{0.003}Sc_{1.99}Cr_{0.01}Ga_3O_{12}$ (GSG*G*:Cr-Tm), and $Gd_{2.997}Yb_{0.003}Sc_{1.99}Cr_{0.01}Ga_3O_{12}$ (GSG*G*:Cr-Yb) were fabricated by a conventional solid-state reaction method (compositions of different garnet samples are summarized in Table 9.1). Gd_2O_3 (99.99%), Y_2O_3 (99.99%), Lu_2O_3 (99.99%), Sc_2O_3 (99.99%), Ga_2O_3 (99.99%), Al_2O_3 (99.99%), Sm_2O_3 (99.99%),

Eu_2O_3 (99.99%), Tm_2O_3 (99.99%), Yb_2O_3 (99.99%) and Cr_2O_3 (99.9%) were used as raw materials. The starting powder was mixed by a ball milling method with anhydrous alcohol for 1 h. The mixed powder was dried at 80 ℃ for 36 h, compacted to form a ceramic green body (ϕ20 mm, 1.5 mm thickness) under uniaxial pressing of 50 MPa, and finally sintered at 1600 ℃ for 10 h in air. The as-prepared samples were double-face polished to be thickness of 1.0 ±0.1 mm using a copper plate and diamond slurry, all of which were confirmed to be single phase by XRD measurement (see Figure 9.2 and 9.3).

Table 9.1. Nominal compositions of different garnet ceramic samples.

Notation	Composition	Notation	Composition
YG*G*:Cr	$\mathbf{Y_3Ga_{4.99}Cr_{0.01}O_{12}}$	**LuSG*G*:Cr**	$\mathbf{Lu_3Sc_{1.99}Cr_{0.01}Ga_3O_{12}}$
GG*G*:Cr	$\mathbf{Gd_3Ga_{4.99}Cr_{0.01}O_{12}}$	**GSG*G*:Cr-Sm**	$\mathbf{Gd_{2.997}Sm_{0.003}Sc_{1.99}Cr_{0.01}Ga_3O_{12}}$
LuG*G*:Cr	$\mathbf{Lu_3Ga_{4.99}Cr_{0.01}O_{12}}$	**GSG*G*:Cr-Eu**	$\mathbf{Gd_{2.997}Eu_{0.003}Sc_{1.99}Cr_{0.01}Ga_3O_{12}}$
YSG*G*:Cr	$\mathbf{Y_3Sc_{1.99}Cr_{0.01}Ga_3O_{12}}$	**GSG*G*:Cr-Tm**	$\mathbf{Gd_{2.997}Tm_{0.003}Sc_{1.99}Cr_{0.01}Ga_3O_{12}}$
GSG*G*:Cr	$\mathbf{Gd_3Sc_{1.99}Cr_{0.01}Ga_3O_{12}}$	**GSG*G*:Cr-Yb**	$\mathbf{Gd_{2.997}Yb_{0.003}Sc_{1.99}Cr_{0.01}Ga_3O_{12}}$

9.2.2. Sample characterization

The diffuse reflectance spectra of the Cr^{3+} singly-doped garnet samples were measured by a spectrophotometer (UV3600, Shimadzu) equipped with an integrating sphere. The lifetime measurement of the Cr^{3+} singly-doped garnet samples were recorded with a compact fluorescence lifetime spectrometer (Quantaurus-Tau-C11367, Hamamatsu Photonics & Co. Ltd.,) using a pulse Xe lamp with a 460 nm band-pass filter. PL and PersL spectra of the garnet samples were measured at 25 ℃ by a Si CCD spectrometer (QE65-Pro, Ocean Optics) and calibrated by a standard halogen lamp (SCL-600, Labsphere). The persistent luminescence excitation (PersLE) spectrum of the GSG*G*:Cr sample after ceasing illumination by monochromatic light for 1 min was measured by a fluorescence spectrophotometer (RF-5000, Shimadzu) using a home-made automatic operation program. Every PersL spectrum was measured at 5 min after ceasing corresponding monochromatic light, the excitation wavelength was changed at 5 nm intervals between 200 and 800 nm, and the emission wavelength was monitored from 600 to 900 nm. A 300 W Xe lamp (MAX-302, Asahi Spectra) with an UV mirror module (250-380 nm) was used as the excitation source for thermoluminescence (TL) two-dimensional (2D) plot measurements. The ceramic sample was set in a cryostat (Helitran LT3, Advanced Research Systems) to control temperatures and firstly illuminated by UV light at 150 K for 10 min, then heated up to 600 K at a rate of 10 K/min at 10 min after ceasing the illumination, and the TL signals were recorded by a Si photo-diode (PD) (S-025-H, Electro-Optical System Inc.,) covered with a 600 nm short-cut filter to monitor Cr^{3+} emission. The same Si CCD spectrometer was operated simultaneously with the TL measurement to monitor the emission spectra at different temperatures. All persistent luminescent decay curves of the garnet samples after being excited for 5 min by the same Xe lamp with the same UV module were measured at 25 ℃ using the same Si PD covered with a 600 nm short-cut filter. Then the decay curves were calibrated to the absolute radiance (in unit of $mW/Sr/m^2$) using a radiance meter (Glacier X, B&W Tek Inc). The low temperature persistent luminescent decay curve of the GSG*G*:Cr sample monitoring at 770 nm was measured by a fluorescence spectrophotometer (RF-5300, Shimadzu). The ceramic sample was firstly set in a closed-cycle helium cryostat (CRT-006-2000, Iwatani Plantech Co.) to cool down to 20 K (lowest temperature in our current condition), and then illuminated by 460 nm monochromatic light for 10 min. Photographs of the garnet samples after excitation by an UV (254 nm) lamp with 6 W output (SLUV-6, AS ONE Co. Ltd.,) for 5 min were taken by a bio-imaging machine (Clairvivo OPT, Shimadzu) equipped with a Si CCD camera (cooled down to 208 K), and the integrating time was set to be 1.0 s.

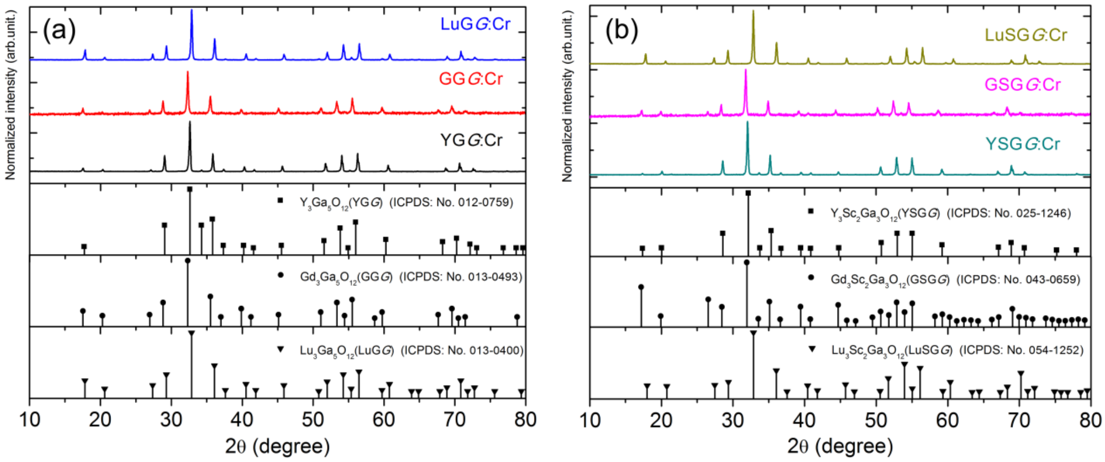

Figure 9.2. X-ray diffraction (XRD) patterns of the (a) YG*G*:Cr, GG*G*:Cr, LuG*G*:Cr and (b) YSG*G*:Cr, GSG*G*:Cr, LuSG*G*:Cr garnet ceramic samples

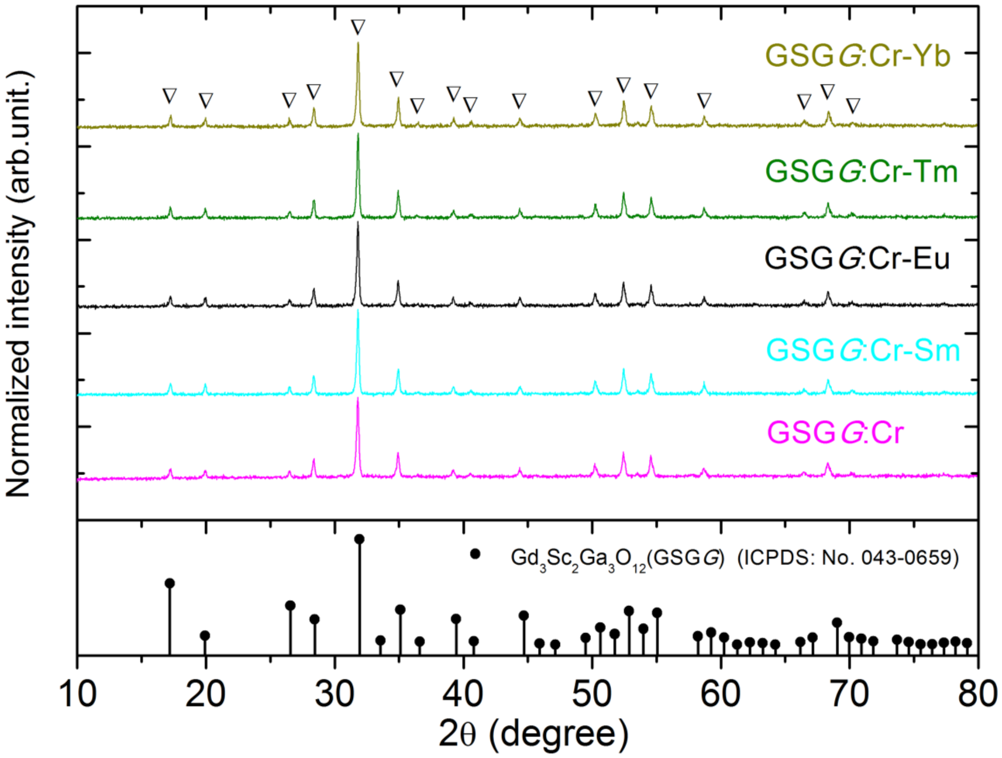

Figure 9.3. X-ray diffraction (XRD) patterns of the GSG*G*:Cr and GSG*G*:Cr-*Ln* (*Ln*=Sm, Eu, Tm, Yb) garnet ceramic samples

9.3. Results and discussion

9.3.1. Crystal field engineering of Cr^{3+} in garnet

Figure 9.4 (a) illustrates the diffuse reflectance spectra of the Cr^{3+} singly-doped garnet ceramic samples. All of them mainly show two broad absorption bands located at around 450 nm and 600 nm, which can be ascribed to the intra-3*d* transitions of Cr^{3+}: $^4A_2\,(^4F)\rightarrow{}^4T_1\,(^4F)$ and $^4A_2\,(^4F)\rightarrow{}^4T_2\,(^4F)$, respectively. Since the emission bands of Cr^{3+} strongly depend on the crystal field strength of hosts, the value of the local crystal field parameter (*Dq*) can be estimated from the mean peak energy of the $^4A_2\,(^4F)\rightarrow{}^4T_2\,(^4F)$ transition given by:

$$Dq=\frac{E(^4A_2\rightarrow{}^4T_2)}{10} \tag{1}$$

Moreover, based on the mean peak energies of the $^4A_2\,(^4F)\rightarrow{}^4T_2\,(^4F)$ and $^4A_2\,(^4F)\rightarrow{}^4T_1\,(^4F)$ transitions, the Racah parameter (*B*) can be evaluated from the following equation:

$$\frac{Dq}{B}=\frac{15(x-8)}{(x^2-10x)} \tag{2}$$

Where the parameter x is defined as[42]

$$x=\frac{E(^4A_2\rightarrow{}^4T_1)-E(^4A_2\rightarrow{}^4T_2)}{Dq} \tag{3}$$

Based on these spectroscopic data, *Dq*/*B* of these garnet samples can be estimated as shown in Table 9.2. According to the Tanabe-Sugano (d^3) diagram[43,44] given in Figure 9.4 (b), there is a cross-point region between the energy levels of $^4T_2\,(^4F)$ and $^2E\,(^2G)$ which represents the intermediate crystal field region between the weak and strong ones. When the value of *Dq*/*B* is small (in the weak crystal field condition), the emission of Cr^{3+} is mainly due to the $^4T_2\,(^4F)\rightarrow{}^4A_2\,(^4F)$ transition (spin allowed). On the other hand, when the value of *Dq*/*B* is large (in the strong crystal field condition), the emission of Cr^{3+} is mainly due to the $^2E\,(^2G)\rightarrow{}^4A_2\,(^4F)$ transition (spin forbidden). Considering the ionic radius that $Gd^{3+}>Y^{3+}>Lu^{3+}$ in the *A* site and $Sc^{3+}>Ga^{3+}$ in the *B* site of the garnet structure, it can be suggested that the crystal field strength of garnet host decreases from LuG*G* to GSG*G* so that the spin type of the Cr^{3+} transition can change from spin forbidden in LuG*G* to spin allowed in GSG*G*. That is confirmed by the fluorescent decay curves monitoring Cr^{3+} emission of these garnet samples under 460 nm excitation recorded at *RT* as shown in Figure 9.4 (c), the lifetime of Cr^{3+}

emission estimated by the single exponential fitting (green line) decreases from LuG*G* (605.2 μs), LuSG*G* (584.1 μs), YG*G* (272.8 μs), GG*G* (162.2 μs), YSG*G* (120.1 μs), to GSG*G* (104.9 μs).

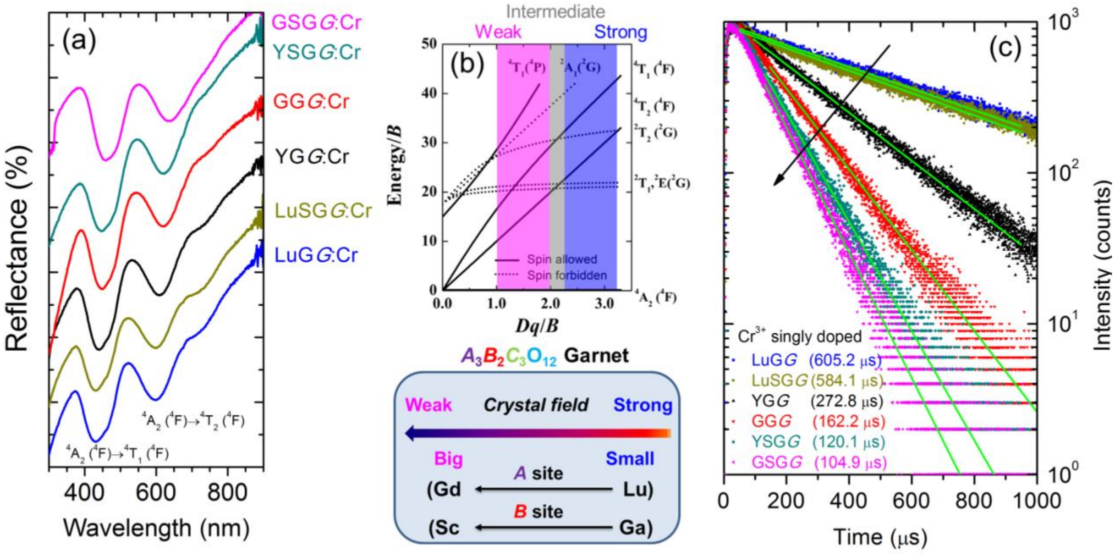

Figure 9.4. (a) Diffuse reflectance spectra of the Cr^{3+} singly-doped garnet samples (b) the Tanabe-Sugano (d^3) diagram and (c) fluorescent decay curves of the garnet ceramic samples (λ_{ex}=460 nm) monitoring Cr^{3+} emission recorded at room temperature (green line: single exponential fitting)

Table 9.2. Estimated crystal field parameters of the Cr^{3+} singly-doped garnet ceramic samples.

Sample	$^4A_2\rightarrow{}^4T_1$ (nm)	$^4A_2\rightarrow{}^4T_2$ (nm)	*Dq* (cm^{-1})	*B* (cm^{-1})	*Dq/B*
LuG*G*:Cr	**434**	**599**	**1669**	**625**	**2.67**
LuSG*G*:Cr	**436**	**603**	**1658**	**627**	**2.64**
YG*G*:Cr	**440**	**613**	**1631**	**638**	**2.56**
GG*G*:Cr	**449**	**627**	**1595**	**630**	**2.53**
YSG*G*:Cr	**450**	**629**	**1590**	**631**	**2.52**
GSG*G*:Cr	**455**	**641**	**1560**	**642**	**2.43**

Figure 9.5 (a) gives the PL spectra of the Cr^{3+} singly-doped garnet ceramic samples under 460 nm excitation at *RT*, all of which show the broad band emission of Cr^{3+} located from 650 nm to 1000 nm. The emission band of Cr^{3+} in the LuG*G* sample is attributed to the typical transition of *R*-line [^2E (^2G)→$^4A_2$ (^4F)] peaked at 690 nm and some phonon sidebands (PSBs) due to the thermal vibration of Cr^{3+} ions.[45,46] When Lu^{3+} in the *A* site and Ga^{3+} in the *B* site are respectively replaced by larger cations, Y^{3+}/Gd^{3+} and Sc^{3+}, the broad band emission of Cr^{3+} due to the $^4T_2$ (^4F)→$^4A_2$

(^{4}F) transition becomes dominant and gradually shifts to longer wavelength. Especially in the GSG*G*:Cr sample, the *R*-line emission is totally disappeared while only the broad band emission peaked at around 770 nm is observed at *RT*, which accords well with the decreasing trend of the crystal field parameter (*Dq*) from LuG*G* to GSG*G* in Table 9.2.

PersL spectra of the garnet samples recorded at 5 min after ceasing UV illumination are shown in Figure 9.5 (b). It is worth noting that the spectral shapes of PL and PersL are almost identical in all of the garnet samples which is quite different from the situation in the ZGO:Cr persistent phosphor, where the anti-site defect ($Ga_{Zn}^{\bullet}$) of the ZGO spinel structure is involved and plays a key role in the carrier trapping and detrapping process responsible for long PersL mainly from the N_2-line emission.[12,19,20,47,48] Therefore, we assume that the PersL due to the delayed charge carrier re-combination process in these Cr^{3+} singly-doped garnet samples occurs through the same kind of Cr^{3+} centers as that in PL. On the other hand, as shown in Figure 9.5 (c), all of the PersL spectra of the garnet samples match well with both the response curve of the Si detector used in this work and the wavelength region of the NIR-I window indicating that they can be potential candidates for *in vivo* bio-imaging applications.

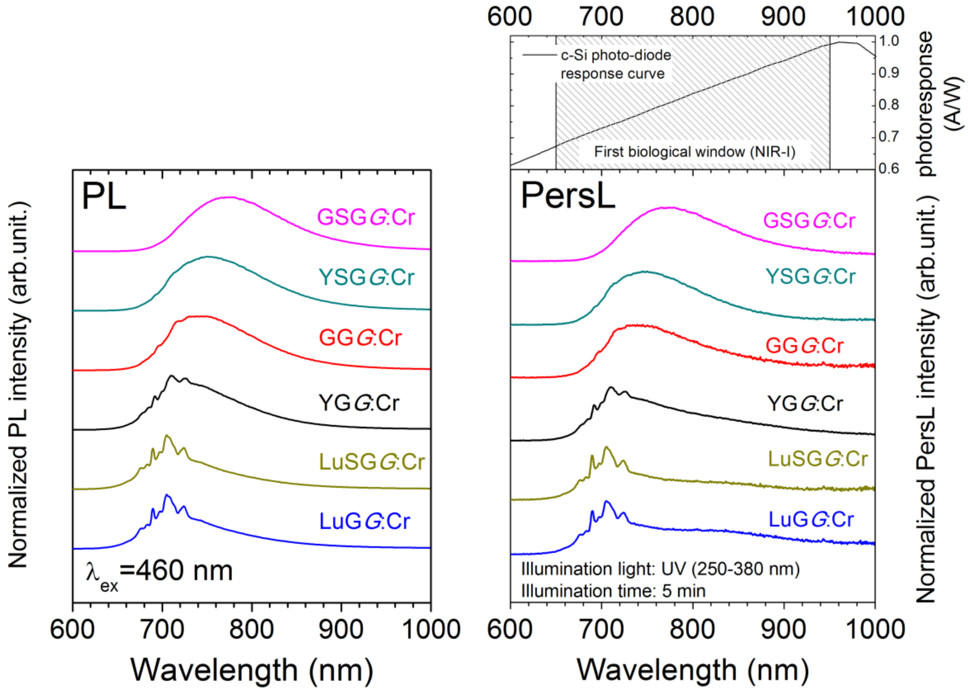

Figure 9.5. (a) PL (λ_{ex}=460 nm) and (b) PersL spectra (at 5 min after ceasing UV illumination for 5 min) of the Cr^{3+} singly-doped garnet ceramic samples measured at room temperature (c) response curve of the crystalline silicon (c-Si) photo-diode (S-025-H, Electro-Optical System Inc.,) and the wavelength region of the first biological window (NIR-I).

Persistent luminescent decay curves of the Cr^{3+} singly-doped garnet ceramic samples after ceasing UV illumination for 5 min at *RT* are shown in Figure 9.6(a), in which the decay curve of the standard ZGO:Cr ceramic sample under the same experimental condition is also plotted as a reference (radiances of all the samples at 5 min, 30 min, 60 min after ceasing UV illumination are summarized in Table. 9.3). Among them, the GSG*G*:Cr sample exhibits the highest PersL intensity, which is also confirmed by the photograph taken by the Si CCD camera at 30 min after ceasing 254 nm illumination shown in Figure 9.6(b). The emission intensity of the GSG*G*:Cr sample is much higher than that of the other garnet samples, and strongly saturated even using a short integrating time (1.0 s) for imaging. Furthermore, the persistent radiance of the GSG*G*:Cr sample (0.54×10^{-1} mW/Sr/m^2) at 60 min after ceasing the excitation is over three times higher than that of the widely used ZGO:Cr deep-red persistent phosphor (0.15×10^{-1} mW/Sr/m^2).[49]

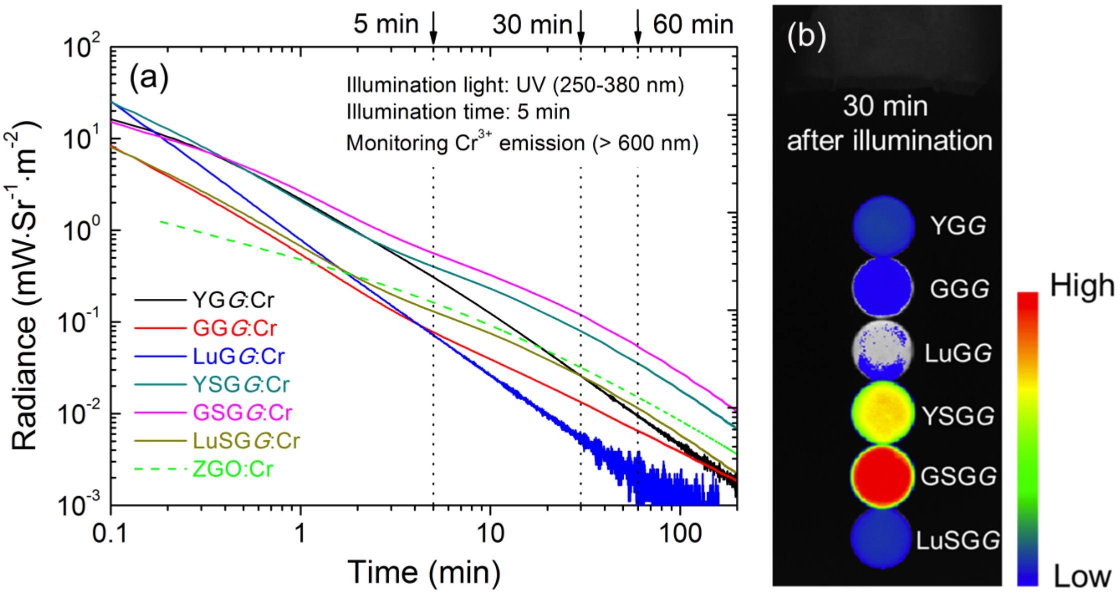

Figure 9.6. (a) Persistent luminescent decay curves of the Cr^{3+} singly-doped garnet ceramic samples after ceasing UV (250-380 nm) illumination for 5 min compared with that of the $ZnGa_2O_4:Cr^{3+}$ reference sample (b) photograph taken by the bio-imaging machine using a Si CCD camera at 30 min after ceasing UV (254nm) illumination for 5 min (integrating time: 1.0 s).

Table 9.3. Radiances of the Cr^{3+} singly-doped garnet ceramic samples after ceasing UV (250-380 nm) illumination for 5 min compared with that of the $ZnGa_2O_4:Cr^{3+}$ reference sample (in units of $mW/Sr/m^2$).

Composition	5 min ($mW/Sr/m^2$)	30 min ($mW/Sr/m^2$)	60 min ($mW/Sr/m^2$)
YG*G*:Cr	**3.09×10^{-1}**	**0.26×10^{-1}**	**0.10×10^{-1}**
GG*G*:Cr	**0.78×10^{-1}**	**0.13×10^{-1}**	**0.07×10^{-1}**
LuG*G*:Cr	**0.72×10^{-1}**	**0.06×10^{-1}**	**0.04×10^{-1}**
YSG*G*:Cr	**4.02×10^{-1}**	**0.80×10^{-1}**	**0.35×10^{-1}**
GSG*G*:Cr	**5.63×10^{-1}**	**1.19×10^{-1}**	**0.54×10^{-1}**
LuSG*G*:Cr	**1.31×10^{-1}**	**0.26×10^{-1}**	**0.11×10^{-1}**
$ZnGa_2O_4$:Cr [49]	**1.63×10^{-1}**	**0.32×10^{-1}**	**0.15×10^{-1}**

Although the detailed mechanism of PersL is still an open question, the most acceptable one can be qualitatively explained by an electron trapping-detrapping process:[28] when persistent phosphors are charged by excitation sources, electron-hole (*e*-*h*) pairs are generated and the excited electrons through *CB* are captured by electron traps. This process is usually called trapping process. Then the stored electrons can be released by thermal stimulation to *CB* (detrapping process) being re-combined with holes followed by PersL. In order to clarify the trapping and detrapping mechanism of the Cr^{3+} singly-doped garnet ceramic samples, TL 2D-mappings (wavelength-temperature contour plots) monitoring Cr^{3+} emission are carried out as shown in Figure 9.7. All of the TL spectra are only composed of one emission band from Cr^{3+} indicating that except Cr^{3+} ions, no additional emission centers (i.e. impurities introduced during sample preparation procedures) contribute to the TL glow curves. Besides, the main TL glow peaks of the GG*G*:Cr, LuG*G*:Cr and LuSG*G*:Cr samples are located below 300 K, which can explain why these samples show weak PersL at *RT*. Because the thermal activation energy below 300 K is high enough to release most of the captured electrons in electron traps so that only small amount of the captured electrons are remained at *RT* inducing weak PersL especially after several minutes ceasing the UV excitation. However, the main TL glow peaks of the other three samples, particularly that of the YSG*G*:Cr and GSG*G*:Cr samples are located above 300 K so that the thermal activation energy below/at *RT* is not high enough to clean up all the captured electrons and most of them can be slowly released being re-combined with holes inducing intense PersL with long duration.

On the other hand, TL glow curves of all the garnet samples exhibit two broad bands located at two different temperature regions in accordance with our previous reports on the YAG*G*:Cr persistent phosphors.[40,50] Since the TL peak temperature is correlated to the trap depth,[5] two different glow peak temperatures indicate two types of traps existing in all of the garnet samples (note the low temperature related trap as Trap-I and the high temperature related trap as Trap-II). Although the detailed characteristic of these two traps such as distribution and relationship is still need to be further investigated, we assume that one of them is owing to the electron trap related to Cr^{3+} ions while the other one is due to intrinsic defects in garnet hosts. For the Cr-related electron traps, we have already discussed a lot in the Ce^{3+}, Cr^{3+} co-doped $Y_3Al_{5-x}Ga_xO_{12}$ (YAG*G*:Ce-Cr) green persistent phosphors, in which Cr^{3+} acts as an efficient electron trap (capture one electron to be Cr^{2+} or $Cr^{3+}+e^-$) with ideal trap depth at x=3 for Ce^{3+} long PersL working at *RT*.[51,52] On the other hand, the intrinsic defects [color centers, either F^+ centers as electron traps or F^- centers as hole traps and oxygen vacancies ($V_O^{\bullet\bullet}$ or $V_O^{\bullet}$) as electron traps are mostly possible] cause significant photochromic phenomena in all the Cr^{3+} singly-doped garnet samples under ambient conditions as shown in Figure 9.8(a). The body color of the garnet samples changes from green to brown under UV (254 nm) charging for 1min, and it takes several days to gradually or a short time under thermal bleaching at a relatively high temperature (i.e. 300 ℃ for 5 min) to return back their original green body color. Furthermore, the coloration and decoloration process in all the garnet samples can repeatedly occur upon UV charging and thermal bleaching for many times, respectively. The photochromic phenomena in other persistent phosphors were also reported by other groups,[13,53] which suggested that photochromic centers due to intrinsic defects in material hosts could serve as electron traps with deep trap depth for photo-generated electrons responsible for PersL or photo-stimulated luminescence (PSL). Therefore, to simplify the trapping and detrapping mechanism in garnet hosts, we assume that both of the two traps are electron traps (hole traps are not discussed here) with energy levels locating below the bottom of *CB*, and the Trap-I with shallow trap depth is due to Cr^{3+} ions while the Trap-II with deep trap depth is due to intrinsic or lattice defects of garnet hosts.

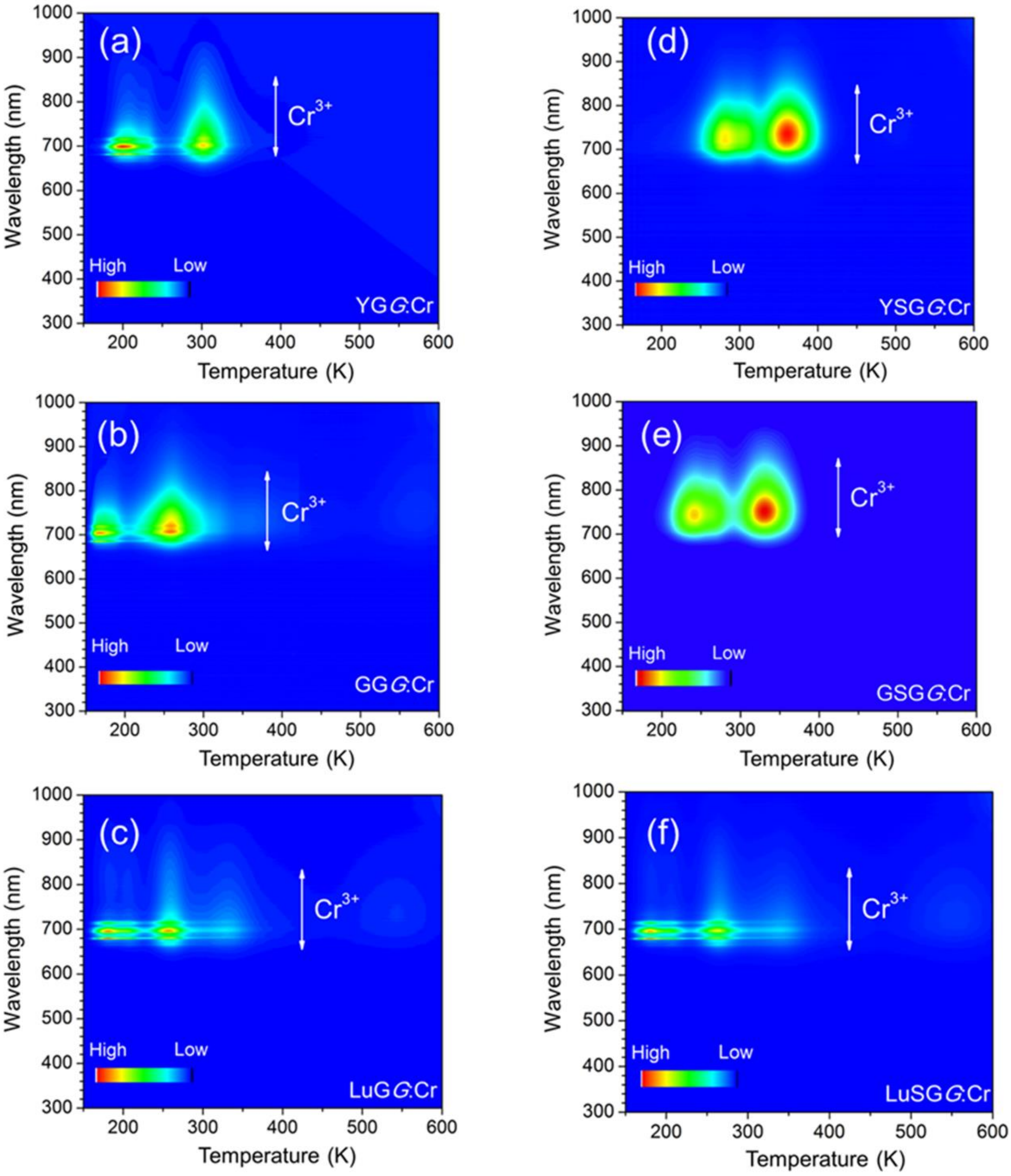

Figure 9.7. Wavelength-temperature (λ-T) contour plots of the (a) YG*G*:Cr (b) GG*G*:Cr (c) LuG*G*:Cr (d) YSG*G*:Cr (e) GSG*G*:Cr and (f) LuSG*G*:Cr ceramic samples monitoring Cr^{3+} emission.

It is also worth noting that all of the Cr^{3+} singly-doped garnet ceramic samples exhibit PersL behaviors even at 20 K after ceasing blue light excitation as shown in

Figure 9.8(b) (take the GSG*G*:Cr sample as an example, it shows the highest PersL intensity than that of the other Cr^{3+} singly-doped garnet samples at *RT*). The reciprocal PersL intensity of the GSG*G*:Cr sample versus time after ceasing 460 nm charging presents a linear behavior which indicates that there is a strong athermal tunneling process in this material.[13,54-56] According to the classical electron trapping-detrapping process through *CB* in persistent phosphors as mentioned before, the excitation energy is high enough (UV light in most cases) to liberate the electrons located at *GS* to the energy levels either within the *CB* or below the bottom of *CB* with a very small energy gap. So the excited electron can freely move through the *CB* with a low thermal assistant energy and be captured by electron traps. After ceasing the excitation light, the captured electrons can be gradually released with certain thermal activation energies leading to PersL.[28] However, as the schematic illustration of the Cr^{3+} energy levels in the GSG*G*:Cr sample shown in Figure 9.8(c), blue light (460 nm) charging can only facilitate the $^4T_1$ (^4F) energy level of Cr^{3+} which has a large energy gap below the bottom of *CB* so that the classical electron trapping-detrapping process through *CB* cannot occur. However, it still exhibits PersL behaviors even at 20 K with a very low thermal assistant energy, which suggests that a tunneling trapping-detrapping process independent of temperature effects occurs in the forbidden band between the Trap-II and the $^4T_1$ (^4F) level inducing corresponding PersL from Cr^{3+}.

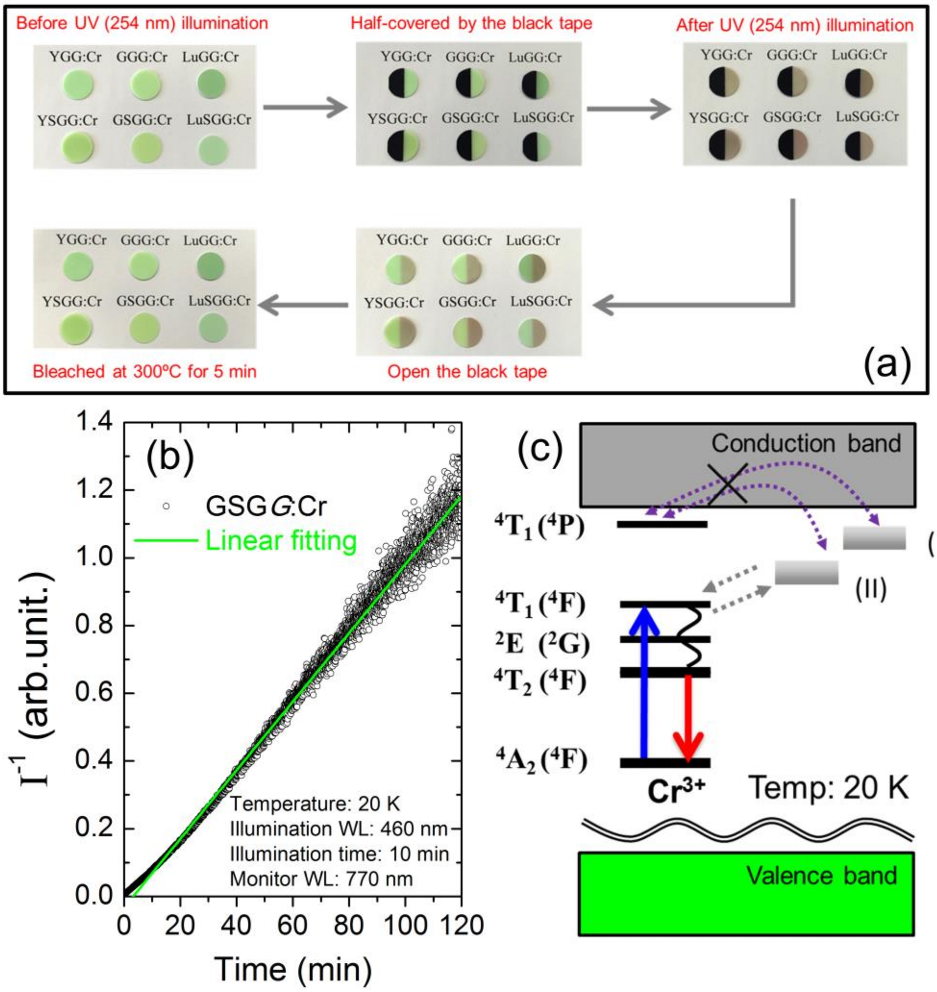

Figure 9.8. (a) Photochromic phenomena in the Cr^{3+} singly-doped garnet ceramic samples (b) low temperature persistent luminescent decay curves of the GSG*G*:Cr ceramic sample monitoring Cr^{3+} emission at 20 K (c) schematic illustration of the trapping and detrapping process in the GSG*G*:Cr ceramic sample under 460 nm excitation.

In order to clarify the charging efficiency of different wavelengths for the GSG*G*:Cr ceramic sample, the PersLE spectrum monitoring Cr^{3+} emission was measured shown in Figure 9.9. As we expected, the main charging wavelength region with high efficiency is located at around 220~300 nm and peaked at around 270 nm. These charging energies are high enough to excite the electrons of Cr^{3+} ions located at *GS* to the $^4T_1$ (^4P) level (very close to the bottom of *CB*) or directly to the *CB* so that the classical trapping-detrapping process through *CB* can smoothly occur. On the other hand, although the charging efficiency is much lower than that of the UV region, the excitation wavelength from near UV (NUV) to visible light is also possible to induce the Cr^{3+} PersL in GSG*G*. Therefore, the trapping-detrapping process under lower energy excitation is mainly due to the mentioned tunneling process between the Trap-II and the $^4T_1$ (^4F) state. Considering the emitting wavelength of commercial LED chips with high efficiency is mainly above 365 nm, the GSG*G*:Cr persistent phosphor is considered to be able to store energies from LED lamps and emit long PersL in the NIR region. It is also worth noting that compared with the ZGO:Cr deep-red persistent phosphor which can be charged by even lower energy (orange/red light) pumping the $^4T_2$ (^4F) state of Cr^{3+},[12,19,20] the charging efficiency using red or even NIR light is almost zero indicating that the tunneling process between the Trap-II and the $^4T_2$ (^4F) state of Cr^{3+} cannot occur in the GSG*G*:Cr persistent phosphor.

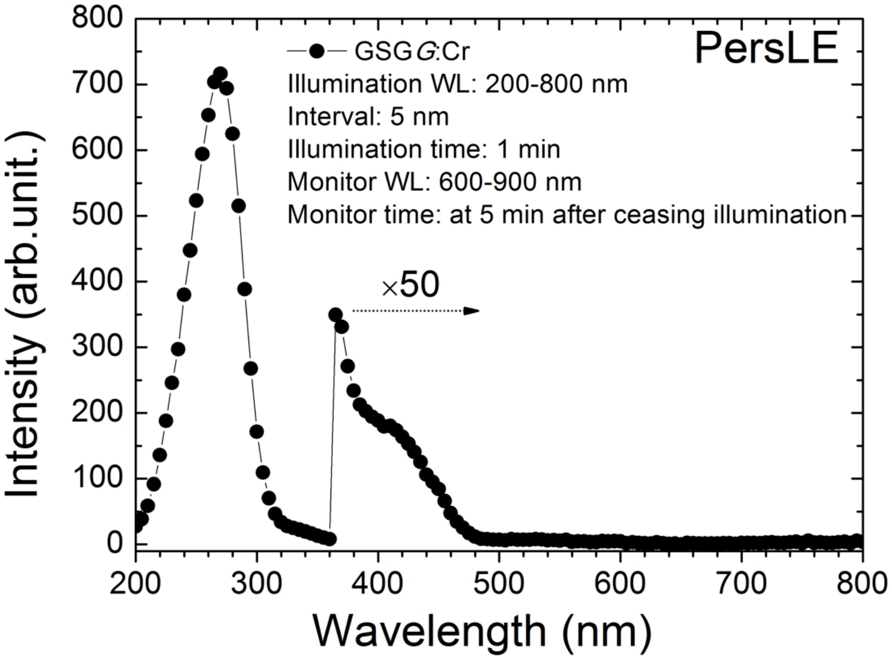

Figure 9.9. PersLE spectrum of the GSG*G*:Cr sample at 5 min after ceasing illumination by monochromatic light for 1 min (intensity ×50 from 365 nm to 800 nm).

9.3.2. Selecting suitable lanthanide ions as efficient electron traps

As mentioned in the introduction part, co-doping strategy using lanthanide ions as additional electron traps is widely used to further enhance the PersL intensity of persistent phosphors.[33,34] The representative example is the well-known SAO:Eu-Dy persistent phosphor, although the Eu^{2+} singly doped SAO phosphor shows weak PersL at *RT*, when co-doped with Dy^{3+} as an additional electron trap, its PersL intensity at 5 min after ceasing the excitation source can be greatly enhanced nearly 30 times.[3] However, considering preparing at least 15 different co-doping samples with different lanthanide ions as a trial and error method for one target material host which is an inefficient approach relying on serendipity, employ theoretical predictions, especially energy level locations of lanthanide ions in the target host is a much more efficient way to select suitable lanthanide ions as additional electron traps. The *HRBE* diagram of 15 lanthanides, proposed by Dorenbos,[26-30] provides a strong predicting power since the characteristic variation in electron and hole trapping depths of lanthanide ions is given by the shape of the two zigzag curves representing the *GS* of divalent and trivalent lanthanide ions.[31-34] Therefore, we again take the GSG*G*:Cr sample as an example to demonstrate how to select suitable lanthanide ions as potential electron traps to sensitize the Cr^{3+} PersL.

Figure 9.10 shows the *HRBE* diagram of the GSG*G* host, the binding energy at the top of *VB* ($E_{\mathrm{V.B}}$) is defined as 0 eV. The exciton creation energy of the GSG*G* host is estimated to be 6.01 eV according to the PLE spectrum monitoring Cr^{3+} emission of the GSG*G*:Cr sample recorded at *RT* (see Figure 9.11), then the energy at the bottom of *CB* ($E_{\mathrm{C.B}}$) can be calculated by the exciton binding energy, which is approximately 108% of the sum value of the exciton creation energy at *RT* plus the correction value (0.15 eV) as a rule of thumb.[30] Therefore, the binding energy at the bottom of *CB* ($E_{\mathrm{C.B}}$) is defined as 6.65 eV [(6.01 eV + 0.15 eV) ×1.08]. Besides, the binding energy of the 4*f* *GS* of Eu^{2+} ($^8S_{7/2}$) relative to $E_{\mathrm{V.B}}$ is estimated to be 4.77 eV according to the charge transfer band (CTB) of Eu^{3+} in the GSG*G*:Eu sample (see Figure 9.12). Since the shapes of the zigzag curves are invariant within several 0.1 eV in the entire family of inorganic compounds, the binding energy of the 4*f* *GS* of all 14 Ln^{2+} ions relative to $E_{\mathrm{V.B}}$ can be estimated and labelled by the red-trigonal zigzag curve.[26,57] Furthermore, the inter 4*f*-electron Coulomb repulsive force of $Eu^{2+/3+}$ [i.e. U(6,A)] in a host is used to evaluate the energy of the 4*f* *GS* of Eu^{3+} and other 13 Ln^{3+} ions relative to $E_{\mathrm{V.B}}$.[27] The value of U(6,A) can be roughly estimated based on an empirical relation between U(6,A) and the centroid shift of Ce^{3+} or Eu^{2+} in a certain host [i.e. $_c$(1,3+,A) or $_c$(7,2+,A)].[58-60] In this paper, we define the value of U(6,A) to be 6.80 eV[52,61] so that the binding energy of the 4*f* *GS* of all 14 Ln^{3+} ions relative to $E_{V.B}$ can be estimated and labelled by the blue-trigonal zigzag curve.

Considering the electron trapping-detrapping process for PersL, the 4*f* *GS* of the Ln^{2+} ion should be located below the bottom of *CB*, in which case the corresponding Ln^{3+} ion is possible to capture one electron from *CB* to be Ln^{2+} or $Ln^{3+}+e^-$ acting as an electron trap. According to the *HRBE* diagram of the GSG*G* host, there are four trivalent lanthanides (Sm^{3+}, Eu^{3+}, Tm^{3+}, Yb^{3+}) whose 2+ *GS* are located below the bottom of *CB* indicating that they can be selected as potential candidates to be an electron trap. Therefore, four GSG*G*:Cr-*Ln* (*Ln*=Sm, Eu, Tm, Yb) garnet ceramic samples were prepared and their feasibility to be sensitizers for enhancing Cr^{3+} PersL are discussed below.

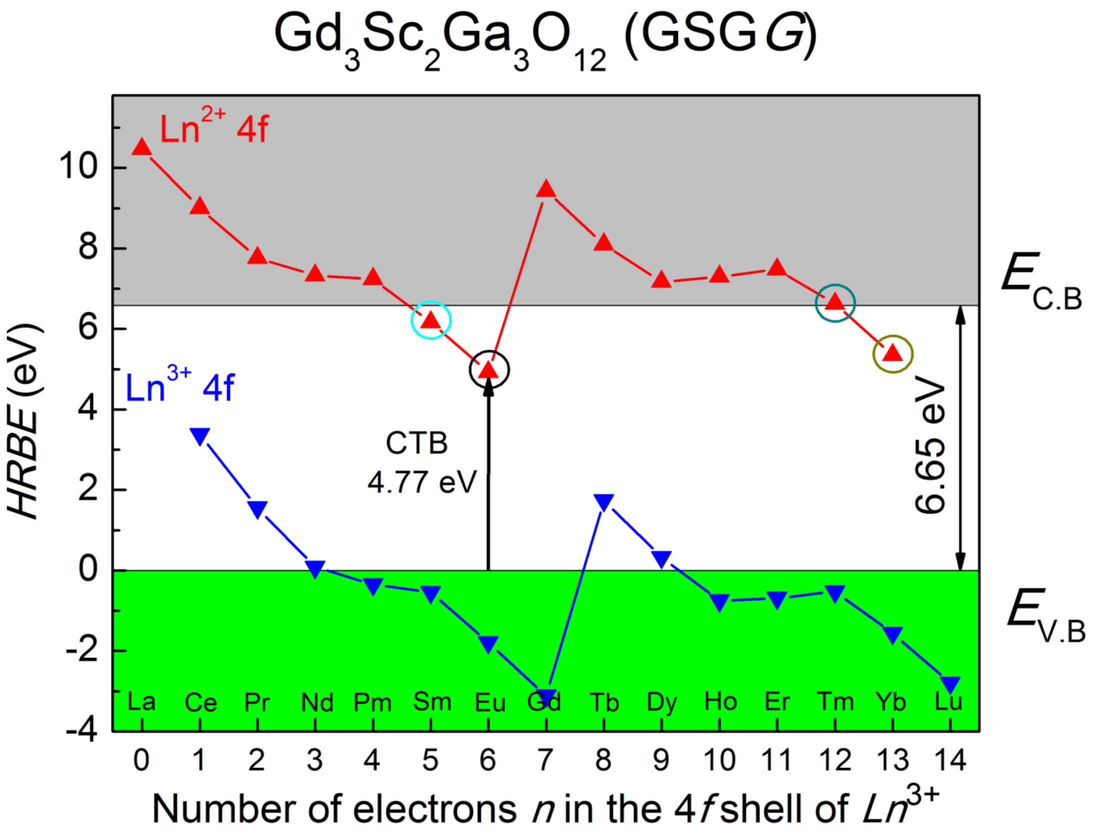

Figure 9.10. The *HRBE* diagram of the GSG*G* host with two zigzag curves representing the ground states of divalent (red-trigonal-line) and trivalent (blue-trigonal-line) lanthanide ions.

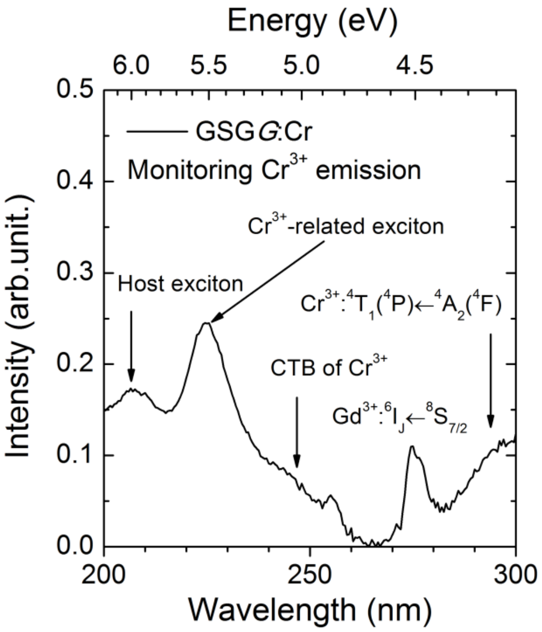

Figure 9.11. Photoluminescence excitation spectrum (PLE) of the GSG*G*:Cr ceramic sample monitoring Cr^{3+} emission (λ_{em}=770 nm)

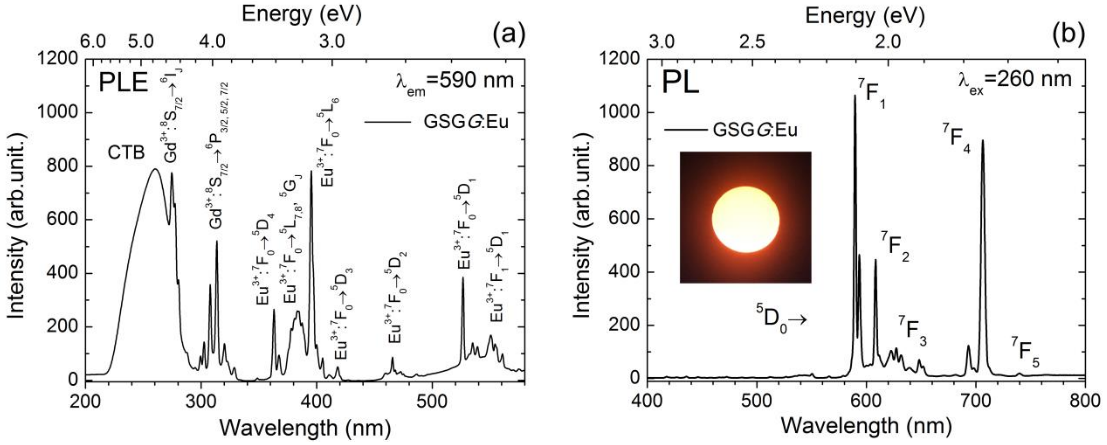

Figure 9.12. (a) PLE (λ_{em}=590 nm) and (b) PL (λ_{ex}=260 nm) of the GSG*G*:Eu ceramic sample (photograph of the GSG*G*:Eu sample under 254 nm illumination inserted)

PL spectra of the GSG*G*:Cr-*Ln* (*Ln*=Sm, Eu, Tm, Yb) garnet ceramic samples under 460 nm excitation at *RT* are given in Figure 9.13(a), in which the PL spectrum of the GSG*G*:Cr sample is also plotted as a reference. All of the spectra mainly show the broad band emission of Cr^{3+} located from 680 to 1050 nm due to the $^4T_2$ (^4F)→$^4A_2$ (^4F) transition. Besides, two *f*-*f* emission bands from Tm^{3+} and Yb^{3+} are also observed in the GSG*G*:Cr-Tm and GSG*G*:Cr-Yb samples, which can be ascribed to the Tm^{3+}: $^3H_4$→$^3H_6$ (peaked at 784 nm) and Yb^{3+}: $^2F_{5/2}$→$^2F_{7/2}$ transitions (peaked at 1025 nm) due to the energy transfer (ET) process from Cr^{3+} to Tm^{3+} and Yb^{3+}, respectively.[62] After ceasing UV illumination for 5 min at *RT*, PersL spectra of all the garnet samples are observed shown in Figure 9.13(b) while the Cr-Eu co-doped sample shows the weakest PersL intensity with lowest SNR compared with that of the other four samples. The spectral shapes of PL and PersL are almost identical in all of the garnet samples indicating that the emission centers are the same under and after excitation.

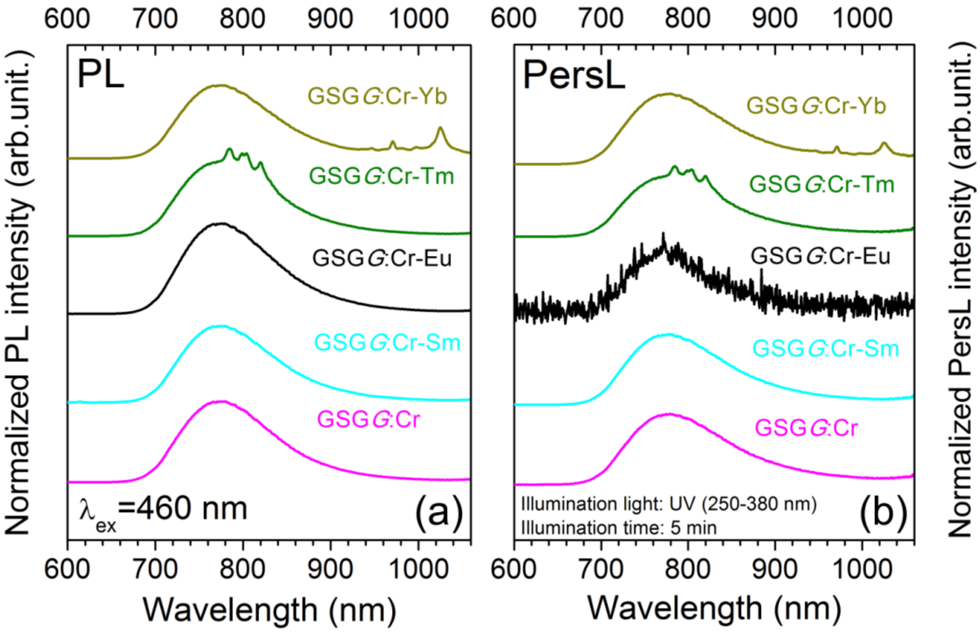

Figure 9.13. (a) PL (λ_{ex}=460 nm) and (b) PersL spectra (at 5 min after ceasing UV illumination for 5 min) of the GSG*G*:Cr and GSG*G*:Cr-*Ln* (*Ln*=Sm, Eu, Tm, Yb) garnet ceramic samples.

Persistent luminescent decay curves of the GSG*G*:Cr-*Ln* (*Ln*=Sm, Eu, Tm, Yb) garnet ceramic samples after ceasing UV illumination for 5 min at *RT* are shown in Figure 9.14(a), in which the decay curve of the GSG*G*:Cr sample is also plotted as a reference (radiances of all the samples at 5 min, 30 min, 60 min after ceasing UV illumination are summarized in Table. 9.4). Among them, the Cr-Sm and Cr-Tm co-doped samples exhibit nearly the same PersL behaviors compared with that of the Cr^{3+} singly doped GSGG sample. On the other hand, the PersL intensity dramatically decreases after Eu^{3+} co-doping while the Cr-Yb co-doped sample exhibits the enhanced PersL intensity, which is also confirmed by the photograph taken by the Si CCD camera at 60 min after ceasing 254 nm illumination shown in Figure 9.14(b).

The emission intensity of the GSG*G*:Cr-Yb sample is much higher than that of the other garnet samples while that of the GSG*G*:Cr-Eu sample is too weak to be captured. Furthermore, after co-doping with Yb^{3+}, the persistent radiance of the GSG*G*:Cr-Yb sample (1.56×10^{-1} mW/Sr/m^2) at 60 min after ceasing the excitation is enhanced to be nearly three times higher than that of the GSG*G*:Cr persistent phosphor (0.54×10^{-1} mW/Sr/m^2).

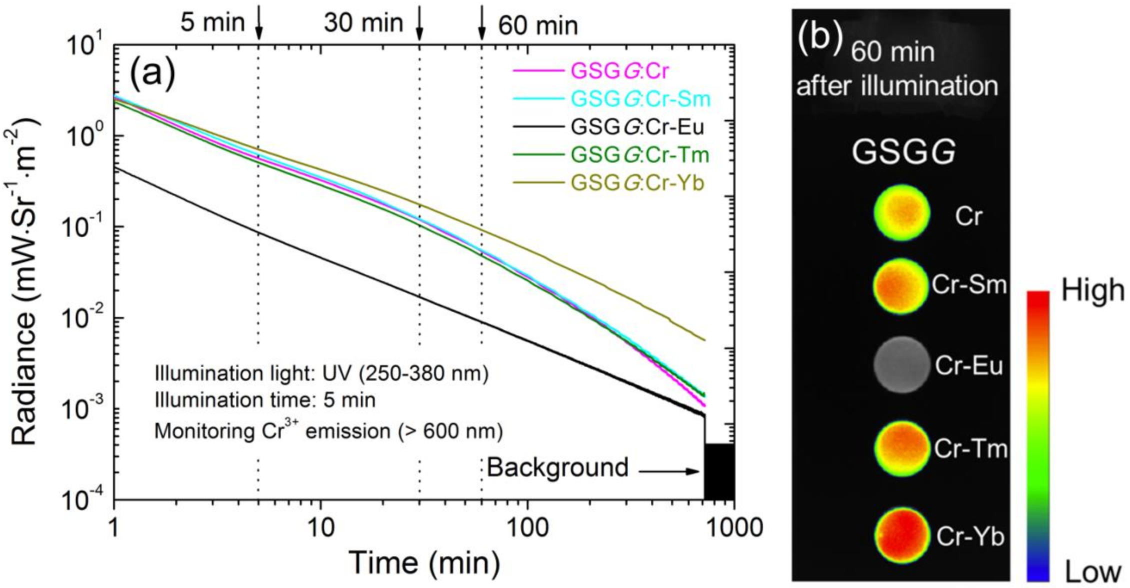

Figure 9.14. (a) Persistent luminescent decay curves of the GSG*G*:Cr and GSG*G*:Cr-*Ln* (*Ln*=Sm, Eu, Tm, Yb) garnet ceramic samples after ceasing UV (250-380 nm) illumination for 5 min (b) photographs taken by the bio-imaging machine using a Si CCD camera at 60 min after ceasing UV (254nm) illumination for 5 min (integrating time: 1.0 s).

Table 9.4. Radiances of the GSG*G*:Cr and GSG*G*:Cr-*Ln* (*Ln*=Sm, Eu, Tm, Yb) garnet ceramic samples after ceasing UV (250-380 nm) illumination for 5 min (in units of mW/Sr/m^2).

Composition	5 min (mW/Sr/m^2)	30 min (mW/Sr/m^2)	60 min (mW/Sr/m^2)
GSG*G*:Cr	**5.63×10^{-1}**	**1.19×10^{-1}**	**0.54×10^{-1}**
GSG*G*:Cr-Sm	**6.17×10^{-1}**	**1.22×10^{-1}**	**0.55×10^{-1}**
GSG*G*:Cr-Eu	**0.86×10^{-1}**	**0.17×10^{-1}**	**0.09×10^{-1}**
GSG*G*:Cr-Tm	**5.08×10^{-1}**	**1.04×10^{-1}**	**0.49×10^{-1}**
GSG*G*:Cr-Yb	**14.68×10^{-1}**	**3.19×10^{-1}**	**1.56×10^{-1}**

Figure 9.15(a) illustrates TL glow curves of the GSG*G*:Cr and GSG*G*:Cr-*Ln* (*Ln*=Sm, Eu, Tm, Yb) garnet ceramic samples. Compared with the GSG*G*:Cr sample,

the TL glow curves nearly remain unchanged after Sm^{3+} and Tm^{3+} co-doping composed of the two glow peaks located at around 240 K and 330 K, which is also confirmed by the 2D mappings of the GSG*G*:Cr, GSG*G*:Cr-Sm and GSG*G*:Cr-Tm samples shown in Figure 9.15(b-c) and (e). The sharp PersL bands due to the Tm^{3+}: $^3H_4 \rightarrow {}^3H_6$ transition in the GSG*G*:Cr-Tm sample is attributed to the persistent ET process from Cr^{3+} to Tm^{3+}, which is similar to the same process as that in the YAG*G*:Cr-Nd persistent phosphor, where it occurs from Cr^{3+} to Nd^{3+}.[32] The similar TL glow curves between the GSG*G*:Cr and the GSG*G*:Cr-Sm/Tm samples suggest that no additional electron traps are introduced after Sm^{3+}/Tm^{3+} co-doping. Considering the energy level locations between the *GS* of Sm^{2+}/Tm^{2+} and the bottom of *CB* according to the *HRBE* diagram of GSG*G* host, also the real energy level of *CB* should not be a straight line but wave function type according to the density functional theory (DFT),[22] we assume that the real *GS* of Sm^{2+}/Tm^{2+} is either located inside the *CB* or below the bottom of *CB* with a very small energy gap (the highest temperature to totally release the captured electrons in Sm/Tm-related electron traps is too low to be recorded in our experimental condition). In both cases, co-doping Sm^{3+} or Tm^{3+} cannot contribute to the enhancement of Cr^{3+} PersL in GSG*G*.

On the other hand, the main TL glow peak of the GSG*G*:Cr-Eu sample shifts to higher temperature peaked at around 485 K compared with that of the GSG*G*:Cr sample, and its intensity is much higher than the two original glow peaks (240 K and 330 K). It indicates that Eu^{3+} acts as an additional electron trap with even deeper trap depth than the Trap-II shown in Figure 9.15(a) and (d). Since the main glow temperature of the GSG*G*:Cr-Eu sample is much higher than *RT*, the essential thermal activation energy to release the captured electrons in the Eu-related trap is much higher than that at *RT*. Therefore, the PersL intensity of the GSG*G*:Cr-Eu sample is much lower than that of the GSG*G*:Cr sample at *RT*.

Unlike the main TL glow peak of the GSG*G*:Cr-Eu sample shifting to higher temperature, the main glow peak located at around 330 K in the GSG*G*:Cr-Yb sample is greatly enhanced and its intensity is much higher than that of the original glow peak located at around 240 K in the GSG*G*:Cr sample as shown in Figure 9.15(a) and (f). It suggests that co-doping Yb^{3+} introduces a new electron trap overlapped with the Trap-II with the similar trap depth and the glow peak located at around 330 K becomes broader. Considering the energy level location of the Eu^{2+} and Yb^{2+} *GS* in the *HRBE* diagram of GSG*G* host, it is quite reasonable that the detrapping temperature for the captured electrons in the Yb-related trap is lower than that in the Eu-related trap. Furthermore, since the enhanced glow peak temperature is very close to *RT* after Yb^{3+} co-doping, the PersL intensity of the GSG*G*:Cr-Yb sample recorded at *RT* is much higher than that of the GSG*G*:Cr sample.

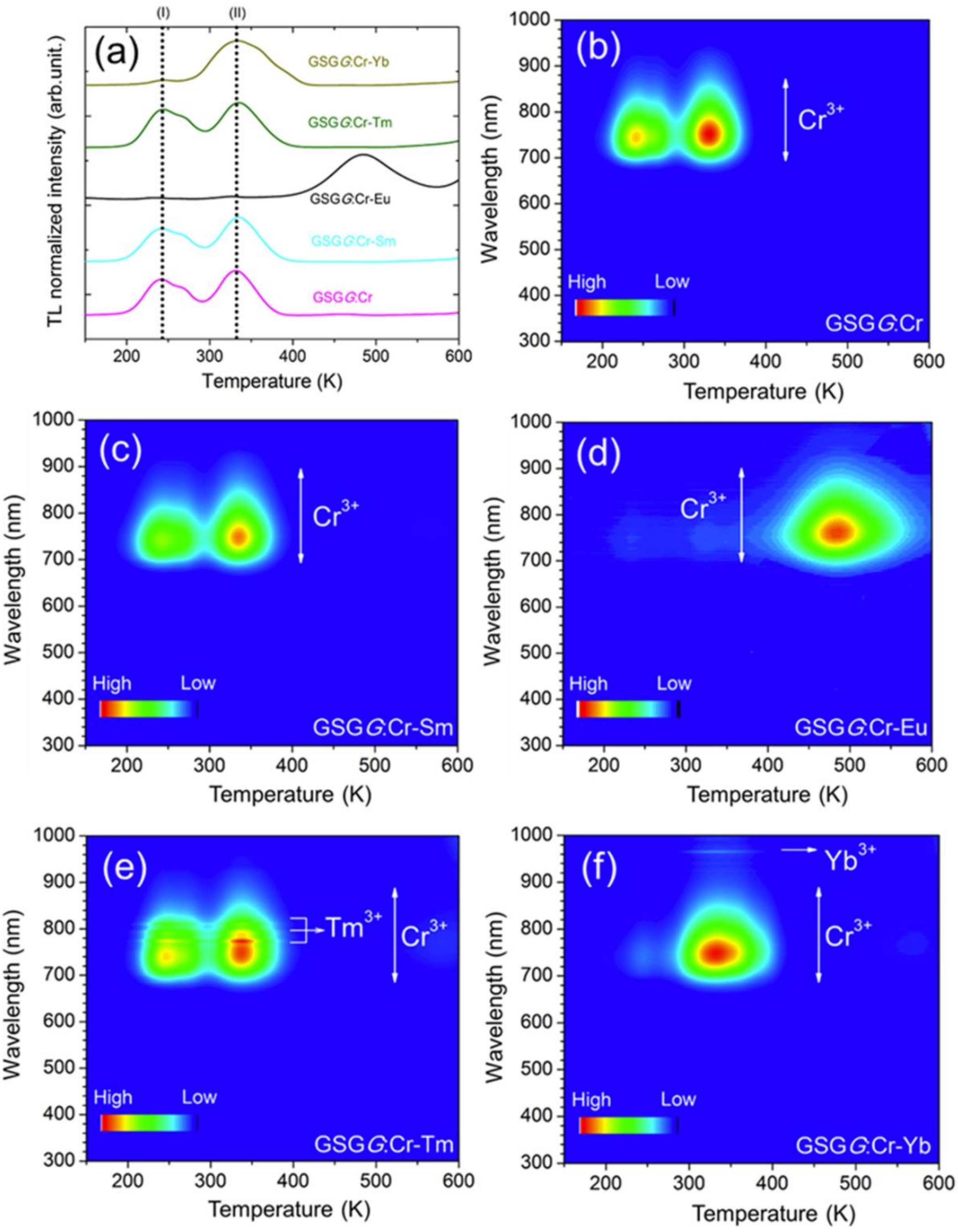

Figure 9.15. (a) TL glow curves of the GSG*G*:Cr and GSG*G*:Cr-*Ln* (*Ln*=Sm, Eu, Tm, Yb) garnet ceramic samples and wavelength-temperature (λ-T) contour plots of the (b) GSG*G*:Cr (c) GSG*G*:Cr-Sm (d) GSG*G*:Cr-Tm (e) GSG*G*:Cr-Eu (f) GSG*G*:Cr-Yb ceramic samples monitoring Cr^{3+} emission.

9.4. Conclusion

In summary, we have successfully developed six different Cr^{3+} singly-doped garnets with cubic structure of $A_3B_2C_3O_{12}$: YG*G*:Cr, GG*G*:Cr, LuG*G*:Cr, YSG*G*:Cr, GSG*G*:Cr and LuSG*G*:Cr, which exhibit PersL due to Cr^{3+} emission matching well with both the response curve of the Si detector and the wavelength region of the NIR-I window. The main emission band of Cr^{3+} in garnet hosts can be easily tunable from the sharp *R*-line emission due to the $^2E\ (^2G)\rightarrow{}^4A_2\ (^4F)$ transition in the strong crystal field strength to the broad band emission due to the $^4T_2\ (^4F)\rightarrow{}^4A_2\ (^4F)$ transition in the weak one when Lu^{3+} in the *A* site and Ga^{3+} in the *B* site are respectively replaced by larger cations, Y^{3+}/Gd^{3+} and Sc^{3+}. Especially the GSG*G*:Cr sample, its *R*-line emission was totally disappeared while only the broad band emission peaked at around 770 nm was observed, and its persistent radiance (0.54×10^{-1} mW/Sr/m^2) at 60 min after ceasing the UV excitation was over three times higher than that of the widely used ZGO:Cr deep-red persistent phosphor (0.15×10^{-1} mW/Sr/m^2) at *RT*. Furthermore, based on the knowledge of 4*f* energy levels of lanthanide ions in the *HRBE* diagram of GSG*G* host, four trivalent lanthanides (Sm^{3+}, Eu^{3+}, Tm^{3+}, Yb^{3+}) whose 2+ *GS* located below the bottom of *CB* were selected as potential candidates to be an electron trap in order to enhance the Cr^{3+} PersL. Among them, Yb^{3+} could introduce a new electron trap with a TL glow peak located around 330 K overlapped with the intrinsic defect (photochromic center)-related electron trap in garnet host, and the persistent radiance of the GSG*G*:Cr-Yb sample (1.56×10^{-1} mW/Sr/m^2) at 60 min after ceasing the UV excitation was enhanced to be nearly three times higher than that of the GSG*G*:Cr persistent phosphor (0.54×10^{-1} mW/Sr/m^2) at *RT*. Since the body temperature of Mammalia (around 310 K) is very close to the main TL glow temperature of the GSG*G*:Cr-Yb sample, *in vivo* bio-imaging in the NIR-I window with deep tissue penetration depth can be expected in the near future by using this material (in the form of nano-particles) as a functionalized bio-probe. Furthermore, Gd^{3+} ion is also widely used as a T1-weighted agent in magnetic resonance imaging (MRI) due to its capability to provide an enhanced positive contrast.[63,64] Therefore, the GSG*G*:Cr-Yb nano-particles also possesses a possibility to be a dual-model medical diagnosis platform featuring both the deep tissue penetration for *in vivo* bio-imaging absence of background noise and the excellent spatial resolution for MRI.

It is also worth noting that, although compared with the trap depth of the Yb^{3+}-related electron trap in the GSG*G* host, that of the Eu^{3+}-related electron trap is too deep to meet the requirement for the detrapping process working at *RT* or the body temperature of Mammalia. As we played in the Cr^{3+} singly-doped GG*G* phosphor,[41] once we lowered the energy level of the bottom of *CB* to decrease the electron trap depth from the *GS* of Eu^{2+}, Eu^{3+} ions also can act as efficient electron traps to greatly enhance the PersL intensity of Cr^{3+} at *RT* in the GG*G*:Cr phosphor.

With this paper, we took different Cr^{3+} doped garnet materials as an example to introduce this facile way to develop red/NIR persistent phosphors using both the crystal field engineering to tune the emission band of Cr^{3+} and the *HRBE* diagram to select suitable lanthanide ions as efficient electron traps to further enhance the Cr^{3+} PersL intensity. Since the crystal field engineering also makes sense in other material hosts (i.e. perovskite) which has different types of cation sites able to be occupied by different cation ions, and lanthanide ions are commonly used as additional trap centers for enhancing PersL, this flexible and efficient material design method can be a useful guidance, in a more general and convenient way to design novel persistent phosphors with high brightness and long duration in different material matrices.

Acknowledgement

I would like to acknowledge Dr. Li Zhao and Prof. Naoki Komatsu from Graduate School of Human and Environmental Studies, Kyoto University for supporting persistent luminescence imaging by the Clairvivo OPT *in vivo* bio-imaging machine.

This work was supported by a Grant-in-Aid for JSPS Fellows (No. 16J09849) and JSPS Grant-in-Aid for Scientific Research on Innovative Areas “Mixed anion” (No. JP16H6441).

References

[1] Yen, W. M.; Weber, M. J. *Inorganic Phosphors: Compositions, Preparation and Optical Properties;* CRC Press, Boca Raton, FL, 2004, pp. 446.

[2] Hölsä, J. Persistent Luminescence Beats the Afterglow: 400 Years of Persistent Luminescence. *Electrochem. Soc. Interface*. **2009**, *18 (4)*, 42−45.

[3] Matsuzawa, T.; Aoki, Y.; Takeuchi, N.; Murayama, Y. A New Long Phosphorescent Phosphor with High Brightness, $SrAl_2O_4$:Eu^{2+}, Dy^{3+}. *J. Electrochem. Soc.* **1996**, *143 (8)*, 2670−2673.

[4] Van den Eeckhout, K.; Smet, P. F.; Poelman, D. Persistent Luminescence in Eu^{2+}-Doped Compounds: A Review. *Materials*. **2010**, *3*, 2536−2566.

[5] Brito, H. F.; Hölsä, J.; Laamanen, T.; Lastusaari, M.; Malkamäki, M.; Rodrigues, L. C. V. Persistent Luminescence Mechanisms: Human Imagination at Work. *Opt. Mater. Express*. **2012**, *2*, 371-381.

[6] Botterman, J.; Smet, P. F. Persistent Phosphor $SrAl_2O_4$:Eu, Dy in Outdoor Conditions: Saved by the Trap Distribution. *Opt. Express*. **2015**, *23*, A868-A881.

[7] Le Masne de Chermont, Q.; Chanéac, C.; Seguin, J.; Pellé, F.; Maitrejean, S.; Jolivet J, P.; Gourier, D.; Bessodes, M.; Scherman, D. Nanoprobes with Near-Infrared Persistent Luminescence for *in vivo* Imaging. *Proc. Natl. Acad. Sci. U.S.A*. **2007**,*104*, 9266-9271.

[8] Van den Eeckhout, K.; Poelman, D.; Smet, P. F. Persistent Luminescence in Non-Eu^{2+}-Doped Compounds: A Review. *Materials*. **2013**, *6*, 2789−2818.

[9] Zhuang, Y.; Katayama, Y.; Ueda, J.; Tanabe, S. A Brief Review on Red to Near-Infrared Persistent Luminescence in Transition-Metal-Activated Phosphors. *Opt. Mater.* **2014**, *36*, 1907-1912.

[10] Singh, S. K. Red and Near Infrared Persistent Luminescence Nano-Probes for Bioimaging and Targeting Applications. *RSC Adv*. **2014**, *4,* 58674-58698.

[11] Li, Y.; Gecevicius, M.; Qiu, J. Long Persistent Phosphors−From Fundamentals to Applications. *Chem. Soc. Rev.* **2016**, *45*, 2090−2136.

[12] Maldiney, T.; Bessière, A.; Seguin, J.; Teston, E.; Sharma, S. K.; Viana, B.; Bos, A. J. J.; Dorenbos, P.; Bessodes, M.; Gourier, D.; Scherman, D.; Richard, C. The *in vivo* Activation of Persistent Nanophosphors for Optical Imaging of Vascularization, Tumours and Grafted Cells. *Nat. Mater.* **2014**, *13*, 418−426.

[13] Liu, F.; Yan, W.; Chuang, Y-J.; Zhen, Z.; Xie, J.; Pan, Z. W. Photostimulated Near-Infrared Persistent Luminescence as A New Optical Read-Out from Cr^{3+}-Doped $LiGa_5O_8$. *Sci. Rep.* **2013**, *3*, 1554-1562.

[14] Viana, B.; Sharma, S. K.; Gourier, D.; Maldiney, T.; Teston, E.; Scherman, D.; Richard, C. Long Term *in vivo* Imaging with Cr^{3+} Doped Spinel Nanoparticles Exhibiting Persistent Luminescence. *J. Lumin*. **2016**, *170*, 879-887.

[15] Smet, P. F.; Viana, B.; Tanabe, S.; Peng, M.; Hölsä, J.; Chen, W. Feature Issue Introduction: Persistent and Photostimulable Phosphors-An Established Research Field with Clear Challenges Ahead. *Opt. Mater. Express*. **2016**, *6(4)*, 1414-1419.

[16] Weissleder, R. A Clearer Vision for *in vivo* Imaging. *Nat. Biotechnol.* **2001**, *19*, 316-317.

[17] Pan, Z. W.; Lu, Y-Y.; Liu, F. Sunlight-Activated Long-Persistent Luminescence in the Near-Infrared from Cr^{3+}-Doped Zinc Gallogermanates. *Nat. Mater.* **2012**, *11*, 58−63.

[18] Allix, M.; Chenu, S.; Véron, E.; Poumeyrol, T.; Kouadri-Boudjelthia, El. A.; Alahraché, S.; Porcher, F.; Massiot, D.; Fayon, F. Considerable Improvement of Long-Persistent Luminescence in Germanium and Tin Substituted $ZnGa_2O_4$. *Chem. Mater*. **2013**, *25*, 1600-1606.

[19] Bessière, A.; Jacquart, S.; Priolkar, K.; Lecointre, A.; Viana, B.; Gourier, D. $ZnGa_2O_4$:Cr^{3+}: A New Red Long-Lasting Phosphor with High Brightness. *Opt. Express*. **2011**, *19*, 10131-10137.

[20] Bessière, A.; Sharma, S. K.; Basavaraju, N.; Priolkar, K. R.; Binet, L.; Viana, B.; Bos, A. J. J.; Maldiney, T.; Richard, C.; Scherman, D.; Gourier, D. Storage of Visible Light for Long-Lasting Phosphorescence in Chromium-Doped Zinc Gallate. *Chem. Mater*. **2014**, *26*, 1365-1373.

[21] Basavaraju, N.; Sharma, S. K.; Bessière, A.; Viana, B.; Gourier, D.; Priolkar, K. R. Red Persistent Luminescence in $MgGa_2O_4$:Cr^{3+}: A New Phosphor for *in vivo* Imaging. *J. Phys. D: Appl. Phys.* **2013**, *46*, 375401 (5 pp).

[22] Xu, Y-N.; Ching, W. Y.; Brickeen, B. K. Electronic structure and bonding in garnet crystals $Gd_3Sc_2Ga_3O_{12}$, $Gd_3Sc_2Al_3O_{12}$, and $Gd_3Ga_3O_{12}$ compared to $Y_3Al_3O_{12}$. *Phys. Rev. B.* **2000**, *61*, 1817-1824.

[23] Örücü, H.; Özen, G.; Bartolo, B. D.; Collins, J. Site-Selective Spectroscopy of Garnet Crystals Doped with Chromium Ions. *J. Phys. Chem. A*. **2012**, *116(35)*, 8815–8826.

[24] Struve, B.; Huber, G. The Effect of the Crystal Field Strength on the Optical Spectra of Cr^{3+} in Gallium Garnet Laser Crystals. *Appl. Phys. B*. **1985**, *36*, 195-201.

[25] Li, Y.; Li, Y.; Chen, R.; Sharafudeen, K.; Zhou, S.; Gecevicius, M.; Wang, H.; Dong, G.; Wu, Y.; Qin, X.; Qiu. J. Tailoring of the Trap Distribution and Crystal Field in Cr^{3+}-Doped Non-Gallate Phosphors with Near-Infrared Long-Persistence Phosphorescence. *NPG Asia Mater.* **2015**, *7*, e108 (11 pp).

[26] Dorenbos, P. Systematic Behaviour in Trivalent Lanthanide Charge Transfer Energies. *J. Phys.: Condens. Matter*. **2003**, *15*, 8417-8434.

[27] Dorenbos, P. The Eu^{3+} Charge Transfer Energy and the Relation with the Band Gap of Compounds. *J. Lumin*. **2005**, *111*, 89-104.

[28] Dorenbos, P. Mechanism of Persistent Luminescence in Eu^{2+} and Dy^{3+} Codoped Aluminate and Silicate Compounds. *J. Electrochem. Soc*. **2005**, *152*, H107-H110.

[29] Dorenbos, P. Electronic Structure Engineering of Lanthanide Activated Materials. *J. Mater. Chem*. **2012**, *22*, 22344-22349.

[30] Dorenbos, P. Electronic Structure and Optical Properties of the Lanthanide Activated $RE_3(Al_{1-x}Ga_x)_5O_{12}$ (RE=Gd, Y, Lu) Garnet Compounds. *J. Lumin*. **2013**, *134*, 310-318.

[31] Luo, H.; Bos, A. J. J.; Dorenbos, P. Controlled Electron-Hole Trapping and Detrapping Process in $GdAlO_3$ by Valence Band Engineering. *J. Phys. Chem. C.*, **2016**, *120*, 5916-5925.

[32] Xu, J.; Ueda, J.; Tanabe, S. Novel Persistent Phosphors of Lanthanide-Chromium Co-Doped Yttrium Aluminum Gallium Garnet: Design Concept with Vacuum Referred Binding Energy Diagram. *J. Mater. Chem. C.* **2016**, *4*, 4380-4386.

[33] Lecointre, A.; Bessière, A.; Bos, A. J. J.; Dorenbos, P.; Viana, B.; Jacquart, S. Designing a Red Persistent Luminescence Phosphor: The Example of YPO_4:Pr^{3+}, Ln^{3+} (Ln=Nd, Er, Ho, Dy). *J. Phys. Chem. C*. **2011**, *115*, 4217-4227.

[34] Luo, H.; Bos, A. J. J.; Dobrowolska, A.; Dorenbos, P. Low-Temperature VUV Photoluminescence and Thermoluminescence of UV Excited Afterglow Phosphor $Sr_3Al_xSi_{1-x}O_5$:Ce^{3+}, Ln^{3+} (Ln=Er, Nd, Sm, Dy and Tm). *Phys. Chem. Chem. Phys.* **2015**, *17*, 15419-15427.

[35] Blasse, G.; Bril, A. A New Phosphor for Flying-spot Cathode-Ray Tubes for Color Television:

Yellow-Emitting $Y_3Al_5O_{12}$-Ce^{3+}. *Appl. Phys. Lett*. **1967**, *11*, 53-54.

[36] Nishiura, S.; Tanabe, S.; Fujioka, K.; Fujimoto, Y. Properties of Transparent Ce:YAG Ceramic Phosphors for White LED. *Opt. Mater.* **2011**, *33*, 688-691.

[37] Kaminskii, A. A. *Crystalline Lasers: Physical Processes and Operating Schemes*; CRC Press, New York, 1996.

[38] Ikesue, A.; Aung, Y. L. Ceramic Laser Materials. *Nat. Photon.* **2008**, *2*, 721-727.

[39] Ueda, J.; Tanabe, S. Visible to Near Infrared Conversion in Ce^{3+}-Yb^{3+} Co-Doped YAG Ceramics. *J. Appl. Phys.* **2009**, *106*, 043101 (5 pp).

[40] Xu, J.; Ueda, J.; Zhuang, Y.; Viana, B.; Tanabe, S. $Y_3Al_{5-x}Ga_xO_{12}$:Cr^{3+}: A Novel Red Persistent Phosphor with High Brightness. *Appl. Phys. Express*. **2015**, *8*, 042602 (4 pp).

[41] Xu, J.; Ueda, J.; Tanabe, S. Design of Deep-Red Persistent Phosphors of $Gd_3Al_{5-x}Ga_xO_{12}$:Cr^{3+} Transparent Ceramics Sensitized by Eu^{3+} as an Electron Trap Using Conduction Band Engineering. *Opt. Mater. Express.* **2015**, *5*, 963−968.

[42] Casalboni, M.; Luci, A.; Grassano, U. M.; Mill, B. V.; Kaminskii, A. A. Optical Spectroscopy of $La_3Ga_5SiO_{14}$:Cr^{3+} Crystals. *Phys. Rev. B*. **1994**, *49*, 3781-3790.

[43] Tanabe, Y.; Sugano, S. On the Absorption Spectra of Complex Ions I. *J. Phys. Soc. Jpn.* **1954**, *9*, 753-766.

[44] Tanabe, Y.; Sugano, S. On the Absorption Spectra of Complex Ions II. *J. Phys. Soc. Jpn.* **1954**, *9*, 766-779.

[45] Seltzer, M. D. Interpretation of the Emission Spectra of Trivalent Chromium-Doped Garnet Crystals Using Tanabe-Sugano Diagrams. *J. Chem. Educ.* **1995**, *72*, 886-888.

[46] Wamsley, P. R.; Bray, K. L. The Effect of Pressure on the Luminescence of Cr^{3+}:YAG. *J. Lumin.* **1994**, *59*, 11-17.

[47] Gourier, D.; Bessière, A.; Sharma, S. K.; Binet, L.; Viana, B.; Basavaraju, N.; Priolkar, K. R. Origin of the Vsible Light Induced Persistent Luminescence of Cr^{3+}-Doped Zinc Gallate. *J. Phys Chem. Solids*. **2014**, 75, 826-837.

[48] Vos, A. D.; Lejaeghere, K.; Vanpoucke, D. E. P.; Joos, J. J.; Smet, P. F.; Hemelsoet, K. First-Principles Study of Antisite Defect Configurations in $ZnGa_2O_4$:Cr Persistent Phosphors. *Inorg. Chem.* **2016**, *55*, 2402-2412.

[49] Zhuang, Y.; Ueda, J.; Tanabe, S. Enhancement of Red Persistent Luminescence in Cr^{3+}-Doped

$ZnGa_2O_4$ Phosphors by Bi_2O_3 Codoping. *Appl. Phys. Express*. **2013**, *6*, 052602 (4 pp).

[50] Katayama, Y.; Viana, B.; Gourier, D.; Xu, J.; Tanabe, S. Photostimulation Induced Persistent Luminescence in $Y_3Al_2Ga_3O_{12}$:Cr^{3+}. *Opt. Mater. Express*. **2016**, *6*, 1405-1413.

[51] Ueda, J.; Kuroishi, K.; Tanabe, S. Bright Persistent Ceramic Phosphors of Ce^{3+}-Cr^{3+}-Codoped Garnet Able to Store by Blue Light. *Appl. Phys. Lett*. **2014**, *104*, 101904 (5 pp).

[52] Ueda, J.; Dorenbos, P.; Bos, A. J. J.; Kuroishi, K.; Tanabe, S. Control of Electron Transfer Between Ce^{3+} and Cr^{3+} in the $Y_3Al_{5-x}Ga_xO_{12}$ Host *via* Conduction Band Engineering. *J. Mater. Chem. C*. **2015**, *3*, 5642-5651.

[53] Liang, Y-J.; Liu, F.; Chen, Y-F.; Wang, X-J.; Sun, K-N.; Pan, Z. W. New Function of the Yb^{3+} Ion As An Efficient Emitter of Persistent Luminescence in the Short-Wave Infrared. *Light-Sci. Appl.* **2016**, *5*, e16124 (6 pp).

[54] Avouris, P.; Morgan, T. N. A Tunneling Model for the Decay of Luminescence in Inorganic Phosphor: the Case of Zn_2SiO_4:Mn. *J. Chem. Phys.* **1981**, *74*, 4347–4355.

[55] Dobrowolska, A.; Bos, A. J. J.; Dorenbos, P. Electron Tunnelling Phenomena in YPO_4:Ce,Ln (Ln = Er, Ho, Nd, Dy). *J. Phys. D: Appl. Phys.* **2014**, *47*, 335301 (10 pp).

[56] Wang, B.; Lin, H.; Xu, J.; Chen, H.; Lin, Z.; Huang, F.; Wang, Y. Design, Preparation, and Characterization of a Novel Red Long-Persistent Perovskite Phosphor: $Ca_3Ti_2O_7$:Pr^{3+}. *Inorg. Chem.* **2015**, *54*, 11299-11306.

[57] Dorenbos, P. Determining Binding Energies of Valence-Band Electrons in insulators and Semiconductors *via* Lanthanide Spectroscopy. *Phys. Rev. B*. **2013**, *87*, 035118 (8 pp).

[58] Dorenbos, P. Relating the Energy of the [Xe]$5d^1$ Configuration of Ce^{3+} in Inorganic Compounds with Anion Polarizability and Cation Electronegativity. *Phys. Rev. B*. **2002**, *65*, 235110 (6 pp).

[59] Dorenbos, P. Relation between Eu^{2+} and Ce^{3+} f↔d-Transition Energies in Inorganic Compounds. *J. Phys.: Condens. Matter*. **2003**, *15*, 4797-4808.

[60] Dorenbos, P. Modeling the Chemical Shift of Lanthanide 4*f* Electron Binding Energies. *Phys. Rev. B*. **2012**, *85*, 165107 (10 pp).

[61] Dorenbos, P. Ce^{3+} 5d-Centroid Shift and Vacuum Referred 4f-Electron Binding Energies of All Lanthanide Impurities in 150 Different Compounds. *J. Lumin*. **2013**, *135*, 93-104.

[62] Chen, D. Q.; Chen, Y.; Lu, H.; Ji, Z. A Bifunctional Cr/Yb/Tm:$Ca_3Ga_2Ge_3O_{12}$ Phosphor with Near-Infrared Long-Lasting Phosphorescence and Upconversion Luminescence. *Inorg. Chem.*

2014, *53*, 8638–8645.

[63] Burnett, K. R.; Wolf, G. L.; Shumacher Jr, H. R.; Goldstein, E. J. Gadolinium Oxide A Protoype Agent for Contrast Enhanced Imaging of the Liver and Spleen with Magnetic Resonance. *Magn. Reson. Imaging*. **1985**, *3*, 65-71.

[64] Na, H. B.; Song, I. C.; Hyeon, T. Inorganic Nanoparticles for MRI Contrast Agents. *Adv. Mater.* **2009**, *21*, 2133-2148.

Figure Captions

Summary

In Chapter 1, we start from two applications of persistent phosphors (i) safety signage/night vision applications in the visible light region; (ii) *in vivo* bio-imaging applications in the NIR region. Brief histories, important progresses, some existing problems, and personal perspectives are introduced. As described in this part, although persistent luminescence was observed and firstly recorded in China nearly 1000 years ago, the progress on the understanding of this mysterious “self-sustained” luminescence phenomenon and the development of new persistent phosphors with high brightness and long duration is rather slow. Until 1993, T. Matsuzawa et al from Nemoto & Co., Ltd. (Japan) dropped a bomb to this “unpopular” research field because of the discovery of the super long green persistent phosphor, $SrAl_2O_4$:Eu^{2+}-Dy^{3+}. Since then, this “unpopular” research field becomes more and more “popular”, great efforts have been made on either understanding the mechanism of persistent luminescence or developing novel persistent phosphors with different emitting colors. As a result, numerous persistent phosphors emitting long persistent luminescence in the visible light region have been successfully developed, and some of them have been commercialized for watch dials, toys, and safety signage, *etc* that are now commonly used in our daily lives. On the other hand, in 2007, Q. le Masne de Chermont et al from France gave anthor shockwave to this research field since they demonstrated that NIR persistent phosphors can be used as a new generation bio-probes for *in vivo* bio-imaging with high signal-to-noise ratio. The merits of such kind of NIR perssistent luminescence nano-particles (PLNPs) like excitation-free, non-auto-fluorescence, long monitoring time, deep penetration for living bodies, *etc* describe a bright and pormising future for the *in vivo* bio-imaging, and thus motive the fast development of NIR persistent phosphors, especially in the recent 3-4 years

In Chapter 2, basic knowledge on luminescence is summarized. Starting from the *f-f* and *f-d* transitions from lanthanide ions, and *d-d* transitions from transition metal ions (emphasized on Cr^{3+}). The progress playing an important role in the dynamics of persistent luminescence, the electron trapping-detrapping process, is discussed.

Finally, as the only disscussed crystal structure in this dissertation, garnet structure in the form of $A_3B_2C_3O_{12}$ is briefly introduced, its flexible structure for either doping with rare-earth ions in the *A* site or transition metal ions in the *B*, *C* sites acts as fundamentals in my research life.

In Chapter 3, blue-light-chargeable $Y_3Al_2Ga_3O_{12}$ (YAG*G*):Ce^{3+}-Cr^{3+} green transparent ceramic persistent phosphors with different thicknesses were fabricated by solid state reaction and vacuum sintering method. Compared with an opaque YAG*G*:Ce^{3+}-Cr^{3+} ceramic phosphor of the same composition, the corresponding transparent ceramic phosphors exhibited brighter persistent luminescence after ceasing blue light excitation (460 nm) due to a typical “volume effect” of transparent materials. Because in the transparent ceramic phosphors, not only the surface but also the interior of the sample can be excited under illumination owing to their lower optical scattering coefficient than that of powder or conventional opaque pellets. In powder and opaque samples, only the surface part can efficiently be excited due to the strong scattering of the excitation light. For a transparent ceramic persistent phosphor, the persistent luminance can be increased with increasing sample thickness. The duration that the persistent luminescence intensity reaches 2 mcd/m^2 of the YAG*G*:Ce^{3+}-Cr^{3+} transparent ceramic (846 min) with 2.8 mm thickness was nearly twice of that of the compacted pellet made of the most widely used $SrAl_2O_4$:Eu^{2+}-Dy^{3+} commercial powder (433 min). Such novel transparent ceramic phosphors showing both high transparency and persistent luminescence possess great potentials for the future persistent illumination applications under w-LED illumination containing blue light source.

In Chapter 4, based on the vacuum referred binding energy (*VRBE*) diagram of the $Y_3Al_2Ga_3O_{12}$ (YAG*G*) host, Pr^{3+}, Nd^{3+}, Tb^{3+}, Dy^{3+} ions were selected and co-doped with Cr^{3+} ions to develop novel persistent phosphors. Since the energy gaps between the ground states of Pr^{3+}/Tb^{3+} and the top of valence band (*VB*) are large enough so that Pr^{3+}/Tb^{3+} ions can be stable hole traps, collaborating with Cr^{3+} electron traps to induce the long persistent luminescence. The persistent luminance duration upon 0.32 mcd/m^2 of the YAG*G*:Pr-Cr and YAG*G*:Tb-Cr samples due to Pr^{3+} (orange) and Tb^{3+} (light green) emission could reach about 8 h and 12 h, respectively. However, because of the small energy gaps between the ground states of Nd^{3+}/Dy^{3+} and the top of *VB*, Nd^{3+}/Dy^{3+} ions cannot act as stable hole traps. Therefore, the persistent luminescent intensities of YAG*G*:Nd-Cr and YAG*G*:Dy-Cr samples are quite weak and dominated mainly by the deep-red transition of Cr^{3+}. With this paper, we introduced a way to design novel garnet persistent phosphors from the knowledge of energy levels of lanthanide dopants. Since lanthanide ions are widely used as emission centers and/or trap centers for persistent luminescence, this theoretical prediction diagram can be a useful guidance for choosing proper lanthanide ions, in a more general and convenient manner to design new storage phosphors in different matrices.

In Chapter 5, a novel red ceramic phosphor: $Y_3Al_{5-x}Ga_xO_{12}$:Cr^{3+} (YAG*G*:Cr^{3+}, x from 0 to 5), showing bright persistent luminescence was developed by conventional solid-state reaction method. After ceasing UV illumination, the radiance of this material was nearly 5 times higher than that of the commonly used $ZnGa_2O_4$:Cr^{3+} red persistent phosphor. This behavior was mainly attributed to the efficient electron trapping and detrapping processes and one could adjust electron trap depth through different Ga^{3+} contents. Since garnet materials have been widely used for various applications, such novel red persistent phosphors are considered to possess a great potential for an improved *in vivo* bio-imaging application. Practical applications with better signal-to-noise ratio (SNR) in the *in vivo* bio-imaging field can be expected in the near future by using YAG*G*:Cr^{3+} garnet nano-particles with bright red persistent luminescence.

In Chapter 6, we developed bright deep-red persistent phosphors of Cr^{3+}-Eu^{3+} co-doped $Gd_3Al_{5-x}Ga_xO_{12}$ garnets (GAG*G*:Cr^{3+}-Eu^{3+}), in which only Cr^{3+} ion shows emission bands centered at 730 nm after ceasing UV illumination and Eu^{3+} ion acts as an excellent electron trap capturing one electron to be Eu^{2+} with tunable trap depth by varying conduction band with Ga^{3+} content, x. The persistent radiance of the GG*G*:Cr^{3+}-Eu^{3+} (x=5) sample at 1 h after ceasing UV light is approximately 25 times higher than that of the Cr^{3+} singly doped GG*G* sample, and is over 6 times higher than that of the widely used $ZnGa_2O_4$:Cr^{3+} red persistent phosphor. Practical applications in the *in vivo* bio-imaging field can be expected in the near future by using GG*G*:Cr^{3+}-Eu^{3+} nano-particles as optical probes.

In Chapter 7, we developed a persistent phosphor of $Y_3Al_2Ga_3O_{12}$ doped with Nd^{3+}, Ce^{3+}, Cr^{3+} ions (YAG*G*:Nd-Ce-Cr) exhibiting long (>10 h) persistent luminescence at multi-wavelengths of around 880, 1064, and 1335 nm due to *f-f* transitions of Nd^{3+} and at 505 nm due to the Ce^{3+}:$5d_1 \rightarrow 4f$ transition. The intense near-infrared (NIR) persistent luminescence bands from Nd^{3+} match well with the first (650~950 nm) and second (1000~1350 nm) bio-imaging windows. The NIR persistent radiance of the YAG*G*:Nd-Ce-Cr phosphor (0.33×10^{-1} mW/Sr/m^2) at 60 min after ceasing blue light illumination was over 2 times higher than that of the widely used $ZnGa_2O_4$:Cr^{3+} red persistent phosphor (0.15×10^{-1} mW/Sr/m^2). Multi-functional applications not only in the *in vivo* bio-imaging but also in the drug delivery and cancerous chemotherapy can be expected in the near future by using this material as a nano-sized bio-probe with surface modification connected with functional organic radical groups.

In Chapter 8, by utilizing efficient persistent energy transfer from Ce^{3+} to Er^{3+}, we have successfully developed a novel garnet persistent phosphor of $Y_3Al_2Ga_3O_{12}$ doped with Er^{3+}, Ce^{3+}, Cr^{3+} ions (YAG*G*:Er-Ce-Cr) exhibiting long (>10 h) near-infrared (NIR) persistent luminescence (PersL) in the broad range from 1450 nm to 1670 nm due to the typical Er^{3+}:${}^4I_{13/2} \rightarrow {}^4I_{15/2}$ transition in garnet. The NIR PersL bands of Er^{3+} match well with the third bio-imaging window (NIR-III, approximately from 1500 nm to 1800 nm) and the response curve of InGaAs detectors. The photon emission rate (8.33×10^{17} cps/Sr/m^2) of the YAG*G*:Er-Ce-Cr persistent phosphor at 10 min after ceasing blue light illumination was over two times higher than that of the widely used $ZnGa_2O_4$:Cr^{3+} deep-red persistent phosphor (3.30×10^{17} cps/Sr/m^2). We also show the first PersL imaging by a commercial InGaAs camera monitoring Er^{3+} emission indicating that this material can be a promising candidate for *in-vivo* bio-imaging in the NIR-III window.

In Chapter 9, we have successfully developed six different Cr^{3+} singly-doped garnets with cubic structure of $A_3B_2C_3O_{12}$: $Y_3Ga_{4.99}Cr_{0.01}O_{12}$ (YG*G*:Cr),

$Gd_3Ga_{4.99}Cr_{0.01}O_{12}$ (GG*G*:Cr), $Lu_3Ga_{4.99}Cr_{0.01}O_{12}$ (LuG*G*:Cr), $Y_3Sc_{1.99}Cr_{0.01}Ga_3O_{12}$ (YSG*G*:Cr), $Gd_3Sc_{1.99}Cr_{0.01}Ga_3O_{12}$ (GSG*G*:Cr) and $Lu_3Sc_{1.99}Cr_{0.01}Ga_3O_{12}$ (LuSG*G*:Cr), which exhibit persistent luminescence due to Cr^{3+} emission matching well with both the response curve of the Si detector and the wavelength region of the first biological window (NIR-I). The main emission band of Cr^{3+} in garnet hosts can be easily tunable from the sharp *R*-line emission due to the ^2E (^2G)→$^4A_2$ (^4F) transition in the strong crystal field strength to the broad band emission due to the $^4T_2$ (^4F)→$^4A_2$ (^4F) transition in the weak one when Lu^{3+} in the *A* site and Ga^{3+} in the *B* site are respectively replaced by larger cations, Y^{3+}/Gd^{3+} and Sc^{3+}. Especially the GSG*G*:Cr sample, its *R*-line emission was totally disappeared while only the broad band emission peaked at around 770 nm was observed, and its persistent radiance (0.54×10^{-1} mW/Sr/m^2) at 60 min after ceasing the UV excitation was over three times higher than that of the widely used ZGO:Cr deep-red persistent phosphor (0.15×10^{-1} mW/Sr/m^2) at *RT*. Furthermore, based on the knowledge of 4*f* energy levels of lanthanide ions in the host referred binding energy (*HRBE*) diagram of GSG*G* host, four trivalent lanthanides (Sm^{3+}, Eu^{3+}, Tm^{3+}, Yb^{3+}) whose 2+ *GS* located below the bottom of *CB* were selected as potential candidates to be an electron trap in order to enhance the Cr^{3+} PersL. Among them, Yb^{3+} could introduce a new electron trap with a TL glow peak located around 330 K overlapped with the intrinsic defect (photochromic center)-related electron trap in garnet host, and the persistent radiance of the GSG*G*:Cr-Yb sample (1.56×10^{-1} mW/Sr/m^2) at 60 min after ceasing the UV excitation was enhanced to be nearly three times higher than that of the GSG*G*:Cr persistent phosphor (0.54×10^{-1} mW/Sr/m^2) at *RT*. Since the body temperature of Mammalia (around 310 K) is very close to the main TL glow temperature of the GSG*G*:Cr-Yb sample, *in vivo* bio-imaging in the NIR-I window with deep tissue penetration depth can be expected in the near future by using this material (in the form of nano-particles) as a functionalized bio-probe. Furthermore, Gd^{3+} ion is also widely used as a T1-weighted agent in magnetic resonance imaging (MRI) due to its capability to provide an enhanced positive contrast. Therefore, the GSG*G*:Cr-Yb nano-particles also possesses a possibility to be a dual-model medical diagnosis platform featuring both the deep tissue penetration for *in vivo* bio-imaging absence of background noise and the excellent spatial resolution for MRI.

List of Publications

Chapter 3

Jian Xu, Jumpei Ueda, Keisuke Kuroishi, Setsuhisa Tanabe, [Fabrication of Ce^{3+}-Cr^{3+} co-doped yttrium aluminium gallium garnet transparent ceramic phosphors with super long persistent luminescence], 『***Scripta Materialia***』, Vol. 102, pp 47-50, (2015)

Chapter 4

Jian Xu, Jumpei Ueda, Setsuhisa Tanabe, [Novel persistent phosphors of lanthanide-chromium co-doped yttrium aluminum gallium garnet: design concept with vacuum referred binding energy diagram], 『***Journal of Materials Chemistry C***』, Vol. 4, pp 4380-4386, (2016)

Chapter 5

Jian Xu, Jumpei Ueda, Yixi Zhuang, Bruno Viana, Setsuhisa Tanabe, [$Y_3Al_{5-x}Ga_xO_{12}$: a novel red persistent phosphor with high brightness], 『***Applied Physics Express***』, Vol. 8(4), pp 042602 (4p), (2015)

Chapter 6

Jian Xu, Jumpei Ueda, Setsuhisa Tanabe, [Design of deep-red persistent phosphors of $Gd_3Al_{5-x}Ga_xO_{12}:Cr^{3+}$ transparent ceramics sensitized by Eu^{3+} as an electron trap using conduction band engineering], 『***Optical Materials Express***』, Vol. 5(5), pp 963-968, (2015)

Chapter 7

Jian Xu, Setsuhisa Tanabe, Atul D. Sontakke, Jumpei Ueda [Near-infrared multi-wavelengths long persistent luminescence of Nd^{3+} ion through persistent energy transfer in Ce^{3+}, Cr^{3+} co-doped $Y_3Al_2Ga_3O_{12}$ for the first and second bio-imaging windows], 『***Applied Physics Letters***』, Vol. 107, pp 081903 (4p), (2015)

Chapter 8

Jian Xu, Daisuke Murata, Jumpei Ueda, Setsuhisa Tanabe, [Near-infrared long persistent luminescence of Er^{3+} in garnet for the third bio-imaging window], 『***Journal of Materials Chemistry C***』, Vol. 4, pp 11096-11103 (2016)

Achievements

International Academic Journal

2015

1. **<u>Jian Xu</u>**, Jumpei Ueda, Keisuke Kuroishi, Setsuhisa Tanabe, [Fabrication of Ce^{3+}-Cr^{3+} co-doped yttrium aluminium gallium garnet transparent ceramic phosphors with super long persistent luminescence], 『***Scripta Materialia***』, Vol. 102, pp 47-50, (2015)
2. **<u>Jian Xu</u>**, Jumpei Ueda, Yixi Zhuang, Bruno Viana, Setsuhisa Tanabe, [$Y_3Al_{5-x}Ga_xO_{12}$: a novel red persistent phosphor with high brightness], 『***Applied Physics Express***』, Vol. 8(4), pp 042602 (4p), (2015)
3. **<u>Jian Xu</u>**, Jumpei Ueda, Setsuhisa Tanabe, [Design of deep-red persistent phosphors of $Gd_3Al_{5-x}Ga_xO_{12}$:Cr^{3+} transparent ceramics sensitized by Eu^{3+} as an electron trap using conduction band engineering], 『***Optical Materials Express***』, Vol. 5(5), pp 963-968, (2015)
4. **<u>Jian Xu</u>**, Setsuhisa Tanabe, Atul D. Sontakke, Jumpei Ueda [Near-infrared multi-wavelengths long persistent luminescence of Nd^{3+} ion through persistent energy transfer in Ce^{3+}, Cr^{3+} co-doped $Y_3Al_2Ga_3O_{12}$ for the first and second bio-imaging windows], 『***Applied Physics Letters***』, Vol. 107, pp 081903 (4p), (2015)

2016

5. **<u>Jian Xu</u>**, Jumpei Ueda, Setsuhisa Tanabe, [Novel persistent phosphors of lanthanide-chromium co-doped yttrium aluminum gallium garnet: design concept with vacuum referred binding energy diagram], 『***Journal of Materials Chemistry C***』, Vol. 4, pp 4380-4386, (2016)
6. **<u>Jian Xu</u>**, Daisuke Murata, Jumpei Ueda, Setsuhisa Tanabe, [Near-infrared long persistent luminescence of Er^{3+} in garnet for the third bio-imaging window], 『***Journal of Materials Chemistry C***』, Vol. 4, pp 11096-11103 (2016)
7. Masaki Mori, **<u>Jian Xu</u>**, Go Okada, Takayuki Yanagida, Jumpei Ueda, Setsuhisa Tanabe, [Comparative study of optical and scintillation properties of Ce:YAGG, Ce:GAGG and Ce:LuAGG transparent ceramics], 『***Journal of the Ceramic Society of Japan***』, Vol. 124(5), pp 569-573, (2016)
8. Masaki Mori, **<u>Jian Xu</u>**, Go Okada, Takayuki Yanagida, Jumpei Ueda, Setsuhisa Tanabe, [Scintillation and optical properties of Ce-doped YAGG transparent ceramics], 『***Journal of Rare Earths***』, Vol. 34(8), pp 763-767, (2016)
9. Lingcong Fan, **<u>Jian Xu</u>**, Ying Shi, Jianjun Xie, Fang Lei, Lei Zhang, [Effects of hydroxy propyl cellulose (HPC) surfactant on fabrication, microstructure and optical properties of Ce^{3+}:$Lu_3Al_5O_{12}$ (Ce:LuAG) transparent ceramics], 『***Advanced Powder Technology***』, Vol. 27, pp 610-617, (2016)
10. Atul D.Sontakke, Jumpei Ueda, **<u>Jian Xu</u>**, Kazuki Asami, Misaki Katayama, Yasuhiro Inada, Setsuhisa Tanabe, [A comparison on Ce^{3+} luminescence in borate glass and YAG ceramic: understanding the role of host's characteristics], 『***The Journal of Physical Chemistry C***』, Vol. 120(31), pp 17683-17691, (2016)
11. Yumiko Katayama, Bruno Viana, Didier Gourier, **<u>Jian Xu</u>**, Setsuhisa Tanabe, [Photostimulation induced persistent luminescence in $Y_3Al_2Ga_3O_{12}$:Cr^{3+}], 『***Optical Materials Express***』, Vol. 6(4), pp 1405-1413, (2016)

12. Yixi Zhuang, Ying Lv, Ye Li, Tianliang Zhou, **Jian Xu**, Jumpei Ueda, Setsuhisa Tanabe, Rong-Jun Xie, [Study on trap levels in $SrSi_2AlO_2N_3:Eu^{2+}$, Ln^{3+} persistent phosphors based on host-referred binding energy scheme and thermoluminescence analysis], 『***Inorganic Chemistry***』, Vol. 55(22), pp 11890-11897, (2016).

2017

13. Yumiko Katayama, Atsunori Hashimoto, **Jian Xu**, Jumpei Ueda, Setsuhisa Tanabe, [Thermoluminescence investigation on $Y_3Al_{5-x}Ga_xO_{12}:Ce^{3+}$-$Bi^{3+}$ green persistent phosphors], 『***Journal of Luminescence***』, Vol. 183, pp 355-359, (2017)

Presentation (International Conference)

2015

1. **(Invited Oral) Jian Xu**, Jumpei Ueda, Setsuhisa Tanabe, [Fabrication and luminescent properties of transparent ceramic persistent phosphors with garnet structure for white LED], 『***The 3rd International Workshop on Persistent and Photostimulable Phosphors***』, No. S-24, Texas, USA, (Nov. 9-13, 2015)
2. **(Oral) Jian Xu**, Jumpei Ueda, Setsuhisa Tanabe, [Fabrication of polycrystalline garnet persistent phosphors with super long persistent luminescence], 『***11th Laser Ceramics Symposium International Symposium on Transparent Ceramics for Photonic Applications***』, No. Th-O-5, Xu'Zhou, China, (Nov. 30-Dec. 4, 2015)
3. **(Poster) Jian Xu**, Jumpei Ueda, Setsuhisa Tanabe, [Fabrication of polycrystalline garnet persistent phosphors with super long persistent luminescence], 『***The 2nd International Workshop on Luminescent Materials 2015 (LumiMat'15)***』, No. P-7, Kyoto, Japan, (Dec. 12-13, 2015)

2016

4. **(Oral) Jian Xu**, Jumpei Ueda, Setsuhisa Tanabe, [Design of novel garnet persistent phosphors with red/NIR persistent luminescence for the first bio-imaging window based on Tanabe-Sugano (d^3) and host referred binding energy (HRBE) diagrams], 『***The International Conference on Rare Earths***』, No. C09-18, Sapporo, Japan, (Jun. 5-10, 2016)
5. **(Oral) Jian Xu**, Jumpei Ueda, Setsuhisa Tanabe, [Near-infrared long persistent luminescence of Er^{3+} in garnet for the third bio-imaging window], 『***Phosphor Safari 2016 Hong Kong-Hong Kong International Symposium on Luminescence, Spectroscopy and Applications***』, No. S-15, Hong Kong, China, (Nov. 28-Dec. 1, 2016)

Presentation (Domestic Conference in Japan)

2014

1. **(Oral) Jian Xu**, Keisuke Kuroishi, Jumpei Ueda, Setsuhisa Tanabe, [Fabrication and luminescent properties of persistent transparent ceramic phosphors for white light-emitting diode (wLED)]、『*日本セラミックス協会年会　第27回秋季シンポジウム*』、No. 1C-08 (鹿児島, 9/9-11, 2014)
2. **(Oral) Jian Xu**, Jumpei Ueda, Keisuke Kuroishi, Setsuhisa Tanabe, [Fabrication and Luminescent

Properties of Ce^{3+}:$Gd_3Al_{5-x}Ga_xO_{12}$ Garnet (Ce:GAGG) Persistent Transparent Ceramic Phosphors with Cr^{3+} and Pr^{3+} Codopant for White LED]、『***第 55 回ガラスおよびフォトニクス材料討論会と第 10 回ガラス技術シンポジウム（GIC-10）***』、No. OA-04 (東京, 11/13-14, 2014)

2015

3. **(Oral)** **Jian Xu**, Jumpei Ueda, Setsuhisa Tanabe, [$Y_3Al_{5-x}Ga_xO_{12}$:Cr^{3+}: a novel red persistent ceramic phosphor with high brightness]、『***日本セラミックス協会 2015年 年会***』、No. 3B-10 (岡山, 3/18-20, 2015)
4. **(Oral)** **Jian Xu**, Jumpei Ueda, Setsuhisa Tanabe, [Multi-wavelengths long persistent luminescence of $Y_3Al_2Ga_3O_{12}$:Ce^{3+}, Nd^{3+}, Cr^{3+} through persistent energy transfer for the first and second bio-imaging window of NIR region]、『***日本セラミックス協会年会 第28回秋季シンポジウム***』、No. 3F-15 (富山, 9/16-18, 2015)

2016

5. **(Oral)** **Jian Xu**, Jumpei Ueda, Setsuhisa Tanabe, [Design of novel persistent phosphors using vacuum referred binding energy (VRBE) diagram in yttrium aluminum gallium garnet (YAGG) host]、『***日本セラミックス協会 2016年 年会***』、No. 1C-19 (東京, 3/14-16, 2016)
6. **(Oral)** **Jian Xu**, Jumpei Ueda, Setsuhisa Tanabe, [Design of novel garnet persistent phosphors with red/NIR persistent luminescence for the first bio-imaging window]、『***日本セラミックス協会年会 第 29 回秋季シンポジウム***』、No. 3H-15 (広島, 9/7-9, 2016)

Academic Funding (PI)

1. 平成26年度 第18回丸文財団交流研究助成(150 万円)
   研究課題:『長残光機能を有する白色 LED 用 Ce^{3+}添加ガーネット透光性セラミックスの創製及び光物性評価』
2. 平成28年度 日本学術振興会 科学研究費助成事業（特別研究員奨励費）(120 万円)
   研究課題:『電子構造制御に基いた長残光透光性セラミック材料の創製及び光物性評価』
3. 平成29年度 日本学術振興会 科学研究費助成事業（特別研究員奨励費）(110 万円)
   研究課題:『電子構造制御に基いた長残光透光性セラミック材料の創製及び光物性評価』

Award

1. 『2015 Chinese Government Award for Outstanding Self-financed Students Abroad』
   『2015 年度国家优秀自费留学生奖学金』**Jian Xu**, Tokyo, Japan, (Apr. 25, 2016)

Acknowledgements

Although only my own name is on the cover of this dissertation, I would like to take this opportunity to express my sincere appreciation to these important persons, whose supports, encouragements and wishes help/motivate me to finish this dissertation.

First of all, I would like to express my deepest gratitude to my supervisor, Prof. Setsuhisa Tanabe, who is the principle investigator (PI) of the Tanabe Lab (Photonic Materials Laboratory) at Graduate School of Human and Environmental Studies in Kyoto University. Under his careful and patient guidance, my research work becomes more accurate and efficient with the help of spectroscopy knowledge than ever before, and definitely I become more and more interested in this research field. Furthermore, beyond the solid knowledge on science, his passionate living style and so many wonderful academic/non-academic events he organized make me fully enjoyed in Japan, and also motivate me to be more confident and positive to face different challenges both on research and life in the future.

At the same time, I would like to sincerely thank another big man in Tanabe Lab, Assistant Prof. Jumpei Ueda for so many fruitful discussions on this dissertation during these three years. His keen insight on the research, great power on designing experimental strategies and constructing measurement setups make me greatly impressive. No doubt, he has already been a bright star in the research field of photonic materials among all the new generation scientists in the world, and of course set an excellent example for me to follow.

Deep gratitude is also expressed to the previous members of the Tanabe Lab: Assistant Prof. Yixi Zhuang from College of Materials, Xiamen University, for his heartfelt recommending me to this lab, many important suggestions/helps for me to live well in Japan. Honestly to say, without his help and recommendation, I totally cannot knock the door of this lab; Assistant Prof. Yumiko Katayama from Graduate School of Arts and Sciences, the University of Tokyo, for her excellent cooperation and many valuable discussions on the research; Assistant Prof. Takayuki Nakanishi from Faculty of Engineering, Hokkaido University, for his heartful encouragement and passionate personality; Dr. Atul D. Sontakke from Chimie-Paris Tech, for his patiently answering a torrent of academic questions.

I would like also thank Prof. Pieter Dorenbos from Delft University of Technology, Prof. Bruno Viana from Chimie-Paris Tech and Prof. Peter A Tanner from the Hong Kong Institute of Education, who stayed at Kyoto University as visiting professors (2013-2015), for their excellent and comprehensive tutorial talks every Monday afternoon. The charming knowledge about materials design, materials chemistry, quantum physics, spectroscopy, and even biology they taught and shared has already been a brilliant light in my research life and led me to go

forward with confidence.

I would like also thank Prof. Kazuyuki Hirao, Prof. Katsuhisa Tanaka, Associate Prof. Koji Fujita, Assistant Prof. Masayuki Nishi, Assistant Prof. Masahiro Shimizu and Assistant Prof. Shunsuke Murai, from Graduate School of Engineering, Kyoto University for their continued support and encouragement. The precious time in every mid-term joint research seminar and every energetic sports camp will be a sweet memory I will never forget.

Special thanks I would like to give to Prof. Takayuki Yanagida, Assistant Prof. Go Okada, and Mr. Masaki Mori from Graduate School of Materials, Nara Institute of Science and Technology (NAIST), for the fruitful cooperation on the scintillation behaviors of garnet transparent ceramics; Dr. Morgane Pellerin from Chimie-Paris Tech, and Dr. Michele Back from Ca' Foscari University of Venice, for their important discussions on persistent luminescence nano-particles (PLNPs) and optical thermometers, respectively.

I also would like to thank Prof. Naoki Komatsu, Dr. Li Zhao, and Dr. Hongmei Qin from Graduate School of Human and Environmental Studies, Kyoto University for the promising cooperation and fruitful discussion on the knowledge of surface modification for nano-particles, cell experiments and *in vivo* bio-imaging.

I also wish to acknowledge other members and previous members of the Tanabe Lab: Ms. Maki Kubo for so many supports for me to live well in Kyoto, also the homepage of the Tanabe lab under her management is the best one among what I have ever seen before; Mr. Keisuke Kuroishi and Mr. Atsunori Hashimoto for their pioneering work on YAG*G* persistent phosphors; Mr. Tomohiro Kayumi for his excellent one-to-one Japanese teaching courses; Mr. Kazuki Aasami for his many helps on the optical measurements; Mr. Daisuke Murata for his great efforts on the development of Er^{3+} doped persistent phosphors; Associate Prof. Song Ye, Mr. Tatsuaki Shinoda, Mr. Takayuki Shimizu, Mr. Hiroki Nakahara, Miss. Noriko Matsuzaki, Mr. Hiroaki Kobayashi, Mr. Atsushi Hoshino, Mr. Ryomei Maki, Mr. Shun Miyano, Mr. Kotaro Yasuda, Mr. Takayuki Tokunaga, Mr. Masaya Harada, Mr. Yuuki Kitagawa for many many wonderful moments we together with.

Finally, I would like to deeply thank my parents, Dongyan Xu and Yanyuan Gu for their supports, understanding and encouragements; and also my wife, Min Feng for her endless love and careful consideration for my daily life in Japan. So many delicious and classical Chinese foods she cooked, and memorable moments we together experienced make me realize that what a happiest and lucky person I am.

Jian Xu

2017/01/18 in Kyoto, Japan